

**GAZIANTEP UNIVERSITY GRADUATE  
SCHOOL OF NATURAL & APPLIED SCIENCES**

**MESHFREE METHODS FOR  
2D ELASTO-PLASTIC LARGE  
DEFORMATION PROBLEMS**

**Ph.D. THESIS  
IN  
MECHANICAL ENGINEERING**

**BY  
Ö. YAVUZ BOZKURT  
JAN 2011**

**Meshfree Methods for 2D Elasto-Plastic Large  
Deformation Problems**

**Ph.D. Thesis  
in  
Mechanical Engineering  
University of Gaziantep**

**Supervisor  
Assoc. Prof. Dr. Bahattin KANBER**

**by  
Ö.Yavuz BOZKURT**

**Jan 2011**


T.C.  
UNIVERSITY OF GAZIANTEP  
GRADUATE SCHOOL OF  
NATURAL & APPLIED SCIENCES  
NAME OF THE DEPARTMENT

Name of the thesis: Meshfree methods for 2d elasto-plastic large deformation problems


Name of the student: Ömer Yavuz BOZKURT

Exam date: 28-01-2011


Approval of the Graduate School of Natural and Applied Sciences

  
Prof. Dr. Ramazan KOÇ  
Director

I certify that this thesis satisfies all the requirements as a thesis for the degree of Doctor of Philosophy.

  
Prof. Dr. L. Canan DÜLGER  
Head of Department

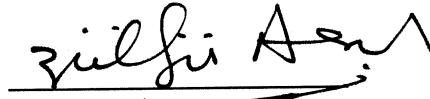
This is to certify that we have read this thesis and that in our consensus it is fully adequate, in scope and quality, as a thesis for the degree of Doctor of Philosophy.

  
Assoc. Prof. Dr. Bahattin KANBER  
Supervisor

Examining Committee Members

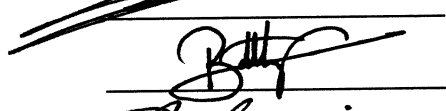
signature

Prof. Dr. M. Zülfü AŞIK

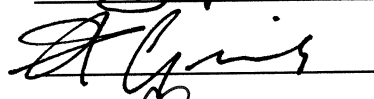


Prof. Dr. İ. Halil GÜZELBEY

Assoc. Prof. Dr. Bahattin KANBER



Assoc. Prof. Dr. Abdülkadir ÇEVİK



Assist. Prof. Dr. Ahmet ERKLİĞ



## ABSTRACT

### MESHFREE METHODS FOR 2D ELASTO-PLASTIC LARGE DEFORMATION PROBLEMS

BOZKURT Ö. Yavuz

Ph.D. in Mechanical Eng.

Supervisor: Assoc. Prof. Dr. Bahattin KANBER

Jan 2011, 172 pages

In this work, PIM and RPIM are used in the solution of 2D geometrical nonlinear and elasto-plastic problems. The effect of shape parameters are investigated in the solutions. The optimum values of shape parameters are either validated or proposed.

The singular moment matrix problem in the PIM is discussed in detail and two new algorithms are proposed: A diagonal offset algorithm and Regular based algorithm. They are numerically tested and applied in the solution of 2D elastic problems. The regular basis algorithm gives excellent results with regular distributed field nodes.

A number of programs are developed for the solution of 2D geometrically nonlinear and elasto-plastic problems. Mathematica, Fortran 95 and Matlab are used in the programming stages. The PIM and RPIM shape function are successfully implemented in these programs.

**Keywords:** Meshfree Methods, PIM, RPIM, Radial basis functions, Polynomial basis functions, Moment matrix, Geometrically nonlinear problems, Elasto-plastic problems.

## ÖZET

### 2B BÜYÜK DEFORMASYON PROBLEMLERİ İÇİN AĞSIZ YÖNTEMLER

BOZKURT Ö. Yavuz  
Doktora Tezi, Mak Müh. Bölümü  
Tez Yöneticisi: Doç. Dr. Bahattin KANBER  
Ocak 2011, 172 sayfa

Bu çalışmada PIM ve RPIM 2B geometrik nonlinear ve elasto-plastik problemlerin çözümünde kullanılmıştır. Şekil parametrelerinin çözümde etkisi araştırılmıştır. Şekil parameterelerinin optimum değerlerinin doğrulanması veya önerilmesi gerçekleştirilmiştir.

PIM'deki moment matris problemi detaylı olarak tartışılmış ve iki yeni algoritma önerilmiştir: Köşegen öteleme algoritması ve Düzgün taban algoritması. Algoritmalar numeric olarak test edilmiş ve 2B lineer elastic problemlere uygulanmıştır. Düzgün taban algoritması düzgün dağıtılmış düğüm noktaları ile mükemmel sonuç vermektedir.

2B geometric nonlinear ve elasto-plastik problemler için programlar yazılmıştır. Mathematica, Fortran 95 ve Matlab programlama aşamasında kullanılmıştır. PIM ve RPIM şekil fonksiyonları geliştirilen programlarda uygulanmıştır.

**Keywords:** Ağsız Yöntemler, PIM, RPIM, Radyal temel fonksiyonu, Polinom temel fonksiyonu, Moment matris, Geometrik nonlinear problemler, Elasto-plastik problemler.

## ACKNOWLEDGEMENTS

I would like to express my debt of gratitude to my supervisor Assoc.Prof.Dr. Bahattin KANBER for his guidance and suggestions during the preparation of this thesis.

I would also like to thank Prof.Dr. M. Zülfü AŞIK and Assist.Prof.Dr. Ahmet ERKLİĞ for their helps and discussions. I also appreciate to Prof.Dr. İbrahim Halil GÜZELBEY for his encouragement of all problems solution.

My very special thanks go to my best friend İbrahim GÖV.

The financial support of the TÜBİTAK is gratefully acknowledged.

I am also grateful to my wife and my daughter for their love and support.

## CONTENTS

ABSTRACT .....	i
ÖZET .....	ii
ACKNOWLEDGEMENTS .....	iii
TABLE OF CONTENTS .....	iv
LIST OF FIGURES .....	vii
LIST OF TABLES .....	xv
LIST OF SYMBOLS .....	xvi
1. INTRODUCTION.....	1
1.1. GENERAL INTRODUCTION .....	1
1.2. RESEARCH OBJECTIVES AND TASKS.....	2
1.3. LAYOUT OF THESIS .....	2
2. LITERATURE SURVEY .....	4
2.1. INTRODUCTION .....	4
2.2. GENERAL REVIEW OF MESHFREE METHODS .....	4
2.2.1. Smoothed Particle Hydrodynamics Method.....	4
2.2.2. Diffuse Element Method.....	4
2.2.3. Element Free Galerkin Method .....	5
2.2.4. Meshless Local Petrov-Galerkin Method.....	6
2.3. DETAILED REVIEW OF POINT INTERPOLATION METHOD.....	7
2.4. MESHFREE METHODS IN THE SOLUTION OF GEOMETRIC NONLINEAR AND ELASTO-PLASTIC PROBLEMS .....	7
2.5. CONCLUSIONS ON LITERATURE SURVEY .....	11
3. POINT INTERPOLATION METHODS.....	12
3.1. INTRODUCTION .....	12
3.2. A BRIEF REVIEW OF APPLICATION PROCEDURE FOR MESHFREE METHODS.....	12
3.3. BASIC DEFINITIONS FOR MESHFREE METHODS.....	13
3.3.1. Local Domains(Support and Influence Domains).....	13
3.3.2. Background Cells .....	14
3.4. POINT INTERPOLATION METHOD SHAPE FUNCTIONS.....	15
3.4.1. Polynomial Point Interpolation Method Shape Functions.....	15
3.4.2. Radial Point Interpolation Method Shape Functions.....	17
3.5. IMPLEMENTATION OF PIM SHAPE FUNCTIONS TO 2D LINEAR ELASTIC PROBLEMS.....	19
3.6. NUMERICAL EXAMPLES .....	24
3.7. RESULTS AND DISCUSSIONS.....	26
4. ANALYSES OF 2-D GEOMETRIC NONLINEAR PROBLEMS.....	27
4.1. INTRODUCTION .....	27
4.2. THE RPIM FORMULATION FOR GEOMETRICALLY NONLINEAR PROBLEMS..	28

4.3. NUMERICAL PROCEDURES .....	31
4.4. NUMERICAL EXAMPLES .....	32
4.4.1. Axially Loaded Plate .....	32
4.4.2. Plate with Hole .....	39
4.4.3. Cantilever Beam .....	46
4.4.4. Pressurized Thick-Walled Cylinder.....	53
4.5. RESULTS AND DISCUSSIONS.....	62
5. ANALYSES OF 2-D ELASTO-PLASTIC PROBLEMS .....	63
5.1. INTRODUCTION .....	63
5.2. THE ESSENTIALS ELEMENTS OF ELASTO-PLASTIC ANALYSIS .....	63
5.2.1. The Yield Criterion.....	63
5.2.1.1. The Tresca Yield Criterion.....	65
5.2.1.2. The von-Mises Yield Criterion .....	65
5.2.2. Hardening .....	66
5.2.3. Elasto-Plastic Stress-Strain Relation .....	68
5.3. THE RPIM FORMULATION FOR ELASTO-PLASTIC PROBLEMS.....	69
5.4. SUMMARY OF SOLUTION PROCEDURES .....	70
5.5. NUMERICAL EXAMPLES .....	72
5.5.1. End Loaded Cantilever Beam.....	72
5.5.2. Thick Walled Internally Pressurized Cylinder .....	77
5.5.3. Simply Supported Circular Plate .....	82
5.6. RESULTS AND DISCUSSIONS.....	87
6. A DIAGONAL OFFSET ALGROTIHM FOR THE POLYNOMIAL POINT INTERPOLATION METHOD .....	88
6.1. INTRODUCTION .....	88
6.2. SINGULARITY IN THE MOMENT MATRIX.....	88
6.3. A DIAGONAL OFFSET ALGORITHM TO AVOID SINGULARITY .....	89
6.4. NUMERICAL RESULTS AND DISCUSSIONS.....	90
6.4.1. Patch Tests.....	90
6.4.2. Axially Loaded Plate .....	97
6.4.3. Cantilever Beam .....	99
6.5. RESULTS AND DISCUSSIONS.....	100
7. A REGULAR BASIS ALGROTIHM FOR THE POLYNOMIAL POINT INTERPOLATION METHOD .....	101
7.1. INTRODUCTION .....	101
7.2. A DETAILED VIEW TO THE SELECTION OF THE POLYNOMIAL TERMS .....	101
7.3. A REGULAR BASIS ALGORITHM FOR THE POLYNOMIAL POINT INTERPOLATION METHOD.....	102
7.4. NUMERICAL TESTS .....	106
7.4.1. Patch Tests.....	106
7.4.2. Case Studies.....	108
7.4.2.1. Axially Loaded Bar .....	108
7.4.2.2. Cantilever Beam .....	111
7.4.2.3. Simply Supported Circular Plate .....	114
7.5. RESULTS AND DISCUSSIONS.....	117
8. CONCLUSIONS.....	118
FUTURE WORKS.....	120



APPENDIX.....	121
REFERENCES.....	156
VITAE.....	172

## LIST OF FIGURES

Figure 3.1	Illustration of background cells for integrations, support domain and influence domain .....	14
Figure 3.2	The Pascal's Triangle .....	15
Figure 3.3	The cantilever beam problem .....	24
Figure 3.4	The regular and irregular PIM model of cantilever beam problem .....	24
Figure 3.5	The transverse deflection along AB line of cantilever beam.....	25
Figure 3.6	The stress along AB line of cantilever beam .....	25
Figure 4.1	Axially loaded plate.....	32
Figure 4.2	RPIM models with regular and irregular distributed nodes and FEM model of axially loaded plate .....	33
Figure 4.3	RPIM solution steps of large deformation of the plate with regular distributed nodes .....	34
Figure 4.4	Displacement variations against load steps for RPIM regular and irregular distributed nodes and FEM at the point A on the axially loaded plate .....	34
Figure 4.5	Stress variations against load steps for RPIM regular and irregular distributed nodes and FEM at the point B on the axially loaded plate....	34
Figure 4.6	The convergence rate of displacements at the last load increment at the point A on the axial plate by increasing number of nodes used in the models .....	35
Figure 4.7	The convergence rate of stresses at the last load increment at point B on the axial plate by increasing number of nodes used in the models .....	35
Figure 4.8	Displacement variations at the point A on the plate against load steps for $q=1.03$ , $m=3$ and various $\alpha_c$ .....	36
Figure 4.9	Stress variations at the point B on the plate against load steps for $q=1.03$ , $m=3$ and various $\alpha_c$ .....	36
Figure 4.10	Displacement variations at the point A on the plate against load steps for $\alpha_c =4$ , $m=3$ and various $q$ .....	37

Figure 4.11 Stress variations at the point B on the plate against load steps for $\alpha_c = 4$ , $m=3$ and various $q$ .....	37
Figure 4.12 Displacement variations at the point A on the plate against load steps for $\alpha_c = 4$ , $q=1.03$ and various $m$ .....	38
Figure 4.13 Stress variations at the point B on the plate against load steps for $\alpha_c = 4$ , $q=1.03$ and various $m$ .....	38
Figure 4.14 A plate with hole.....	39
Figure 4.15 RPIM models with regular and irregular distributed nodes and FEM model of plate-hole problem.....	39
Figure 4.16 Initial coarse node distribution of RPIM model and its deformed shape in the last load increment.....	41
Figure 4.17 Initial fine node distribution of RPIM model and its deformed shape in the last load increment.....	41
Figure 4.18 Displacement variations against load steps for RPIM regular and irregular distributed nodes and FEM at the point A on the plate-hole problem.....	41
Figure 4.19 Stress variations against load steps for RPIM regular and irregular distributed nodes and FEM at the point B on the plate-hole problem....	42
Figure 4.20 The convergence rate of displacements at the last load increment at the point A on the plate with hole by increasing number of nodes used in the models.....	42
Figure 4.21 The convergence rate of stresses at the last load increment at the point A on the plate with hole by increasing number of nodes used in the models.....	43
Figure 4.22 Displacement variations at the point A on the plate with hole against load steps for $q=1.03$ , $m=3$ and various $\alpha_c$ .....	43
Figure 4.23 Stress variations at the point B on the plate with hole against load steps for $q=1.03$ , $m=3$ and various $\alpha_c$ .....	44
Figure 4.24 Displacement variations at the point A on the plate with hole against load steps for $\alpha_c = 4$ , $m=3$ and various $q$ .....	44
Figure 4.25 Stress variations at the point B on the plate with hole against load steps for $\alpha_c = 4$ , $m=3$ and various $q$ .....	45
Figure 4.26 Displacement variations at the point A on the plate with hole against load steps for $\alpha_c = 4$ , $q=1.03$ and various $m$ .....	45
Figure 4.27 Stress variations at the point B on the plate with hole against load steps for $\alpha_c = 4$ , $q=1.03$ and various $m$ .....	46

Figure 4.28 Cantilever beam .....	46
Figure 4.29 RPIM models with regular and irregular distributed nodes and FEM model of cantilever beam .....	47
Figure 4.30 RPIM solution steps of large deformation of the cantilever beam with regular distributed nodes .....	48
Figure 4.31 Displacement variations against load steps for RPIM regular and irregular distributed nodes and FEM at the point B on the cantilever beam .....	48
Figure 4.32 Stress variations against load steps for RPIM regular and irregular distributed nodes and FEM at the point A on the cantilever beam .....	49
Figure 4.33 The convergence rate of displacements at the last load increment at the point B on the cantilever beam by increasing number of nodes used in the models .....	49
Figure 4.34 The convergence rate of stresses at the last load increment at the point A on the cantilever beam by increasing number of nodes used in the models .....	50
Figure 4.35 Displacement variations at the point B on the cantilever beam against load steps for $q=1.03$ , $m=3$ and various $\alpha_c$ .....	50
Figure 4.36 Stress variations at the point A on the cantilever beam against load steps for $q=1.03$ , $m=3$ and various $\alpha_c$ .....	51
Figure 4.37 Displacement variations at the point B on the cantilever beam against load steps for $\alpha_c =4$ , $m=3$ and various $q$ .....	51
Figure 4.38 Stress variations at the point A on the cantilever beam against load steps for $\alpha_c =4$ , $m=3$ and various $q$ .....	52
Figure 4.39 Displacement variations at the point B on the cantilever beam against load steps for $\alpha_c =4$ , $q=1.03$ and various $m$ .....	52
Figure 4.40 Stress variations at the point B on the cantilever beam against load steps for $\alpha_c =4$ , $q=1.03$ and various $m$ .....	53
Figure 4.41 Thick-walled pressurized cylinder.....	53
Figure 4.42 RPIM models with regular and irregular distributed nodes and FEM model of thick-walled pressurized cylinder .....	54
Figure 4.43 RPIM solution steps of large deformation of the thick-walled pressurized cylinder with regular distributed nodes.....	55
Figure 4.44 Radial displacement variations against load steps for RPIM regular and irregular distributed nodes and FEM at the point A	

on the thick-walled pressurized cylinder.....	55
Figure 4.45 Tangential stress variations against load steps for RPIM regular and irregular distributed nodes and FEM at the point A on the thick-walled pressurized cylinder.....	56
Figure 4.46 Radial stress variations against load steps for RPIM regular and irregular distributed nodes and FEM at the point A on the thick-walled pressurized cylinder.....	56
Figure 4.47 Radial stress variations against load steps for different RPIM regular distributed nodes and FEM at the point A on the thick-walled pressurized cylinder.....	57
Figure 4.48 The convergence rate of radial displacements at the last load increment at the point A on the thick-walled pressurized cylinder by increasing number of nodes used in the models.....	57
Figure 4.49 The convergence rate of radial stresses at the last load increment at the point A on the thick-walled pressurized cylinder by increasing number of nodes used in the models.....	58
Figure 4.50 The convergence rate of tangential stresses at the last load increment at the point A on the thick-walled pressurized cylinder by increasing number of nodes used in the models.....	58
Figure 4.51 Radial displacement variations at the point A against load steps for $q=1.03$ , $m=3$ and various $\alpha_c$ .....	59
Figure 4.52 Radial stress variations at the point A on the thick-walled pressurized cylinder against load steps for $q=1.03$ , $m=3$ and various $\alpha_c$ .....	59
Figure 4.53 Radial displacement variations at the point A on the thick-walled pressurized cylinder against load steps for $\alpha_c =4$ , $m=3$ and various $q$ ...	60
Figure 4.54 Radial stress variations at the point A on the thick-walled pressurized cylinder against load steps for $\alpha_c =4$ , $m=3$ and various $q$ ...	60
Figure 4.55 Radial displacement variations at the point A on the thick-walled pressurized cylinder against load steps for $\alpha_c =4$ , $q=1.03$ and various $m$ .....	61
Figure 4.56 Radial stress variations at the point A on the thick-walled pressurized cylinder against load steps for $\alpha_c =4$ , $q=1.03$ and various $m$ .....	61
Figure 5.1 Yield surface in two dimensional case .....	64
Figure 5.2 Tresca yield criteria in plane stress.....	65
Figure 5.3 The von Mises yield criteria in plane stress.....	66

Figure 5.4	Mathematical model for representation of hardening behaviours .....	67
Figure 5.5	Cantilever beam with an end load of 320 N .....	72
Figure 5.6	RPIM models with regular and irregular distributed nodes and FEM model of cantilever beam .....	73
Figure 5.7	The propagation of the plastic region and deformed shape as the load increases ( • shows the nodes in the plastic region. ) .....	73
Figure 5.8	Displacement variations against load steps for RPIM regular distributed nodes with $\alpha_c = 2$ and $q = 1.03$ at the free end of cantilever beam .....	74
Figure 5.9	Displacement variations against load steps for RPIM irregular distributed nodes with $\alpha_c=2$ and $q=1.03$ at the free end of cantilever beam .....	74
Figure 5.10	Displacement variations against load steps for ANSYS with different number of nodes at the free end of cantilever beam.....	75
Figure 5.11	Displacement variations against load steps for RPIM regular distributed nodes with $q = 1.03$ and different $\alpha_c$ at the free end of cantilever beam .....	75
Figure 5.12	Displacement variations against load steps for RPIM irregular distributed nodes with $q = 1.03$ and different $\alpha_c$ at the free end of cantilever beam .....	76
Figure 5.13	Displacement variations against load steps for RPIM regular distributed nodes with $\alpha_c = 7.0$ and different $q$ at the free end of cantilever beam .....	76
Figure 5.14	Displacement variations against load steps for RPIM irregular distributed nodes with $\alpha_c = 7.0$ and different $q$ at the free end of cantilever beam .....	77
Figure 5.15	Thick-walled pressurized cylinder and its axisymmetric model .....	78
Figure 5.16	PIM models with regular and irregular distributed nodes and FEM model of thick-walled pressurized cylinder .....	78
Figure 5.17	The propagation of the plastic region and deformed shape of thick walled cylinder as the load increases ( • shows the nodes in the plastic region. ) .....	78
Figure 5.18	Displacement variations against load steps for RPIM regular distributed nodes with $\alpha_c=4$ and $q=1.03$ at the outer surface of thick walled pressurized cylinder.....	79
Figure 5.19	Displacement variations against load steps for RPIM irregular distributed nodes with $\alpha_c=4$ and $q=1.03$	

at the outer surface of thick walled pressurized cylinder .....	79
Figure 5.20 Displacement variations against load steps for ANSYS with different number of nodes at the outer surface of thick walled pressurized cylinder.....	80
Figure 5.21 Displacement variations against load steps for RPIM regular distributed nodes with $q = 1.03$ and different $\alpha_c$ at the outer surface of thick walled pressurized cylinder.....	80
Figure 5.22 Displacement variations against load steps for RPIM regular distributed nodes with $\alpha_c = 7.0$ and different $q$ at the free end of cantilever beam .....	81
Figure 5.23 Displacement variations against load steps for RPIM irregular distributed nodes with $q = 1.03$ and different $\alpha_c$ at the outer surface of thick walled pressurized cylinder.....	81
Figure 5.24 Displacement variations against load steps for RPIM irregular distributed nodes with $\alpha_c = 7.0$ and different $q$ at the free end of cantilever beam .....	82
Figure 5.25 Axi-symmetric model and its dimensions of uniform pressurized simply supported circular plate .....	83
Figure 5.26 RPIM models with regular and irregular distributed nodes and FEM model of uniform pressurized simply supported circular plate .....	83
Figure 5.27 The propagation of the plastic region and deformed shape of uniform pressurized simply supported circular plate as the pressure increases ( • shows the nodes in the plastic region. ) .....	83
Figure 5.28 Central deflections of uniform pressurized simply supported circular plate against load steps for RPIM regular distributed nodes ..	84
Figure 5.29 Central deflections of uniform pressurized simply supported circular plate against load steps for RPIM irregular distributed .....	84
Figure 5.30 Central deflections of uniform pressurized simply supported circular plate against load steps for ANSYS with different number of nodes .....	85
Figure 5.31 Central deflections of uniform pressurized simply supported circular plate against load steps for RPIM regular distributed nodes with $q=1.03$ and different $\alpha_c$ .....	85
Figure 5.32 Central deflections of uniform pressurized simply supported circular plate against load steps for RPIM irregular distributed nodes with $q=1.03$ and different $\alpha_c$ .....	86
Figure 5.33 Central deflections of uniform pressurized simply supported	

	circular plate against load steps for RPIM regular distributed nodes with $\alpha_c = 7.0$ and different $q$ .....	86
Figure 5.34	Central deflections of uniform pressurized simply supported circular plate against load steps for RPIM irregular distributed nodes with $\alpha_c = 7.0$ and different $q$ . .....	87
Figure 6.1	A local domain causes singularity in the moment matrix .....	89
Figure 6.2	Patch tests with a) 3x3 regular nodes, b) 4x3 regular nodes, c) 9 irregular nodes, d) 12 irregular nodes .....	91
Figure 6.3	The axial displacements ( $U_x$ ) at node 5 for different values of $k$ (The patch of 3x3 regular distributed nodes) .....	92
Figure 6.4	The axial stress ( $\sigma_x$ ) at node 5 for different values of $k$ (The patch of 3x3 regular distributed nodes) .....	93
Figure 6.5	The axial displacements ( $U_x$ ) at node 5 for different values of $k$ (The patch of 4x3 regular distributed nodes) .....	93
Figure 6.6	The axial stress ( $\sigma_x$ ) at node 5 for different values of $k$ (The patch of 4x3 regular distributed nodes) .....	94
Figure 6.7	The axial displacements ( $U_x$ ) at node 5 for different values of $k$ (The patch of 9 irregular distributed nodes) .....	95
Figure 6.8	The axial stress ( $\sigma_x$ ) at node 5 for different values of $k$ (The patch of 9 irregular distributed nodes) .....	96
Figure 6.9	The axial displacements ( $U_x$ ) at node 5 for different values of $k$ (The patch of 12 irregular distributed nodes) .....	96
Figure 6.10	The axial stress ( $\sigma_x$ ) at node 5 for different values of $k$ (The patch of 12 irregular distributed nodes) .....	97
Figure 6.11	Axially loaded plate and its PIM model .....	97
Figure 6.12	Axial displacement distributions of rectangular plate with $k=6$ .....	98
Figure 6.13	Axial stress distributions of rectangular plate with $k=6$ .....	98
Figure 6.14	Cantilever beam and its PIM model .....	99
Figure 6.15	Vertical displacement distributions along the neutral line of cantilever beam with $k=6$ .....	99
Figure 6.16	Axial stress distributions along the upper line of cantilever beam with $k=6$ .....	100
Figure 7.1	A regular basis algorithm for selection of the basis function terms ....	103
Figure 7.2	A rectangular support domain with irregular distributed nodes .....	104



Figure 7.3	Illustration of selection of the basis function terms for a rectangular support domain .....	104
Figure 7.4	An ellipse support domain with irregular distributed nodes.....	105
Figure 7.5	Illustration of selection of the basis function terms for an ellipse support domain.....	105
Figure 7.6	A patch test causes singularity in original PIM.....	106
Figure 7.7	Patch tests with regular node distributions .....	107
Figure 7.8	Axially loaded bar and the PIM model.....	109
Figure 7.9	Axial displacements of the bar .....	109
Figure 7.10	The axial stress distributions of the bar .....	110
Figure 7.11	The cantilever beam problem .....	111
Figure 7.12	The PIM model of cantilever beam problem.....	111
Figure 7.13	The lateral displacements along the mid-point of the cantilever beam.....	112
Figure 7.14	The axial stress distributions along the top surface of the cantilever beam.....	113
Figure 7.15	Simply supported circular plate .....	114
Figure 7.16	The PIM model of simply supported circular plate .....	115
Figure 7.17	The deflection profile of simply supported circular plate .....	115
Figure A.1	Thin plate .....	121

## LIST OF TABLES

Table 4.1	Comparison of data used in the RPIM and FEM models of axially loaded plate .....	33
Table 4.2	Comparison of data used in the RPIM and FEM models of the plate with hole. ....	40
Table 4.3	Comparison of data used in the RPIM and FEM models of cantilever beam .....	47
Table 4.4	Comparison of data used in the RPIM and FEM models of pressurized thick-walled cylinder .....	54
Table 6.1	PIM shape functions ( $\Phi$ ) for Node 5 for different values of $k$ (3x3 regular nodes).....	91
Table 6.2	PIM shape functions ( $\Phi$ ) for Node 5 for different values of $k$ (4x3 regular nodes).....	91
Table 6.3	PIM shape functions ( $\Phi$ ) for Node 5 for different values of $k$ (3x3 regular nodes).....	94
Table 6.4	PIM shape functions ( $\Phi$ ) for Node 5 for different values of $k$ (4x3 regular nodes).....	95
Table 7.1	Singularity and accuracy results of the patch tests. ....	108
Table 7.2	The displacement and stress values in axial direction of the bar for different sizes of the domains. (Original PIM has singularity problem. Only PIM with regular based results listed.) .....	111
Table 7.3	The transverse displacements and $S_x$ along AB line using different domain sizes. (Original PIM has singularity problem. Only PIM with regular based results listed.) .....	114
Table 7.4	The deflection profile of simply supported circular plate for different domain sizes. (Original PIM has singularity problem. Only PIM with regular based results listed.) .....	116

## LIST OF SYMBOLS

$x_Q$	=	Point of interest
$p$	=	Polynomial basis function
$a$	=	Coefficient for the radial basis functions
$\mathbf{U}_S$	=	Nodal displacement vector of local domain
$\mathbf{a}$	=	Coefficients vector of radial basis functions
$\mathbf{b}$	=	Coefficients vector of polynomial basis functions
$\mathbf{P}_Q$	=	Polynomial moment matrix
$\phi$	=	Shape function
$\Phi$	=	Shape function matrix
$u^h$	=	Approximated displacement of a point of interest
$\mathbf{u}$	=	Displacement vector
$R$	=	Radial basis function
$b$	=	coefficient for the polynomial basis function
$\alpha_c$	=	Dimensionless shape parameter of RPIM
$q$	=	Dimensionless shape parameter of RPIM
$\mathbf{R}_Q$	=	Moment matrix of radial basis functions
$\mathbf{G}$	=	Combination of polynomial and radial moment matrix
$\Omega$	=	Domain
$\Gamma$	=	Boundary of domain
$\mathbf{L}$	=	Differential operator
$\Gamma_u$	=	Part of the boundary where displacements are prescribed
$\Gamma_t$	=	Part of the boundary where traction is applied
$\mathbf{D}$	=	Material matrix (constitutive matrix)

$\boldsymbol{\varepsilon}$	=	Strain vector
$\mathbf{B}$	=	The matrix of derivatives of the nodal shape functions
$\boldsymbol{\sigma}$	=	Stress vector
$\mathbf{K}$	=	Global stiffness matrix
$w$	=	Gauss weighting factor
$\mathbf{J}$	=	Jacobian matrix for the area integration of the background cell
$\mathbf{F}$	=	Deformation gradient tensor
$d$	=	Displacement tensor
$\hat{\mathbf{S}}$	=	Second Piola-Kirchhoff stress
$\mathbf{f}_b$	=	Body force vector
$\mathbf{f}_q$	=	Surface force vector
$\hat{\boldsymbol{\varepsilon}}$	=	Green-Lagrange strain vector
$\mathbf{F}$	=	Matrix form of deformation gradient tensor
$\mathbf{c}_1$	=	Right Cauchy-Green tensor
$\lambda$	=	Lame's constant
$\mu$	=	Lame's constant
$\bar{\mathbf{S}}$	=	Initial stress matrix
$\mathbf{S}$	=	Second Piola-Kirchhoff stresses in a vector form
$A^0$	=	Initial domain
$\mathbf{K}_c$	=	Current stiffness matrix
$\mathbf{K}_s$	=	Geometric stiffness matrix
$\mathbf{r}_i$	=	Equivalent nodal load vector due to stresses in the current known configuration
$\mathbf{r}_q$	=	Equivalent nodal load vector due to surface forces
$\mathbf{r}_b$	=	Equivalent nodal load vector due to body forces
$\bar{\mathbf{F}}$	=	Arranged deformation gradient matrix
$\mathbf{I}$	=	Unit matrix

$\mathbf{c}_2$	=	Left Cauchy-Green tensor
$\mathbf{K}_T$	=	Tangential stiffness matrix
$\Delta \mathbf{f}$	=	Residual forces vector in geometric nonlinear problems
$\mathbf{f}^{int}$	=	Internal forces vector due to the stresses
$\mathbf{f}^{ext}$	=	Applied forces vector
$f_y$	=	Yield function
$w^p$	=	Plastic work
$\boldsymbol{\alpha}$	=	Vector denoting the translation of the yield surface
$I$	=	Invariants of the stress tensor
$J$	=	Invariants of the deviatoric stress tensor
$\tau$	=	Shear stress
$k$	=	Material parameter
$\sigma_0$	=	Yield stress value in the uniaxial tension test
$\sigma_e$	=	Effective stress (or equivalent stress)
$\boldsymbol{\varepsilon}_p$	=	Plastic strain vector
$\boldsymbol{\varepsilon}_e$	=	Elastic strain vector
$Q$	=	Plastic potential
$d\lambda$	=	Plastic multiplier
$\mathbf{D}_{ep}$	=	Generalized form tangent modulus
$\delta \mathbf{u}$	=	Internal displacements
$\mathbf{N}$	=	Matrix of shape functions
$\delta \mathbf{d}$	=	Virtual displacement vector
$\psi$	=	Residual force vector in elasto-plastic problems
$\delta \boldsymbol{\varepsilon}$	=	Virtual strain vector
$off$	=	Offset value
$Mde$	=	minimum value in the diagonal line of the moment matrix

# CHAPTER 1

## INTRODUCTION

### 1.1 General Introduction

The usage of numerical methods for the solution of a variety of problems encountered in engineering makes the numerical methods an important tool for engineering analysis and designs. The numerical methods become more effective and more powerful by proposing new algorithms. Meshfree methods are the particular class of numerical simulation techniques and developed to improve efficiency of engineering analysis by eliminating short-comings in the popular numerical methods such as finite element method (FEM), boundary element method (BEM) and finite difference method (FDM).

The FEM and BEM are robust numerical methods. FEM is well established. However, BEM still includes some problems such as singularity near to the boundary. The mesh requirement, such as predefined element in FEM, BEM and predefined grid in FDM, is common short-coming points of them. This causes the following limitations [1]:

- An analyst spends most of his/her time to the creation of proper mesh using predefined elements.
- The discontinuities of stress at the element interfaces are encountered.
- Distortion in elements causes accuracy loss.
- Crack growth and element boundary must coincide with each other to eliminate discontinuity.
- Remeshing of the regions that have high stresses like crack tips, contact points etc., is a difficult task and very complex mesh generation algorithm is required to update predefined elements.

The Meshfree methods are proposed to eliminate predefined mesh requirement which causes the above limitations. In Meshfree methods, a set of scattered nodes is used to define the domain and its boundary without forming a

predefined mesh. The field variables are interpolated according to the position of the scattered nodes without using any element either using moving least square (MLS) shape functions or point interpolation shape functions. Elimination of the mesh requirement solves the problems mentioned above. The developing stage of meshfree methods is very new and still continuing. Some issues, such as stability, accuracy, convergency and efficiency, must be solved to get more useful methods.

## **1.2 Research Objectives and Tasks**

In this study, the main objective is the investigation of meshfree methods to analyze elasto-plastic problems using Meshfree methods and proposing an improved or new Meshfree method. The research tasks can be summarized as follows,

- I. Reviewing the Meshfree methods in the literature.
- II. Obtaining the Meshfree shape functions.
- III. Implementing the Meshfree shape functions to Meshfree methods.
- IV. Using Meshfree methods for the solution of 2D linear elastic problems.
- V. Using Meshfree methods for the solution of 2D geometrically nonlinear problems.
- VI. Using Meshfree methods for the solution of 2D elasto-plastic problems.
- VII. Proposing new algorithms for Meshfree methods.
- VIII. Writing a general Meshfree method program to solve 2D elastic, 2D geometrically non-linear and elasto-plastic problems.

## **1.3 Layout of Thesis**

A literature review about Meshfree methods, implementation of Meshfree methods in geometrically nonlinear problems and elasto-plastic problems has been summarized in chapter two.

The Point Interpolation Method (PIM) is reviewed in chapter three. It starts with a brief description of PIM procedure and explanation of some basic terms used in it. Chapter three continues with construction of polynomial PIM and radial PIM (RPIM) shape functions. PIM formulation for 2D linear elastic problems are defined. Some 2D linear elastic case studies are presented.

Geometrically nonlinear analysis of 2D solids using RPIM is treated in chapter four. The solution procedure used is briefly described. Some case studies are presented.

Elasto-plastic analysis of 2D solids using radial RPIM is studied in chapter five. Some 2D elasto-plastic problems are solved and compared with FEM.

Chapter six is devoted to eliminate the singularity of the moment matrix in polynomial PIM. To do this, a diagonal offset algorithm is proposed and several patch tests are performed.

Chapter seven deals with the selection of polynomial terms for polynomial PIM. A regular basis algorithm for the polynomial PIM is proposed and it is tested.



## **CHAPTER 2**

### **LITERATURE REVIEW**

#### **2.1 Introduction**

There are lots of Meshfree methods can be found in the literature. The Smoothed Particle Hydrodynamics (SPH) method [3-6], the Diffuse Element Method (DEM) [7,8], the Element Free Galerkin (EFG) method [9-62], the Meshless Local Petrov-Galerkin (MLPG) method [63-85] and the Point Interpolation Method (PIM) [86-] are some of the proposed Meshfree methods.

The short review of the SPH method, DEM, EFG method and MLPG method are given in Section 2.2. The detailed literature review of PIM which is used during the study is represented in Section 2.3.

#### **2.2 General Review of Some Meshfree Methods**

##### **2.2.1 Smoothed Particle Hydrodynamics Method**

SPH method was developed by Lucy [3] and Gingold and Monaghan [4]. They used it to model astrophysical problems. In this method, the state of a system is represented by a set of moving particles and the governing partial differential equations are transformed into selected finite integral form [1,5]. The moving particles are used for interpolation through nodes. Since the proposition of method, many studies have been done to improve the consistency and accuracy of the method [5]. Application of method has been extended from astrophysical problems to wide range of engineering problems such as computational fluid dynamics, heat conduction, molecular dynamics, simulation of finite deformations, fracture, and crack growth [1,5,6].

##### **2.2.2 Diffuse Element Method**

DEM is the first Meshfree method based on global weak form [5]. It was proposed by Nayroles et al. [7]. The aim of the method is to eliminate discontinuity problem found in some derivatives of approximate solution and mesh generation. In

order to accomplish this, an element and its shape functions in FEM is replaced by local domains and the Moving Least Square (MLS) shape functions defined for local domains [8].

### 2.2.3 Element Free Galerkin Method

EFG method is a meshfree method which was proposed by Belytschko et al. [9]. In this method, the moving least square (MLS) shape functions are used for the interpolations. The problem domain and its boundary are represented by arbitrary distributed nodes. The MLS shape functions are obtained using the nodes in a local domain which is generally called as *support domain* or *influence domain*. Some predefined background cells must be defined for the integrations of Galerkin weak form integrals.

Belytschko et al. show that EFG method converges more rapidly than the FEM and the irregular distribution of nodes does not affect the accuracy of the solution. However, MLS shape functions lack Kronecker delta function property and Lagrange multipliers are used to enforce the essential boundary condition [9,10]. The use of Lagrange multipliers increases the cost of solving the linear algebraic equations. Therefore, a method has been developed to overcome this problem based on a modified variational principle [11]. It was shown that the speed of the computations in EFG method can be increased by smoothing the interpolants [12]. The shortcomings through the use of a set of MLS interpolants can also be alleviated by redefining the discrete norm [13], employing singular weight functions [14], modifying the collocation method using the actual nodal values of the trial function [15] and using the moving kriging (MK) interpolation [16].

EFG method also complicates the application of point loads because of the character of MLS. However, the concentrated forces should be transformed into distributed forces by a Dirac function. After such a transformation, the contribution of concentrated forces to the discrete equations can be evaluated in a way similar to the calculation of distributed load's contribution [17].

Volumetric locking is a problem which is appeared when the Poisson's ratio approaches the incompressibility limit 0.5. Volumetric locking causes some numerical problems and to solve these problems different EFG formulations have

been proposed [18-20]. It was shown that the problem can be avoided by considering appropriate nodal arrangements and integration cells.

EFG method does not require predefined meshes and converges rapidly. Therefore, the method has been used in the solution of many problems. It has been used for the solution of 2D and 3D fracture mechanics and crack propagation problems [21-29], the linear and nonlinear analysis of plates and shells [30-38], thermal and vibration analysis of composite structures [39-41].

To improve the efficiency and to use the advantages of different methods in the solutions of a specific problem, EFG method has been coupled with other numerical methods such as FEM, BEM and PIM [42-47]. The method has been also used for the elasto-plastic analysis of structures [48-50], the shape sensitivity analysis and shape optimization [51,52] and the analysis of porous solids [53,54].

Because of element free property of the method, it is very suitable for adaptive analyses. Therefore it is applied to error estimation and adaptive refinement problems [55-59]. It has been also applied to the heat transfer analysis of composite slabs [60], the structures with cyclic symmetry [61] and the structures with multi-scale geometries [62].

#### **2.2.4 Meshless Local Petrov-Galerkin Method**

Because of the global weak forms, EFG method and PIM requires background cells for the integration of Galerkin weak form integrals. Therefore, these methods are not accepted as truly Meshfree method [63]. In order to carry the numerical integration on a local domain, the weak forms should be defined on a local domain. In case of it, the dependency to global background integration cells is also eliminated. Therefore, the method can be called truly meshless method. To avoid the use of global background integration cells, a meshless local Petrov-Galerkin method (MLPG) was proposed by Atluri and Zhu [63]. In the MLPG method, the integration is carried on a local quadrature domain defined for a node. As in the EFG method, the MLS interpolation shape functions are used for the approximation of field variables.

The different versions of the MLPG method have been proposed and their performances have been investigated for the solution of 2D elasto-static and potential

problems [64-72]. The method has been also used for the analysis of thin and thick beams and plates under different boundary conditions [73-78]. It has been shown that the method is very effective in the solution of heat transfer and fluid mechanic problems [79-81].

The MLPG method has been also applied in the solution of free and forced vibration of solids [82], 2D frictionless dynamic contacts of large deformable bodies [83], semi-linear second-order hyperbolic problems [84] and the materials with strain-gradient effects [85].

The MLPG method is accepted as truly meshless method. However, it is computationally more expensive because of nodal numerical integrations and solution of asymmetric stiffness matrix [1,2].

### **2.3 Detailed Review of Point Interpolation Method**

In spite of the successful applications, meshless methods based on MLS have two major gaps in applications [86-88]. First one is the difficulties in the implementation of essential boundary conditions. The lack of Kronecker delta function properties for its shape functions cause this problem. Complexity of algorithms for the computations of shape functions and their derivatives is the second one. This increases the computational cost. Several approaches have been proposed to improve these points [89-92]. However, they cannot provide a full solution.

The solution to these gaps comes from another meshfree method named as Point Interpolation Method (PIM). It was proposed by Liu and Gu [93,94]. The field variables are interpolated using point interpolation shape functions. PIM shape functions are formed from polynomials. The polynomials are selected symmetrically from Pascal's triangle [94]. This makes the computation algorithm simple and straightforward for the shape function and its derivatives [95]. In contrast to MLS shape functions, point interpolation shape functions possess the Kronecker delta function property and they do not require an extra algorithm to compute nodal values of field variables. Also, the accuracy of PIM is higher than MLS approximation, especially for regular node distributions [95]. However, PIM is not perfect and it has its own weakness. The main problem in the polynomial PIM is the singularity of the moment matrix. Some algorithms are developed to overcome this problem.

Arbitrary scattered nodes in a local domain is one of the reasons of the singularity of moment matrix in some situations [1,94,95]. To eliminate this, changing the location of nodes in a local domain by a small amount [1,94] or the coordinate transformation in a local domain [1] can be used. However these cannot be guaranteed to eliminate singularity of moment matrix [1,95].

Improper selection of monomials in the basis is the another reason of the singularity [95]. To solve this, Matrix Triangularization Algorithm (MTA) was proposed by Liu and Gu [95]. In MTA, the nodes and the monomials, which cause the singularity in the moment matrix, are determined and are excluded from the influence domain, and monomials are excluded from moment matrix. PIM with the MTA is very effective in constructing Meshfree shape functions. It seems that MTA try to guarantee the proper construction of local domains and the proper selection of monomials. However, it may be numerically unstable especially for the larger influence domains [95].

Using the radial functions as the basis is also a solution of the singularity problem [1,86,87,96]. PIM based on radial basis functions (RBF) was developed by Wang and Liu [97]. RPIM shape functions also posses delta function property and computations of shape functions and their derivatives are simpler than MLS. To guarantee the solution of singularity problem, the polynomials are augmented to RBF [87,95,97]. The use of RBF solves the singularity, but it has some drawbacks. The accuracy of radial basis PIM is less than the polynomial basis PIM especially for regular node distributions [87,95]. The determination of shape parameters used in RPIM shape functions are required for the accuracy solution [1,95,98]. The computational efficiency is extremely reduced when the radial functions are used as the basis [86,87,96,99-101].

A simple and efficient algorithm to obtain an invertible moment matrix was proposed by Kanber and Bozkurt [102]. The idea behind the proposed method comes from changing the coordinates of a node in a local domain. Changing the value of coordinates of a node causes the change in the relevant row of the moment matrix. For example, if the coordinate of the  $n^{\text{th}}$  node in a local domain is changed, it results a change in the  $n^{\text{th}}$  row of the moment matrix. In spite of changing the moment matrix fully, change of the elements (except the first element) in the diagonal line of

the moment matrix is tried to avoid the singularity. It results a simple and effective algorithm. Compared to other singularity elimination methods, it does not add any extra calculations.

PIMs can be based on the Galerkin weak form [94]. This requires background cells for the integration. PIMs can be based on local Petrov-Galerkin weak forms [103-108]. These are truly Meshfree methods. PIMs can be used with boundary integration equation (BIE) [109].

The easy implementation and high accuracy give wide range application areas to polynomial PIM. It has been used for 2D and 3D elasticity problems [109-116], beam and shells [103,117], thermoelastic problems [118], piezoelectric structures [119] and microelectromechanical systems [120]. It can also be coupled with other numerical methods [121].

Stability and flexibility of the radial PIM is higher than polynomial PIM. Therefore, it is used in the solution of many structural problem solutions. It has been used for 2D and 3D solid mechanics problems [122,123], smart materials [124], beam, plates and shells [103,125-130], contact problems [131] and metal forming simulations [132]. It is used in the vibration analysis of 2D solids and shells [107,133], analysis of shell problems [134], geometrically nonlinear analysis of plates and cylindrical shells [135].

As mentioned before, the radial basis functions include some shape parameters which directly affect the shape function quality and solution accuracy. The effect of these parameters for the solution of solid mechanics problems were studied by Wang and Liu [86,136] and Liu et al. [122]. And the optimum range of values for  $q$  and  $\alpha_c$ , dimensionless shape parameters of multi-quadrics (MQ) type RBF, were proposed in this studies. Although, traditional values of  $q$  are -0.5 and 0.5, its optimum value is used as  $q=1.03$  in many studies [86, 106,107,122,128,133, 135,136]. Other values of  $q=0.999$  [137] and  $q=1.05$  [131] are very near to 1.03. The common result of many studies is that  $q$  cannot be an exact number, because it causes a non-invertible moment matrix [86,122,136].

$\alpha_c$  is an another dimensionless shape parameter and generally used as greater than 3 for most of the problems [2,122,130].  $\alpha_c= 3.5$  and  $\alpha_c= 4.0$  are proposed as

it's optimum values [122,130]. In addition, it is shown that when the polynomial terms are increased in the usual MQ basis functions, the effect of  $\alpha_c$  on the shape function quality is reduced [130].

#### **2.4 Meshfree Methods in the Solution of Geometric Nonlinear and Elasto-plastic Problems**

The finite element method (FEM) is a powerful technique and is widely used for the solution of a variety of problems encountered in engineering and science. However, the FEM has some defects such as low accuracy at large deformation problems and the discontinuity of stresses at the element boundaries. The source of these weaknesses comes from the mesh structure of the FEM which uses element based shape functions. Meshfree methods are used to eliminate such problems. Therefore, in this section, some Meshfree techniques for the solution of geometrically nonlinear and elastoplastic problems are reviewed.

Kargamovin et al. [138] used the EFG method to elasto-plastic stress analysis and applied for a crack problem. An enriched meshless method for fracture analysis of 2D nonlinear elastic solids under mode-I loading was proposed by Rao and Rahman [139]. The method comprises from an EFG method which enriched with two new basis functions. Xu and Saigal [140,141] developed an EFG based formulation for steady dynamic crack growth and quasi-static dynamic crack growth. Crack growth was simulated using small scale yielding condition in this formulation. EFG method was extended to elasto-plastic analysis of isotropic plates by Belinha and Dinis [142]. Liu et al. [143] proposed an EFG-FE coupling method with linear mathematical programming to solve elasto-plastic contact problems. Liu et al [144] employed an adaptive FE-EFG coupling method to simulate bulk metal forming process. It was examined with forging and extrusion examples. Barry and Saigal [145] applied EFG method to 3D elasto-plastic problems.

Guo et al. [146] implemented a rigid-plastic point collocation method to metal forming problem. Liu et al. [147] employed the Reproducing Kernel Particle Method (RKPM) to solve large deformation problems for structural dynamics. Chen et al. [148] used a Lagrangian RPKM for metal forming analysis. The large plastic deformations can be handled easily by the proposed method. The RKPM were used

in plane strain forging problem [149] and bulk forming problems [150]. The RPKM was also used for analysis of nonlinear hyperelasticity [151,152].

A point interpolation meshfree method for solving in elastic problems based Hencky's deformation theory was proposed by Dai et al. [153]. Wang et al. [154] developed parallel point interpolation method for simulation of 3D large deformation metal forming analysis. It is based on Galerkin weak form and shape functions uses radial basis functions. The large deformation analysis of elastic and elasto-plastic 3D beams based on the Natural Neighbour RPIM (NNRPIM) was proposed by Dinish et al. [155]. The NNRPIM is an improved version of RPIM.

## **2.5 Conclusions on Literature Survey**

The following conclusions were obtained from the literature reviews;

1. The PIM has singularity problem and there isn't an algorithm that fully solve this problem. The complexities of the proposed algorithms in the literature were another problem of the PIM. Also, it is seen that there is a gap for the selection of polynomial terms. The solution of singularity problem and the definition of a rule for the selection of polynomial terms may improve the PIM.
2. The RPIM is robust and stable. The optimum values for the solution of 2D and 3D elastic problems, plates, shells, smart materials and beams are already proposed in the literature. However, the effects of RPIM shape parameters for both geometrically nonlinear and elasto-plastic problems have not been investigated.



## **CHAPTER 3**

### **POINT INTERPOLATION METHOD**

#### **3.1 Introduction**

The Point Interpolation Method (PIM) is a Meshfree method. In the PIM, a set of arbitrarily distributed points is used to represent the problem domain and shape functions are constructed by using local groups of the arbitrarily distributed points. The shape functions of PIM have Kronecker delta function property which allows simple application of essential and natural boundary conditions [1]. In the literature, two common basis function forms, polynomial basis functions (PBF) and radial basis functions (RBF), are developed so far to form PIM shape functions.

In this chapter, application procedure of Meshfree methods in solid mechanics are briefly explained in section 3.2. The construction of shape functions using polynomial basis functions are detailed in section 3.3.1, and using radial basis functions are described in section 3.3.2. Some case studies are solved using polynomial PIM and radial PIM in section 3.4.

#### **3.2 A Brief Review of Application Procedure for Meshfree methods**

The application procedure of Meshfree methods can be summarized in four steps. These are domain representation, field interpolation, formulation of system equations and solution for field variables. In the first step, a set of nodes is used to represent the problem domain and its boundary. This does not mean domain is discretized and there is not any relation found between the nodes. After the domain representation, shape functions are constructed to compute field variables at any point in the problem domain. Construction of Meshfree shape functions are done in a local domain and using the nodes of that local domain. Shape functions and the number of nodes used in the formation of them are not known before they are constructed. These are opposed to FEM in which the shape functions and the number of nodes used is not predefined. The system equations are formulated in the third step. The equations of a Meshfree method can be formulated by a strong form system

equation or a weak form system equation for a local domain. The system equations of local domains are then combined to obtain global system equations for entire problem domain. The procedures of forming system equations are slightly different for different Meshfree methods. Last step comprises from the solution of global system equations for field variables. Any equation solver according to the problem type can be used.

### **3.3 Basic Definitions for Meshfree Methods**

In the application procedure of Meshfree methods, one always encounter a term named as local domain and a term called as background cell is sometimes experienced. The description of these terms is given in below sections.

#### **3.3.1 Local Domains (Support and Influence Domains)**

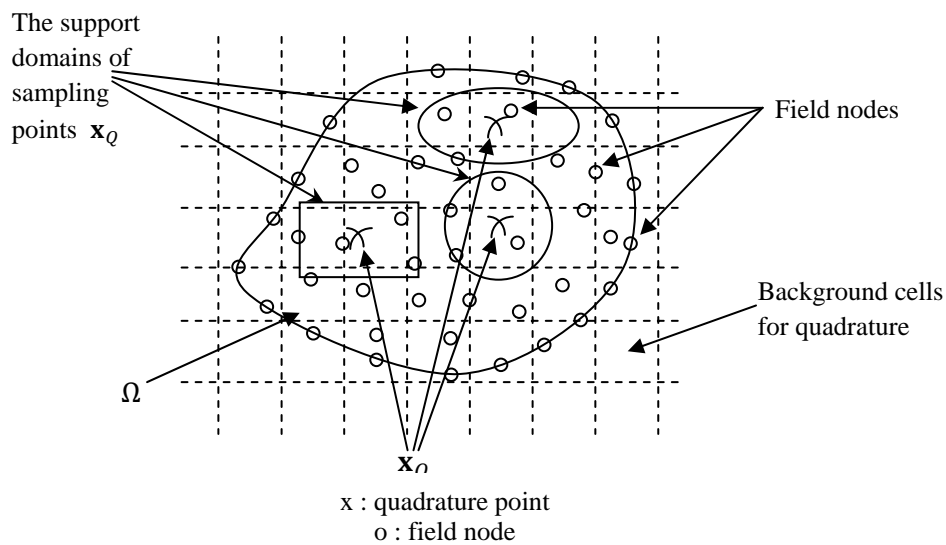
In FEM and BEM, the field variable is approximated in an element. The shape functions of elements are constructed before the usage of elements, and the number of nodes in an element is predetermined. However, in Meshfree methods, the field variable is interpolated using local domains and shape functions are constructed after the determination of local domains. Local domain construction does not contain any preliminary information about the number of nodes of the local domain.

Two types of local domains have been used to construct shape functions in Meshfree methods: Support domain and Influence domain. Support domain and Influence domain are often used for the same meaning. Support domain defines a selected area for the Meshfree interpolation of a point of interest. Also, it indicates the number of nodes that supported the approximation of field variable at the point of interest. Influence domain is an area that represents the area of the influence of the node. The influence domain works better than the support domain for irregularly distributed nodes [1].

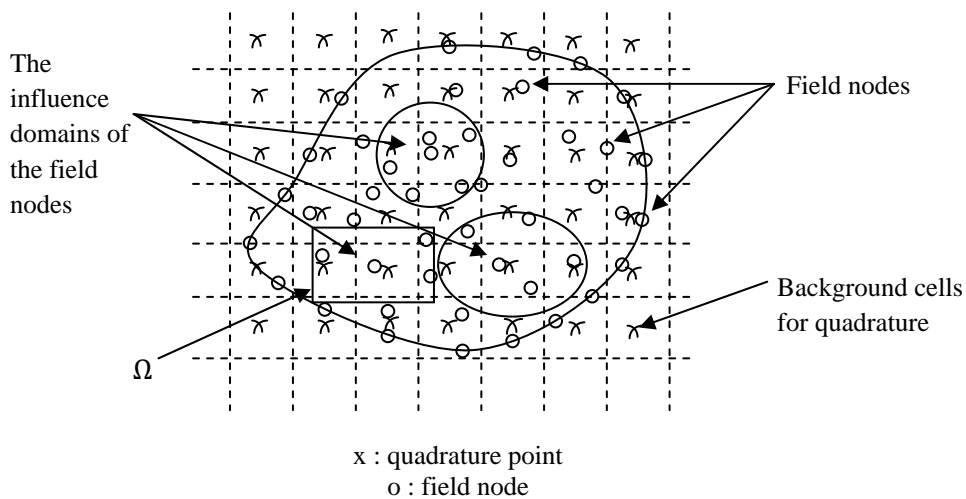
The centre of a support domain can be a sampling point or a field node and usually a Gauss sampling point is used. However, the centre of an influence domain must be a field node. The illustration of support domain and influence are shown in Figure 3.1.

### 3.3.2 Background Cells

To perform the numerical integrations in a Galerkin weak form formulation used Meshfree method, global problem domain is discretized into cells. These cells are called background cells and they can be rectangular or triangular for a two-dimensional domain. The background cells can be appeared as a mesh, but they aren't. In FEM, the mesh is used for both field approximation and integration, however, in the Meshfree methods, the background cells are used only for integration during the calculation of stiffness matrix. The background cells can be depicted as in Figure 3.1.



a) Support Domain; the centre is a quadrature point.



b) Influence Domain; the centre is a field node.

**Figure 3.1** Illustration of background cells for integrations, support domain and influence domain.

### 3.4. Point Interpolation Method (PIM) Shape Functions

#### 3.4.1 Polynomial Point Interpolation Shape Functions

The polynomial PIM approximates the displacement components using the nodes of local surrounding domain, support domain or influence domain, of the point of interest. This approximation is expressed as follows;

$$u(\mathbf{x}, \mathbf{x}_Q) = \sum_{i=1}^n p_i(\mathbf{x}) a_i(x_Q) = \mathbf{p}^T(\mathbf{x}) \mathbf{a}(x_Q) \quad (3.1)$$

where  $n$  is the number of nodes in the local surrounding domain of point of interest,  $\mathbf{x}_Q$ ,  $p_i(\mathbf{x})$  is the polynomial basis functions defined in the Cartesian coordinates and  $a_i(\mathbf{x}_Q)$  is the coefficient for the polynomial basis function  $p_i(\mathbf{x})$  of the point  $x_Q$ .

The polynomial basis functions are constructed from Pascal's triangle by selecting the terms symmetrically as shown in Figure 3.2.

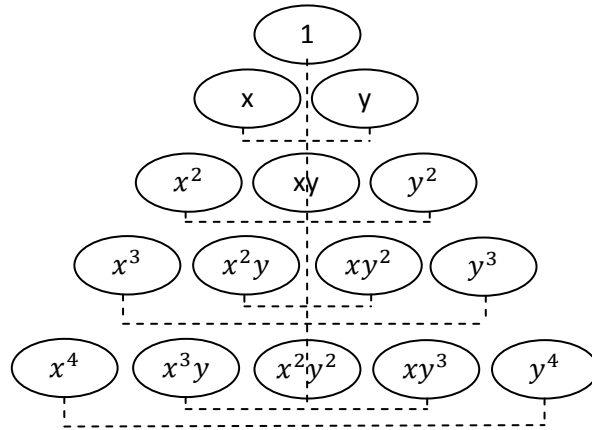


**Figure 3.2** The Pascal's Triangle

For one-dimensional domain, the polynomial basis functions have the following general form:

$$\mathbf{p}^T(\mathbf{x}) = \{1, x, x^2, x^3, x^4, \dots \dots x^n\} \quad (3.2)$$

and the general form of polynomial basis functions in two-dimensional domain is expressed as;

$$\mathbf{p}^T(\mathbf{x}) = \{1, x, y, xy, x^2, y^2, \dots \dots x^n, y^n\} \quad (3.3)$$

In a local surrounding domain Equation 3.1 must be satisfied for all nodes and this condition is defined as

$$\begin{aligned}
u_1 &= \sum_{i=1}^m a_i p(\mathbf{x}_1) = a_1 + a_2 x_1 + a_3 y_1 + \cdots + a_m p_m(\mathbf{x}_1) \\
u_2 &= \sum_{i=1}^m a_i p(\mathbf{x}_2) = a_1 + a_2 x_2 + a_3 y_2 + \cdots + a_m p_m(\mathbf{x}_2) \\
u_3 &= \sum_{i=1}^m a_i p(\mathbf{x}_3) = a_1 + a_2 x_3 + a_3 y_3 + \cdots + a_m p_m(\mathbf{x}_3) \\
&\quad \vdots \\
u_n &= \sum_{i=1}^m a_i p(\mathbf{x}_n) = a_1 + a_2 x_n + a_3 y_n + \cdots + a_m p_m(\mathbf{x}_n)
\end{aligned} \tag{3.4}$$

where  $p_m(\mathbf{x}_i)$  is the nodal value of last basis function term for node  $i$ ,  $m$  is the number of terms of basis function. Equation (3.4) can be written in the following matrix form:

$$\mathbf{U}_S = \mathbf{P}_Q \mathbf{a} \tag{3.5}$$

where

$$\mathbf{U}_S = \begin{bmatrix} u_1 \\ u_2 \\ \vdots \\ u_m \end{bmatrix} \tag{3.6}$$

is the nodal displacement vector of local domain,

$$\mathbf{a} = \begin{bmatrix} a_1 \\ a_2 \\ \vdots \\ a_m \end{bmatrix} \tag{3.7}$$

is the coefficients vector, and

$$\mathbf{P}_Q = \begin{bmatrix} 1 & x_1 & y_1 & x_1 y_1 & \cdots & p_m(\mathbf{x}_1) \\ 1 & x_2 & y_2 & x_2 y_2 & \cdots & p_m(\mathbf{x}_2) \\ 1 & x_3 & y_3 & x_3 y_3 & \cdots & p_m(\mathbf{x}_3) \\ \vdots & \vdots & \vdots & \vdots & \ddots & \vdots \\ 1 & x_n & y_n & x_n y_n & \cdots & p_m(\mathbf{x}_n) \end{bmatrix} \tag{3.8}$$

is the moment matrix of local domain. The number of nodes in a local surrounding domain,  $n$ , always equals to the number of terms of basis functions,  $m$ , in polynomial PIM.

The solution of Equation 3.5 for coefficients,  $\mathbf{a}$ , gives

$$\mathbf{a} = \mathbf{P}_Q^{-1} \mathbf{U}_S \quad (3.9)$$

The coefficients,  $\mathbf{a}$ , are constants for the nodes of same local domain groups.

Substitution of Equation 3.9 into Equation 3.1. yields

$$u(\mathbf{x}) = \mathbf{\Phi}(\mathbf{x}) \mathbf{U}_S \quad (3.10)$$

where  $\mathbf{\Phi}(\mathbf{x})$  is the matrix of shape functions and is defined by [1]

$$\mathbf{\Phi}(\mathbf{x}) = \mathbf{p}^T(\mathbf{x}) \mathbf{P}_Q^{-1} = [\phi_1(\mathbf{x}), \phi_2(\mathbf{x}), \phi_3(\mathbf{x}), \dots, \phi_n(\mathbf{x})] \quad (3.11)$$

### 3.4.2 Radial Point Interpolation Shape Functions

The radial basis function with polynomial terms approximates field variable using the nodes of local surrounding domain of the point  $x_Q$ . This approximation can be expressed as [1]

$$u^h(\mathbf{x}, \mathbf{x}_Q) = \sum_{i=1}^n R_i(\mathbf{x}) a_i + \sum_{j=1}^m p_j(\mathbf{x}) b_j = \mathbf{R}^T(\mathbf{x}) \mathbf{a} + \mathbf{p}^T(\mathbf{x}) \mathbf{b} \quad (3.12)$$

where  $n$  is the number of nodes in the local surrounding domain of point  $\mathbf{x}_Q$ ,  $a_i$  is the coefficient for the radial basis  $R_i(\mathbf{x})$ ,  $m$  is the number of polynomial basis functions and  $b_j$  is the coefficient for the polynomial basis function  $p_j(\mathbf{x})$ .

The distance between the point of interest  $\mathbf{x}_Q$  and a node at  $\mathbf{x}_i$  is the variable of the radial basis function  $R_i(\mathbf{x})$ .

$$r = \sqrt{(x_Q - x_i)^2 + (y_Q - y_i)^2} \text{ for 2-D problems} \quad (3.13)$$

There are different types of radial basis functions. The two most often used forms and their dimensionless parameters are listed in Table 1.

	Name	Equation	Shape Parameters
1	Multi-quadrics	$R_i(x, y) = (r_i^2 + (\alpha_c d_c)^2)^q$	$\alpha_c, q$
2	Gaussian	$R_i(x, y) = e^{-\alpha_c (\frac{r_i}{d_c})^2}$	$\alpha_c$

Table 1: Radial basis functions and their dimensionless shape parameters.

Enforcement of Equation 3.12 for all nodes within the local domain allows determining the coefficients  $a_i$  and  $b_j$ . It can be written in matrix form

$$\mathbf{U}_S = \mathbf{R}_Q \mathbf{a} + \mathbf{P}_m \mathbf{b} \quad (3.14)$$

where  $\mathbf{U}_S$  is the nodal displacement vector of local domain,

$$\mathbf{U}_S = \begin{bmatrix} u_1 \\ u_2 \\ \vdots \\ u_n \end{bmatrix} \quad (3.15)$$

$\mathbf{R}_Q$  is the moment matrix of radial basis functions,

$$\mathbf{R}_Q = \begin{bmatrix} R_1(r_1) & R_2(r_1) & \cdots & R_n(r_1) \\ R_1(r_2) & R_2(r_2) & \cdots & R_n(r_2) \\ \vdots & \vdots & \ddots & \vdots \\ R_1(r_n) & R_2(r_n) & \cdots & R_n(r_n) \end{bmatrix} \quad (3.16)$$

$\mathbf{P}_m$  is the polynomial moment matrix,

$$\mathbf{P}_m^T = \begin{bmatrix} 1 & 1 & \cdots & 1 \\ x_1 & x_2 & \cdots & x_n \\ y_1 & y_2 & \cdots & y_n \\ \vdots & \vdots & \ddots & \vdots \\ p_m(\mathbf{x}_1) & p_m(\mathbf{x}_2) & \cdots & p_m(\mathbf{x}_n) \end{bmatrix} \quad (3.17)$$

$\mathbf{a}$  is the coefficients vector of radial basis functions,

$$\mathbf{a}^T = \{a_1 \quad a_2 \quad \cdots \quad a_n\} \quad (3.18)$$

$\mathbf{b}$  is the coefficients vector of polynomial.

$$\mathbf{b}^T = \{b_1 \quad b_2 \quad \cdots \quad b_m\} \quad (3.19)$$

However, there are  $n + m$  variables in Equation 3.14. The additional  $m$  equations can be added using the following  $m$  constraint conditions.

$$\sum_{i=1}^n p_j(\mathbf{x}_i) a_i = \mathbf{P}_m^T \mathbf{a} = 0 \quad j = 1, 2, \dots, m \quad (3.20)$$

Combining Equations 3.14 and 3.20 yields the following set of equations in the matrix form

$$\tilde{\mathbf{U}}_S = \begin{bmatrix} \mathbf{U}_S \\ \mathbf{0} \end{bmatrix} = \begin{bmatrix} \mathbf{R}_Q & \mathbf{P}_m^T \\ \mathbf{P}_m^T & \mathbf{0} \end{bmatrix} \begin{Bmatrix} \mathbf{a} \\ \mathbf{b} \end{Bmatrix} = \mathbf{G} \mathbf{a}_0 \quad (3.21)$$

where

$$\mathbf{a}_0^T = \{a_1 \quad a_2 \quad \cdots \quad a_n \quad b_1 \quad b_2 \quad \cdots \quad b_m\} \quad (3.22)$$

$$\widetilde{\mathbf{U}}_S = \{u_1 \quad u_2 \quad \cdots \quad u_n \quad 0 \quad 0 \quad \cdots \quad 0\} \quad (3.23)$$

Because the matrix  $\mathbf{R}_Q$  is symmetric, the matrix  $\mathbf{G}$  will also be symmetric. Solving Equation 3.21, we obtain

$$\mathbf{a}_0 = \begin{Bmatrix} \mathbf{a} \\ \mathbf{b} \end{Bmatrix} = \mathbf{G}^{-1} \widetilde{\mathbf{U}}_S \quad (3.24)$$

Equation 3.12 can be re-written as

$$u^h(\mathbf{x}) = \mathbf{R}^T(\mathbf{x})\mathbf{a} + \mathbf{p}^T(\mathbf{x})\mathbf{b} = \{\mathbf{R}^T(\mathbf{x}) \quad \mathbf{p}^T(\mathbf{x})\} \begin{Bmatrix} \mathbf{a} \\ \mathbf{b} \end{Bmatrix} \quad (3.25)$$

Using Equation 3.24 we can obtain

$$u^h(\mathbf{x}) = \{\mathbf{R}^T(\mathbf{x}) \quad \mathbf{p}^T(\mathbf{x})\} \mathbf{G}^{-1} \widetilde{\mathbf{U}}_S \quad (3.26)$$

where the RPIM shape functions can be expressed as [2]

$$\widetilde{\Phi}^T(\mathbf{x}) = \{\mathbf{R}^T(\mathbf{x}) \quad \mathbf{p}^T(\mathbf{x})\} \mathbf{G}^{-1} \quad (3.27)$$

Finally, the RPIM shape functions corresponding to the nodal displacements vector  $\Phi(\mathbf{x})$  can be obtained considering the n-terms of shape functions.

### 3.5. Implementation of PIM Shape Functions to 2D Linear Elastic Problems

A two-dimensional linear solid mechanics problem defined in domain  $\Omega$  and bounded by  $\Gamma$  is considered for the formulation of PIM. The equilibrium, strain-displacement and constitutive equations can be used to describe the problem and they can be given as

$$\mathbf{L}^T \sigma + \mathbf{f}_b = 0 \quad \text{Equilibrium equation in problem domain } \Omega \quad (3.28)$$

$$\sigma \cdot \mathbf{n} = \bar{\mathbf{t}} \quad \text{Natural boundary condition on } \Gamma_t \quad (3.29)$$

$$\mathbf{u} = \bar{\mathbf{u}} \quad \text{Essential boundary condition on } \Gamma_u \quad (3.30)$$

where  $\mathbf{L}$  is the differential operator and is given by



$$\mathbf{L} = \begin{bmatrix} \frac{\partial}{\partial x} & 0 \\ 0 & \frac{\partial}{\partial y} \\ \frac{\partial}{\partial y} & \frac{\partial}{\partial x} \end{bmatrix} \quad (3.31)$$

$\boldsymbol{\sigma}^T = \{\sigma_{xx} \quad \sigma_{yy} \quad \tau_{xy}\}$  is the stress vector,  $\mathbf{u}^T = \{u \quad v\}$  is the displacement vector,  $\mathbf{f}_b^T = \{b_x \quad b_y\}$  is the body force vector,  $\bar{\mathbf{t}}$  is the prescribed traction on the natural boundaries,  $\bar{\mathbf{u}}$  is the prescribed displacement on the essential boundaries, and  $\mathbf{n}$  is the vector of unit outward normal at a point on the boundary.

The variational form of the equilibrium equation is expressed as [1]

$$\int_{\Omega} (\mathbf{L}\delta\mathbf{u})^T (\mathbf{D}\mathbf{L}\mathbf{u}) d\Omega - \int_{\Omega} \delta\mathbf{u}^T \mathbf{f}_b d\Omega - \int_{\Gamma_t} \delta\mathbf{u}^T \bar{\mathbf{t}} d\Gamma = 0 \quad (3.32)$$

where  $\mathbf{D}$  is the material matrix. Equation 3.32 is defined for the global problem domain,  $\Omega$ , so that it requires the background cells to evaluate integrals [1]. The point loads are defined in the traction force.

It should be remembered that the problem domain is represented by arbitrarily distributed nodes in the PIM, and the nodes are used for approximation of field variables by means of shape functions. The displacements at any point of interest can be approximated using the nodes of local surrounding domain of the point and it may be expressed as the follows [1];

$$\mathbf{u}_{(2 \times 1)}^h = \begin{Bmatrix} u \\ v \end{Bmatrix} = \begin{bmatrix} \phi_1 & 0 & \cdots & \phi_n & 0 \\ 0 & \phi_1 & \cdots & 0 & \phi_n \end{bmatrix} \begin{Bmatrix} u_1 \\ v_1 \\ \vdots \\ u_n \\ v_n \end{Bmatrix} = \boldsymbol{\Phi}_{(2 \times 2n)} \mathbf{u}_{(2n \times 1)} \quad (3.33)$$

where  $n$  is the number of nodes in the local surrounding domain, and  $\mathbf{u}$  is the displacement vector of nodes of local surrounding domain. Equation 3.33 can also be expressed as

$$\mathbf{u}_{(2 \times 1)}^h = \sum_i^n \begin{bmatrix} \phi_i & 0 \\ 0 & \phi_i \end{bmatrix} \begin{Bmatrix} u_i \\ v_i \end{Bmatrix} = \sum_i^n \boldsymbol{\Phi}_i \mathbf{u}_i \quad (3.34)$$

where  $\Phi_i$  is the matrix of shape functions of node  $i$ ,  $\mathbf{u}_i$  is the nodal displacements and  $\mathbf{u}^h$  is the approximated displacement of a point of interest. From Equation 3.34, we can obtain

$$\delta \mathbf{u} = \Phi_{(2 \times 2n)} \delta \mathbf{u}_{(2n \times 1)} = \sum_i^n \Phi_i \delta \mathbf{u}_i \quad (3.35)$$

The approximated displacements are used to obtain strains.

$$\begin{aligned} \boldsymbol{\varepsilon}_{(3 \times 1)} &= \mathbf{L} \mathbf{u}^h = \mathbf{L}_{(3 \times 2n)} \Phi_{(2 \times 2n)} \mathbf{u}_{(2n \times 1)} \\ &= \begin{bmatrix} \frac{\partial}{\partial x} & 0 \\ 0 & \frac{\partial}{\partial y} \\ \frac{\partial}{\partial y} & \frac{\partial}{\partial x} \end{bmatrix} \begin{bmatrix} \phi_1 & 0 & \dots & \phi_n & 0 \\ 0 & \phi_1 & \dots & 0 & \phi_n \end{bmatrix} \begin{Bmatrix} u_1 \\ v_1 \\ \vdots \\ u_n \\ v_n \end{Bmatrix} \\ &= \begin{bmatrix} \frac{\partial \phi_1}{\partial x} & 0 & \dots & \frac{\partial \phi_n}{\partial x} & 0 \\ 0 & \frac{\partial \phi_1}{\partial y} & \dots & 0 & \frac{\partial \phi_n}{\partial y} \\ \frac{\partial \phi_1}{\partial y} & \frac{\partial \phi_1}{\partial x} & \dots & \frac{\partial \phi_n}{\partial y} & \frac{\partial \phi_n}{\partial x} \end{bmatrix} \begin{Bmatrix} u_1 \\ v_1 \\ \vdots \\ u_n \\ v_n \end{Bmatrix} \\ &= \mathbf{B}_{(3 \times 2n)} \mathbf{u}_{(2n \times 1)} \\ &= \sum_i^n \mathbf{B}_i \mathbf{u}_i \end{aligned} \quad (3.36)$$

where  $\mathbf{B}$  is a matrix that includes the derivatives of the shape functions of the local surrounding domain.  $\mathbf{B}_i$  is the matrix that includes the derivatives of shape functions of node  $i$ . Using this,  $\mathbf{L} \delta \mathbf{u}^h$  can be expressed as

$$\begin{aligned} \mathbf{L} \delta \mathbf{u}^h &= \mathbf{L}_{(3 \times 2)} \Phi_{(2 \times 2n)} \delta \mathbf{u}_{(2n \times 1)} \\ &= \mathbf{B}_{(3 \times 2n)} \delta \mathbf{u}_{(2n \times 1)} \\ &= \sum_i^n (\mathbf{B}_i)_{(3 \times 2)} (\delta \mathbf{u}_i)_{(2 \times 1)} \end{aligned} \quad (3.37)$$

Using the constitutive equations for the material at the point, the stress vector can be expressed as

$$\begin{aligned}
\boldsymbol{\sigma} &= \mathbf{D}\boldsymbol{\varepsilon} = \mathbf{D}_{(3 \times 3)} \mathbf{B}_{(3 \times 2n)} \mathbf{u}_{(2n \times 1)} \\
&= \sum_i^n \mathbf{D}_{(3 \times 3)} (\mathbf{B}_i)_{(3 \times 2)} (\mathbf{u}_i)_{(2 \times 1)}
\end{aligned} \tag{3.38}$$

After the substitution of Equations (3.36) and (3.37) into the first term of Equation (3.32), we have

$$\begin{aligned}
\int_{\Omega} (\mathbf{L}\delta\mathbf{u})^T (\mathbf{D}\mathbf{L}\mathbf{u}) d\Omega &= \int_{\Omega} \left( \sum_i^n \mathbf{B}_i \delta\mathbf{u}_i \right)^T \left( \sum_j^n \mathbf{D}\mathbf{B}_j \mathbf{u}_j \right) d\Omega \\
&= \int_{\Omega} \sum_i^n \sum_j^n \delta\mathbf{u}_i^T [\mathbf{B}_i^T \mathbf{D}\mathbf{B}_j] \mathbf{u}_j d\Omega
\end{aligned} \tag{3.39}$$

Up to the present, the index  $i$  and  $j$  are used only for the nodes of a local surrounding domain. After this stage, they are changed from local surrounding domain to global problem domain. Therefore, both  $i$  and  $j$  in Equation (3.39) can now vary from 1 to  $N$ .  $N$  is the total number of nodes in the problem domain. With this modification, the integral in Equation 3.39 works only if nodes  $i$  and  $j$  are in the same local domain. Equation 3.39 can rewritten as

$$\int_{\Omega} (\mathbf{L}\delta\mathbf{u})^T (\mathbf{D}\mathbf{L}\mathbf{u}) d\Omega = \int_{\Omega} \sum_i^N \sum_j^N \delta\mathbf{u}_i^T [\mathbf{B}_i^T \mathbf{D}\mathbf{B}_j] \mathbf{u}_j d\Omega \tag{3.40}$$

The integration is taken inside of the summations to arrive at

$$\int_{\Omega} (\mathbf{L}\delta\mathbf{u})^T (\mathbf{D}\mathbf{L}\mathbf{u}) d\Omega = \sum_i^N \sum_j^N \delta\mathbf{u}_i^T \underbrace{\left( \int_{\Omega} \mathbf{B}_i^T \mathbf{D}\mathbf{B}_j d\Omega \right)}_{\mathbf{K}_{ij}} \mathbf{u}_j \tag{3.41}$$

where  $\mathbf{K}_{ij}$  is the nodal stiffness matrix. It is a  $2 \times 2$  matrix, and is defined as

$$\mathbf{K}_{ij} = \int_{\Omega} (\mathbf{B}_i^T)_{2 \times 3} \mathbf{D}_{3 \times 3} (\mathbf{B}_j)_{3 \times 2} d\Omega \tag{3.42}$$

Note that when node  $i$  and node  $j$  are not in the same local domain of the same quadrature point of integration,  $\mathbf{K}_{ij}$  vanishes.

To obtain numerically the nodal stiffness matrix, Gauss quadrature method is used. Gauss quadrature method is used in the same form as used in FEM, but this time

integrations are performed over the background cells not over the elements. The nodal stiffness matrix can be obtained using the Gauss quadrature method as follows [1]:

$$\mathbf{K}_{ij} = \sum_k^{n_c} \sum_{l=1}^{n_g} w_l \mathbf{B}_i^T(\mathbf{x}_{Ql}) \mathbf{D} \mathbf{B}_j(\mathbf{x}_{Ql}) |\mathbf{J}_{lk}^D| = \sum_k^{n_c} \sum_{l=1}^{n_g} (\mathbf{K}_{ij}^{lk})_{(2 \times 2)} \quad (3.43)$$

where  $n_c$  is the number of background cells,  $n_g$  is the number of gauss points used in the background cell,  $w_l$  is the gauss weighting factor for the  $l$ th gauss point at  $\mathbf{x}_{Ql}$ ,  $\mathbf{J}_{lk}^D$  is the Jacobian matrix for the area integration of the background cell  $k$ , at which the gauss point  $\mathbf{x}_{Ql}$  located, and  $\mathbf{K}_{ij}^{lk}$  is defined as

$$\mathbf{K}_{ij}^{lk} = w_l \mathbf{B}_i^T(\mathbf{x}_{Ql}) \mathbf{D} \mathbf{B}_j(\mathbf{x}_{Ql}) |\mathbf{J}_{lk}^D| \quad (3.44)$$

Equation (3.41) can be now expressed as

$$\int_{\Omega} (\mathbf{L} \delta \mathbf{u})^T (\mathbf{D} \mathbf{L} \mathbf{u}) d\Omega = \sum_i^N \sum_j^N \delta \mathbf{u}_i^T \mathbf{K}_{ij} \mathbf{u}_j \quad (3.45)$$

Note that the summation in the right-hand side of this equation is in fact an assembly process. To view this, we perform the following operation [1].

$$\begin{aligned} \sum_i^N \sum_j^N \delta \mathbf{u}_i^T \mathbf{K}_{ij} \mathbf{u}_j &= \delta \mathbf{u}_1^T \mathbf{K}_{11} \mathbf{u}_1 + \delta \mathbf{u}_1^T \mathbf{K}_{12} \mathbf{u}_2 + \dots + \delta \mathbf{u}_1^T \mathbf{K}_{1N} \mathbf{u}_N \\ &\quad + \delta \mathbf{u}_2^T \mathbf{K}_{21} \mathbf{u}_1 + \delta \mathbf{u}_2^T \mathbf{K}_{12} \mathbf{u}_2 + \dots + \delta \mathbf{u}_2^T \mathbf{K}_{2N} \mathbf{u}_N \\ &\quad + \delta \mathbf{u}_3^T \mathbf{K}_{31} \mathbf{u}_1 + \delta \mathbf{u}_3^T \mathbf{K}_{32} \mathbf{u}_2 + \dots + \delta \mathbf{u}_3^T \mathbf{K}_{3N} \mathbf{u}_N \\ &\quad \vdots \\ &\quad + \delta \mathbf{u}_N^T \mathbf{K}_{N1} \mathbf{u}_1 + \delta \mathbf{u}_N^T \mathbf{K}_{N2} \mathbf{u}_2 + \dots + \delta \mathbf{u}_N^T \mathbf{K}_{NN} \mathbf{u}_N \\ &= \delta \mathbf{U}^T \mathbf{K} \mathbf{U} \end{aligned} \quad (3.46)$$

Finally, Equation (3.41) becomes

$$\int_{\Omega} (\mathbf{L} \delta \mathbf{u})^T (\mathbf{D} \mathbf{L} \mathbf{u}) d\Omega = \delta \mathbf{U}^T \mathbf{K} \mathbf{U} \quad (3.47)$$

where  $\mathbf{K}$  is the global stiffness matrix in the form of

$$\mathbf{K}_{(2N \times 2N)} = \begin{bmatrix} \mathbf{K}_{11} & \mathbf{K}_{12} & \cdots & \mathbf{K}_{1N} \\ \mathbf{K}_{21} & \mathbf{K}_{22} & \cdots & \mathbf{K}_{2N} \\ \vdots & \vdots & \ddots & \vdots \\ \mathbf{K}_{N1} & \mathbf{K}_{N2} & \cdots & \mathbf{K}_{NN} \end{bmatrix} \quad (3.48)$$

The dimension of the matrix  $\mathbf{K}$  should be  $(2N) \times (2N)$ , because nodal stiffness matrix  $\mathbf{K}_{ij}$  is of  $2 \times 2$ , and the total number of nodes in the problem domain is  $N$ .

Because of the Kronecker delta function property the natural and essential boundary conditions are applied as in FEM. This property eliminates the accuracy loss during the enforcement of essential and natural boundary conditions and increase the efficiency by eliminating the requirement of the supplementary operations.

### 3.6 Numerical Examples

An elasto-static cantilever beam problem is solved to implement the PIM shape functions. The cantilever beam is loaded as shown in Figure 3.3 and the models used for the PIM solution is shown in Figure 3.4. The material properties are as follows:  $E = 200$  GPa and  $\nu = 0$ . The geometry of cantilever beam is modeled by regularly distributed 63 nodes and by 51 irregularly distributed nodes. 10 background cells are used for integration. The sizes of the formed support domains are  $0.2 \text{ m} \times 0.1 \text{ m}$ . 9 to 15 nodes are used for interpolation in a local domain. The results are compared with analytical solution results in Figure 3.5.

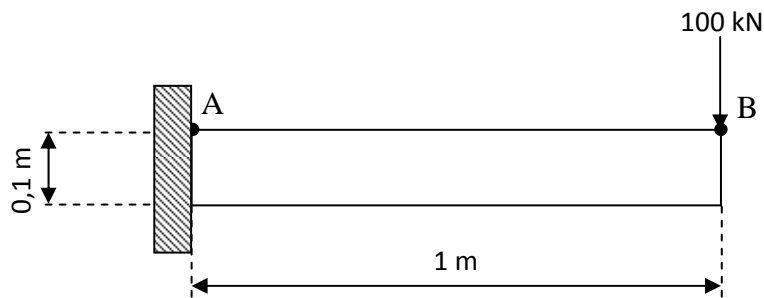


**Figure 3.3** The cantilever beam problem.

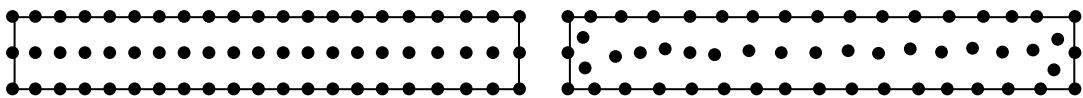


**Figure 3.4** The regular and irregular PIM model of cantilever beam problem.

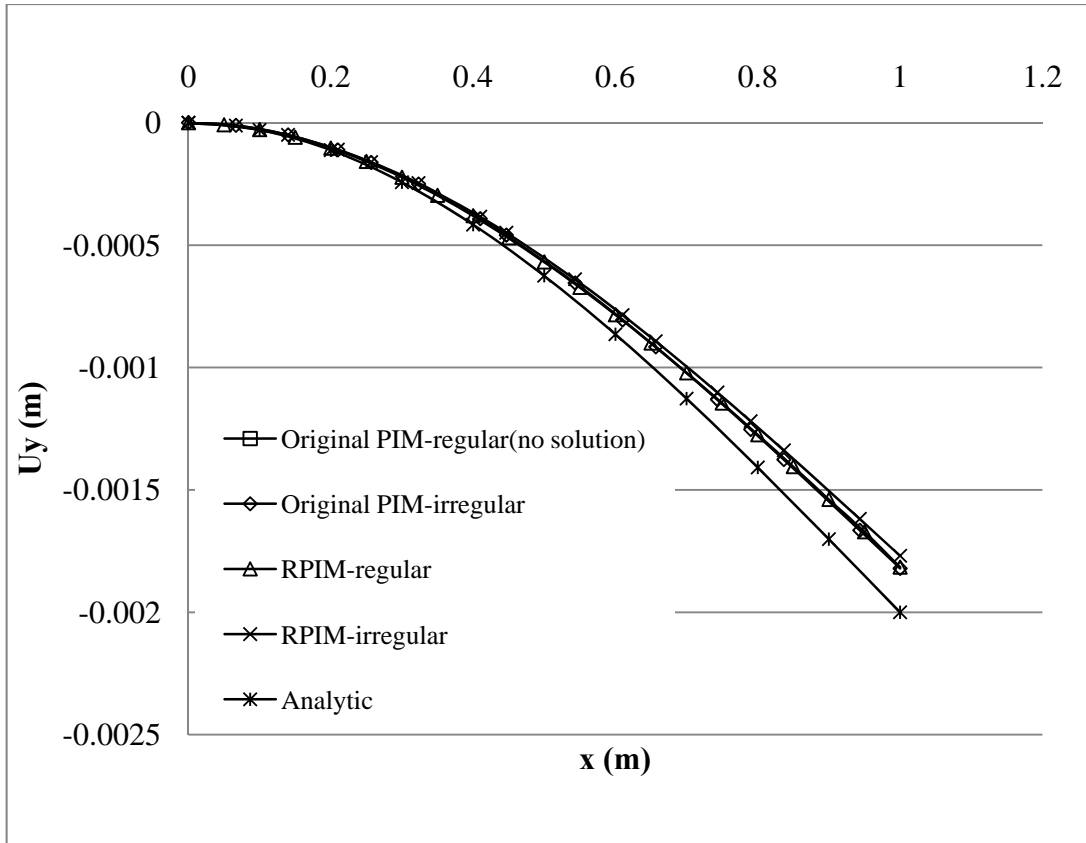


Figure 3.5 The transverse deflection along AB line of cantilever beam.

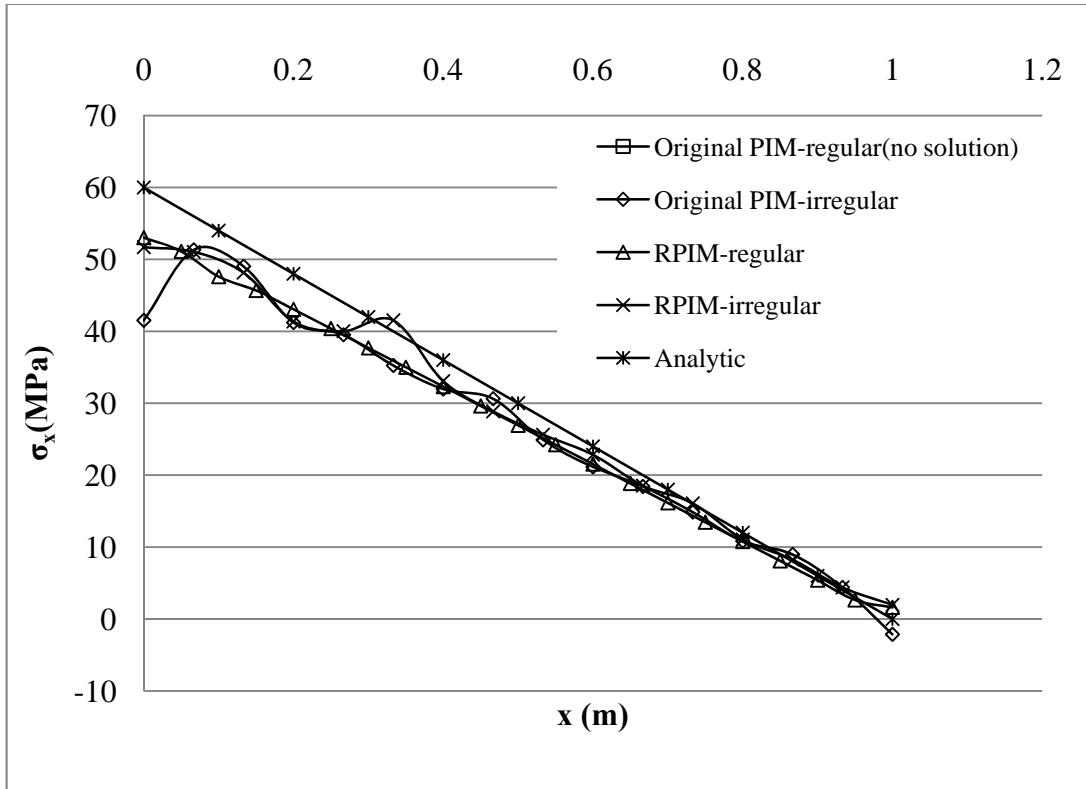


Figure 3.6 The stress along AB line of cantilever beam.

### **3.7 Results and Discussions**

The results of the cantilever beam shows that both PIM and RPIM work for irregular node distribution. However, the PIM has singularity problem for regularly distributed nodes. The RPIM gives more accurate results for irregularly distributed nodes.

## CHAPTER 4

### ANALYSES OF 2D GEOMETRICALLY NONLINEAR PROBLEMS

#### 4.1 Introduction

Most of the problems of solid mechanics in various branches of engineering are solved using linear approximations. Because they are easy to compute, the computational cost is small, and the solutions of linear approximations can be superposed on each other.

However, the behavior of real structures is nonlinear and in some cases approximation of linearity gives unrealistic results. When the displacements cause changes in geometry that have a significant effect on the load deformation behavior and/or strain is not proportional to the stress, the nonlinearities become very important and the linear approximations cannot be used.

There are three types of nonlinear structural problems found in literature

- i. Geometric nonlinearity
- ii. Material nonlinearity
- iii. Boundary nonlinearity

In geometric nonlinearity, the deflections of the structure are large compared with the original dimensions of the structure and this caused to the changes in stiffness and the effects of loads during the structure deformations. Because of these, equilibrium equations must be written with respect to deformed structural geometry. Geometric nonlinearity is characterized by large displacements and/or rotations.

Material nonlinearity occurs when the strain is not proportional to the stress or material properties are functions of the state of stress. Nonlinear elastic, elasto-plastic, visco-elastic and visco-plastic material models are examples of material nonlinearities.



In boundary nonlinearity, the gap between adjacent parts or the contact area between parts change and so the force changes. The contact problems are the most encountered type of the boundary nonlinearity. In crack problems, the displacements are not continuous at the crack tip. Therefore, the crack problems are an another boundary type nonlinearity problems.

In non-linear structural problems, stiffness becomes functions of displacement and stiffness cannot be constructed without a knowledge of displacements. Because of these, the structural equations,  $\mathbf{F} = \mathbf{K}\mathbf{u}$ , cannot be immediately solved for  $\mathbf{u}$ . An iterative solution procedure is needed to solve the structural equations. The Newton-Raphson method is an iterative solution procedure used to solve the non-linear algebraic equations. It has a simple and an effective algorithm.

In this chapter, the strain-displacement relationship of the finite strain is presented in section 4.2, the Newton-Raphson method is revised in section 4.3 and the application of Newton-Raphson method for the solution of non-linear discrete equations of the structure are revised in section 4.4. Some finite strain case studies are solved using PIM in section 4.5.

## 4.2 The RPIM formulation for geometrically nonlinear problems

The well-known deformation gradient tensor has an important role in characterising strains of large deformation problems and can be written as follows:

$$F_{ij} = \sum_{I=1}^{NP} \left[ \frac{\partial \Phi_I}{\partial x_j} d_{iI} \right] + \delta_{ij} \quad (4.1)$$

The linearized weak form for geometrically nonlinear problems can be written in terms of the second Piola-Kirchoff stresses and the Green-Lagrange strains as follows [156]

$$\int_{\Omega} \hat{\mathbf{S}} \delta \hat{\boldsymbol{\varepsilon}} d\Omega = \int_{\Gamma} \delta \mathbf{u}^T \mathbf{f}_q d\Gamma + \int_{\Omega} \delta \mathbf{u}^T \mathbf{f}_b d\Omega \quad (4.2)$$

where  $\mathbf{f}_b$  is the body force,  $\mathbf{f}_q$  is the surface forces and  $\hat{\boldsymbol{\varepsilon}}$  is the Green-Lagrange strain,

$$\hat{\mathbf{e}} = \frac{1}{2}(\mathbf{F}^T \mathbf{F} - \mathbf{I}) \quad (4.3)$$

$\mathbf{F}$  is the matrix form of deformation gradient tensor.

$$\mathbf{F} = \begin{bmatrix} F_{11} & F_{12} \\ F_{21} & F_{22} \end{bmatrix} \quad (4.4)$$

$\hat{\mathbf{S}}$  is the second Piola-Kirchoff stress and can be written for compressible Neo-Hookean material as follows [156],

$$\hat{\mathbf{S}} = \lambda(\ln(\det \mathbf{F}) \mathbf{c}_1^{-1} + \mu(\mathbf{I} - \mathbf{c}_1^{-1})) \quad (4.5)$$

$\lambda$  and  $\mu$  are Lamé's constants. The matrix  $\mathbf{c}_1 = \mathbf{F}^T \mathbf{F}$  is known as right Cauchy-Green tensor.

Equation 4.2 can be written explicitly,

$$\begin{aligned} \iint_{A^0} [\mathbf{B} \bar{\mathbf{S}} \mathbf{B}^T + \mathbf{B} \bar{\mathbf{F}}^T \mathbf{D} \bar{\mathbf{F}} \mathbf{B}^T] dA^0 \Delta \mathbf{d} = & - \iint_{A^0} \mathbf{B} \bar{\mathbf{F}}^T \mathbf{S} dA^0 \\ & + \iint_{A^0} \Phi \mathbf{f}_q^0 dA^0 + \iint_{A^0} \Phi \mathbf{f}_b^0 dA^0 \end{aligned} \quad (4.6)$$

$\mathbf{D}$  is the material matrix,  $\Phi$  is the shape function matrix and  $A^0$  is the initial domain. Equation 4.5 can be written in terms of stiffness matrices and load vectors as follows:

$$(\mathbf{K}_c + \mathbf{K}_s) \Delta \mathbf{d} = \mathbf{r}_i + \mathbf{r}_q + \mathbf{r}_b \quad (4.7)$$

where  $\mathbf{K}_c$  is the current stiffness matrix,

$$\mathbf{K}_c = \int_{\Omega} \mathbf{B}_I \bar{\mathbf{F}}^T \mathbf{D} \bar{\mathbf{F}} \mathbf{B}_J^T d\Omega \quad (4.8)$$

$\mathbf{K}_s$  is the geometric stiffness matrix,

$$\mathbf{K}_s = \int_{\Omega} \mathbf{B}_I \bar{\mathbf{S}} \mathbf{B}_J^T d\Omega \quad (4.9)$$

$\bar{\mathbf{S}}$  is the initial stress matrix,

$$\bar{\mathbf{S}} = \begin{bmatrix} S_{xx} & S_{xy} & 0 & 0 \\ S_{xy} & S_{yy} & 0 & 0 \\ 0 & 0 & S_{xx} & S_{xy} \\ 0 & 0 & S_{xy} & S_{yy} \end{bmatrix} \quad (4.10)$$

$\mathbf{r}_i$  is the equivalent nodal load vector due to stresses in the current known configuration,

$$\mathbf{r}_i = - \iint_{A^0} \mathbf{B}_I \bar{\mathbf{F}}^T \mathbf{S} dA^0 \quad (4.11)$$

$\mathbf{S}$  is the second Piola-Kirchoff stresses in a vector form,

$$\mathbf{S} = [S_{xx} \quad S_{yy} \quad S_{xy}] \quad (4.12)$$

$\mathbf{r}_q$  is the equivalent nodal load vector due to surface forces, and

$$\mathbf{r}_q = \iint_{A^0} \Phi \mathbf{f}_q^0 dA^0 \quad (4.13)$$

$\mathbf{r}_b$  is the equivalent nodal load vector due to body forces.

$$\mathbf{r}_b = \iint_{A^0} \Phi \mathbf{f}_b^0 dA^0 \quad (4.14)$$

The gradient matrices  $\mathbf{B}_I^T$  is expressed as

$$\mathbf{B}_I^T = \begin{bmatrix} \frac{\partial \Phi_I}{\partial x_1} & 0 \\ \frac{\partial \Phi_I}{\partial x_2} & 0 \\ 0 & \frac{\partial \Phi_I}{\partial x_1} \\ 0 & \frac{\partial \Phi_I}{\partial x_2} \end{bmatrix} \quad (4.15)$$

Arranged deformation gradient matrix  $\bar{\mathbf{F}}$ ,

$$\bar{\mathbf{F}} = \begin{bmatrix} F_{11} & 0 & F_{21} & 0 \\ 0 & F_{12} & 0 & F_{22} \\ F_{12} & F_{11} & F_{22} & F_{21} \end{bmatrix} \quad (4.16)$$

Cauchy Stress can be written as follows [138],

$$\hat{\sigma} = \frac{\lambda}{\det \mathbf{F}} \ln(\det \mathbf{F}) \mathbf{I} + \frac{\mu}{\det \mathbf{F}} (\mathbf{c}_2 - \mathbf{I}) \quad (4.17)$$

where  $\mathbf{I}$  is the unit matrix,  $\mathbf{c}_2$  is the left Cauchy-Green tensor ( $\mathbf{c}_2 = \mathbf{F}\mathbf{F}^T$ ).

### 4.3. Numerical Procedure

The solution procedure of Eq. 11 is started with the division of the total load into load increments. At each load increments, the equation is solved iteratively. The iterative procedure can be achieved by the Newton-Raphson method which starts with an assumed solution and then tries to improve it until a specified convergence criteria is satisfied. In this study, the displacement based convergence criteria is used [138]. The algorithm of the procedure, which is used in each load increment and in each iteration, can be given as follows:

1. Loop over integration cells
  - 1.1. Loop over integration points
    - 1.1.1. Determine the local surrounding domain
    - 1.1.2. Compute the shape functions and derivatives of them (Equation 3.27)
    - 1.1.3. Compute the deformation gradient (Equation 4.1)
    - 1.1.4. Compute Green-Lagrange strain (Equation 4.3)
    - 1.1.5. Compute second Piola-Kirchoff stresses (Equation 4.5)
    - 1.1.6. Compute material matrix (for compressible Neo-Hookean material [156])
    - 1.1.7. Compute initial stress matrix (Equation 4.10)
    - 1.1.8. Loop over nodes,  $i$ 
      - 1.1.8.1. Form gradient matrix,  $B_i$ , (Equation 4.15)
      - 1.1.8.2. Form internal force vector (Equation 4.11)
      - 1.1.8.3. Loop over nodes,  $j$ 
        - 1.1.8.3.1. Form gradient matrix,  $B_j$  (Equation 4.15)
        - 1.1.8.3.2. Form the current stiffness matrix (Equation 4.8)
        - 1.1.8.3.3. Form the geometric stiffness matrix (Equation 4.9)
        - 1.1.8.3.4. Assemble the current and geometric stiffness matrix in the usual manner
      - 1.1.8.4. End of node loop,  $j$
    - 1.1.9. End of node loop,  $i$
  - 1.2. End of integration point loop
2. End of integration cell loop
3. Form the tangential stiffness matrix,  $\mathbf{K}_T = \mathbf{K}_c + \mathbf{K}_s$
4. Solve  $\mathbf{K}_T \Delta \mathbf{d} = \Delta \mathbf{f}$  ( $\Delta \mathbf{f} = \mathbf{f}^{ext} - \mathbf{f}^{int}$ )
5. Update displacements

Check the convergency. If it is not satisfied, go to next iteration. If the convergence is achieved, calculate the Cauchy stresses. Because the nodal displacements are known, the stresses can be calculated at nodes using the following algorithm:

1. Loop over nodes
  - 1.1.1. Determine the local surrounding domain
  - 1.1.2. Compute the shape functions and derivatives of them (Equation 3.27)
  - 1.1.3. Compute the deformation gradient(Equation 4.1)
  - 1.1.4. Compute Green-Lagrange strain(Equation 4.3)
  - 1.1.5. Compute the Cauchy stress (Equation 4.17)
2. End of node loop

After calculating the Cauchy stresses, the next load step begins.

#### 4.4 Numerical Examples

The developed RPIM program is tested using three different numerical examples. In all solutions, the same compressible hyperelastic Neo-Hookean material is used ( $\lambda = 3.3 * 10^3$ ,  $\mu = 0.5 * 10^4$ ). The numerical integrations are carried out using 4x4 integration points. Plane stress assumption is used in axially load plate, plate with hole, cantilever beam cases and plane strain assumption is used for pressurized cylinder case. All results are compared with finite element method (FEM) results using displacement based 4 node rectangular elements [156].

##### 4.4.1 Axially Loaded Plate

This case is usually used as a first case in the meshfree studies of geometric nonlinear problems [157-159]. Therefore, a plate with dimensions of 10 cm x 2.5 cm is loaded in tension as shown in Figure 4.1. RPIM models with regular and irregular distributed nodes and FEM model are shown in Figure 4.2. The data used in the RPIM and FEM models are compared in the Table 4.1. The displacements and stresses are discussed for the points A and B respectively.

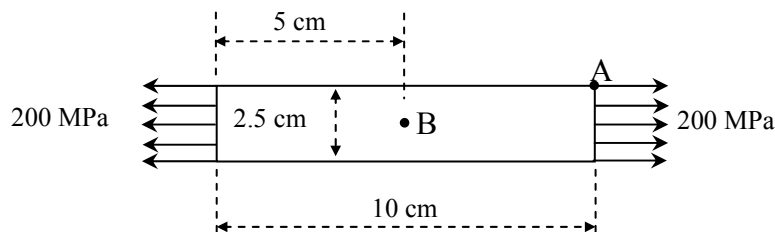


**Figure 4.1** Axially loaded plate

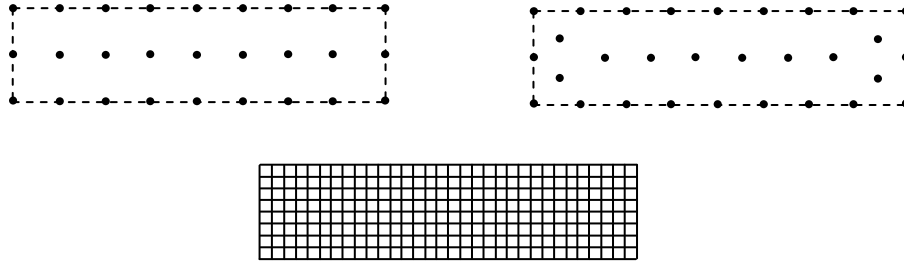


**Figure 4.2** RPIM models with regular and irregular distributed nodes and FEM model of axially loaded plate.

**Table 4.1** Data used in the RPIM and FEM models of axially loaded plate

	<b>RPIM</b>	<b>FEM</b>
<b>Problem Type</b>	Plane stress with unit thickness	Plane stress with unit thickness
<b>Dimensions</b>	10 cm x 2.5 cm	10 cm x 2.5 cm
<b>External load</b>	200 MPa (in 20 increments)	200 MPa (in 20 increments)
<b>Linear solution</b>	$E = 120 \text{ MPa}, \nu = 0.2$	$E = 120 \text{ MPa}, \nu = 0.2$
<b>Geometrically nonlinear solution</b>	Neo-Hookean with $\lambda = 33.33 \text{ MPa}$ $\mu = 50 \text{ MPa}$	Neo-Hookean with $\lambda = 33.33 \text{ MPa}$ $\mu = 50 \text{ MPa}$
<b>Number of nodes in the entire problem domain</b>	27 regular and irregular distributed nodes with 16 background cells	297 nodes with 256 rectangular elements
<b>Number of nodes</b>	<u>in a local domain</u> Changes between 4 and 9	<u>in an element</u> Constant, 4
<b>Sampling points for numerical integrations</b>	4x4	2x2
<b>Number of iteration in each load increment</b>	Changes between 2 and 4	Changes between 2 and 4

#### 4.4.1.1 Convergency rate

The RPIM solutions are carried out with regular and irregular distributed nodes and using  $q = 1.03$ ,  $q = 1.75$ ,  $\alpha_c = 4$  and  $m = 3$ . RPIM gives the deformation steps of the plate as shown in Figure 4.3. Nonlinear displacement solutions separate from linear solutions after the initial load increments as shown in Figure 4.4. Although, the number of elements in the FEM model is 11 times of number of nodes in the RPIM model, all RPIM and FEM displacement solutions are in good agreements. However, RPIM stress solutions show some deviations from FEM solutions when irregular nodes are used as shown in Figure 4.5. Both RPIM

and FEM linear and nonlinear solutions provide an excellent convergency for the displacements and stresses at the last load increment as shown in Figure 4.6 and 4.7.



**Figure 4.3** RPIM solution steps of large deformation of the plate with regular distributed nodes

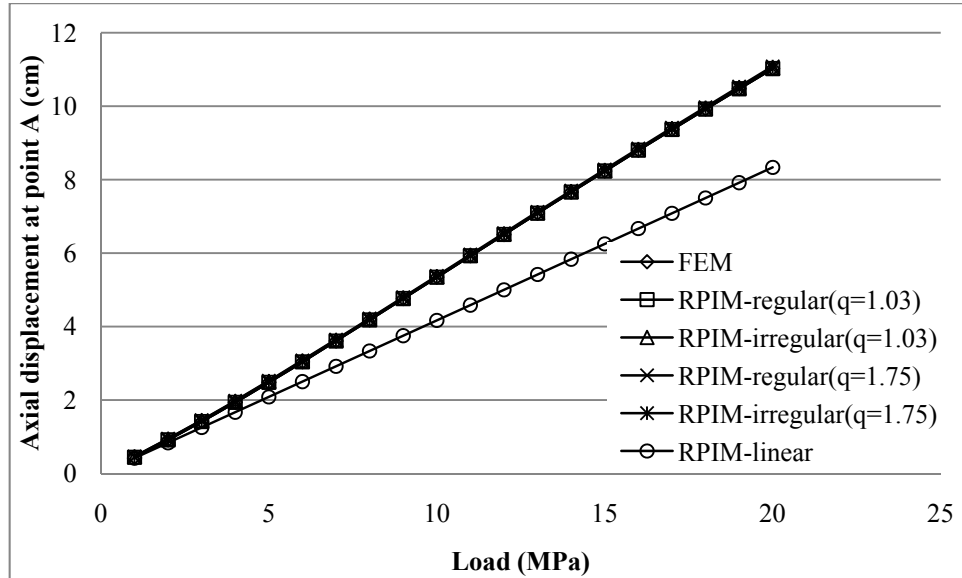


**Figure 4.4** Displacement variations against load steps for RPIM 27 regular and 27 irregular distributed nodes with  $\alpha_c=4$ ,  $m=3$  and FEM (297 nodes) at the point A on the axially loaded plate.

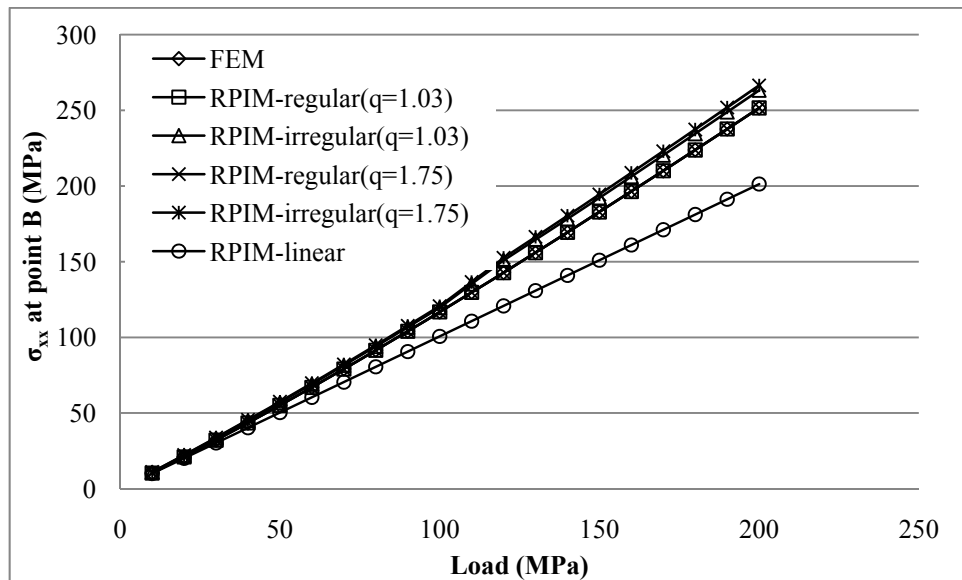


**Figure 4.5** Stress variations against load steps for RPIM 27 regular and 27 irregular distributed nodes with  $\alpha_c=4$ ,  $m=3$  and FEM (297 nodes) at the point B on the axially loaded plate.

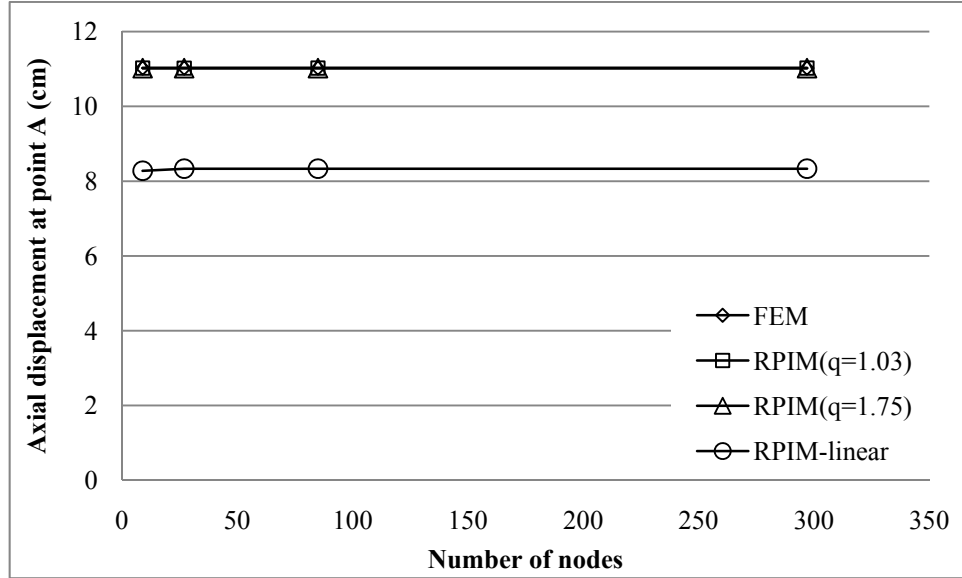


**Figure 4.6** The convergence rate of displacements at the last load increment at the point A on the axial plate by increasing number of nodes with  $\alpha_c=4$ ,  $m=3$  used in the models.

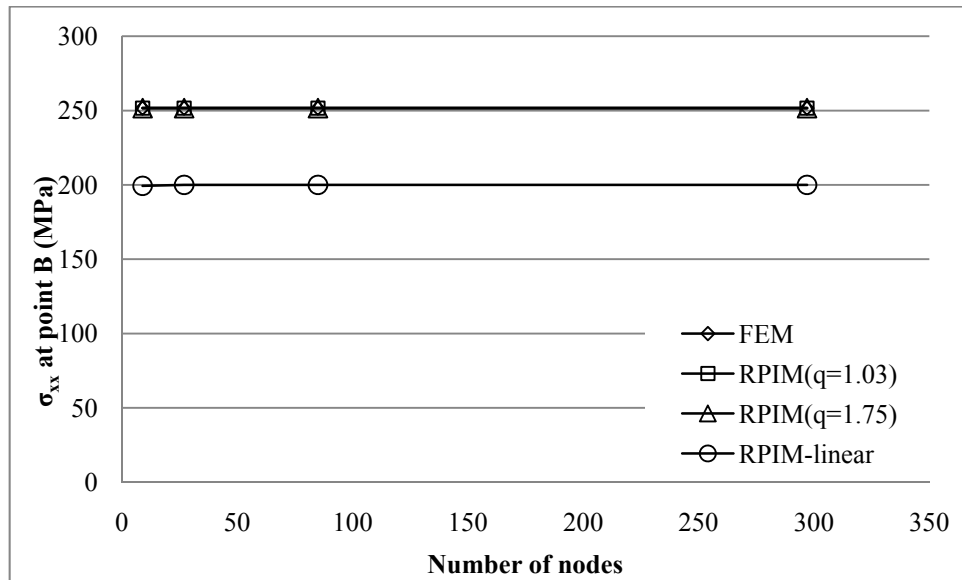


**Figure 4.7** The convergence rate of stresses at the last load increment at point B on the axial plate by increasing number of nodes with  $\alpha_c=4$ ,  $m=3$  used in the models.

#### 4.4.1.2 Effect of $\alpha_c$

The effect of  $\alpha_c$  on the displacements and stresses are investigated for  $q = 1.03$  and  $m = 3$ . The results show that changing  $\alpha_c$  values does not affect the displacement and stress increments as shown in Figure 4.8 and 4.9.



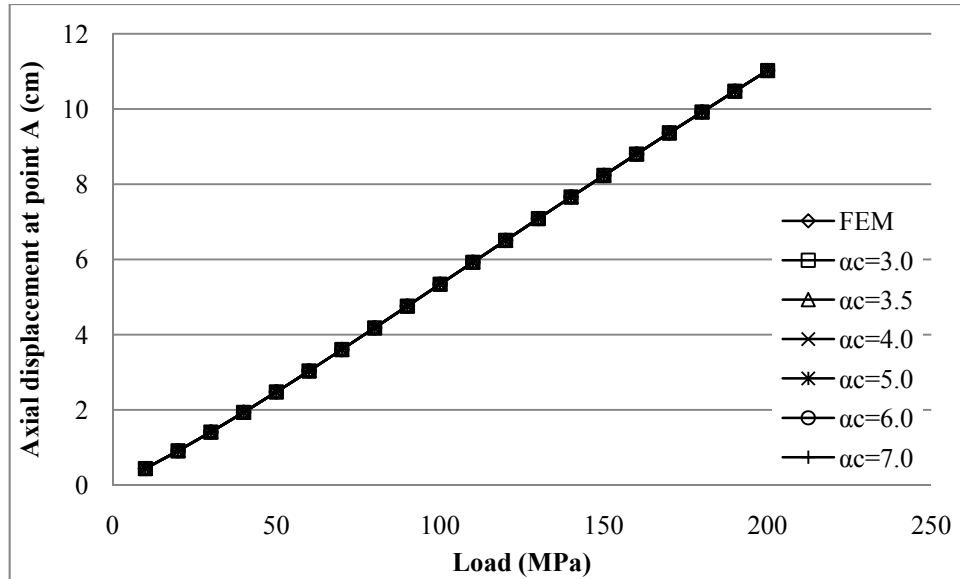


**Figure 4.8** Displacement variations at the point A on the plate against load steps for 27 nodes with  $q = 1.03$ ,  $m = 3$  and various  $\alpha_c$ .

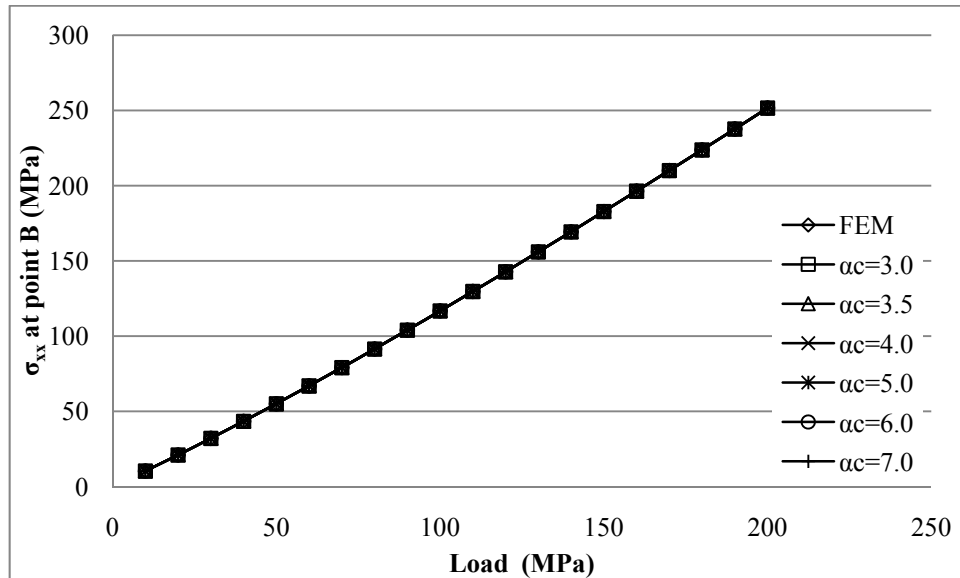


**Figure 4.9** Stress variations at the point B on the plate against load steps for 27 nodes with  $q = 1.03$ ,  $m = 3$  and various  $\alpha_c$ .

#### 4.4.1.3 Effect of q

In this investigation,  $\alpha_c$  and  $m$  are kept constant ( $\alpha_c = 4$  and  $m = 3$ ) while  $q$  is changed. Figure 4.10 and 4.11 show that changing the value of  $q$  do not have an important effect on the displacement and stress results similar to  $\alpha_c$ .

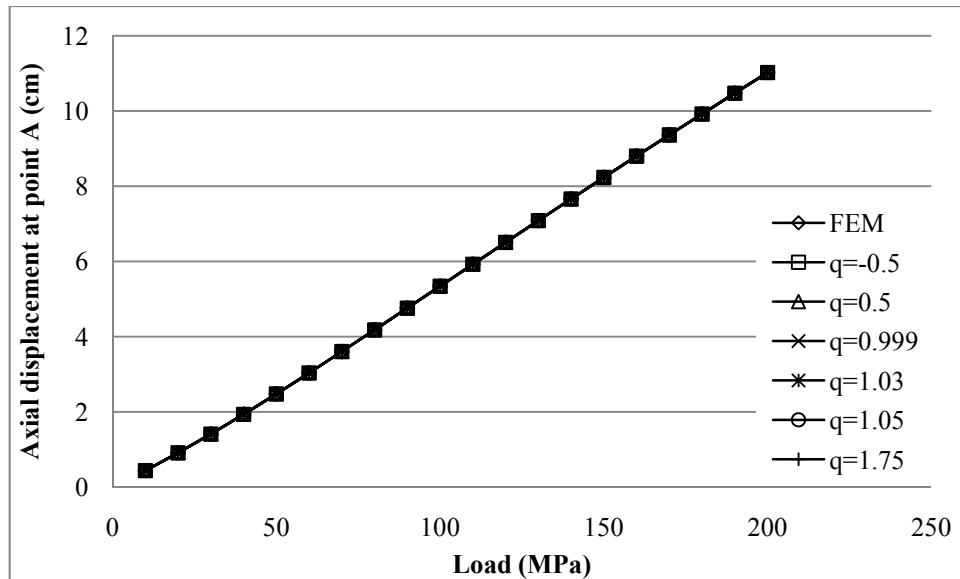


**Figure 4.10** Displacement variations at the point A on the plate against load steps for 27 nodes with  $\alpha_c=4$ ,  $m = 3$  and various  $q$ .

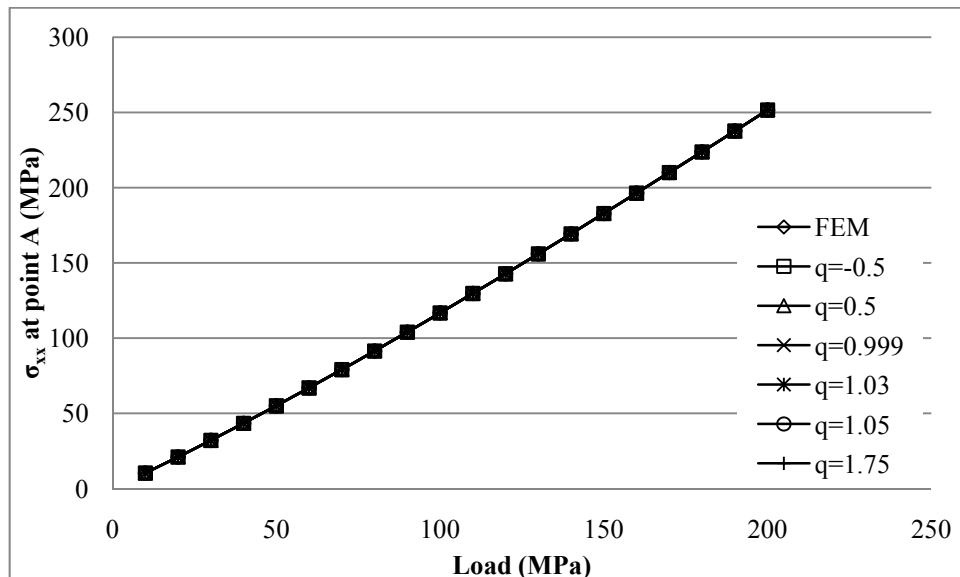


**Figure 4.11** Stress variations at the point B on the plate against load steps for 27 nodes with  $\alpha_c = 4$ ,  $m = 3$  and various  $q$ .

#### 4.4.1.4 Effect of number of monomials

The number of monomials is taken as 0, 3, 4 and 6 while the  $\alpha_c$  and  $q$  are kept constant. The RPIM gives exactly same displacements with FEM results when  $m$  is used 3 and 4. However when it is used as 0 and 6, RPIM shows slightly different displacement results as shown in Figure 4.12. The RPIM stress results also give same stress results with FEM when  $m = 3$  and 4. When  $m$  is used as 0, stresses show some minor differences. However, when it is used as 6, stress increments

shows significant differences between RPIM and FEM results as shown in Figure 4.13.

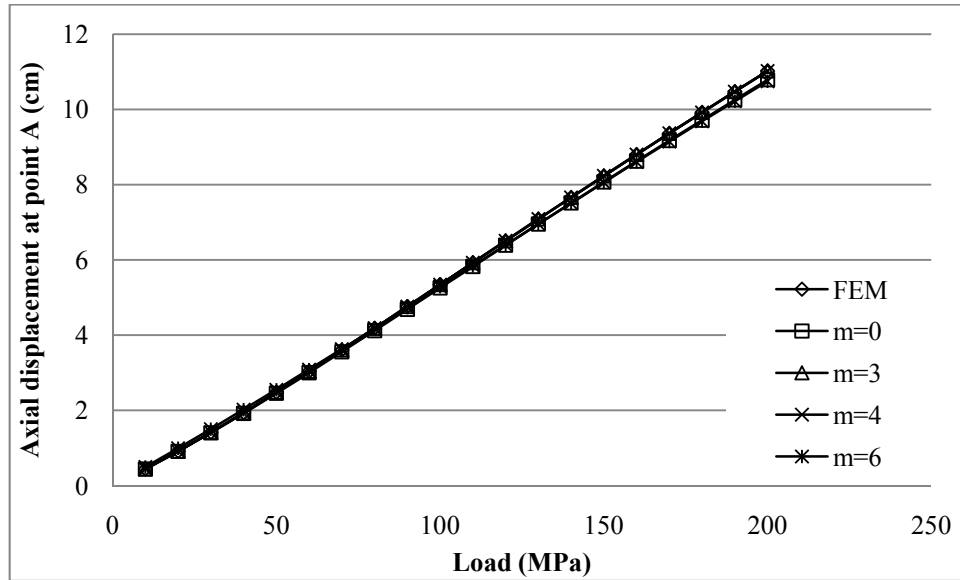


**Figure 4.12** Displacement variations at the point A on the plate against load steps for 27 nodes with  $\alpha_c = 4$ ,  $q = 1.03$  and various  $m$ .

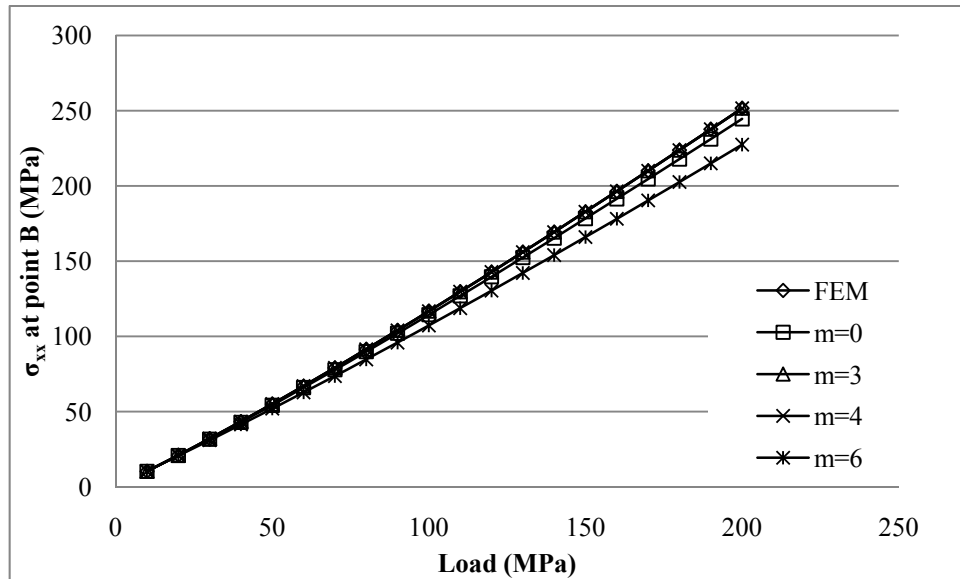


**Figure 4.13** Stress variations at the point B on the plate against load steps for 27 nodes with  $\alpha_c = 4$ ,  $q = 1.03$  and various  $m$ .

#### 4.4.2 Plate with Hole

This case is the common benchmark test in the mesh dependent solutions of linear elastic problems. It is also used in the mesh-free solutions of linear-elastic problems [86]. Therefore, it can be a good measure of the performance of RPIM in the geometric nonlinear solutions. A plate with a hole of radius 1 cm is loaded in

tension as shown in Figure 4.14. The dimensions of the plate and the data used in the models are given in the Table 2. The node distributions in the models are shown in Figure 4.15. The displacement at point A is discussed in the solutions. The stress at point B is well known and it is equal to 3 times of applied tractions in linear elastic solutions [1]. Therefore, it is compared with the stresses obtained in the RPIM and FEM solutions.

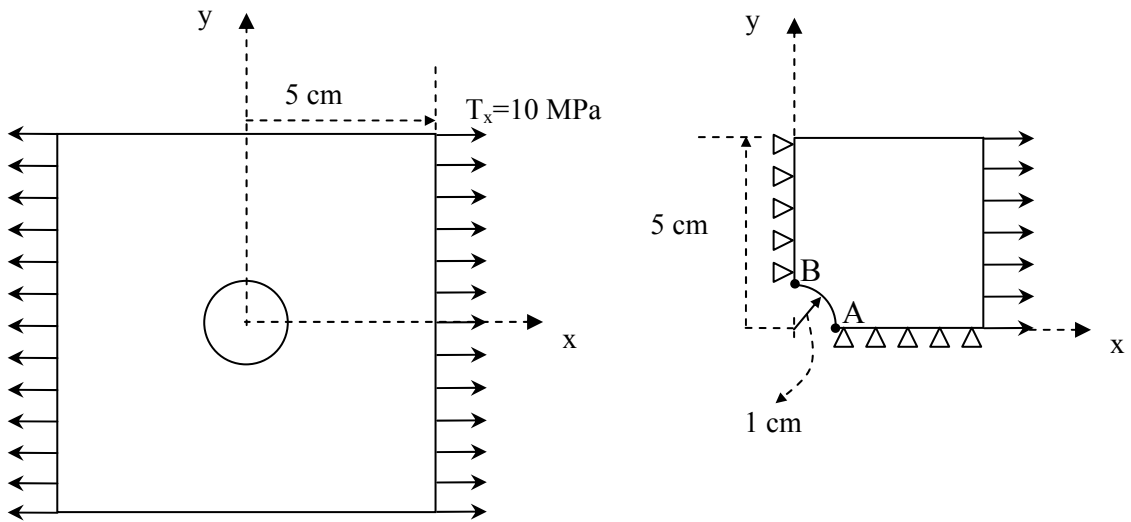


**Figure 4.14** A plate with hole.

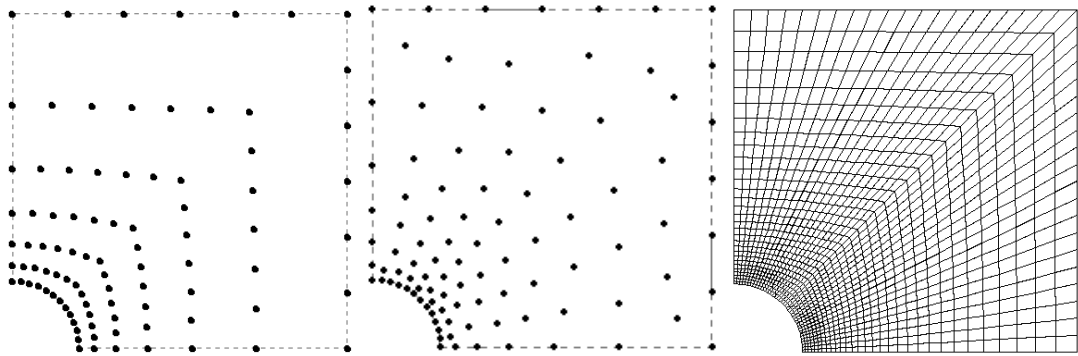


**Figure 4.15** RPIM models with regular and irregular distributed nodes and FEM model of plate-hole problem.

**Table 4.2** Data used in the RPIM and FEM models of the plate with hole.

	<b>RPIM</b>	<b>FEM</b>
<b>Problem type</b>	Plane stress with unit thickness	Plane stress with unit thickness
<b>Dimensions</b>	5 cm x 5 cm	5 cm x 5 cm
<b>External load</b>	10 MPa (in 20 increments)	10 MPa (in 20 increments)
<b>Linear solution</b>	$E = 1 \text{ kPa}, \nu = 0.3$	$E = 1 \text{ kPa}, \nu = 0.3$
<b>Geometrically nonlinear solution</b>	Neo-Hookean with $\lambda = .576923 \text{ kPa}$ $\mu = .384615 \text{ kPa}$	Neo-Hookean with $\lambda = .576923 \text{ kPa}$ $\mu = .384615 \text{ kPa}$
<b>Number of nodes in the entire problem domain</b>	<b>Coarse Model</b> 91 regular and 98 irregular distributed nodes with 72 background cells <b>Fine Model</b> 1271 regular distributed nodes with 1200 background cells	1271 nodes with 1200 rectangular elements
<b>Number of nodes</b>	<u>in a local domain</u> Constant, 4	<u>in an element</u> Constant, 4
<b>Sampling points for numerical integrations</b>	3x3	2x2
<b>Number of iteration in each load increment</b>	Changes between 3 and 5	Changes between 3 and 5

#### 4.4.2.1 Convergency rate

In the RPIM solutions, two different models are used. The deformed shape of the plate in the final load step is shown in Figure 4.16. Because of the errors in the traction line, the RPIM solution is repeated with higher number of nodes as shown in Figure 4.17. The errors in the traction line are removed with higher number of nodes. In these solutions, the shape parameters are used as  $q = 1.03$ ,  $\alpha_c = 4$  and the number of polynomial is  $m = 3$ . In order to see the effect of shape parameters remarkably, all remaining solutions are carried out using coarse node model. Displacement variations against the load increments are shown in Figure 4.18. RPIM linear elastic solutions give radial stresses (at point B) three times of applied load as in the analytical solutions. When  $q$  is used as 1.03 the regular and irregular node RPIM models give nearly same results. The best FEM agreement is obtained with irregular node RPIM ( $q = 1.75$ ). However, in stress variations, the worst FEM agreement is obtained with RPIM-regular ( $q = 1.75$ ) as shown in Figure 4.19. The regular and irregular RPIM models gives same results with  $q = 1.03$ . The best FEM agreement in stress solutions is again obtained with irregular node RPIM ( $q = 1.75$ ). In all solutions, the displacement at the point A converges for number of nodes

greater than 400 as shown in Figure 4.20. The traction is applied as 10 MPa in these solutions. The linear RPIM stress solution at the point B converges better than the linear FEM stress solution as shown in Figure 4.21.

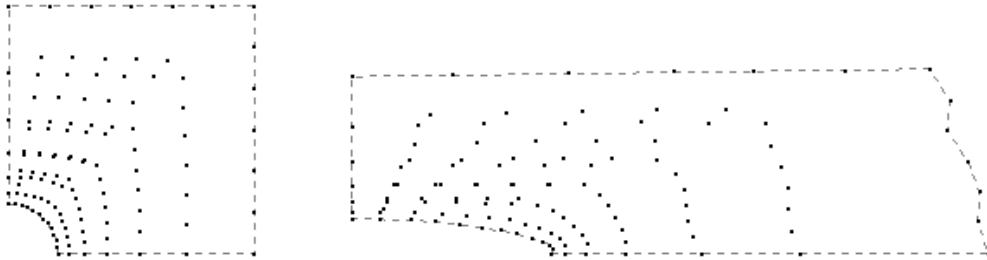


**Figure 4.16** Initial coarse node distribution of RPIM model and its deformed shape in the last load increment.

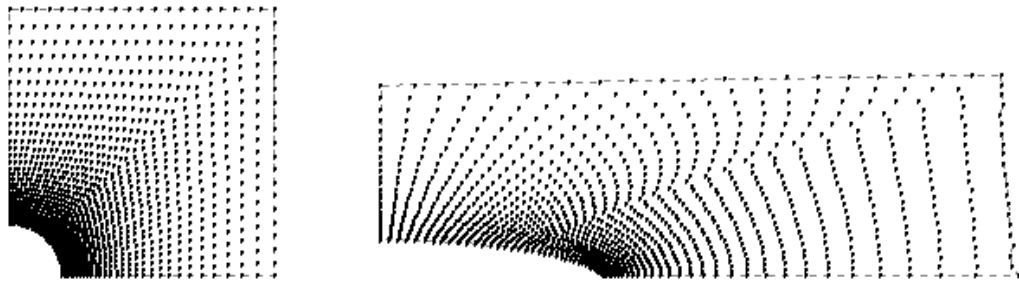


**Figure 4.17** Initial fine node distribution of RPIM model and its deformed shape in the last load increment.

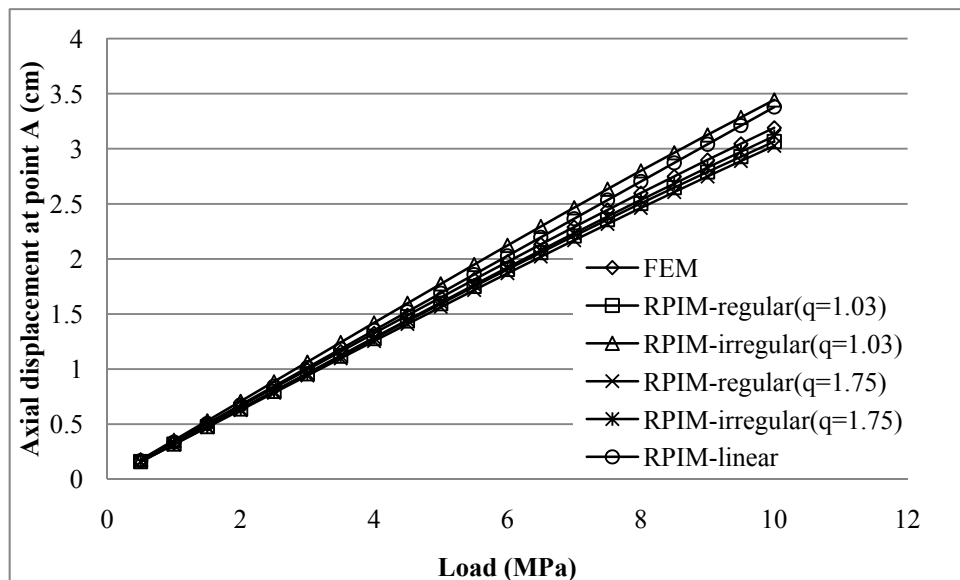


**Figure 4.18** Displacement variations against load steps for RPIM 91 regular and 98 irregular distributed nodes with  $\alpha_c = 4$ ,  $m = 3$  and FEM (1271 nodes) at the point A on the plate-hole problem.

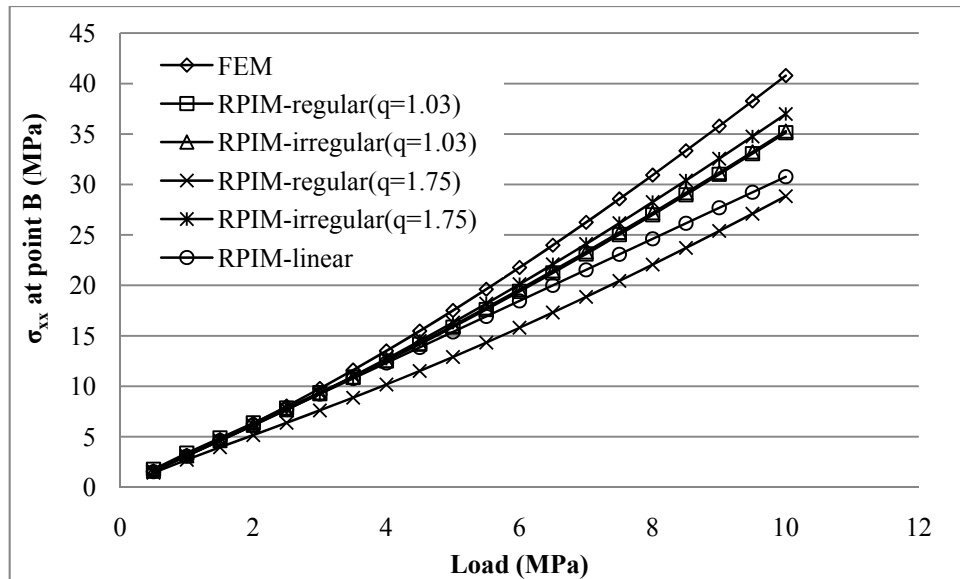


**Figure 4.19** Stress variations against load steps for RPIM 91 regular and 98 irregular distributed nodes with  $\alpha_c = 4$ ,  $m = 3$  and FEM (1271 nodes) at the point B on the plate-hole problem.

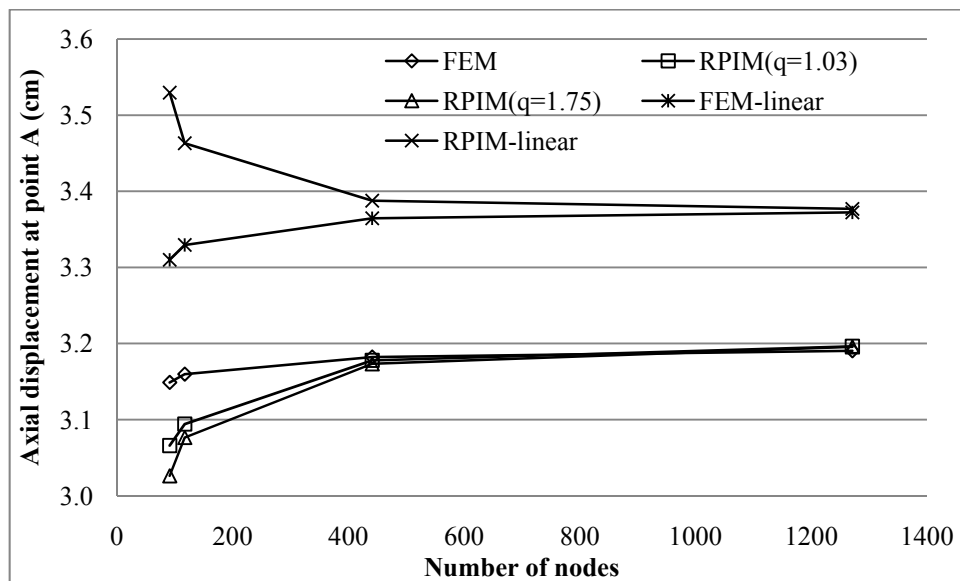


**Figure 4.20** The convergence rate of displacements at the last load increment at the point A on the plate with hole by increasing number of nodes with  $\alpha_c = 4$ ,  $m = 3$  used in the models.

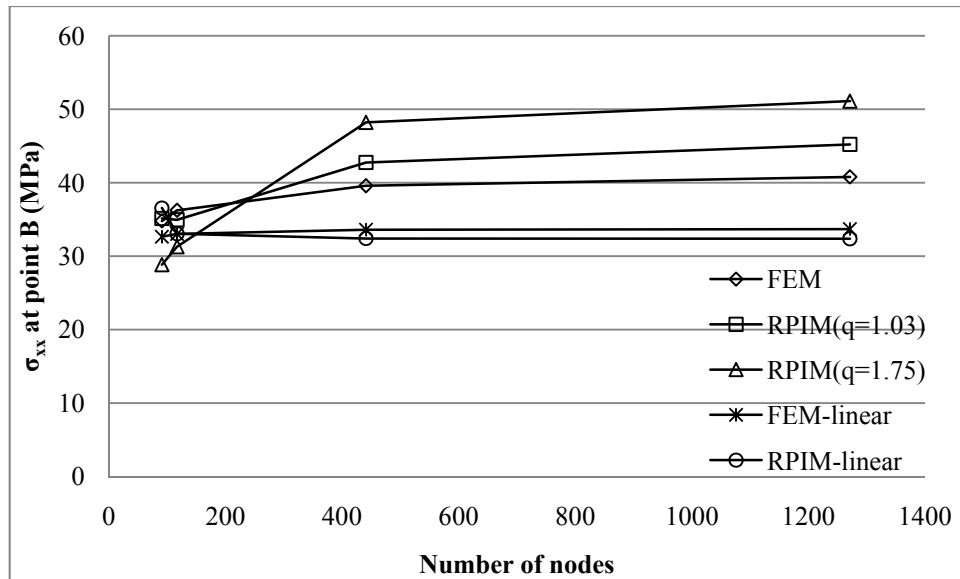


**Figure 4.21** The convergence rate of stresses at the last load increment at the point A on the plate with hole by increasing number of nodes with  $\alpha_c = 4$ ,  $m = 3$  used in the models.

#### 4.4.2.2 Effect of $\alpha_c$

The displacements at the point A are generally in a good agreement for all  $\alpha_c$  values as shown in Figure 4.22. The largest displacement deviation from FEM results is obtained when  $\alpha_c$  is used as 6. The best agreement with FEM is obtained when  $\alpha_c$  is used as 3. The stresses are seriously affected from  $\alpha_c$  values as shown in Figure 4.23. The best agreement between FEM and RPIM results are obtained when  $\alpha_c$  is used as 3.

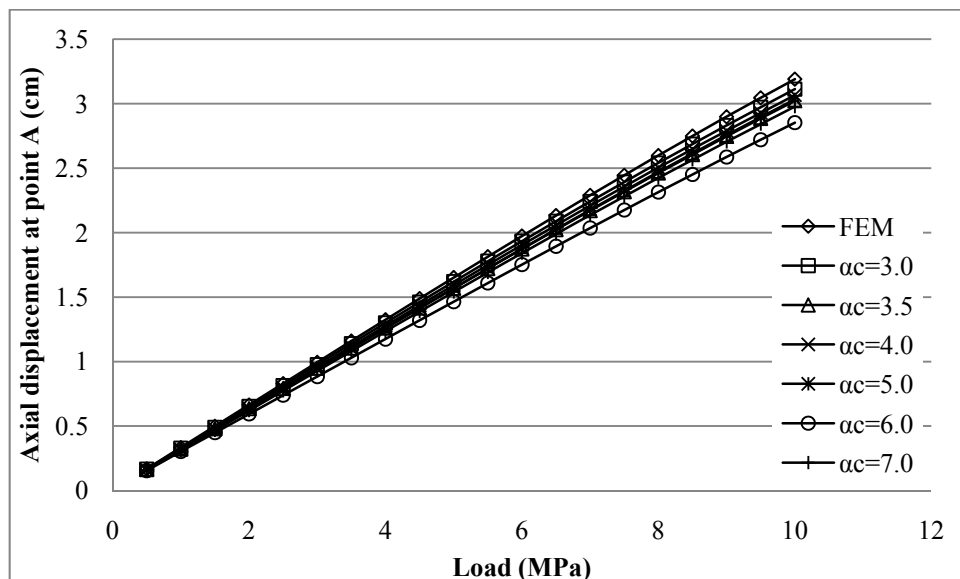


**Figure 4.22** Displacement variations at the point A on the plate with hole against load steps for 91 nodes with  $q = 1.03$ ,  $m = 3$  and various  $\alpha_c$ .



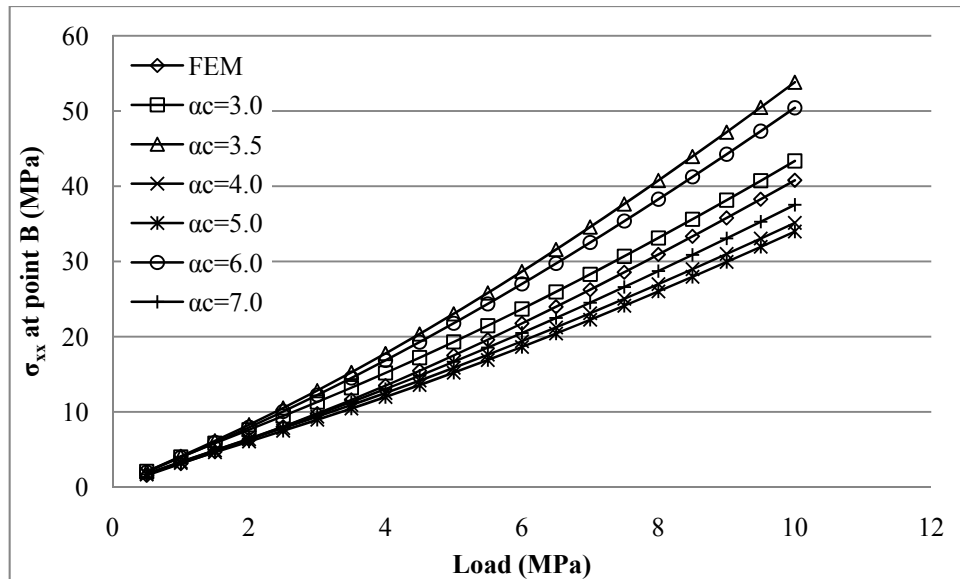


**Figure 4.23** Stress variations at the point B on the plate with hole against load steps for 91 nodes with  $q = 1.03$ ,  $m = 3$  and various  $\alpha_c$ .

#### 4.4.2.3 Effect of $q$

The displacements at point A are almost not affected from the  $q$  values as shown in Figure 4.24. However, the stresses at point B are drastically affected as shown in Figure 4.25. Best agreements between RPIM and FEM solutions are obtained when  $q$  is used between 0.999 and 1.05.

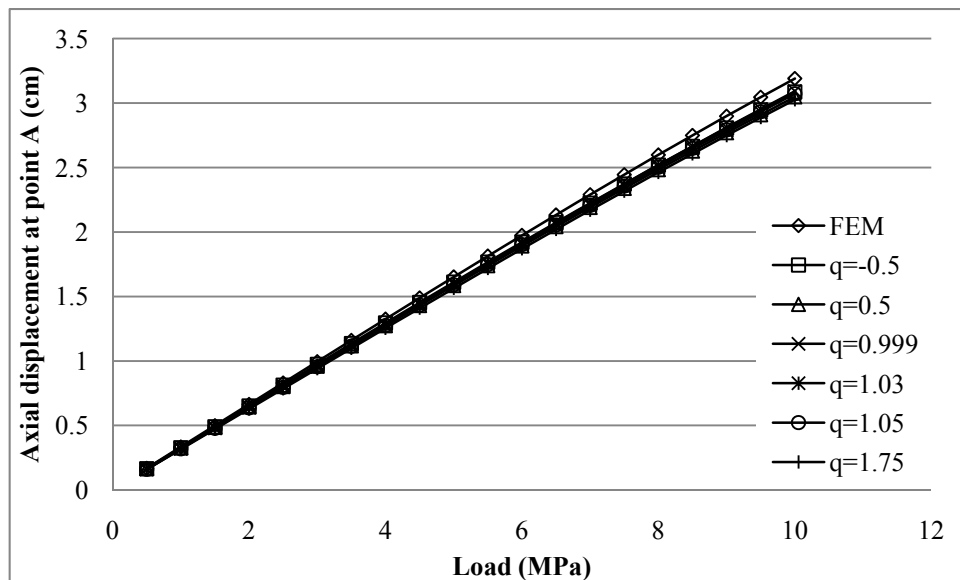


**Figure 4.24** Displacement variations at the point A on the plate with hole against load steps for 91 nodes with  $\alpha_c = 4$ ,  $m = 3$  and various  $q$ .

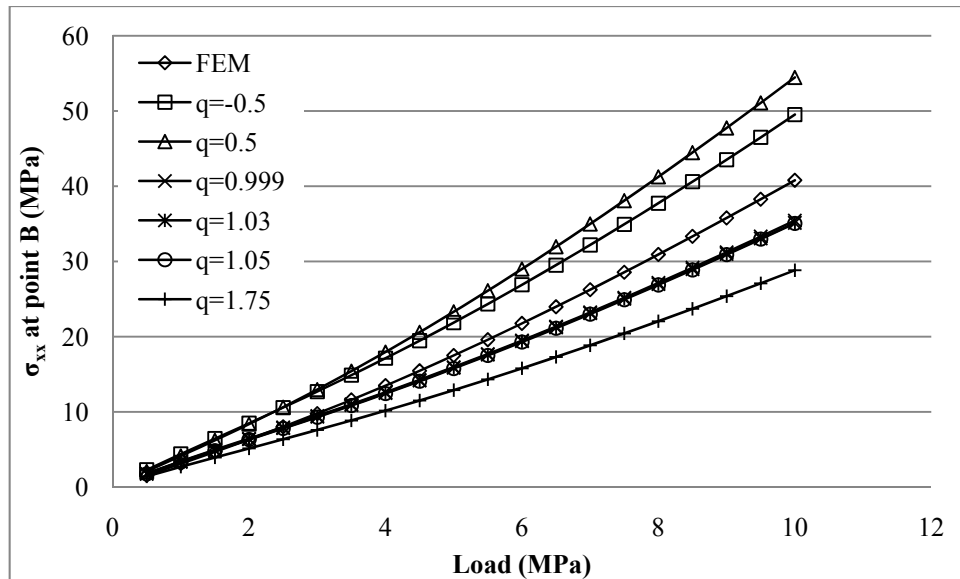


**Figure 4.25** Stress variations at the point B on the plate with hole against load steps for 91 nodes with  $\alpha_c = 4$ ,  $m = 3$  and various  $q$ .

#### 4.4.2.4 Effect of number of monomials

The displacements are not affected by the change of values of  $m$  as shown in Figure 4.26. However, changing values of  $m$  affects the stresses at the point B as shown in Figure 4.27. The best agreement between RPIM and FEM is obtained when  $m$  is used as 3. Increasing the number of monomials causes diverging the stresses from FEM results.

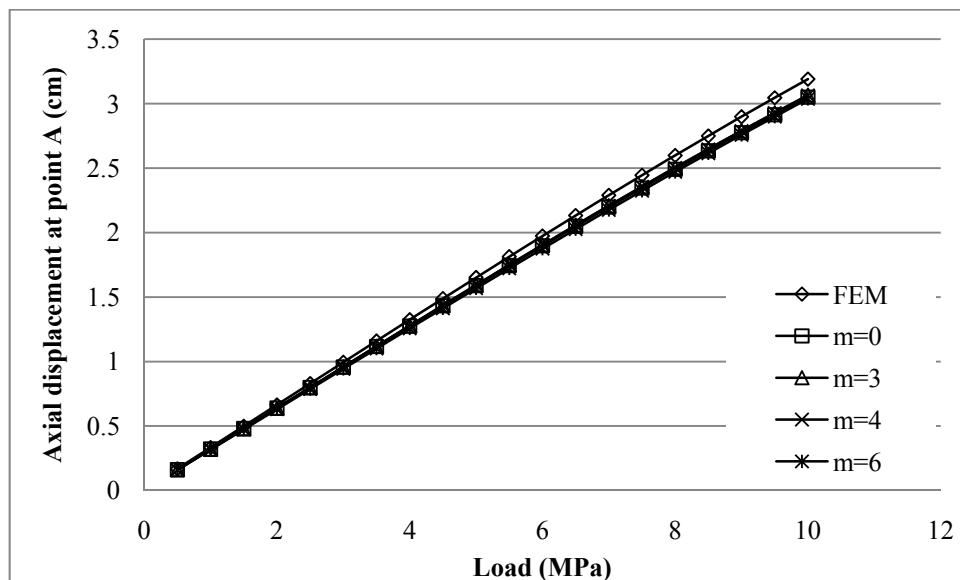


**Figure 4.26** Displacement variations at the point A on the plate with hole against load steps for 91 nodes with  $\alpha_c = 4$ ,  $q = 1.03$  and various  $m$ .

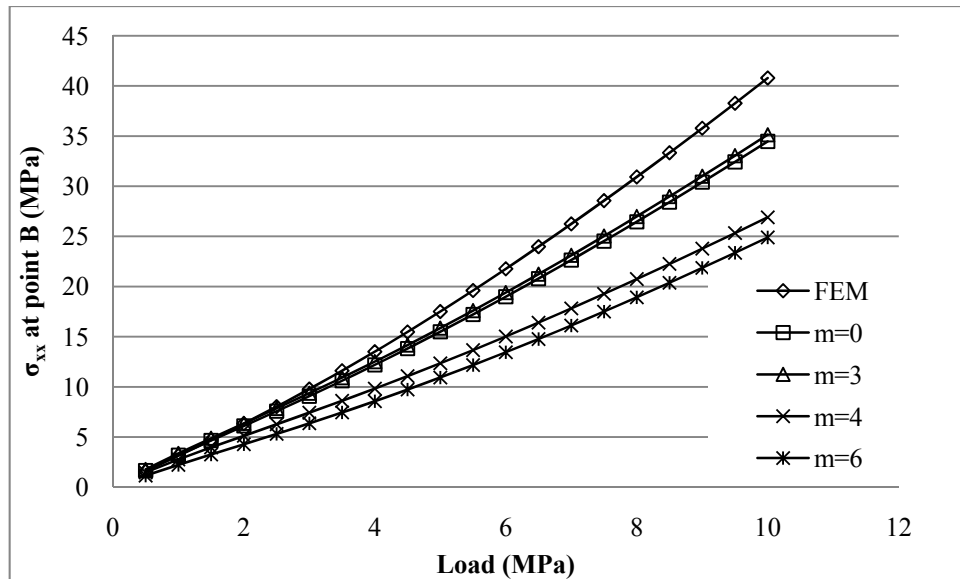


**Figure 4.27** Stress variations at the point B on the plate with hole against load steps for 91 nodes with  $\alpha_c = 4$ ,  $q = 1.03$  and various  $m$ .

#### 4.4.3 Cantilever beam

The cantilever beam is an example which is used for verifications of meshfree methods in the solution of large deformation problems [2,157]. Therefore, a cantilever beam is solved with an initial dimension of  $10\text{ cm} \times 2\text{ cm}$  as shown in Figure 4.28. The regular and irregular RPIM models and FEM model are shown in Figure 4.29. The data used in the cantilever beam is compared for FEM and RPIM as shown in the Table 3. The stresses and displacements are plotted at point A and B respectively.

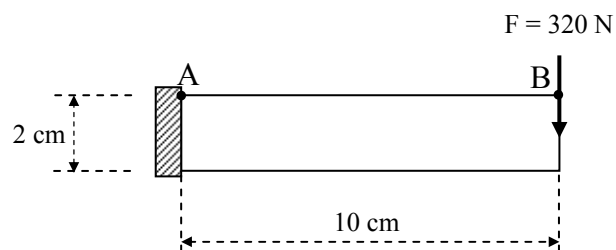


**Figure 4.28** Cantilever beam

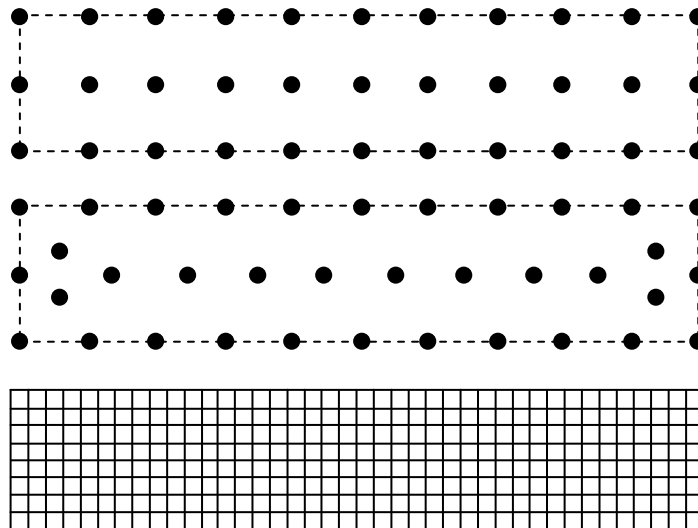


**Figure 4.29** RPIM models with regular and irregular distributed nodes and FEM model of cantilever beam.

**Table 4.3** Data used in the RPIM and FEM models of cantilever beam

	<b>RPIM</b>	<b>FEM</b>
<b>Problem type</b>	Plane stress with unit thickness	Plane stress with unit thickness
<b>Dimensions</b>	10 cm x 2 cm	10 cm x 2 cm
<b>External load</b>	320 N (in 20 increments)	320 N (in 20 increments)
<b>Linear solution</b>	$E = 120 \text{ MPa}$ , $\nu = 0.2$	$E = 120 \text{ MPa}$ , $\nu = 0.2$
<b>Geometrically nonlinear solution</b>	Neo-Hookean with $\lambda = 33.33 \text{ MPa}$ $\mu = 50 \text{ MPa}$	Neo-Hookean with $\lambda = 33.33 \text{ MPa}$ $\mu = 50 \text{ MPa}$
<b>Number of nodes in the entire problem domain</b>	33 regular and 36 irregular distributed nodes with 20 background cells	561 nodes with 500 rectangular elements
<b>Number of nodes</b>	<u>in a local domain</u> Constant, 7	<u>in an element</u> Constant, 4
<b>Sampling points for numerical integrations</b>	4x4	2x2
<b>Number of iteration in each load increment</b>	Changes between 2 and 4	Changes between 3 and 6

#### 4.4.3.1 Convergency rate

The large deformation of the cantilever beam is obtained using RPIM model with regular distributed nodes in the various load steps (Figure 4.30). In these solutions,  $q = 1.03$ ,  $\alpha_c = 4$  and  $m = 3$  are used. The linearity between the displacements and load increments disappear as the load increases and beam

becomes more stiff (Figure 4.31). There is a perfect agreement in the RPIM and FEM displacement solutions. There are also good agreements between stress solutions (Figure 4.32). To see the convergence rate of displacements and stresses, Figure 4.33 and Figure 4.34 are plotted. The RPIM and FEM displacements show nearly same convergence behaviour as shown in Figure 4.34. RPIM stresses convergence more rapidly than FEM as shown in Figure 4.35.

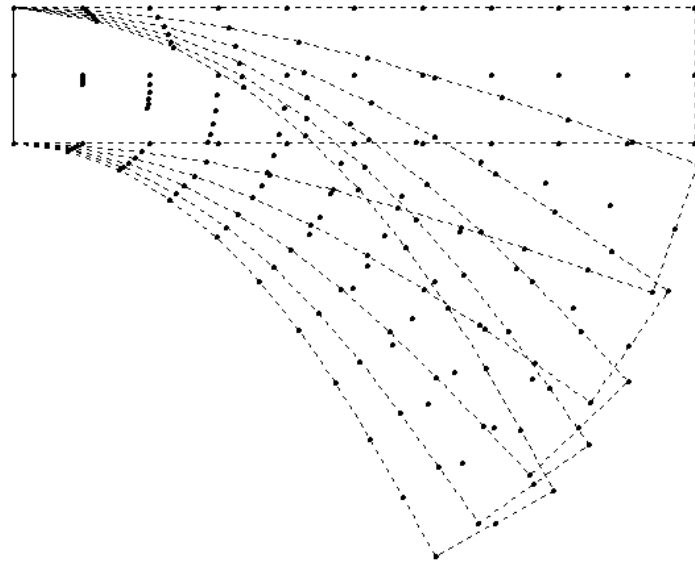


**Figure 4.30** RPIM solution steps of large deformation of the cantilever beam with regular distributed nodes.

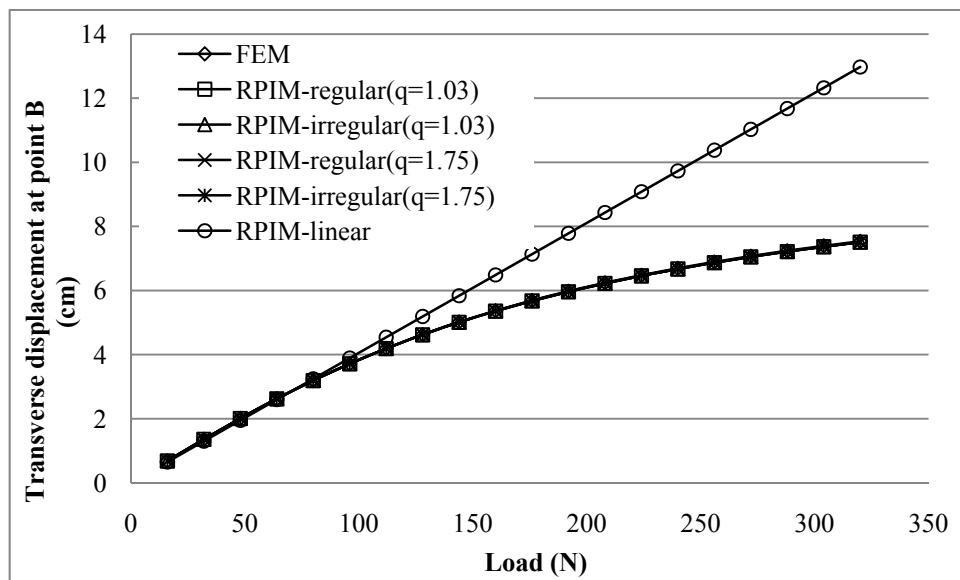


**Figure 4.31** Displacement variations against load steps for RPIM 33 regular and 36 irregular distributed nodes with  $\alpha_c = 4$ ,  $m = 3$  and FEM (561 nodes) at the point B on the cantilever beam.

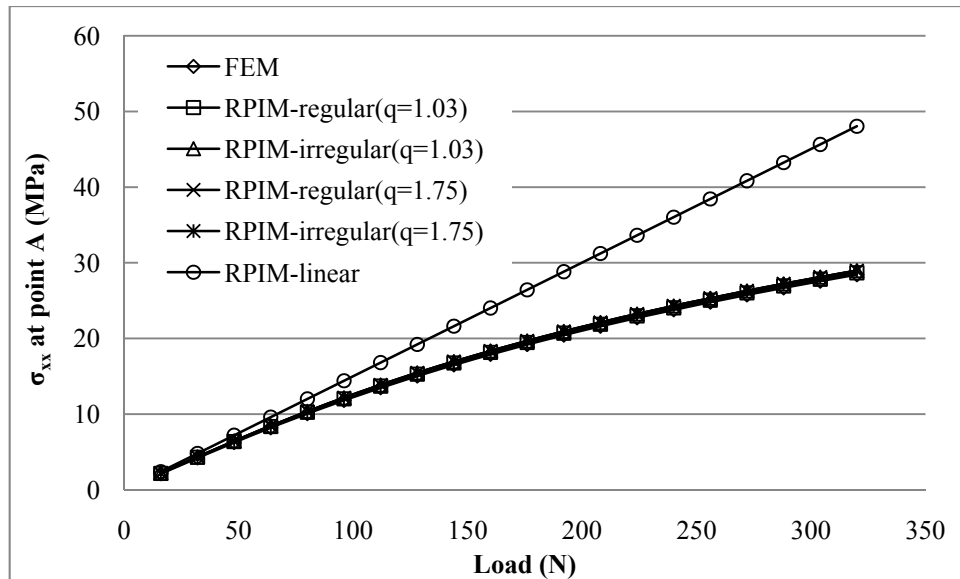


**Figure 4.32** Stress variations against load steps for RPIM 33 regular and 36 irregular distributed nodes with  $\alpha_c = 4$ ,  $m = 3$  and FEM (561 nodes) at the point A on the cantilever beam.

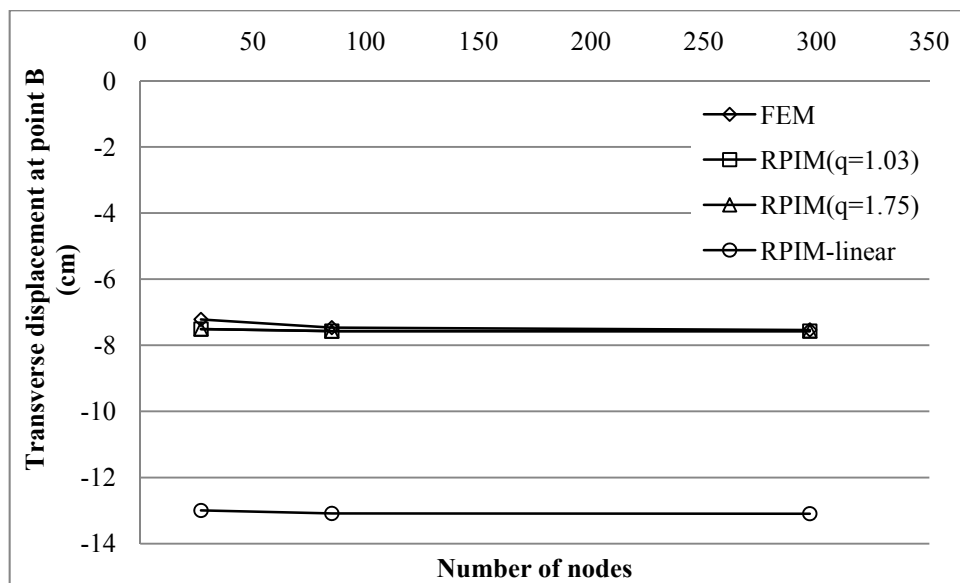


**Figure 4.33** The convergence rate of displacements at the last load increment at the point B on the cantilever beam by increasing number of nodes with  $\alpha_c = 4$ ,  $m = 3$  used in the models.

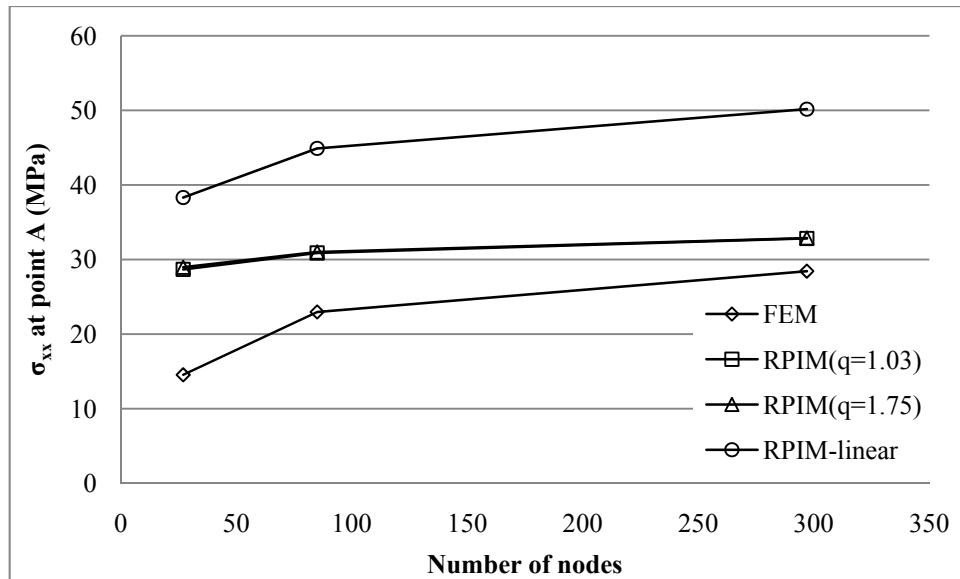


**Figure 4.34** The convergence rate of stresses at the last load increment at the point A on the cantilever beam by increasing number of nodes with  $\alpha_c = 4$ ,  $m = 3$  used in the models.

#### 4.4.3.2 Effect of $\alpha_c$

The displacement and stress variations are investigated for  $q = 1.03$ ,  $m = 3$  and various  $\alpha_c$ . The same displacement distributions are obtained for all values of  $\alpha_c$  (Figure 4.35). However, there are some slight differences in stresses between FEM and RPIM as shown in Figure 4.36.

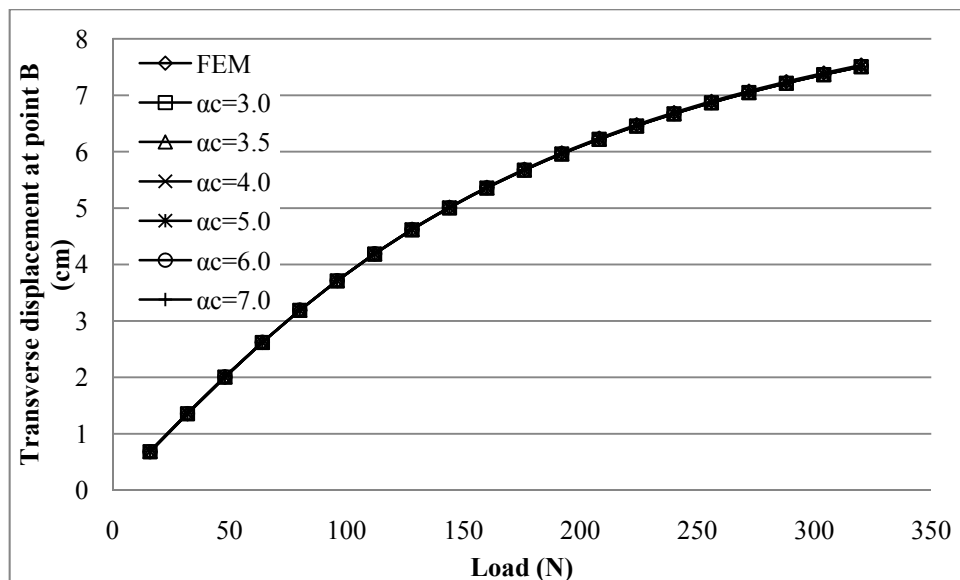


**Figure 4.35** Displacement variations at the point B on the cantilever beam against load steps for 33 nodes with  $q = 1.03$ ,  $m = 3$  and various  $\alpha_c$ .

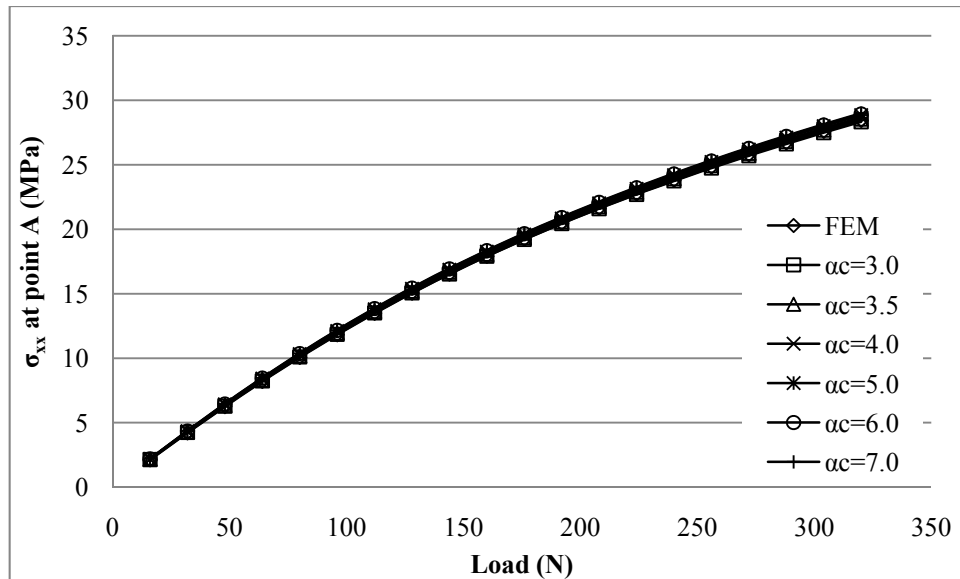


**Figure 4.36** Stress variations at the point A on the cantilever beam against load steps for 33 nodes with  $q = 1.03$ ,  $m = 3$  and various  $\alpha_c$ .

#### 4.4.3.3 Effect of $q$

The displacements and stresses are plotted for  $\alpha_c = 4$ ,  $m = 3$  and various  $q$ . There are good agreements between the RPIM and FEM displacement and stress results for all values of  $q$  as shown in Figure 4.37 and 4.38. The worst displacement and stress distribution are obtained when  $q = -0.5$ .

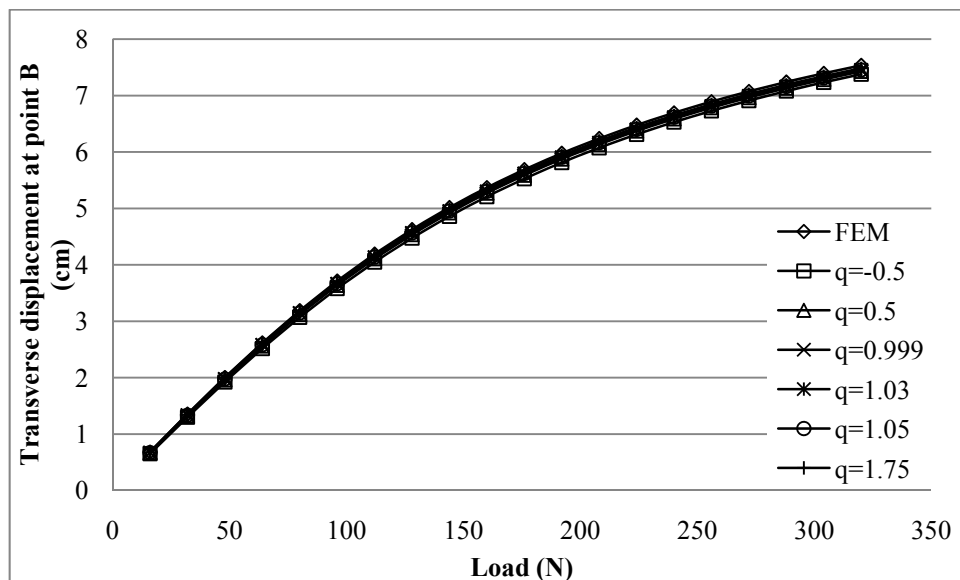


**Figure 4.37** Displacement variations at the point B on the cantilever beam against load steps for 33 nodes with  $\alpha_c = 4$ ,  $m = 3$  and various  $q$ .



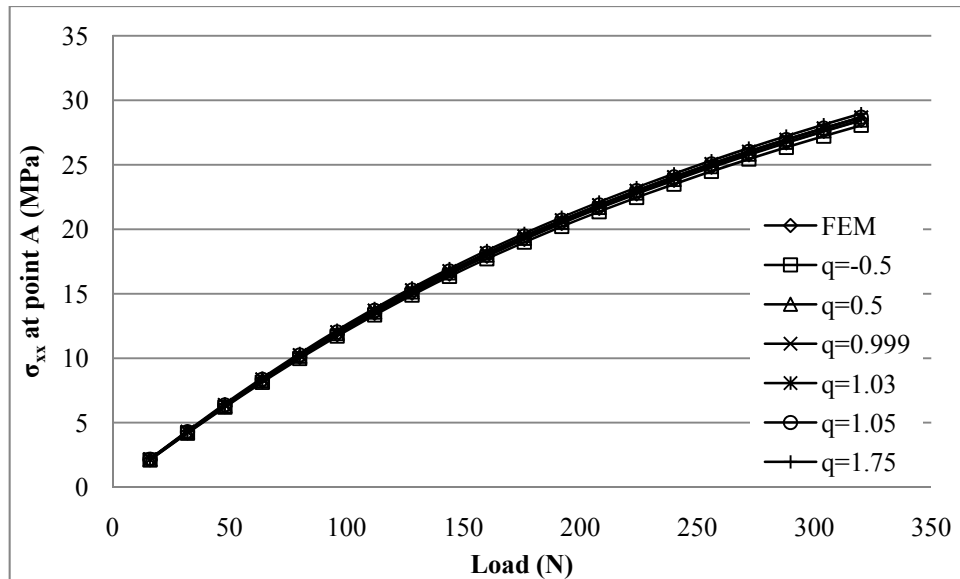


**Figure 4.38** Stress variations at the point A on the cantilever beam against load steps for 33 nodes with  $\alpha_c = 4$ ,  $m = 3$  and various  $q$ .

#### 4.4.3.4 Effect of number of monomials

Because of the number of nodes included in the support domains, the radial shape functions for  $m = 6$  cannot be obtained. The FEM displacement results are same with RPIM displacements for all  $m$  except  $m = 0$ . The displacements show a slight difference when  $m$  is equal to zero (Figure 4.39). There are good agreements between FEM and RPIM stresses for all values of  $m$  as shown in Figure 4.40.

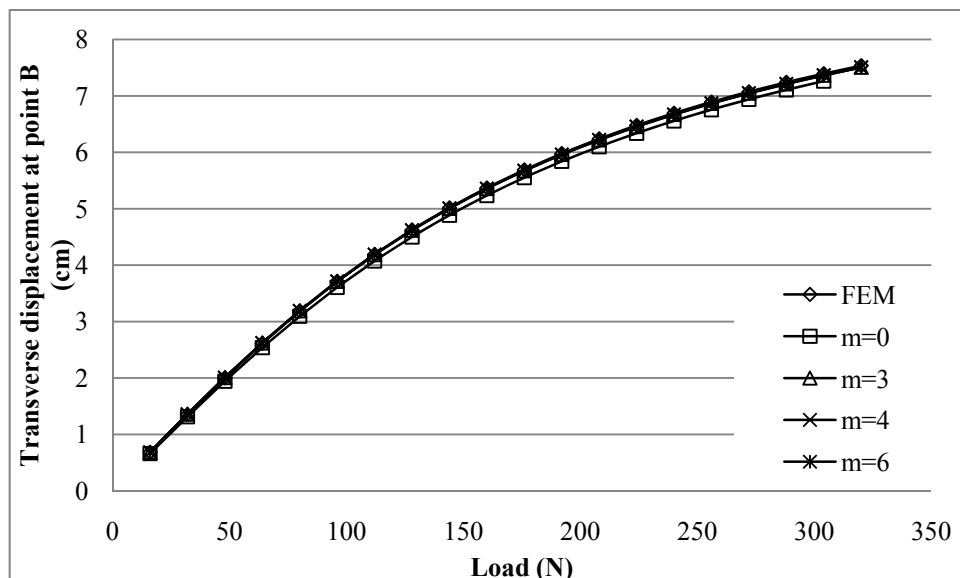


**Figure 4.39** Displacement variations at the point B on the cantilever beam against load steps for 33 nodes with  $\alpha_c=4$ ,  $q = 1.03$  and various  $m$ .

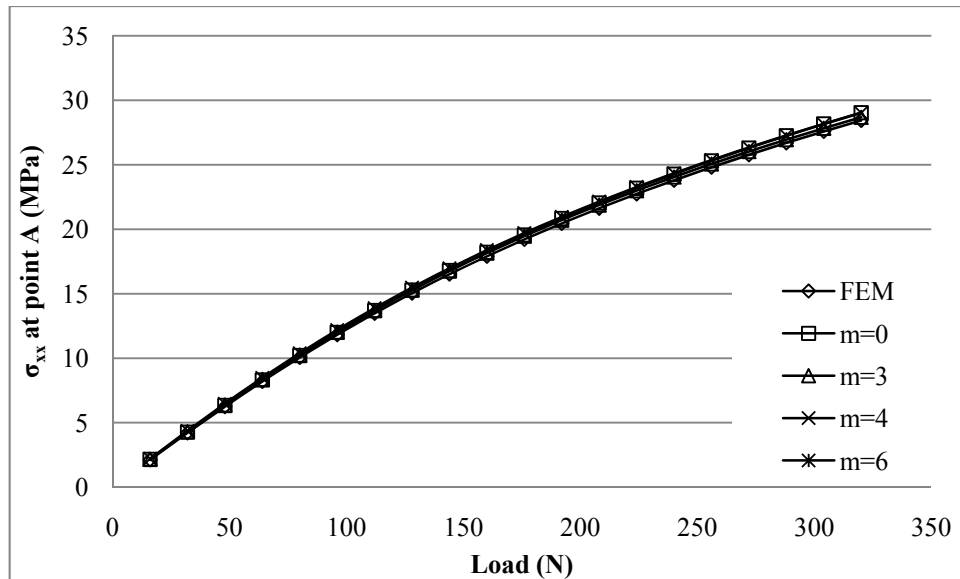


**Figure 4.40** Stress variations at the point B on the cantilever beam against load steps for 33 nodes with  $\alpha_c = 4$ ,  $q = 1.03$  and various  $m$ .

#### 4.4.4 Pressurized thick-walled cylinder

The pressurized cylinder is another case which is used for validation of Meshfree solution of geometrical nonlinear problems [160]. The data of the model, shown in Figure 4.41, is given in the Table 4.4. The irregular and regular RPIM models are shown in Figure 4.42. The stresses and displacements are discussed for the point A in the model.

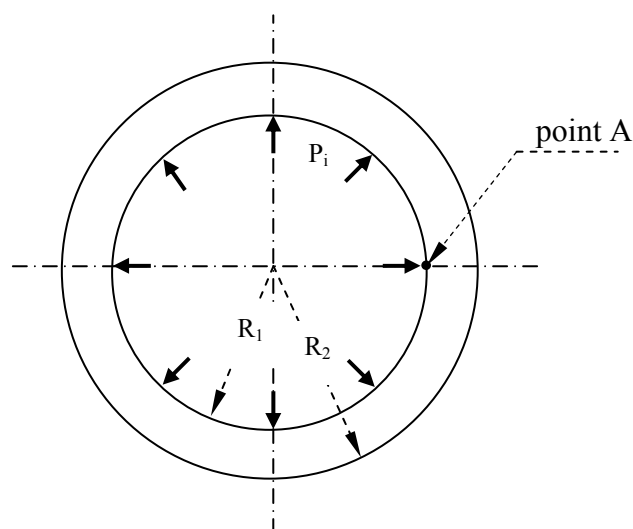


**Figure 4.41** Thick-walled pressurized cylinder

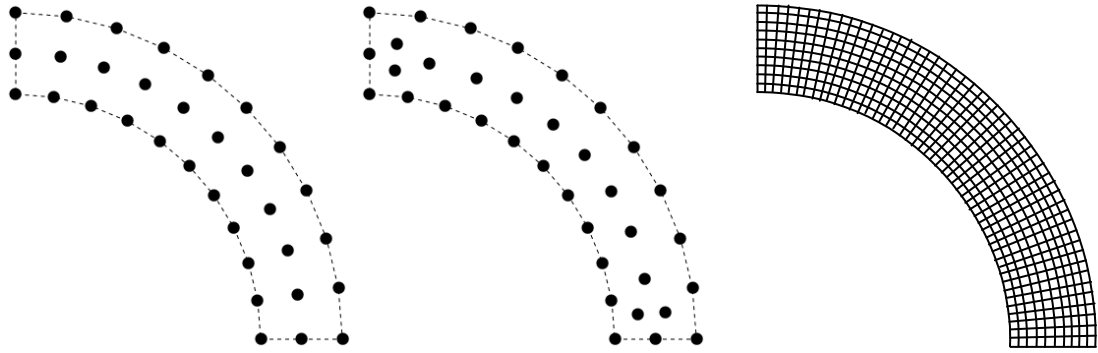


**Figure 4.42** RPIM models with regular and irregular distributed nodes and FEM model of thick-walled pressurized cylinder.

**Table 4.4** Data used in the RPIM and FEM models of pressurized thick-walled cylinder

	RPIM	FEM
<b>Problem type</b>	Plane strain	Plane strain
<b>Dimensions</b>	$R_1=6$ cm and $R_2= 8$ cm	$R_1=6$ cm and $R_2= 8$ cm
<b>External load</b>	$P_i=1.8$ kPa (in 30 increments)	$P_i=1.8$ kPa (in 30 increments)
<b>Linear solution</b>	$E = 120$ MPa, $\nu = 0.2$	$E = 120$ MPa, $\nu = 0.2$
<b>Geometrically nonlinear solution</b>	Neo-Hookean with $\lambda = 33.33$ MPa $\mu = 50$ MPa	Neo-Hookean with $\lambda = 33.33$ MPa $\mu = 50$ MPa
<b>Number of nodes in the entire problem domain</b>	561 regular and 561 irregular distributed nodes with 500 background cells	2121 nodes with 2000 rectangular elements
<b>Number of nodes</b>	<u>in a local domain</u> Changes between 4 and 9	<u>in an element</u> Constant, 4
<b>Sampling points for numerical integrations</b>	4x4	2x2
<b>Number of iteration in each load increment</b>	Constant, 3	Changes between 2 and 3

#### 4.4.4.1 Convergency rate

RPIM with regular distributed nodes gives the deformation steps as shown in Figure 4.43. In this solution,  $q = 1.03$ ,  $\alpha_c = 4$  and  $m = 3$  are used. The displacement variations against load increments are shown in Figure 4.44. Nonlinear solutions diverge from linear elastic solutions at the initial load increments. In contrast to the cantilever beam problem, the cylinder is softened as the load increases. A good agreement is achieved in RPIM and FEM tangential stress solutions as shown in Figure 4.45. However, there are some differences in the radial

stress solutions as shown in Figure 4.46. The RPIM and FEM stress solutions show a small curve near to the last load step. The amount of curvature can be decreased by increasing the number nodes in the models. In addition, the irregular RPIM models are in good agreements with FEM for  $q = 1.03$  and  $1.75$ . The results are seriously affected by number of nodes in the models. In order to check this, the number of nodes used in the regular RPIM models is increased and radial stress distribution is redrawn as shown in Figure 4.47. The convergency rate of both displacements and Cauchy stresses are drawn as shown in Figure 4.48, 4.49 and 4.50. The displacement and stress convergency rate of RPIM and FEM are very close to each others.

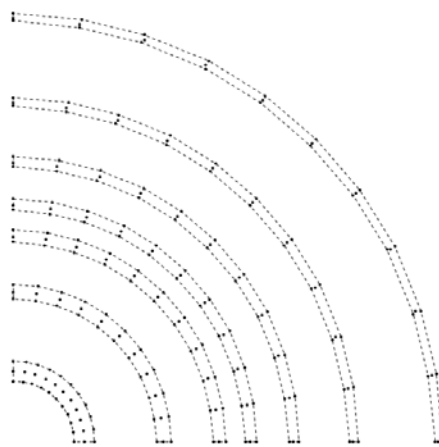


**Figure 4.43** RPIM solution steps of large deformation of the thick-walled pressurized cylinder with regular distributed nodes.

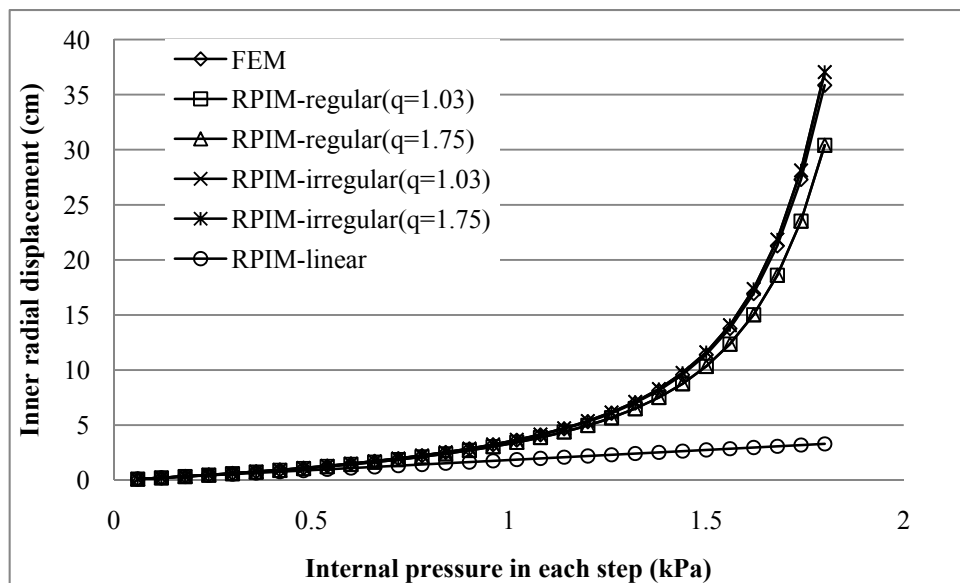


**Figure 4.44** Radial displacement variations against load steps for RPIM 561 regular and 561 irregular distributed nodes  $\alpha_c=4$ ,  $m=3$  and FEM (2121 nodes) at the point A on the thick-walled pressurized cylinder.

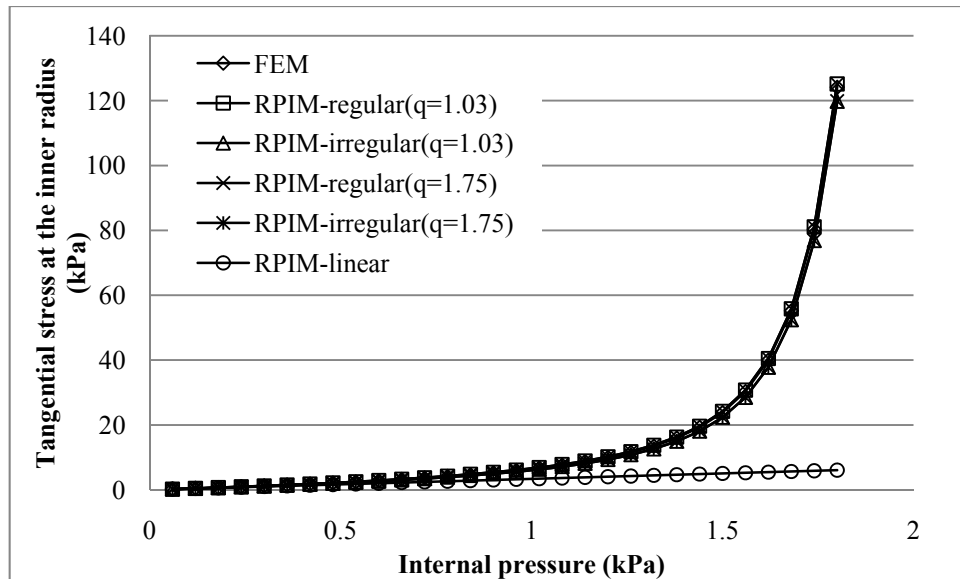


**Figure 4.45** Tangential stress variations against load steps for RPIM 561 regular and 561 irregular distributed nodes  $\alpha_c=4$ ,  $m=3$  and FEM (2121 nodes) at the point A on the thick-walled pressurized cylinder.

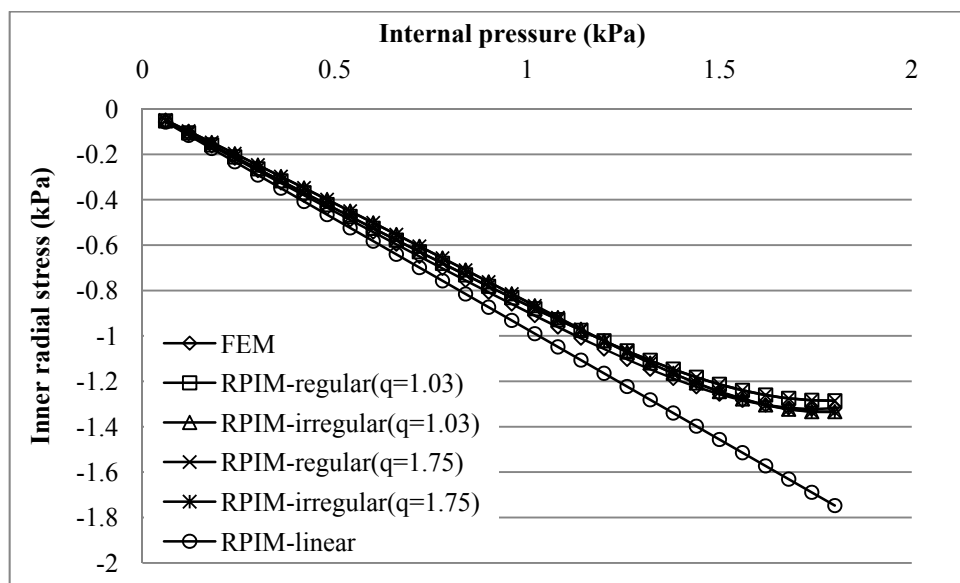


**Figure 4.46** Radial stress variations against load steps for RPIM 561 regular and 561 irregular distributed nodes  $\alpha_c=4$ ,  $m=3$  and FEM (2121 nodes) at the point A on the thick-walled pressurized cylinder.

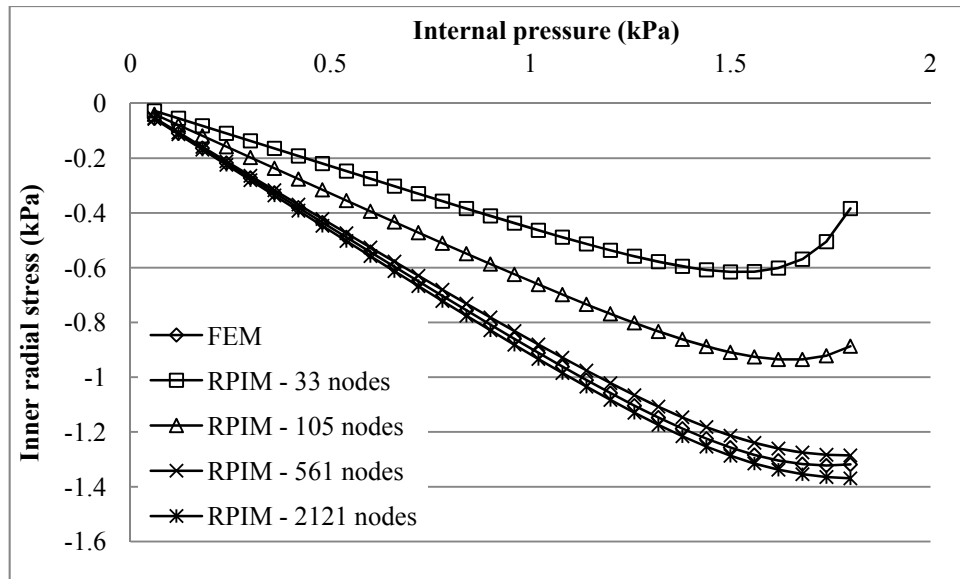


**Figure 4.47** Radial stress variations against load steps for different RPIM 561 regular distributed nodes with  $\alpha_c=4$ ,  $m=3$  and FEM (2121 nodes) at the point A on the thick-walled pressurized cylinder.

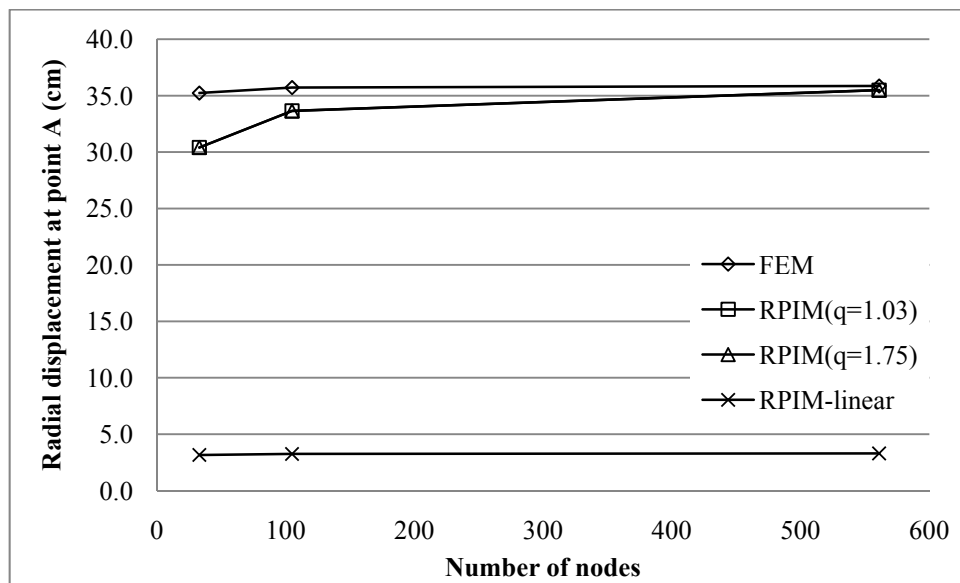


**Figure 4.48** The convergence rate of radial displacements at the last load increment at the point A on the thick-walled pressurized cylinder by increasing number of nodes used in the models with  $\alpha_c=4$ ,  $m=3$ .

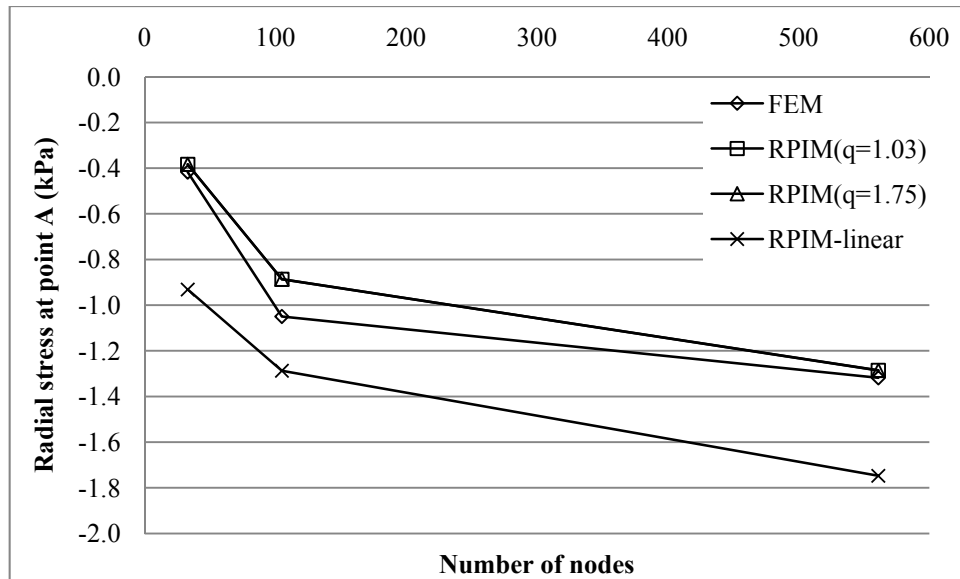


**Figure 4.49** The convergence rate of radial stresses at the last load increment at the point A on the thick-walled pressurized cylinder by increasing number of nodes used in the models with  $\alpha_c=4$ ,  $m=3$ .

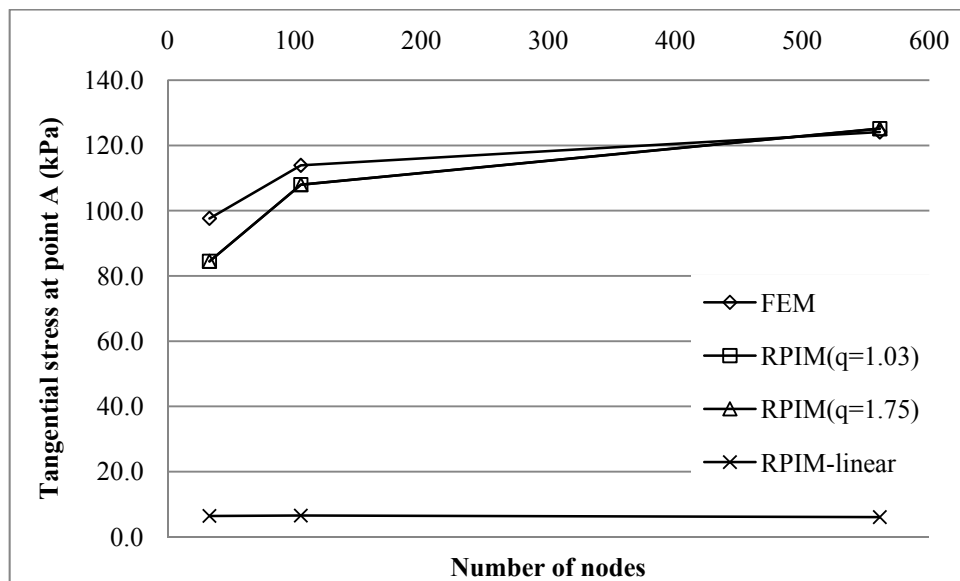


**Figure 4.50** The convergence rate of tangential stresses at the last load increment at the point A on the thick-walled pressurized cylinder by increasing number of nodes used in the models with  $\alpha_c=4$ ,  $m=3$ .

#### 4.4.4.2 Effect of $\alpha_c$

In order to see the effect of shape parameters, the RPIM model with 561 nodes is used. The displacements and stresses are plotted against load increments for  $q=1.03$ ,  $m=3$  and various  $\alpha_c$  as shown in Figure 4.51 and 4.52. It is shown that the

values of  $\alpha_c$  do not affect the behaviour of displacement and radial stress distributions.

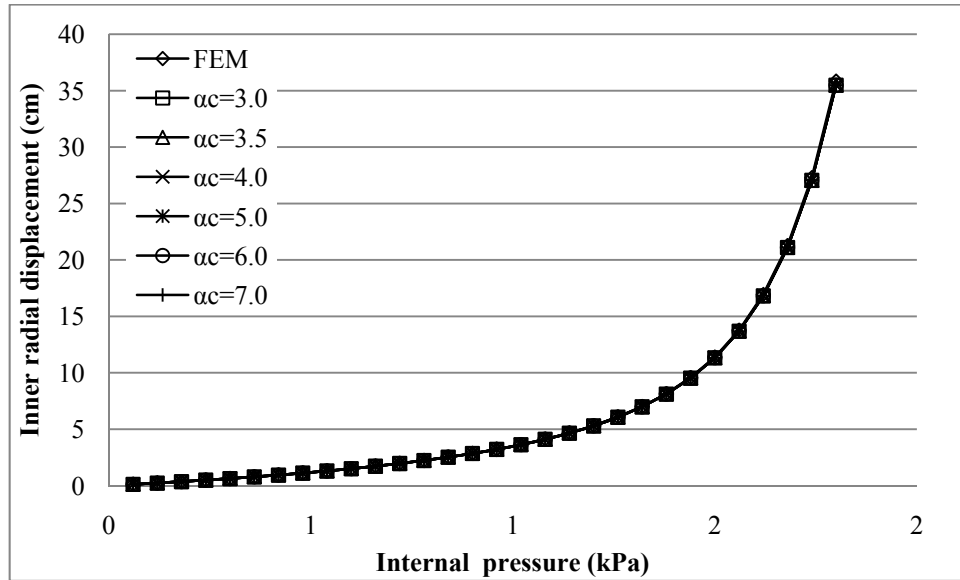


**Figure 4.51** Radial displacement variations at the point A against load steps for 561 nodes with  $q=1.03$ ,  $m=3$  and various  $\alpha_c$ .

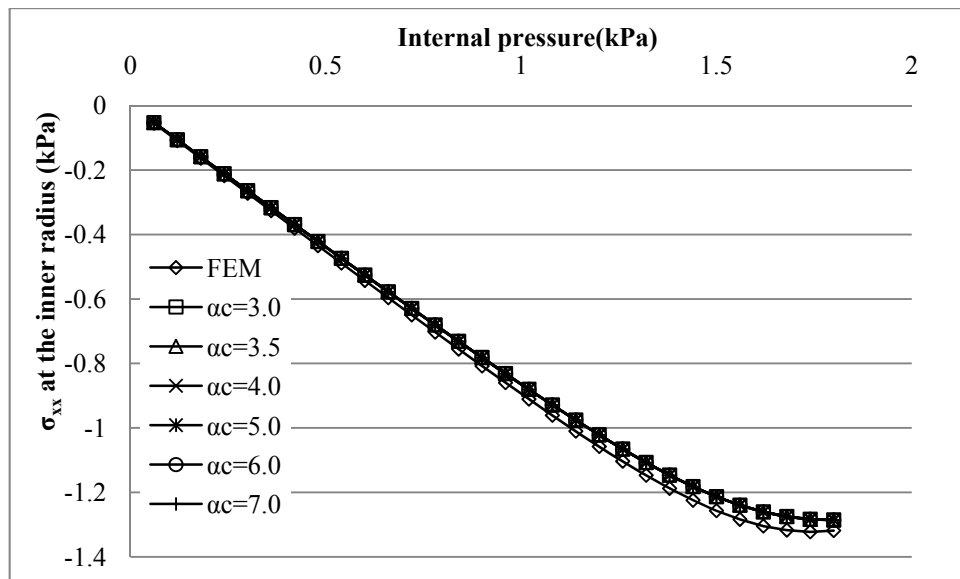


**Figure 4.52** Radial stress variations at the point A on the thick-walled pressurized cylinder against load steps for 561 nodes with  $q=1.03$ ,  $m=3$  and various  $\alpha_c$ .

#### 4.4.4.3 Effect of $q$

The variations of displacements and stresses against load increments are plotted for constant  $\alpha_c = 4$  and  $m=3$  and various  $q$  as shown in Figure 4.53 and 4.54.



Once again, values of  $q$  do not have an important effect in displacement and stress distributions.

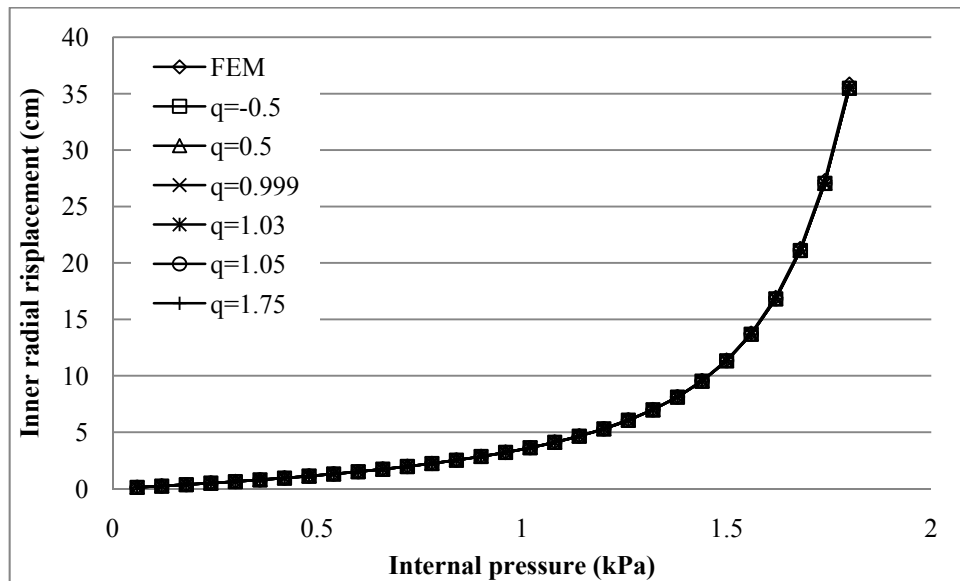


**Figure 4.53** Radial displacement variations at the point A on the thick-walled pressurized cylinder against load steps for 561 nodes with  $\alpha_c = 4$ ,  $m = 3$  and various  $q$ .

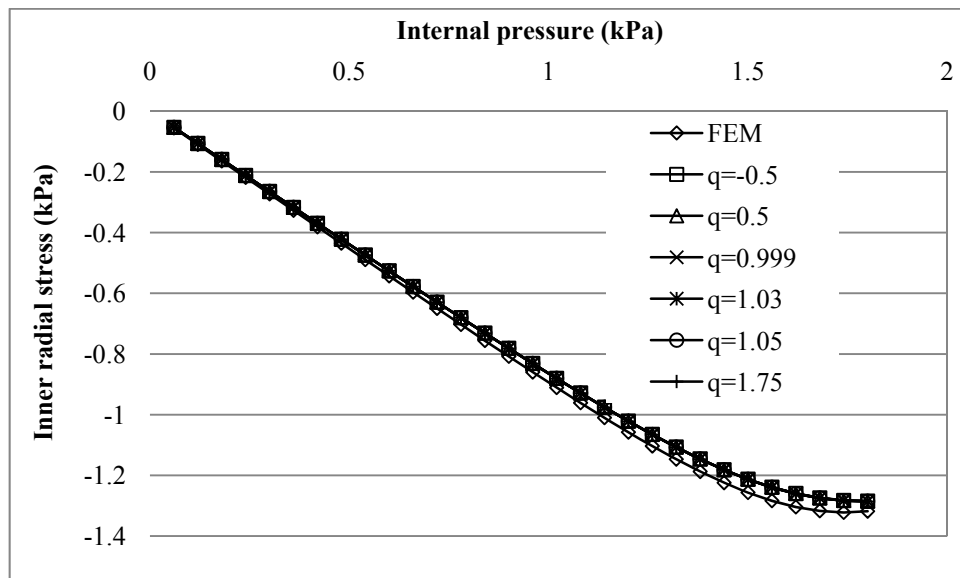


**Figure 4.54** Radial stress variations at the point A on the thick-walled pressurized cylinder against load steps for 561 nodes with  $\alpha_c = 4$ ,  $m = 3$  and various  $q$ .

#### 4.4.4.4 Effect of number of monomials

Because of the number of nodes used in the support domains, the radial shape functions is not obtained for  $m = 4$  and  $6$ . The FEM radial displacement distribution is in good agreement with RPIM for  $m = 3$ . However, RPIM radial stresses with  $m = 0$

shows some deviations (Figure 4.55). The RPIM and FEM radial stresses are in good agreement except RPIM with  $m=0$  as shown in Figure 4.56.

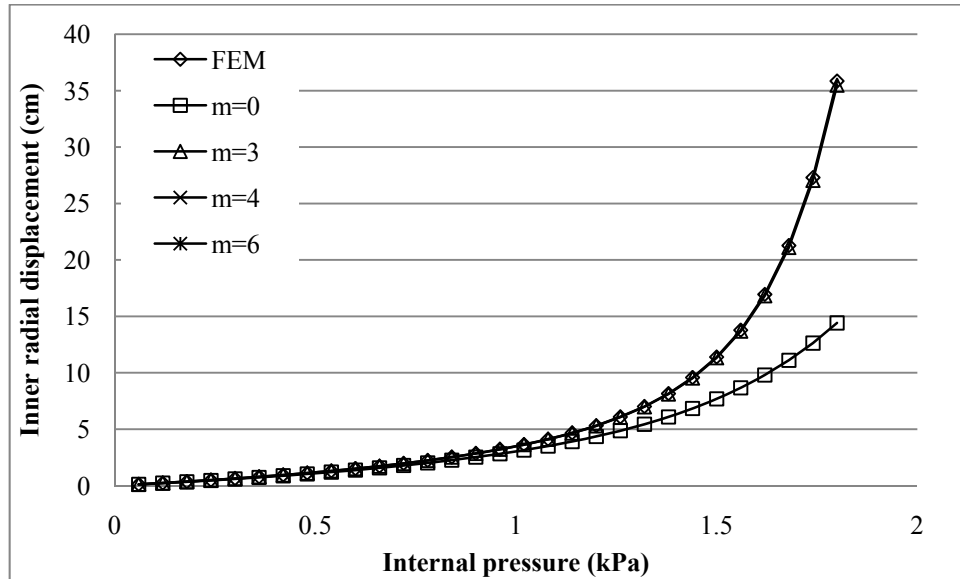


**Figure 4.55** Radial displacement variations at the point A on the thick-walled pressurized cylinder against load steps for 561 nodes with  $\alpha_c = 4$ ,  $q = 1.03$  and various  $m$ .

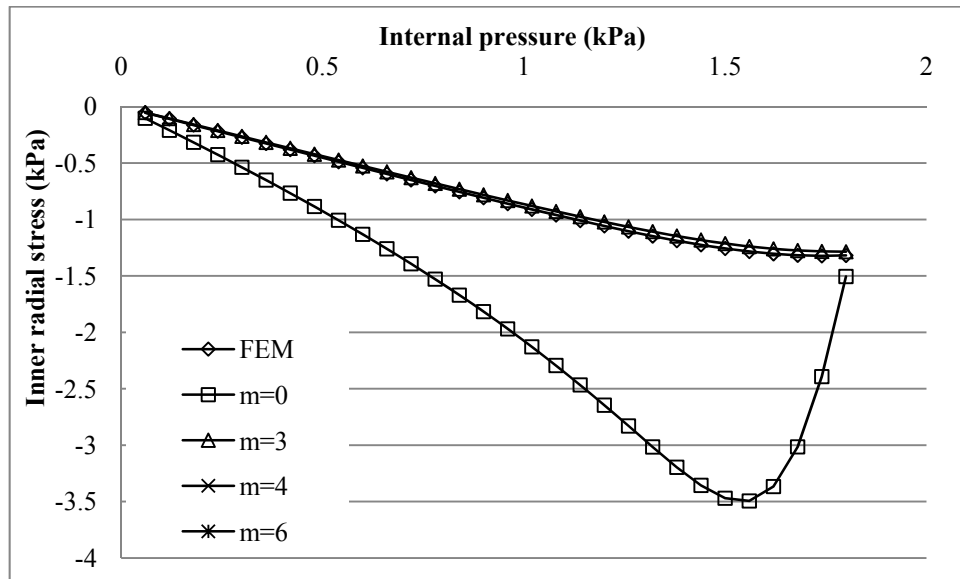


**Figure 4.56** Radial stress variations at the point A on the thick-walled pressurized cylinder against load steps for 561 nodes with  $\alpha_c = 4$ ,  $q = 1.03$  and various  $m$ .

#### 4.5. Results and Discussions

It was observed that the node distribution characteristic is more effective than the shape parameters in the displacement and stress solutions. It was also shown that RPIM shape parameters usually affect the stresses more than displacements. The

values of shape parameters are generally problem dependent. However, more stable results are obtained with shape parameters,  $q = 1.03$  and  $\alpha_c = 3$  and  $m = 3$ .

$q = 1.03$  is used as optimum value in many studies, however, in some cases, the stress results for  $q = 1.75$  can be accurate as much as for  $q = 1.03$ . For example, when irregular nodes are used in the plate with hole and pressurized cylinder examples, they give better stresses with  $q = 1.75$ . This study agrees that the best stress solutions are obtained for the values of  $\alpha_c$  between 3 and 4. It is also shown that when the same increase in the number of nodes is considered, improvements in the RPIM results are better than FEM with suggested values of shape parameters.

It was also shown that increasing number of polynomials does not always improve the results. Depending on the number of nodes used in the support domains, increasing number of polynomial basis may cause shape function construction errors.

## CHAPTER 5

### ANALYSIS OF 2D ELASTO-PLASTIC PROBLEMS USING RPIM

#### 5.1 Introduction

In this chapter, the basics of 2D elasto-plastic analysis are summarized and formulations used for them are reviewed. The essential elements of elasto-plastic analysis are shortly presented in section 5.2. The RPIM formulation for an elasto-plastic analysis is reviewed in section 5.3. The solution procedure used in the elasto-plastic analysis is summarized in section 5.4. To investigate the performance of RPIM in elasto-plastic analyses, some sample problems are solved in section 5.5. They are also compared with analytic results.

#### 5.2 The Essential Elements of Elasto-Plastic Analysis

The theory of plasticity has some fundamental concepts that it cannot be considered without the usage of them. These are the yield criterion, the flow rule and the hardening rule. The yield criterion defines the limit at which the material becomes plastic. The flow rule describes the relationship between stresses and strains once the material has become plastic. The consistency condition which prevents stresses from exceeding the yield limit. The hardening rule describes how the yield criterion is modified by straining beyond initial yield [160].

##### 5.2.1 The Yield Criterion

To determine the stress level at which the plastic deformation begins a scalar yield function is defined and the general form of it can be written as [156,160]

$$f_y(\boldsymbol{\sigma}, w^p, \boldsymbol{\alpha}) = 0 \quad (5.1)$$

where  $\boldsymbol{\sigma}$  is the stress vector,  $w^p$  is the plastic work done, and  $\boldsymbol{\alpha}$  is a vector denoting the translation of the yield surface. According to the hardening model defined yield function gets its specific form. For isotropic hardening model, it is

$$f_y(\boldsymbol{\sigma}, w^p) = 0 \quad (5.2)$$

For kinematic hardening model, it is written as

$$f_y(\boldsymbol{\sigma}, \boldsymbol{\alpha}) = 0 \quad (5.3)$$

Without hardening, it is expressed as

$$f_y(\boldsymbol{\sigma}) = 0 \quad (5.4)$$

The yield function defines a surface in stress space. The two-dimensional case is illustrated in Figure 5.1. The stress level is in the elastic region when  $f_y < 0$ . The boundary  $f_y = 0$  defines the yield surface. The stresses for  $f_y > 0$  is not possible. The incremental change in yield function due to an incremental stress change has two possibilities for stress state on yielding surface:

- $df_y < 0$  unloading occurs and the stress point moves inside the yield surface
- $df_y = 0$  loading, accumulation of plastic strain continues and stress point remains on the yield surface
- $df_y > 0$  not possible (the stress point always remains on the yield surface)

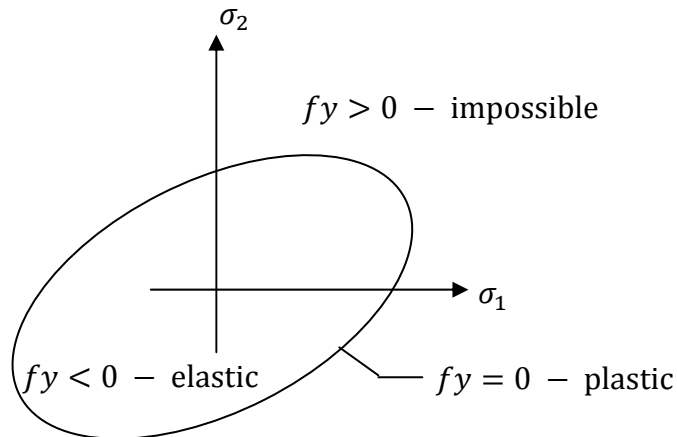


**Figure 5.1.** Yield surface in two dimensional case

The definition of a yield criterion must be independent from the orientation of the coordinate system used [162]. To ensure this, it could be defined in terms of certain invariants, like principal stresses. In many cases, invariants of the stress tensor ( $I_1, I_2$  and  $I_3$ ) or invariants of the deviatoric stress tensor ( $J_1, J_2$  and  $J_3$ ) are also convenient to use.

There are various yield criteria like the Tresca yield criterion, the von Mises yield criterion, the Mohr-Coulomb yield criterion, the Drucker-Prager yield criterion, etc. in the literature. Every yield criterion defines the beginning of plastic deformation using different properties and each yield criterion is suggested for different materials.

### 5.2.1.1 The Tresca Yield Criterion

Tresca yield criteria states that yielding occurs when the maximum shear stress reaches a certain value. This can be written as

$$\tau_{max} = \max\left(\frac{1}{2}|\sigma_1 - \sigma_2|, \frac{1}{2}|\sigma_2 - \sigma_3|, \frac{1}{2}|\sigma_3 - \sigma_1|\right) \quad (5.5.a)$$

$$= \max(\tau_{12}, \tau_{23}, \tau_{31}) = k \quad (5.5.b)$$

where  $k$  is material parameter and it can be determined from simple tension test as

$$k = \frac{1}{2}\sigma_0 \quad (5.6)$$

$\sigma_0$  is the yield stress value in the uniaxial tension test. In plane stress ( $\sigma_3 = 0$ ), the yield surface can be plotted in  $\sigma_1 - \sigma_2$  space as shown in Figure 5.2.

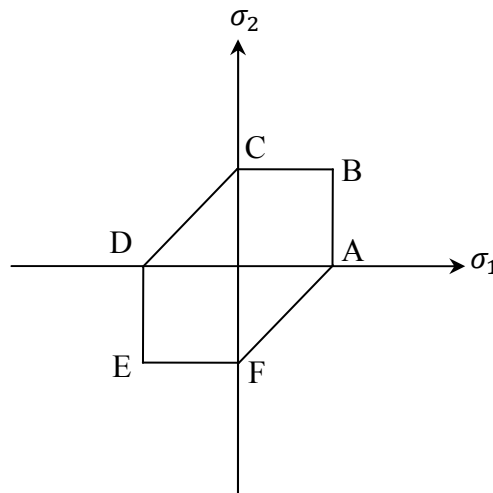


**Figure 5.2.** Tresca yield criteria in plane stress

### 5.2.1.2 The von Mises criterion

The von Mises yield criterion states that yielding takes place when the effective or von Mises stress reaches the yield stress of the material in uniaxial tension. It is given by

$$fy(\boldsymbol{\sigma}) = \sigma_e - \sigma_0 \quad (5.7)$$

where

$$\sigma_e = \sqrt{3J_2} \quad (5.8)$$

and  $\sigma_e$  is named as the effective stress or the equivalent stress. The equation of yield surface for a plane stress problem is obtained as follows,

$$fy(\boldsymbol{\sigma}) = 0 \quad (5.9.a)$$

$$\sqrt{3 \left( \frac{1}{3} (\sigma_1^2 + \sigma_2^2 - \sigma_1 \sigma_2) \right)} - \sigma_0 = 0 \quad (5.9.b)$$

$$\sigma_1^2 + \sigma_2^2 - \sigma_1 \sigma_2 = \sigma_0^2 \quad (5.9.c)$$

Equation 9.c is an equation of ellipse and it can be plotted as in Figure 5.3.

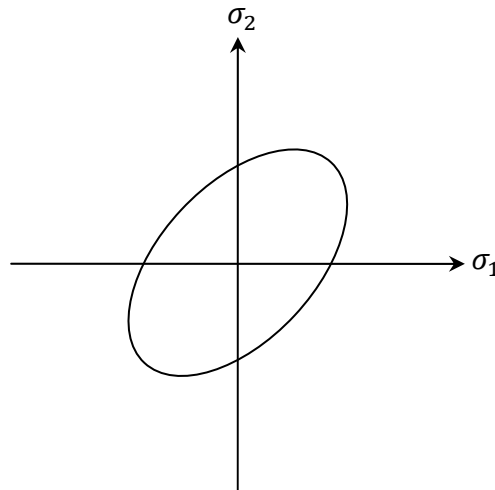


**Figure 5.3.** The von Mises yield criteria in plane stress

### 5.2.2 Hardening

The hardening rule describes how the yield criterion is modified by straining beyond initial yield [161]. Simply, it defines the change in size, shape and position of yield surface during a plastic loading. The isotropic hardening rule and the kinematic hardening rule are two common hardening rules. The isotropic hardening rule, shown in Figure 5.4.(a), states that yield surface can expand without translation under loading, however, the yield surface can move as a rigid body in kinematic hardening rule as shown in Figure 5.4.(b).

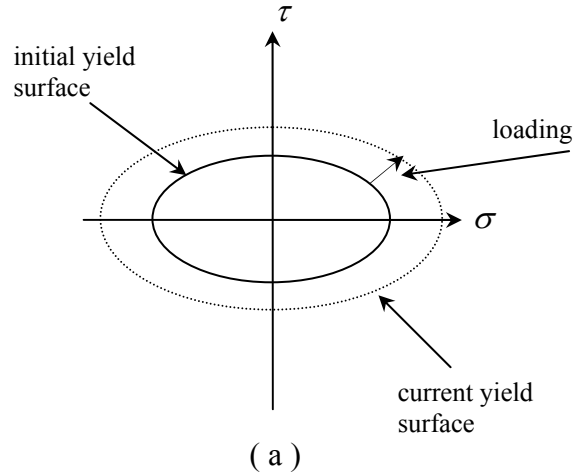


**Figure 5.4.(a).** Mathematical model for representation of isotropic strain hardening behaviour.

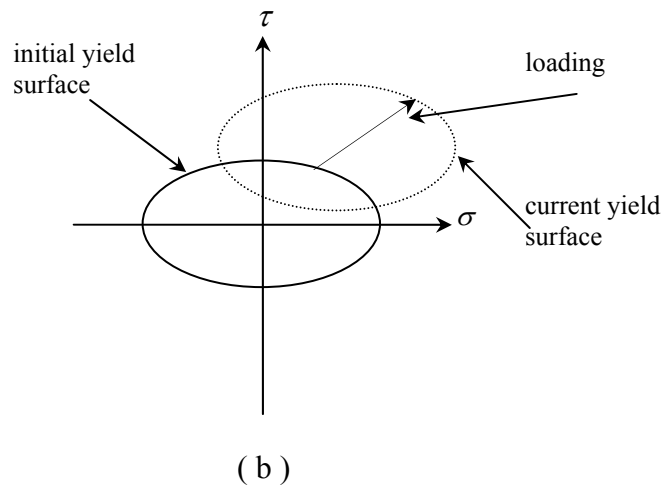


**Figure 5.4.(b).** Mathematical models for representation of kinematic strain hardening behaviour.

In isotropic hardening, the value of  $w^p$  is different from zero and  $\alpha$  must be equal to zero. The translation of the yield surface,  $\alpha$ , must be different from zero in kinematic hardening so that  $\alpha$  must be different from zero and  $w^p$  must be equal to zero.

$$w^p = \int \boldsymbol{\sigma}^T d\boldsymbol{\varepsilon}_p \quad (5.10)$$

$$\alpha = \int \mathbf{D} d\boldsymbol{\varepsilon}_p \quad (5.11)$$



### 5.2.3 Elasto-Plastic Stress-Strain Relation

In an elastic analysis, the stresses can be evaluated using elastic constants and strains, however, in an elasto-plastic analysis it is not simple as the elastic analysis. The load, deformation and stresses are nonlinearly related and they are also history dependent in an elasto-plastic analysis. In the plastic region strain increments are regarded as composed of elastic and plastic components,

$$d\boldsymbol{\varepsilon} = d\boldsymbol{\varepsilon}_e + d\boldsymbol{\varepsilon}_p \quad (5.12)$$

where subscripts  $e$  and  $p$  denote elastic and plastic, respectively. To define the relationship between the plastic strain and stress increment another assumption about material behavior is used. It is supposed that the plastic strain increment is proportional to the rate of change of some function of stress increment. This function is called as plastic potential,  $Q$ .

$$d\boldsymbol{\varepsilon}_p = \frac{\partial Q}{\partial \boldsymbol{\sigma}} d\lambda \quad (5.13)$$

where  $d\lambda$  is the constant of proportionality and named as the plastic multiplier. Equation 5.13 is called as flow rule. The plastic potential function is generally considered equal to the yield function. The flow rule is named as *associated* if two functions are the same, and *non-associated* otherwise. The stress increments are associated with only the elastic component. Therefore,

$$d\boldsymbol{\sigma} = \mathbf{D}d\boldsymbol{\varepsilon}_e = \mathbf{D}(d\boldsymbol{\varepsilon} - d\boldsymbol{\varepsilon}_p) \quad (5.14)$$

where  $\mathbf{D}$  is the elastic constitutive matrix. To obtain the incremental constitutive equation, the constant of proportionality must be established. During an increment of plastic straining,

$$df_y = 0 \quad (5.15)$$

Substitution of Equation 5.1 into Equation 5.15

$$\left(\frac{\partial f_y}{\partial \boldsymbol{\sigma}}\right)^T d\boldsymbol{\sigma} + \left(\frac{\partial f_y}{\partial \boldsymbol{\alpha}}\right)^T d\boldsymbol{\alpha} + \frac{\partial f_y}{\partial w^p} dw^p = 0 \quad (5.16)$$

Substitution of Equations 5.10, 5.11, 5.13 into Equation 5.16 and the resulting equation solved for plastic multiplier  $d\lambda$ .

$$d\lambda = P_\lambda d\boldsymbol{\varepsilon} \quad (5.17)$$

where  $P_\lambda$  is

$$P_\lambda = \frac{\left(\frac{\partial f_y}{\partial \boldsymbol{\sigma}}\right)^T \mathbf{D}}{\left(\frac{\partial f_y}{\partial \boldsymbol{\sigma}}\right)^T \mathbf{D} \left(\frac{\partial \mathbf{Q}}{\partial \boldsymbol{\sigma}}\right) - \left(\frac{\partial f_y}{\partial \boldsymbol{\alpha}}\right)^T \mathbf{D} \left(\frac{\partial \mathbf{Q}}{\partial \boldsymbol{\alpha}}\right) - \frac{\partial f_y}{\partial w^p} \boldsymbol{\sigma}^T \left(\frac{\partial \mathbf{Q}}{\partial \boldsymbol{\sigma}}\right)} \quad (5.18)$$

Although both work hardening and strain hardening are included in Equation 5.18, practical applications will probably use one or the other, or perhaps a fraction of each. Using this, the incremental stress-strain equation can be written as

$$d\boldsymbol{\sigma} = \mathbf{D} \left( d\boldsymbol{\varepsilon} - \frac{\partial \mathbf{Q}}{\partial \boldsymbol{\sigma}} d\lambda \right) = \mathbf{D} \left( d\boldsymbol{\varepsilon} - P_\lambda \frac{\partial \mathbf{Q}}{\partial \boldsymbol{\sigma}} d\boldsymbol{\varepsilon} \right) = \mathbf{D}_{ep} d\boldsymbol{\varepsilon} \quad (5.19)$$

where

$$\mathbf{D}_{ep} = \mathbf{D} - \mathbf{D} P_\lambda \frac{\partial \mathbf{Q}}{\partial \boldsymbol{\sigma}} \quad (5.20)$$

$\mathbf{D}_{ep}$  is the generalized form tangent modulus.

### 5.3 The RPIM Formulation For Elasto-Plastic Problems

The formulations used for the analysis are based on virtual work principle. If a body is subjected to a set of body forces  $\mathbf{r}_b$  and a set of traction loads then the Virtual Work Principle can be written as [162]

$$\int_{\Omega} (\delta \boldsymbol{\varepsilon}^T \boldsymbol{\sigma} - \delta \mathbf{u}^T \mathbf{f}_b) d\Omega - \delta \mathbf{d}^T \mathbf{f}_q = 0 \quad (5.21)$$

where  $\boldsymbol{\sigma}$  is the vector of internal stresses,  $\mathbf{f}_b$  is the body load,  $\mathbf{f}_q$  is the external applied forces comprises from both point loads and surface loads,  $\delta \mathbf{d}$  is the vector of virtual displacements,  $\delta \boldsymbol{\varepsilon}$  is the vector of associated virtual strains,  $\delta \mathbf{u}$  is the internal displacements,  $\Omega$  is the domain of interest.

In the RPIM representation, the displacements and strains within any local domain may be expressed by the relationships [1,2]

$$\delta \mathbf{u} = \mathbf{N} \delta \mathbf{d} \quad (5.22)$$

and

$$\delta \boldsymbol{\varepsilon} = \mathbf{B} \delta \mathbf{d} \quad (5.23)$$

where,  $\mathbf{N}$  is the matrix of shape functions and  $\mathbf{B}$  is the matrix derivatives of the nodal shape functions. Substitution of these into virtual work expression gives

$$\int_{\Omega} \delta \mathbf{d}^T (\mathbf{B}^T \boldsymbol{\sigma} - \mathbf{N}^T \mathbf{f}_b) d\Omega - \delta \mathbf{d}^T \mathbf{f}_q = 0 \quad (5.24)$$

This equation must be true for any arbitrary set of virtual displacements  $\delta \mathbf{d}$

$$\int_{\Omega} \mathbf{B}^T \boldsymbol{\sigma} d\Omega - \mathbf{f}_q - \int_{\Omega} \mathbf{N}^T \mathbf{f}_b d\Omega = 0 \quad (5.25)$$

The solution of Equation 5.25 will not be generally satisfied at any stage of the computation, and

$$\boldsymbol{\psi} = \int_{\Omega} \mathbf{B}^T \boldsymbol{\sigma} d\Omega - \left( \mathbf{f}_q + \int_{\Omega} \mathbf{N}^T \mathbf{f}_b d\Omega \right) \neq 0 \quad (5.26)$$

where  $\boldsymbol{\psi}$  is the residual force vector. To evaluate the tangential stiffness matrix incremental form of Equation 5.26 must be employed. For a load increment the following equation is obtained as

$$\Delta \boldsymbol{\psi} = \int_{\Omega} \mathbf{B}^T \Delta \boldsymbol{\sigma} d\Omega - \left( \Delta \mathbf{f}_q + \int_{\Omega} \mathbf{N}^T \Delta \mathbf{f}_b d\Omega \right) \quad (5.27)$$

Substitution of Equation 5.19 into Equation 5.27 gives

$$\Delta \boldsymbol{\psi} = \mathbf{K}_T \mathbf{d} - \left( \Delta \mathbf{f}_q + \int_{\Omega} \mathbf{N}^T \Delta \mathbf{f}_b d\Omega \right) \quad (5.28)$$

where

$$\mathbf{K}_T = \int_{\Omega} \mathbf{B}^T \mathbf{D}_{ep} \mathbf{B} d\Omega \quad (5.29)$$

#### 5.4. Summary Of Solution Procedures

The summary of equation solving technique is as follows [162]

1. Begin new load increment,  $\mathbf{f} = \mathbf{f} + \Delta \mathbf{f}$ .
2. Set  $\Delta \mathbf{f}$  equal to the current load increment vector.

3. Set  $\mathbf{d}^0$  equal to 0 for the first increment or equal to the total displacement vector at the end of the last load increment.
4. Set  $\boldsymbol{\psi}^0$  equal to the residual force vector at the end of the last increment or equal to 0 for the first load increment.
5. Set  $\boldsymbol{\psi}^0 = \boldsymbol{\psi}^0 + \Delta \mathbf{f}$ .
6. Solve  $\Delta \mathbf{d}^0 = -\mathbf{K}_T^{-1} \boldsymbol{\psi}^0$ . Use old or updated value  $\mathbf{K}_T$ .
7. Set  $\mathbf{d}^1 = \mathbf{d}^0 + \Delta \mathbf{d}^0$ .
8. Evaluate  $\boldsymbol{\psi}^1(\mathbf{d}^1)$ .
9. If solution has converged go to 11; otherwise continue.
10. Iterate until solution has converged.
11. If this is not the last increment go to 1; otherwise stop.

The iteration loop for elasto-plastic 2D problems is as follows [162]

1. Set iteration number  $i = 1$ .
2. Solve  $\Delta \mathbf{d}^i = -\mathbf{K}_T^{-1} \boldsymbol{\psi}^i$ . Use old or updated  $\mathbf{K}_T$ .
3. Set  $\mathbf{d}^{i+1} = \mathbf{d}^i + \Delta \mathbf{d}^i$ .
4. For each Gauss point, evaluate the increments in strain resultants  $\Delta \boldsymbol{\varepsilon}^i = \mathbf{B} \Delta \mathbf{d}^i$
5. Assuming the elastic behaviour compute the increments in stress resultants and hence the total stress resultants at each Gauss point  $\Delta \boldsymbol{\sigma}^i = \mathbf{D} \Delta \boldsymbol{\varepsilon}^i$  hence  $\boldsymbol{\sigma}^{i+1} = \boldsymbol{\sigma}^i + \Delta \boldsymbol{\sigma}^i$ .
6. At each Gauss point,  $\boldsymbol{\sigma}^{i+1}$  is adjusted depending on the states of  $\boldsymbol{\sigma}^i$  and,  $\boldsymbol{\sigma}^{i+1}$  to satisfy the yield criterion and preserve the normality condition.
7. Evaluate the residual force vector  $\boldsymbol{\psi}^{i+1} = \int_A \mathbf{B}^T \boldsymbol{\sigma} dA - \mathbf{f}$
8. Check the convergency. If it is not satisfied, set  $i = i + 1$  and go to 2.
9. Go to next load increment.

## 5.5 Numerical Examples

The effects of RPIM shape parameters on the solution of accuracy of 2D elasto-plastic problems are investigated. The multi-quadric radial basis functions are used in the RPIM algorithm. A number of case studies with regular and irregular node distributions are solved. The convergence rates of RPIM solutions after yielding are investigated for various  $\alpha_c$  and  $q$ . Both regular and irregular node distributions are used in the RPIM models. It is shown that the solutions after yielding can be improved using appropriate shape parameter values. The propagation of plastic region is also represented against load increments.

### 5.5.1 End Loaded Cantilever Beam

The solution of an end loaded elastic-perfectly plastic cantilever beam is derived in detail in Section 4.2.2 of Lubliner [163]. Therefore, it is a good measure to observe RPIM shape parameter effects on the elasto-plastic solution accuracy of it. A cantilever beam is solved with dimensions of  $40\text{ cm} \times 4\text{ cm}$  as shown in Figure 5.5. The regular and irregular RPIM models and FEM model are shown in Fig. 5.6. The material is assumed as perfectly plastic with  $\frac{\sigma_y}{E} = 2 * 10^{-3}$  as in [163]. The propagation of plastic region as the load increases is given in Figure 5.7. The plastic region starts at the high stress point then is spread out toward to neutral axis as the load increases. It is in good agreement with the analytical solution where given in the elementary textbook of mechanics of materials. Figures 5.8, 5.9 and 5.10 show that RPIM gives higher displacements for regular and irregular distributed nodes as the number of nodes in the models is increased. In contrast to RPIM, ANSYS gives lesser displacements in the plastic region. Displacement variations against load steps for RPIM regular and irregular distributed nodes are given in Fig. 5. 11-14 for various values of  $\alpha_c$  and  $q$ . RPIM nearly gives same results for all values of  $\alpha_c$  and  $q$ .

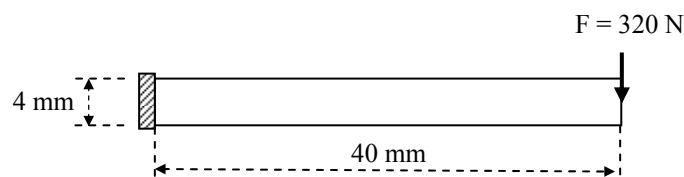


**Figure 5.5** Cantilever beam with an end load of 320 N.

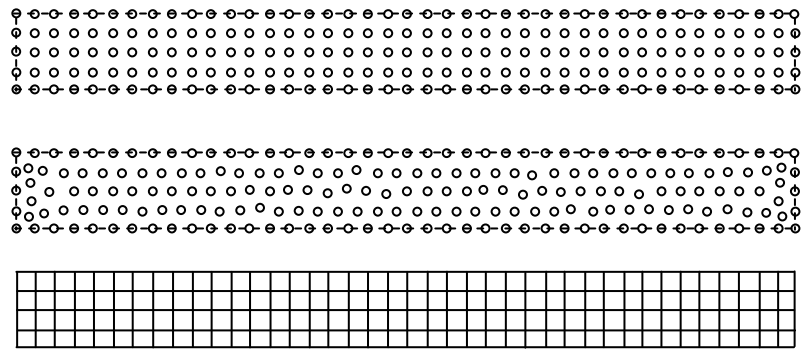


**Figure 5.6** RPIM models with regular and irregular distributed nodes and FEM model of cantilever beam.

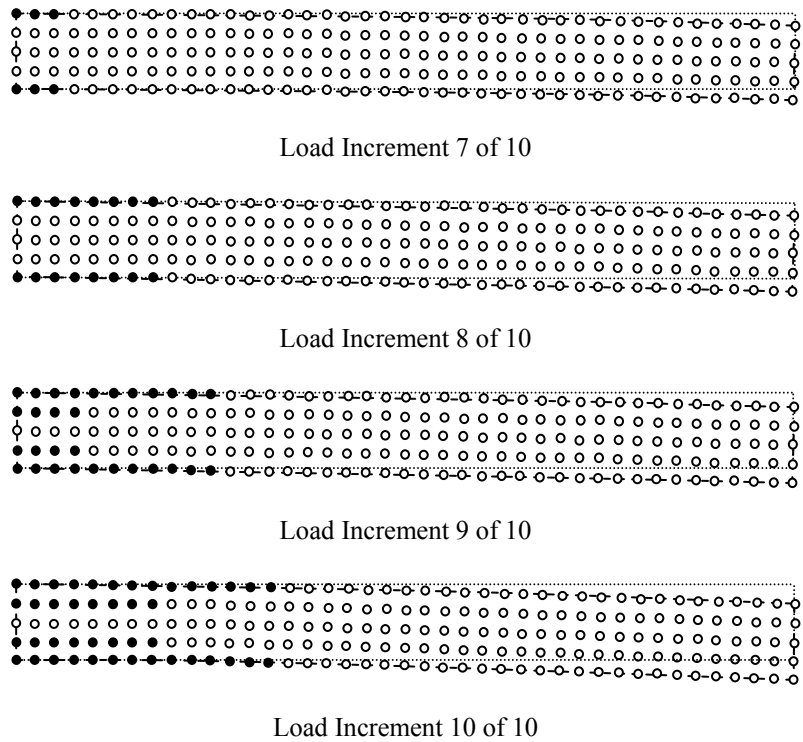


**Figure 5.7** The propagation of the plastic region and deformed shape as the load increases ( ● shows the nodes in the plastic region. )

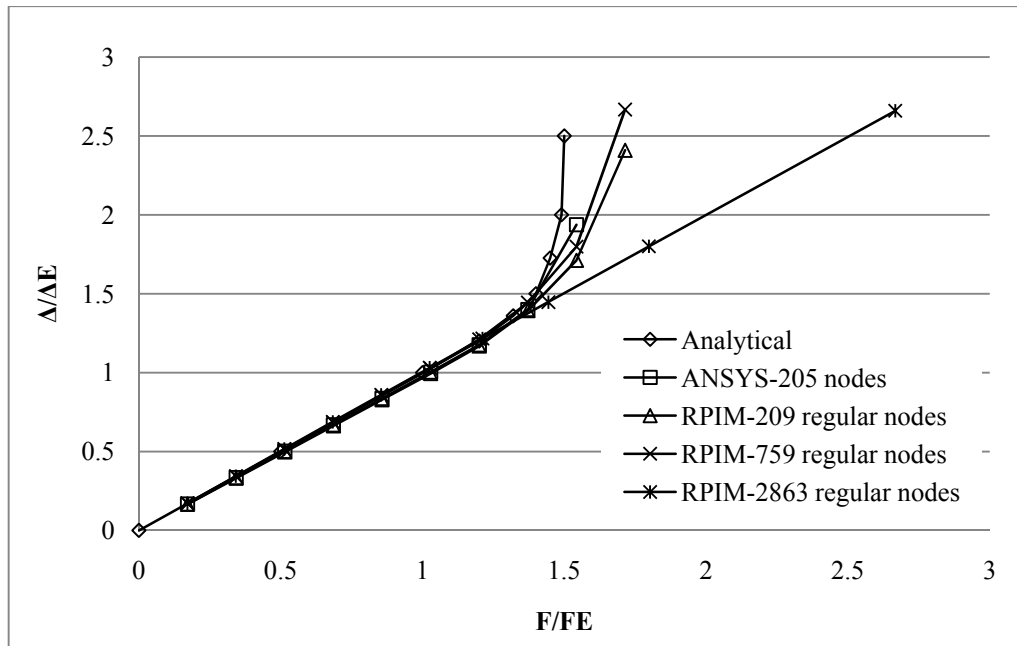


**Figure 5.8** Displacement variations against load steps for RPIM regular distributed nodes with  $\alpha_c = 2$  and  $q = 1.03$  at the free end of cantilever beam.

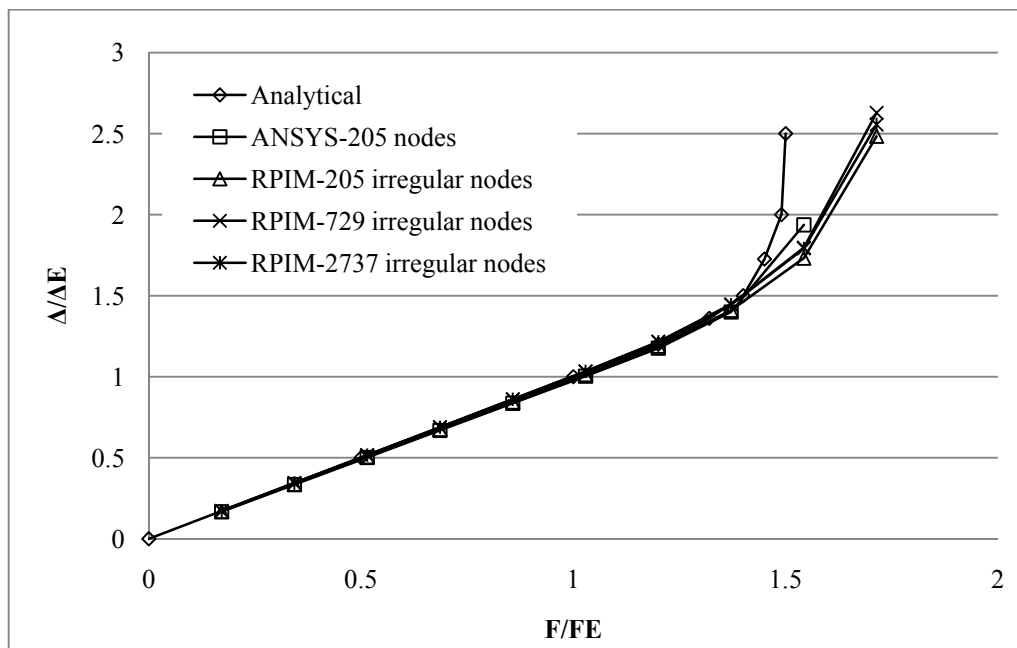


**Figure 5.9** Displacement variations against load steps for RPIM irregular distributed nodes with  $\alpha_c=2$  and  $q=1.03$  at the free end of cantilever beam.

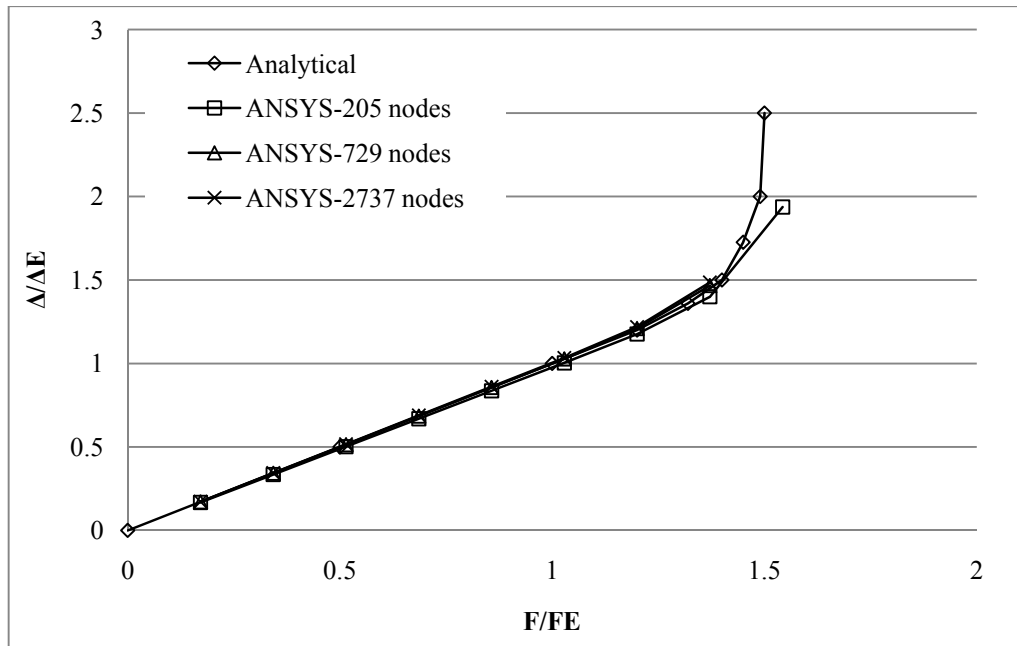


**Figure 5.10** Displacement variations against load steps for ANSYS with different number of nodes at the free end of cantilever beam.

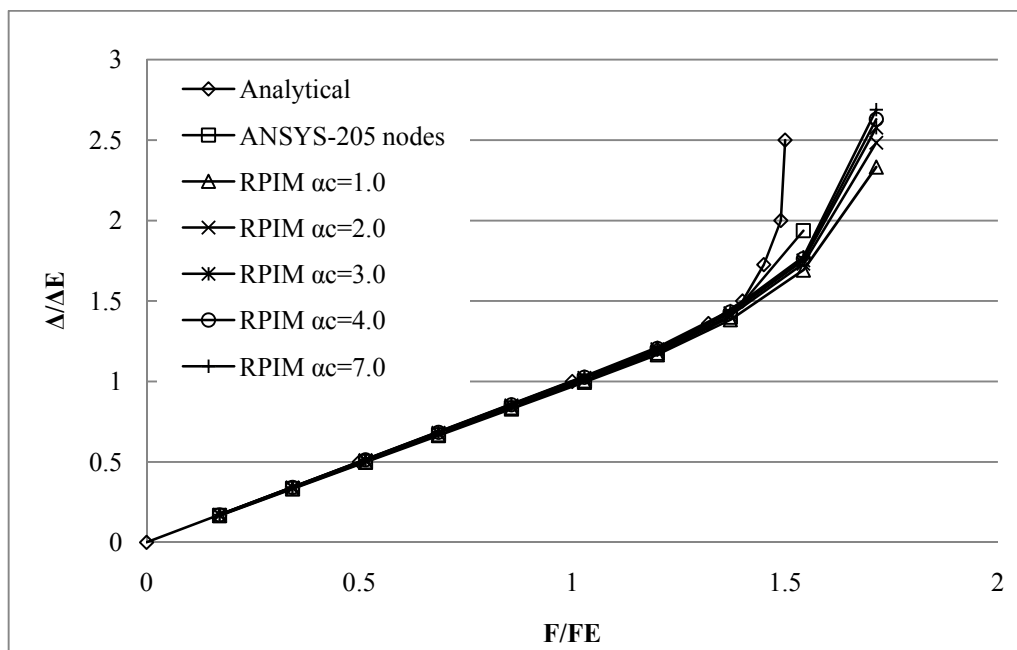


**Figure 5.11** Displacement variations against load steps for RPIM regular distributed nodes with  $q = 1.03$  and different  $\alpha_c$  at the free end of cantilever beam.



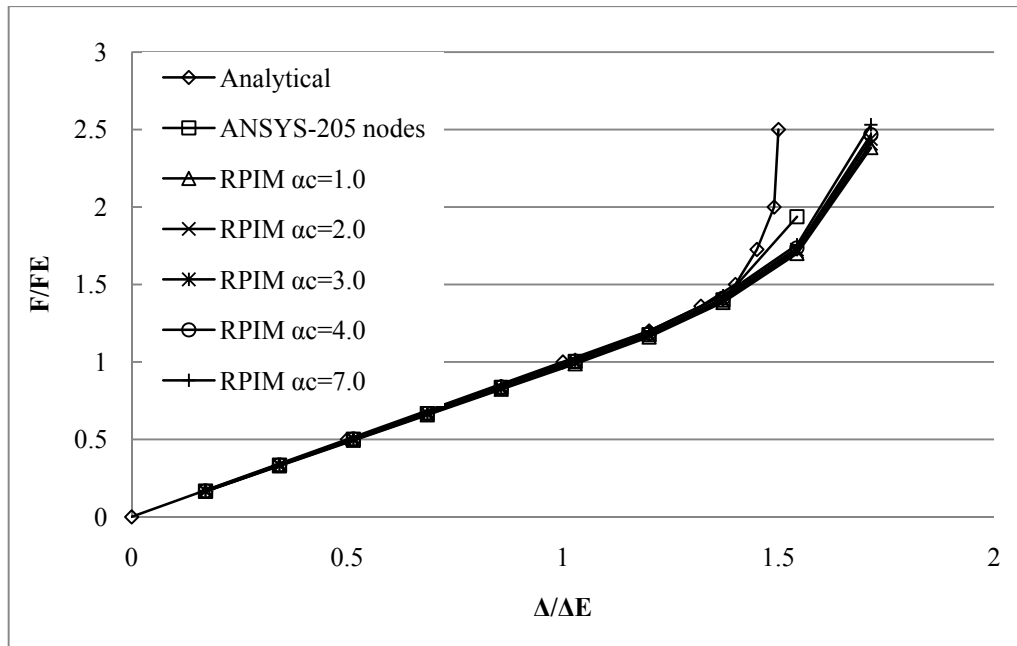


**Figure 5.12** Displacement variations against load steps for RPIM irregular distributed nodes with  $q = 1.03$  and different  $\alpha_c$  at the free end of cantilever beam.

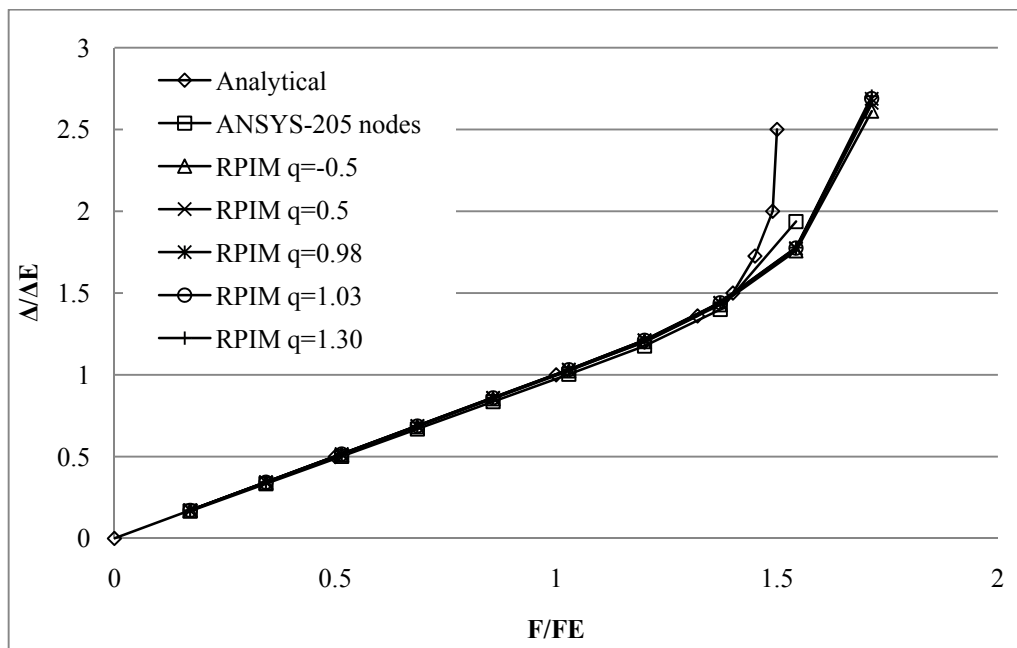


**Figure 5.13** Displacement variations against load steps for RPIM regular distributed nodes with  $\alpha_c = 7.0$  and different  $q$  at the free end of cantilever beam.

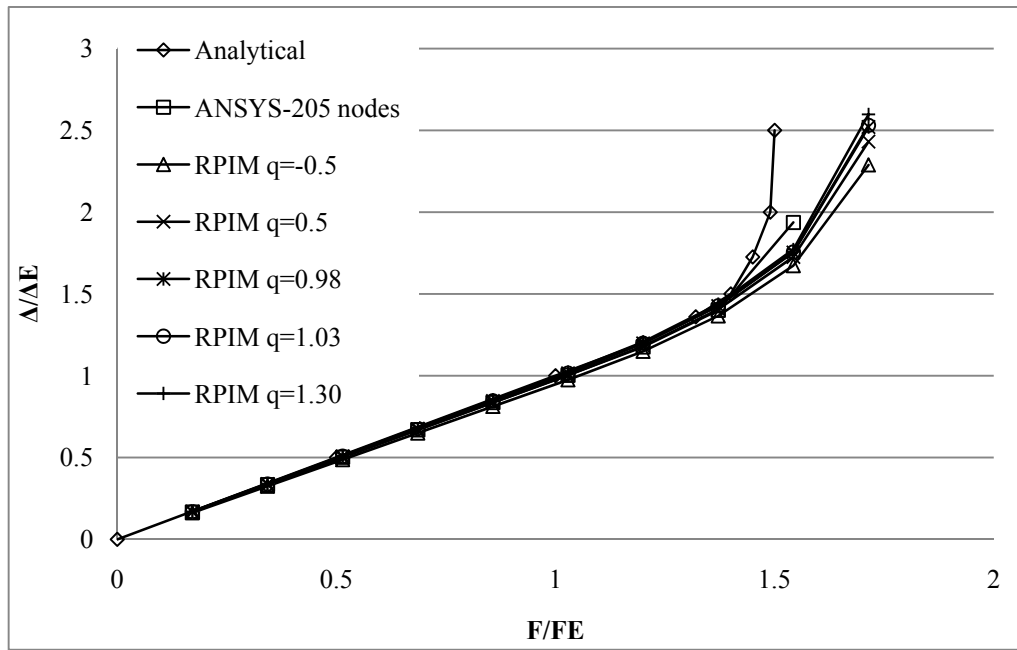


**Figure 5.14** Displacement variations against load steps for RPIM irregular distributed nodes with  $\alpha_c = 7.0$  and different  $q$  at the free end of cantilever beam.

### 5.5.2 Thick Walled Internally Pressurized Cylinder

The elasto-plastic solution of this case is given in Section 7.5.1 of Owen [162,164]. Therefore, the same model is obtained with axi-symmetric assumption (Figure 5.15). The inner and outer radii are 100 mm and 200 mm respectively. The material is again elastic-perfectly plastic with  $E = 210 \text{ GPa}$ ,  $\nu = 0.1$  and  $\sigma_y = 0.24 \text{ GPa}$ . The RPIM models with regular and irregular nodes and FEM model are given in Figure 5. 16. The propagation of plastic region against pressure increments is shown in Figure 5.17. When the pressure reaches the limit load of 0.91209 GPa [164], all nodes enter the plastic region except the nodes at the outer region. For RPIM and FEM solutions, when numbers of nodes in the models are increased, the amount of displacement in the plastic region is also increased as shown in Figures 5.18, 5.19 and 5. 20. However, same amount of large displacements in the plastic region can be obtained without increasing nodes, but with increasing the values of  $\alpha_c$  and  $q$  as shown in Figures 5.20, 5.21, 5.22, 5.23 and 5.24.

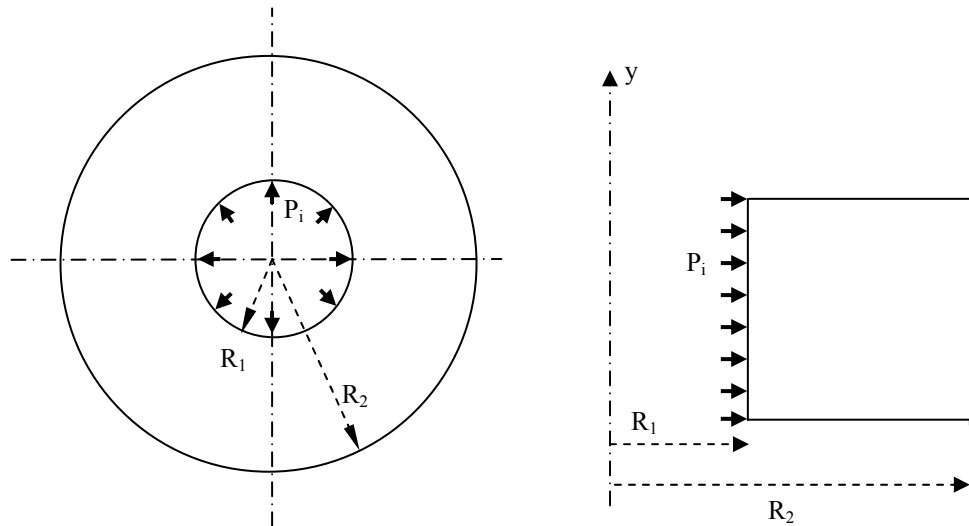


**Figure 5.15** Thick-walled pressurized cylinder and its axisymmetric model

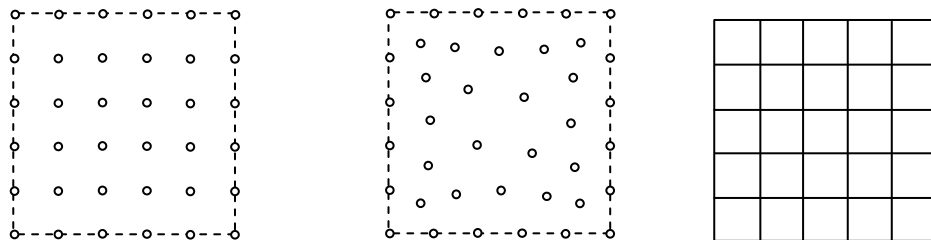


**Figure 5.16** RPIM models with regular and irregular distributed nodes and FEM model of thick-walled pressurized cylinder

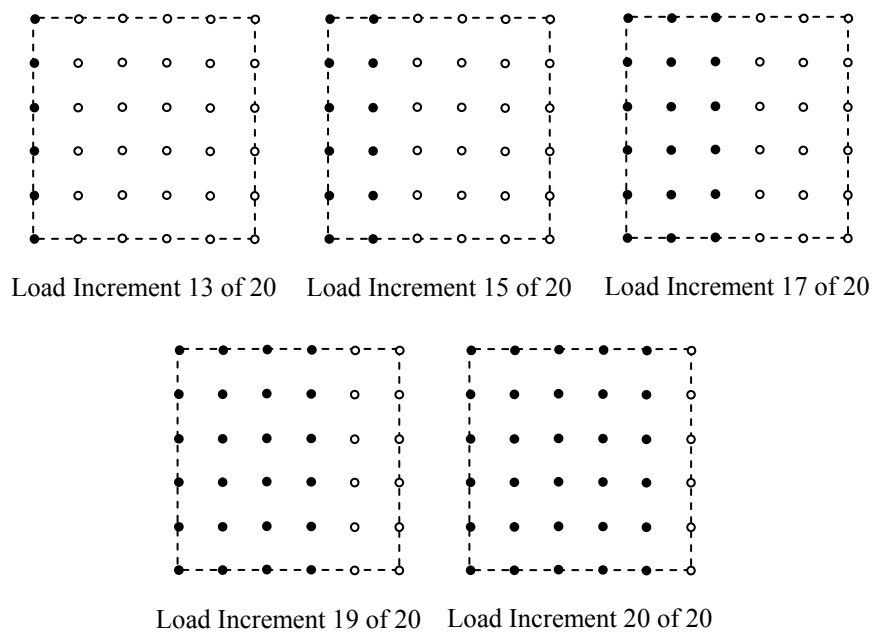


**Figure 5.17** The propagation of the plastic region and deformed shape of thick-walled cylinder as the load increases ( ● shows the nodes in the plastic region. )

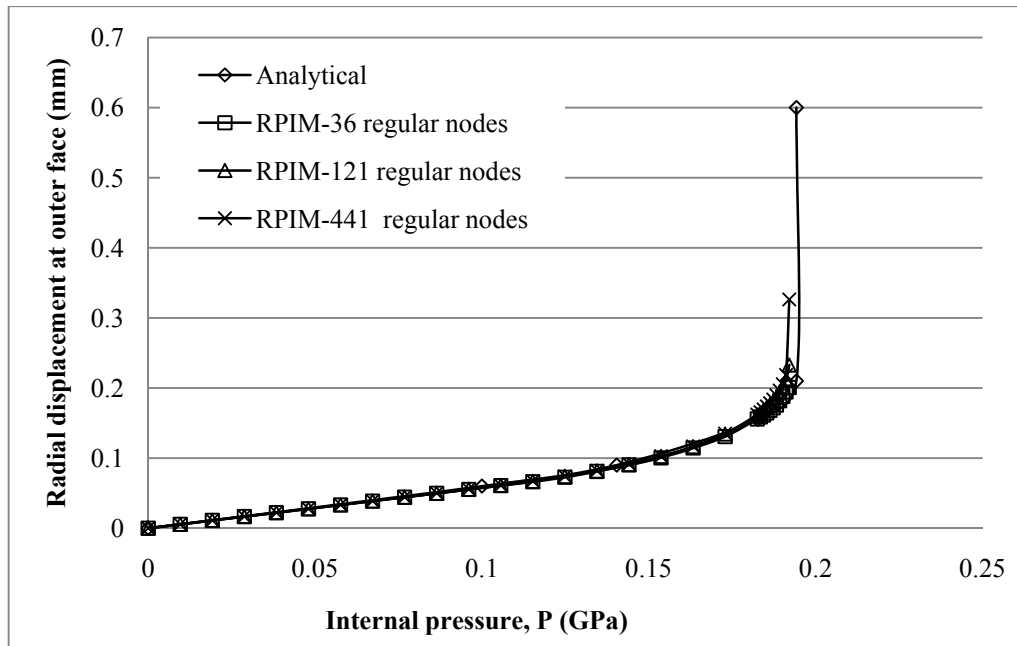


**Figure 5.18** Displacement variations against load steps for RPIM regular distributed nodes with  $\alpha_c=4$  and  $q=1.03$  at the outer surface of thick walled pressurized cylinder.

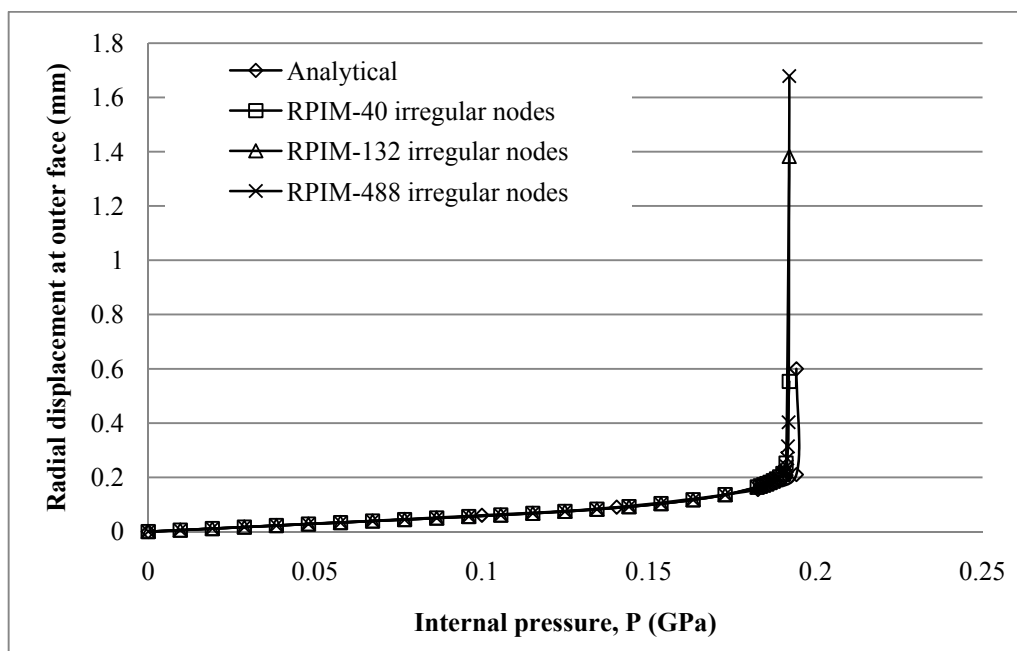


**Figure 5.19** Displacement variations against load steps for RPIM irregular distributed nodes with  $\alpha_c=4$  and  $q=1.03$  at the outer surface of thick walled pressurized cylinder.

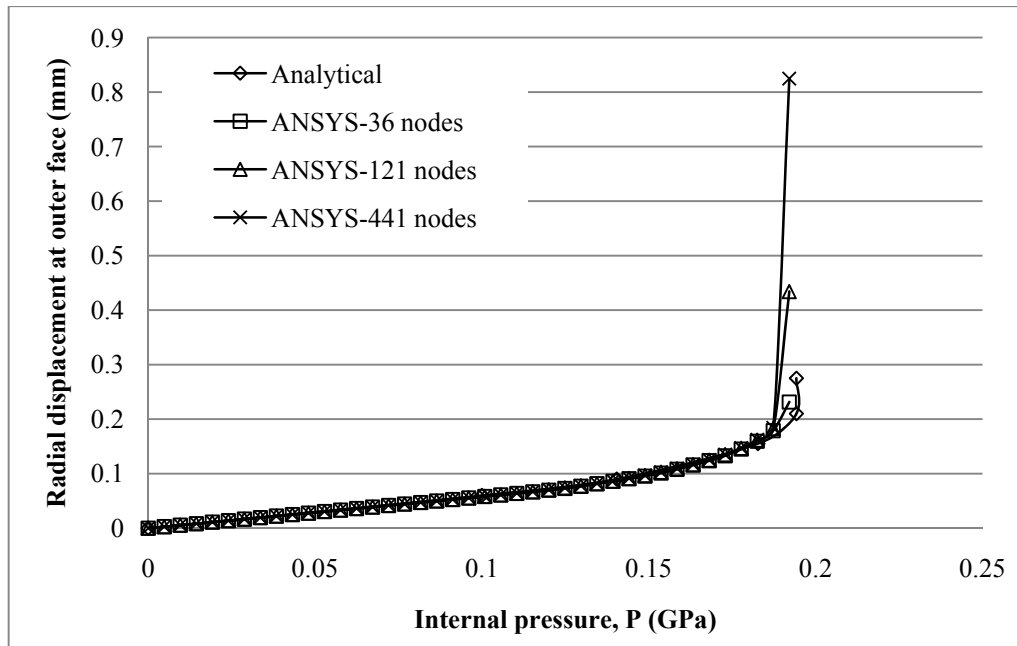


**Figure 5.20** Displacement variations against load steps for ANSYS with different number of nodes at the outer surface of thick walled pressurized cylinder.

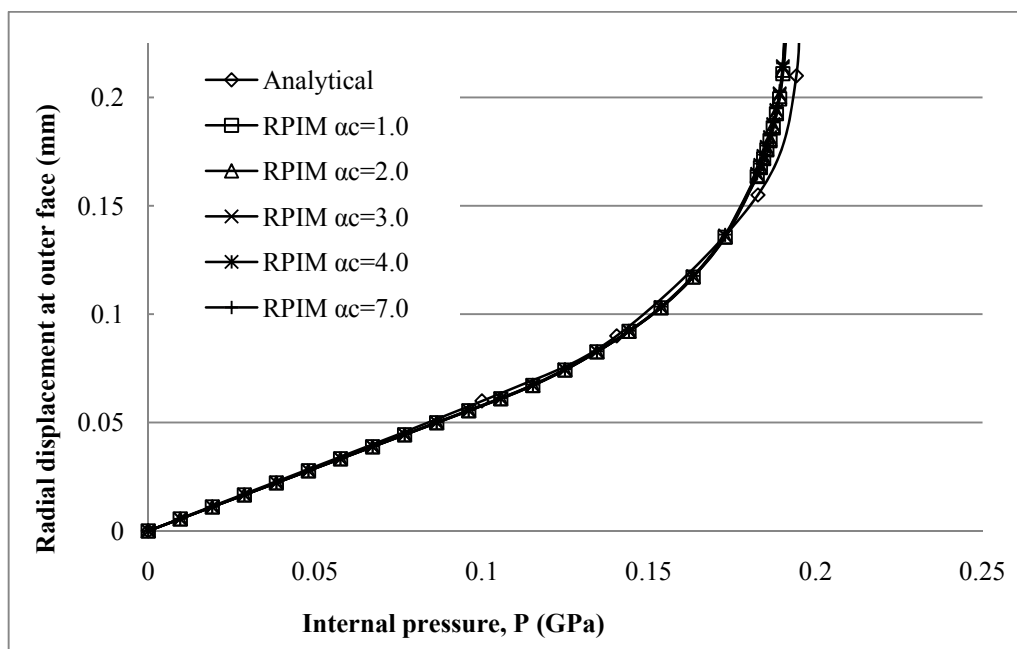


**Figure 5.21** Displacement variations against load steps for RPIM regular distributed nodes with  $q = 1.03$  and different  $\alpha_c$  at the outer surface of thick walled pressurized cylinder.

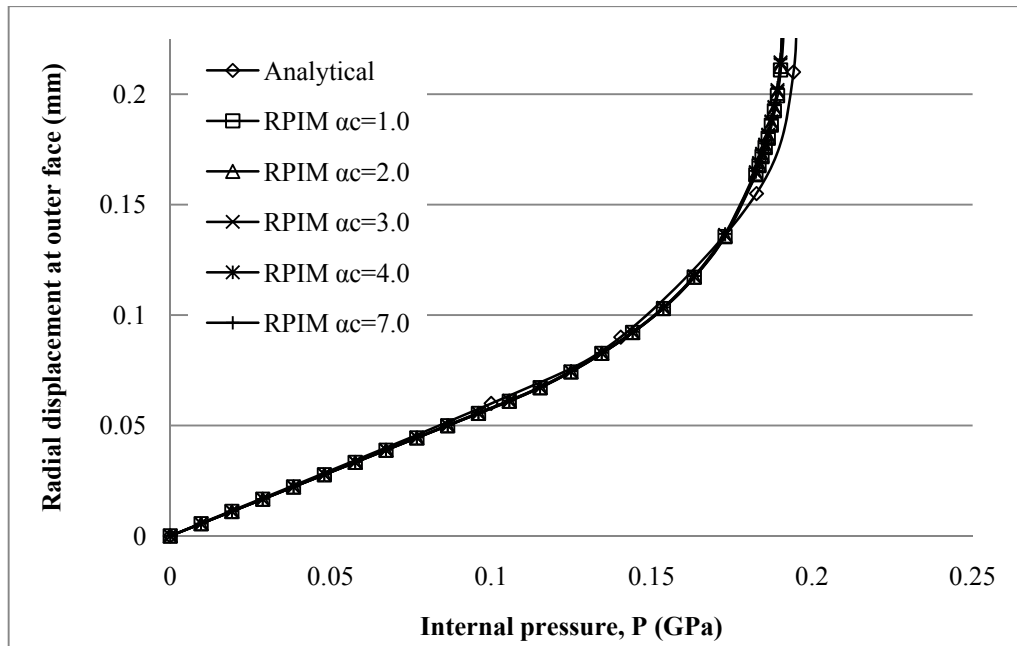


**Figure 5.22** Displacement variations against load steps for RPIM irregular distributed nodes with  $q = 1.03$  and different  $\alpha_c$  at the outer surface of thick walled pressurized cylinder.

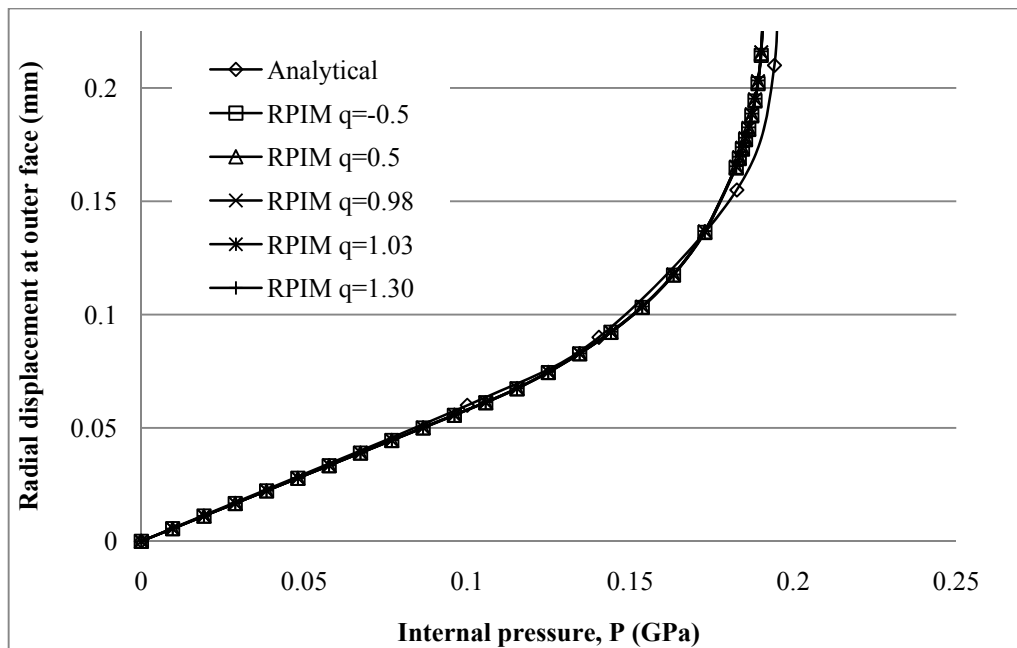


**Figure 5.23** Displacement variations against load steps for RPIM regular distributed nodes with  $\alpha_c = 7.0$  and different  $q$  at the free end of cantilever beam.

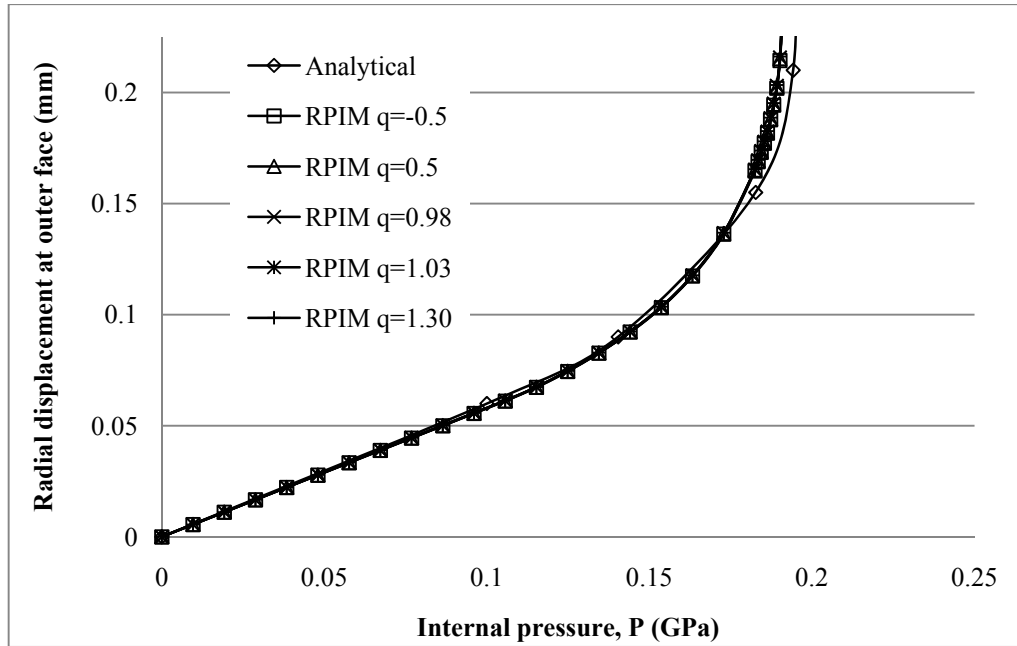


**Figure 5.24** Displacement variations against load steps for RPIM irregular distributed nodes with  $\alpha_c = 7.0$  and different  $q$  at the free end of cantilever beam.

### 5.5.3 Simply Supported Circular Plate

It is well known problem and solved with perfectly plastic material in [162,164]. RPIM and FEM results are compared with the analytical limit pressure of 260.8. The radius and height of the plate are taken as  $R = 10$  and  $h = 1$ . It is simply supported on its edge and exposed to uniform limit pressure of  $P = 260.8$  on its top surface. The axisymmetric model and its dimensions are shown in Figure 5.25. The material constants are  $E = 10^7$ ,  $\nu = 0.24$  and  $\sigma_y = 16000$ . RPIM models with regular and irregular distributed nodes and FEM model are given in Figure 5.26. The propagation of the plastic region and deformed shapes against the pressure increments are given in Figure 5.27. The nodes along upper and lower edges are completely plastic at the load increment of 18. After that point, the plastic region completely propagates towards to neutral axis. Central deflections of the plate are obtained using RPIM regular and irregular distributed nodes and ANSYS as shown in Figure 5.28-5.30. RPIM with regular distributed nodes gives higher displacements than RPIM with irregular distributed nodes after yielding. The results of ANSYS can be seriously improved by increasing number of nodes in the model. Increasing values of  $\alpha_c$  and  $q$  improves the results after yielding as shown in Figures 5.31-5.34.

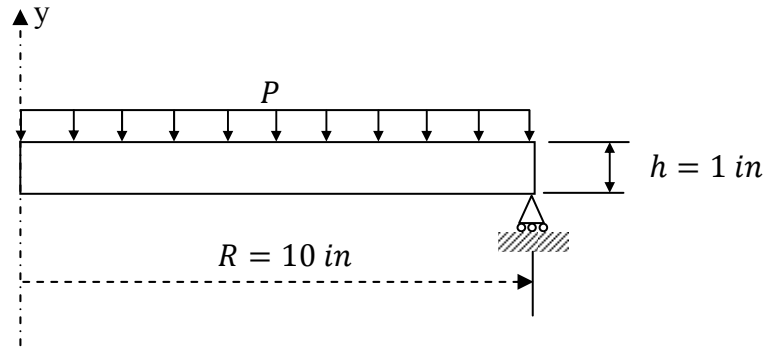


**Figure 5.25** Axi-symmetric model and its dimensions of uniform pressurized simply supported circular plate.

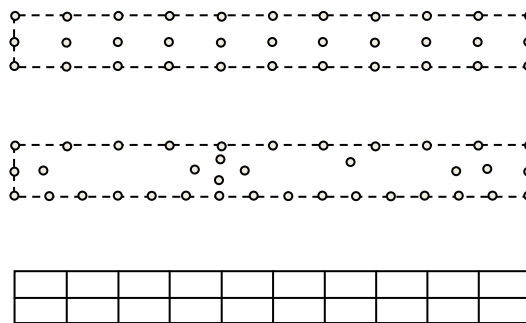


**Figure 5.26** RPIM models with regular and irregular distributed nodes and FEM model of uniform pressurized simply supported circular plate.

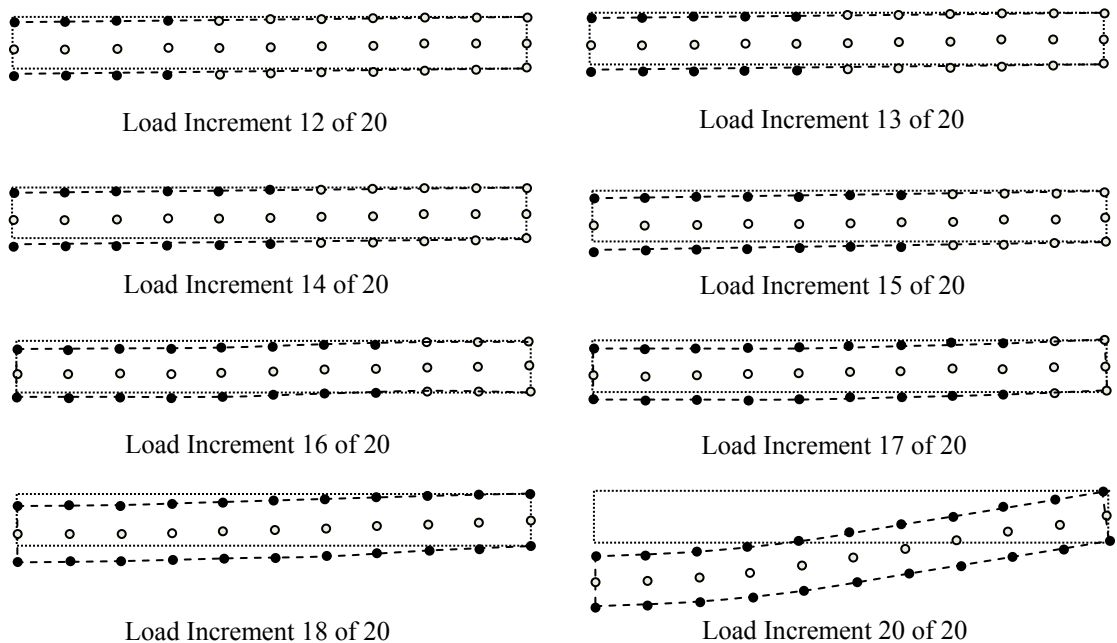


**Figure 5.27** The propagation of the plastic region and deformed shape of uniform pressurized simply supported circular plate as the pressure increases ( • shows the nodes in the plastic region. )



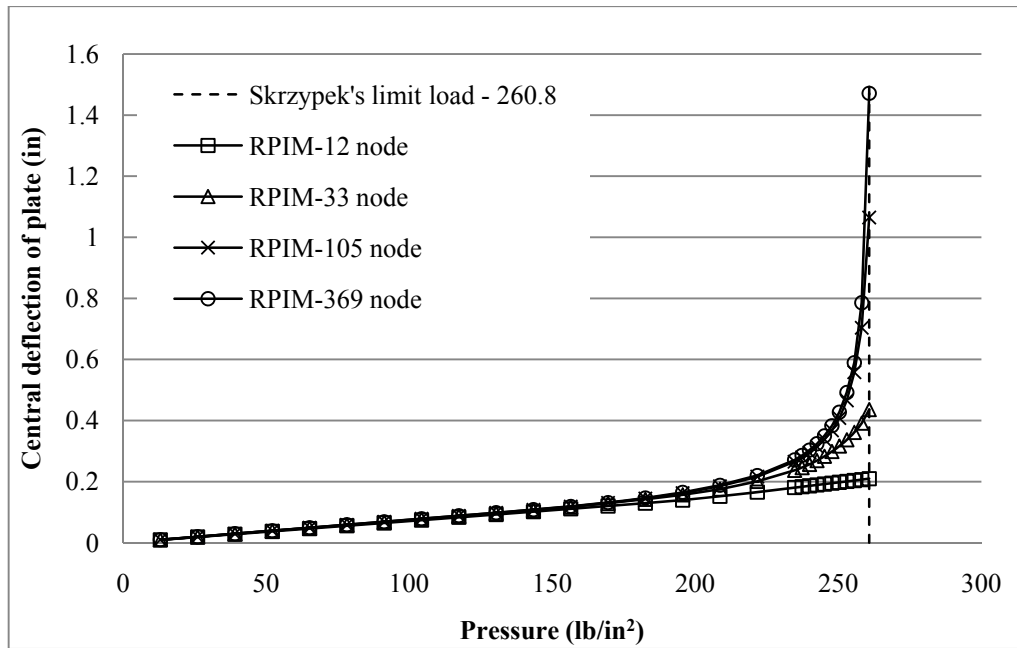


**Figure 5.28** Central deflections of uniform pressurized simply supported circular plate against load steps for RPIM regular distributed nodes with  $\alpha_c=1$  and  $q=1.03$ .

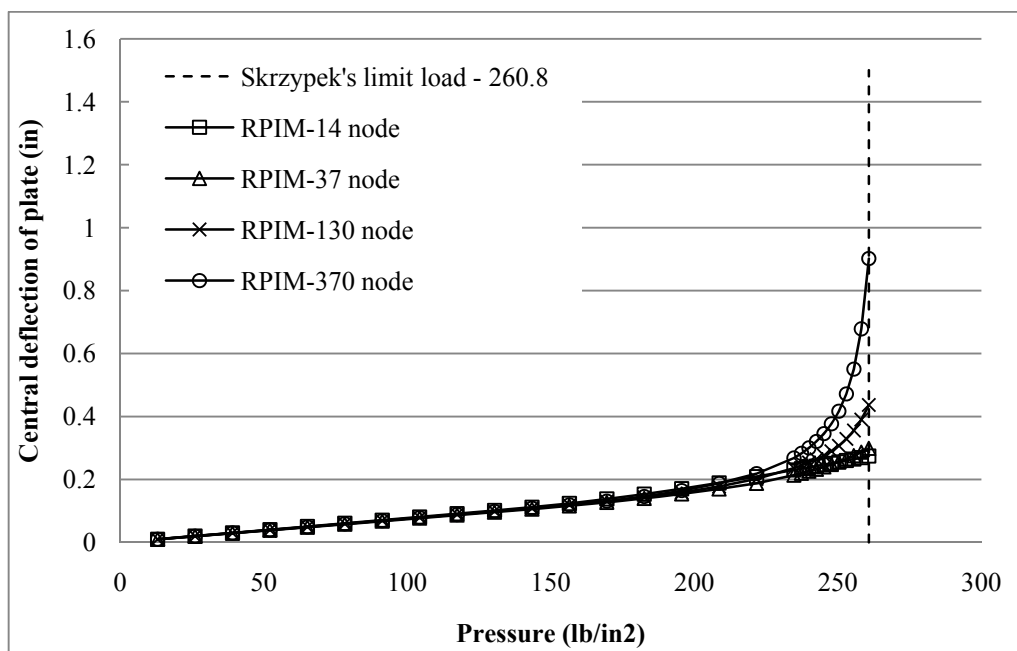


**Figure 5.29** Central deflections of uniform pressurized simply supported circular plate against load steps for RPIM irregular distributed nodes with  $\alpha_c=1$  and  $q=1.03$ .

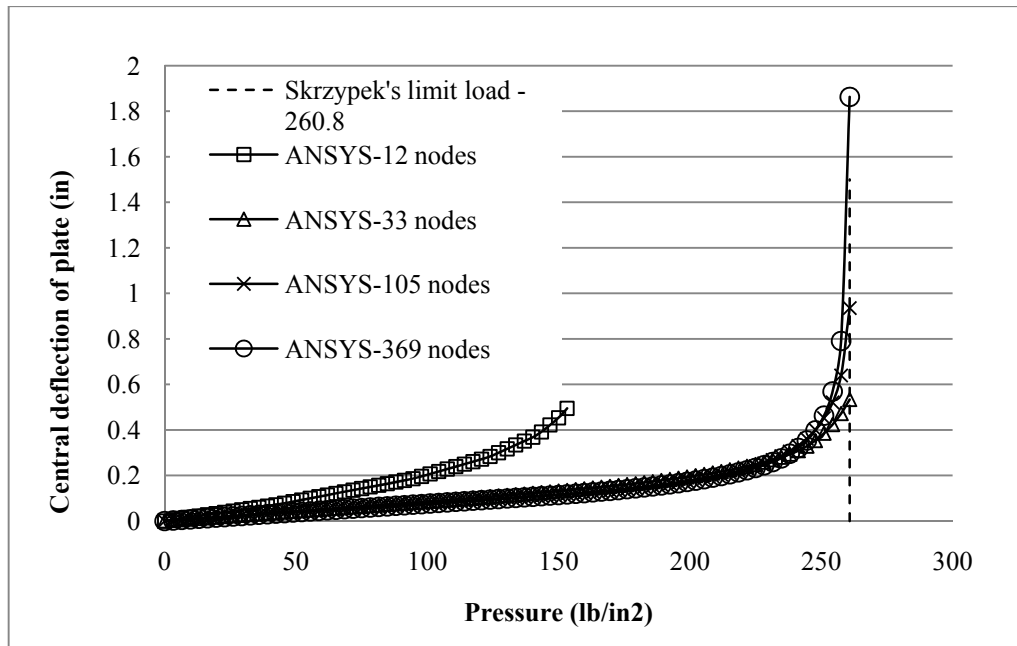


**Figure 5.30** Central deflections of uniform pressurized simply supported circular plate against load steps for ANSYS with different number of nodes.

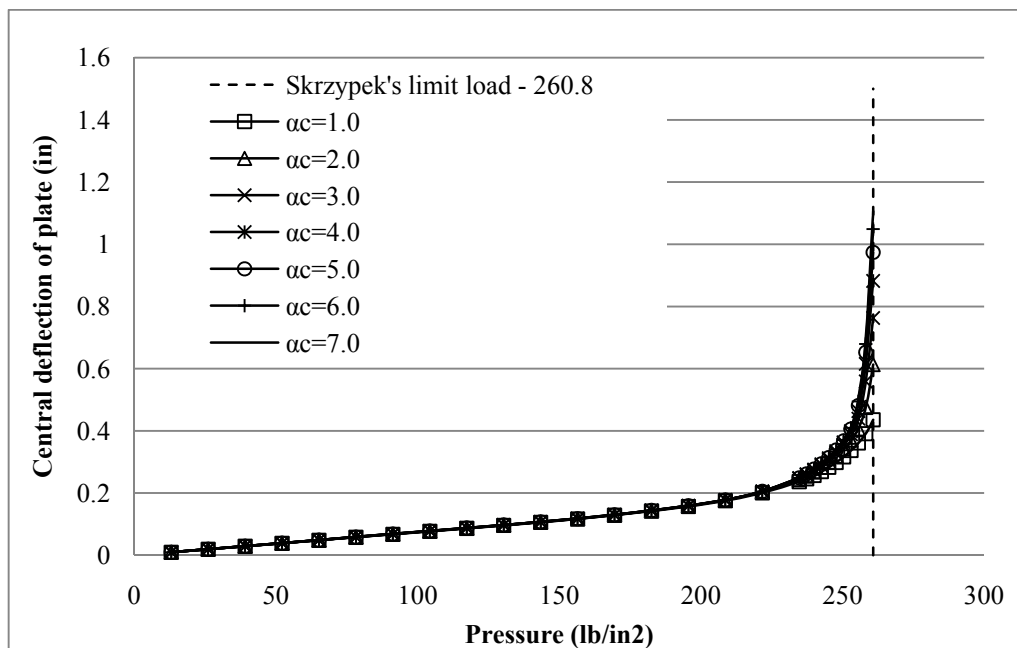


**Figure 5.31** Central deflections of uniform pressurized simply supported circular plate against load steps for RPIM regular distributed nodes with  $q=1.03$  and different  $\alpha_c$ .

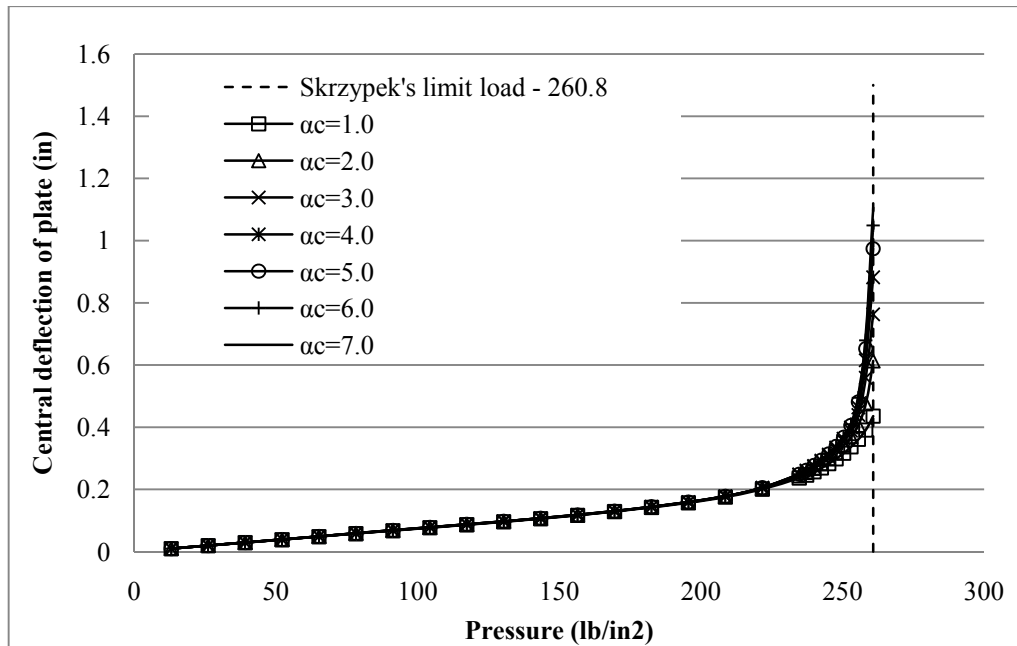


**Figure 5.32** Central deflections of uniform pressurized simply supported circular plate against load steps for RPIM irregular distributed nodes with  $q=1.03$  and different  $\alpha_c$ .

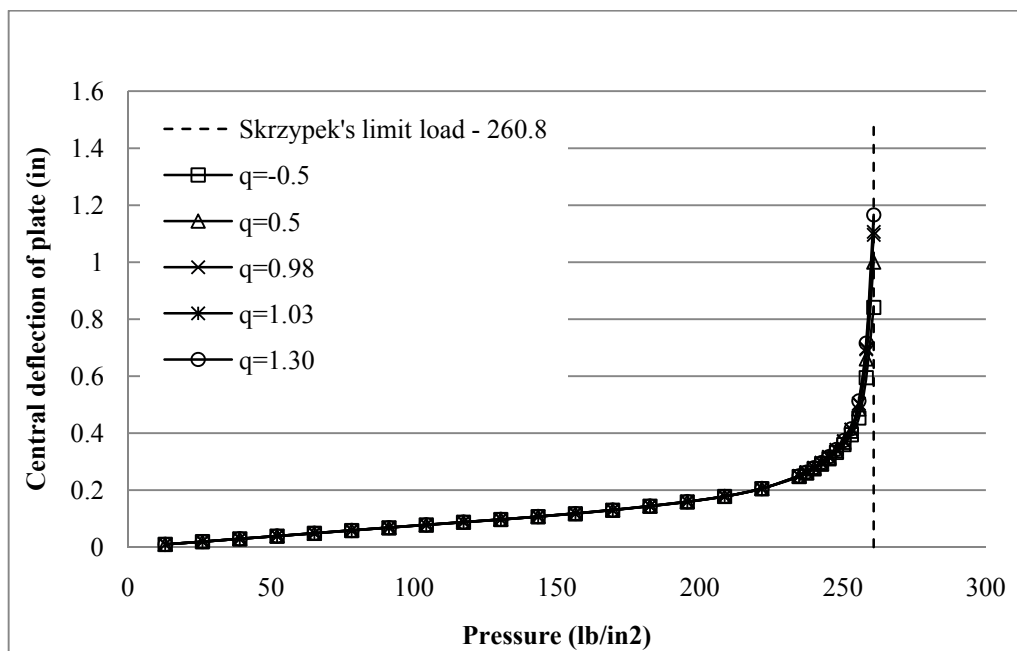


**Figure 5.33** Central deflections of uniform pressurized simply supported circular plate against load steps for RPIM regular distributed nodes with  $\alpha_c = 7.0$  and different  $q$ .

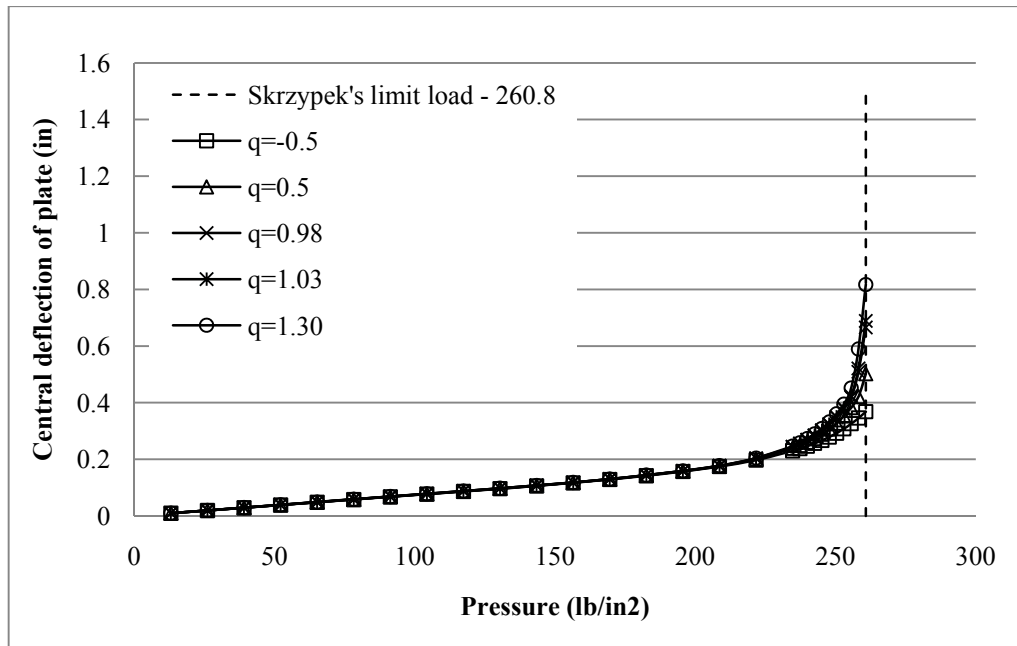


**Figure 5.34** Central deflections of uniform pressurized simply supported circular plate against load steps for RPIM irregular distributed nodes with  $\alpha_c = 7.0$  and different  $q$ .

## 5.6. Results and Discussions

The RPIM shape parameters are investigated in the solution of 2D elasto-plastic problems. It has been shown that FEM have convergence problems after yielding. However, In the RPIM solutions, the convergence can be improved using appropriate shape parameters. Increasing  $\alpha_c$  and  $q$  values after yielding can improve the convergency.

If large deformations are required after yielding as in the metal forming, the shape parameters can be used as  $\alpha_c = 7$  and  $q = 1.3$ .

## CHAPTER 6

### A DIAGONAL OFFSET ALGORITHM FOR THE POLYNOMIAL POINT INTERPOLATION METHOD

#### 6.1 Introduction

Point interpolation method (PIM) is a simple and useful Meshfree technique and originally proposed by Liu and Gu [94]. In the PIM, the field variables are interpolated using point interpolation shape functions. In contrast to MLS shape functions, the point interpolation shape functions possess the Kronecker delta function property and they do not require an extra algorithm to compute nodal values of field variables. Although the background cells are used for the integration in the Galerkin weak formulation, the field variable interpolation is carried on a local domain.

The main problem in the PIM is the singularity of the moment matrix. Because of arbitrary scattered nodes in the influence domain, the moment matrix becomes singular in some situations. Some algorithms are developed to overcome this problem. Moving or shifting the nodes in the local domain by a small distance is the simplest method to avoid singularity [1,94]. However, it is not a complete solution and the moment matrix can still be singular even if the nodes are shifted. Using the radial functions as the basis is a robust solution of this problem [86,87,96,100,101]. However, when the radial basis functions are used in the PIM, the computational efficiency is extremely reduced. Therefore, the matrix triangularization algorithm (MTA) was proposed to avoid singular moment matrix [95]. In MTA, the nodes, which cause the singularity in the moment matrix, are determined and excluded from the influence domain. PIM with the MTA is very effective in constructing Meshfree shape functions. However, it may be numerically unstable especially for the big influence domains [95].

#### 6.2. Singularity in the Moment Matrix

The moment matrix given in Equation 3.8 must be invertible to obtain the PIM shape functions given in the Equation 3.11. It includes the nodal coordinate values of arbitrary distributed nodes in the local domain. Therefore the distribution of

the nodes directly affects the moment matrix. There are some situations where the moment matrix is not invertible. For example, the node configuration in a local domain shown in Figure 6.1 causes the singularity in the moment matrix. The nodes in the local domain sit in the lines parallel to the x-axis and y axis. As a general rule, the terms in the basis functions should be selected symmetrically from the Pascal triangle [1]. So, the basis function terms for the local domain shown in Figure 6.1 can be selected as follows:

$$\mathbf{p}^T(x) = \{1, x, y, xy, x^2, y^2\}$$

It also satisfies the completeness requirements. However, the nodes in the local domain have only two distinct y-coordinate and cannot be represented by second order polynomial in the y-direction. Consequently, the moment matrix is singular.

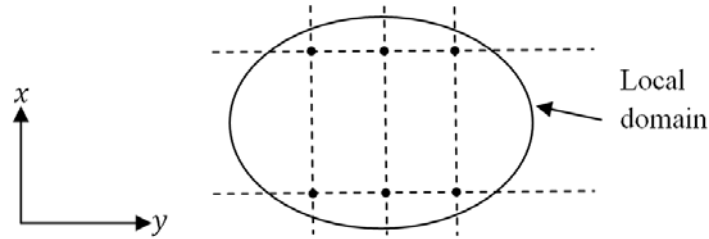


**Figure 6.1** A local domain causes singularity in the moment matrix

### 6.3. A Diagonal Offset Algorithm to Avoid Singularity

Several algorithms are proposed to overcome the singularity in the moment matrix. However, each method has some disadvantages. For example, the computational efficiency is extremely reduced when the radial functions are used as the basis [86,87,96,100,101]. The MTA algorithm may be numerical unstable especially for the big influence domains [95]. Moving or shifting the nodes is the simplest way to avoid singularity [1,2]. However, it is not a complete solution. Changing the coordinates of a node in a local domain causes changing the value of elements in the relevant row of the moment matrix. For example, if the coordinate of the 2<sup>nd</sup> node in a local domain, it results changing the second row of the moment matrix of this local domain. However, the elements in the diagonal line of the moment matrix may be also changed to avoid the singularity. A simple and effective

algorithm can be proposed using this idea. The diagonal elements of the moment matrix of a local domain (except the first element) can be changed with an offset value as follows:

$$\mathbf{P}_Q = \begin{bmatrix} 1 & x_1 & y_1 & x_1 y_1 & \cdots & p_m(\mathbf{x}_1) \\ 1 & x_2 - off & y_2 & x_2 y_2 & \cdots & p_m(\mathbf{x}_2) \\ 1 & x_3 & y_3 - off & x_3 y_3 & \cdots & p_m(\mathbf{x}_3) \\ \vdots & \vdots & \vdots & \vdots & \ddots & \vdots \\ 1 & x_n & y_n & x_n y_n & \cdots & p_m(\mathbf{x}_n) - off \end{bmatrix}$$

Where  $off = \frac{Mde}{10^k}$  and  $Mde$  is the minimum value in the diagonal line of the moment matrix. It must be different from zero.  $k$  is an integer number which determines the amount of the offset value. The first term in the first row is always equal to 1. It is the first term of the basis function and not affected by the nodal coordinates. So, it must be kept as 1.

The PIM shape functions have the Kronecker Delta function and the partition of unity properties. A detailed numerical investigation is presented in the following section to show the effect of using diagonal offset algorithm on the Kronecker delta and partition of unity properties. Its effect on the displacements and stresses are also presented.

## 6.4. Numerical Results and Discussions

### 6.4.1 Patch tests

Four different patches are tested. They include 3x3 and 4x3 regular distributed nodes and 9 and 12 irregular distributed nodes as shown in Figure 6.2. The moment matrix in the original PIM is singular for 4x3 regular and 12 irregular distributed nodes. Therefore, they have no results. The node numbers of Patches are shown in the Figure 6.2. Their coordinates are given in the Tables 6.1-6.4. A single background cell with 4x4 integration points is used for integrations. The dimensions of influence domains are  $2 \times 2 m^2$ . The displacements are prescribed on all outside boundaries by a linear function,  $u_x = 0.6x$  and  $u_y = 0.6y$  [1,2,94]. The material parameters are taken as  $E = 1.0$ , and  $\nu = 0.3$ . The patches pass the tests if the displacements on the interior nodes are equal to the displacements given by linear functions. The test also requires constant stresses and strains in the entire solution domain. Although, the Patches that include the 3x3 regular and 9 irregular

distributed nodes are not singular, the offset algorithm is used on them to see what happens if it is used in non-singular moment matrices.

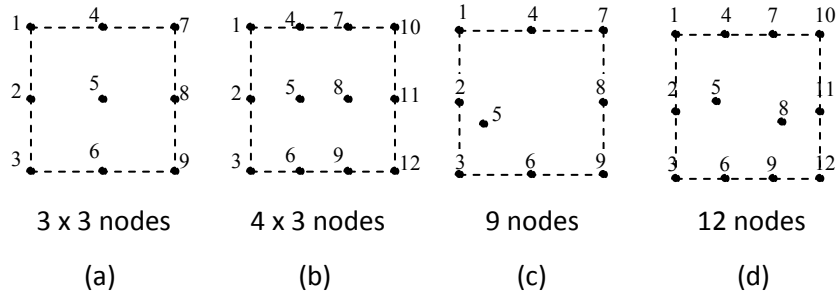


**Figure 6.2** Patch tests with a) 3x3 regular nodes, b) 4x3 regular nodes, c) 9 irregular nodes, d) 12 irregular nodes

**Table 6.1** PIM shape functions (  $\Phi$  ) for Node 5 for different values of  $k$  (3x3 regular nodes).

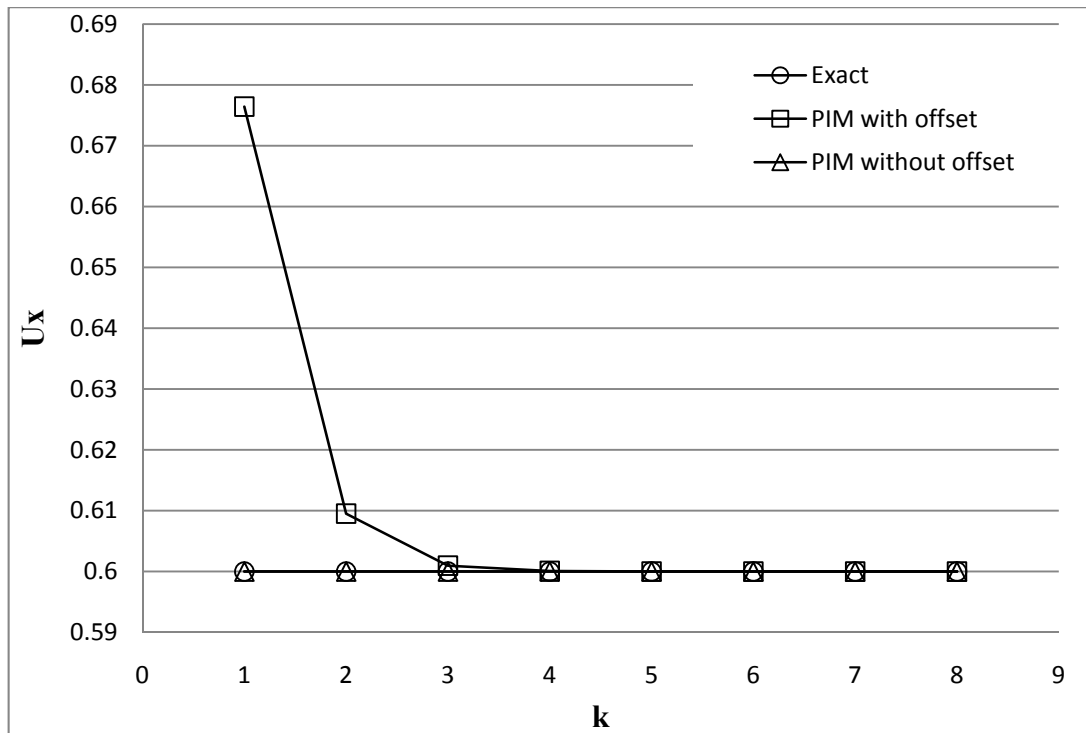
			PIM shape functions for Node 5 ( $\Phi$ )			
Node	x	y	Without Offset	$k=4$	$k=5$	$k=6$
1	0.0	2.0	0.00000000E+00	5.48453833E-20	-9.41511449E-20	6.27788887E-21
2	0.0	1.0	0.00000000E+00	-4.99937473E-09	-4.99993750E-11	-4.99999376E-13
3	0.0	0.0	0.00000000E+00	-9.99724987E-13	-9.99972500E-16	-9.99997252E-19
4	1.0	2.0	0.00000000E+00	3.99982501E-04	3.99998250E-05	3.99999825E-06
<b>5</b>	<b>1.0</b>	<b>1.0</b>	<b>1.00000000E+00</b>	<b>1.00000000E+00</b>	<b>1.00000000E+00</b>	<b>1.00000000E+00</b>
6	1.0	0.0	0.00000000E+00	4.99964274E-13	1.22047368E-15	2.21044577E-16
7	2.0	2.0	0.00000000E+00	-2.00002498E-04	-2.00000250E-05	-2.00000025E-06
8	2.0	1.0	0.00000000E+00	-1.99967502E-04	-1.99996750E-05	-1.99999675E-06
9	2.0	0.0	0.00000000E+00	9.99874996E-05	9.99987500E-06	9.99998752E-07
$\Sigma\Phi$			<b>1.00000000E+00</b>	<b>1.00010000E+00</b>	<b>1.00001000E+00</b>	<b>1.00000100E+00</b>

**Table 6.2** PIM shape functions (  $\Phi$  ) for Node 5 for different values of  $k$  (4x3 regular nodes).

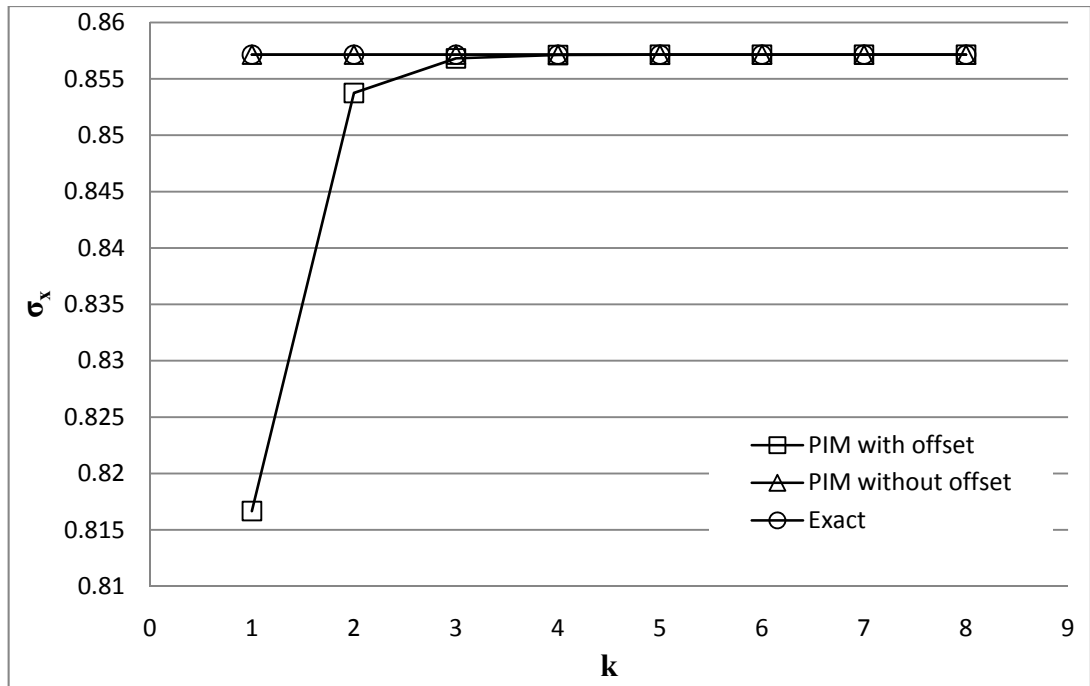
			PIM shape functions for Node 5 ( $\Phi$ )			
Node	x	y	Without Offset	$k=4$	$k=5$	$k=6$
1	0.0000	2.0000	-	1.45519152E-11	-1.16415322E-10	4.65661287E-10
2	0.0000	1.0000	-	3.16602600E-04	3.16653168E-05	3.16696241E-06
3	0.0000	0.0000	-	-7.49823323E-01	-7.49980541E-01	-7.49996261E-01
4	0.6667	2.0000	-	-3.56184530E-04	-3.56237288E-05	-3.56277451E-06
<b>5</b>	<b>0.6667</b>	<b>1.0000</b>	-	<b>9.99929171E-01</b>	<b>9.99992917E-01</b>	<b>9.99999291E-01</b>
6	0.6667	0.0000	-	1.12479333E+00	1.12497664E+00	1.12499498E+00
7	1.3333	2.0000	-	1.03107377E-04	1.03119528E-05	1.03050843E-06
8	1.3333	1.0000	-	7.91684579E-05	7.91647471E-06	7.91391358E-07
9	1.3333	0.0000	-	-4.58393600E-05	-4.58328733E-06	-4.57909652E-07
10	2.0000	2.0000	-	-3.74936669E-01	-3.74992770E-01	-3.74998380E-01
11	2.0000	1.0000	-	-2.81287357E-05	-2.81253597E-06	-2.80793756E-07
12	2.0000	0.0000	-	2.70879329E-05	2.70831564E-06	2.71039045E-07
$\Sigma\Phi$			-	<b>1.00005832E+00</b>	<b>1.00000583E+00</b>	<b>1.00000058E+00</b>



Table 6.1 shows the shape functions of  $3 \times 3$  regular local domain for the node 5. Using the diagonal offset algorithm does not affect the Kronecker delta function property for  $k = 4, 5$  and 6. However, it causes  $1E-6$  error in the partition of unity property for  $k = 6$ . The shape functions of  $4 \times 3$  regular local domain for node 5 are shown in the Table 6.2. The diagonal offset algorithm causes  $7.09E-7$  error in the Kronecker Delta function property and  $5.8E - 7$  error in the partition of unity property for  $k = 6$ . For  $3 \times 3$  regular local domain, these errors do not result any important effects in the stresses and displacements as shown in Figure 6.3 and 6.4. PIM with diagonal offset algorithm gives the same results with original PIM and analytical solutions for  $k > 3$ . For  $4 \times 3$  regular local domain, similar conclusions can be drawn as shown in Figure 6.5 and 6.6. However, the axial stress starts to deviate from exact results for  $k > 8$  as shown in Figure 6.6.



**Figure 6.3** The axial displacements ( $U_x$ ) at node 5 for different values of  $k$  (The patch of  $3 \times 3$  regular distributed nodes)



**Figure 6.4** The axial stress ( $\sigma_x$ ) at node 5 for different values of k (The patch of 3x3 regular distributed nodes)

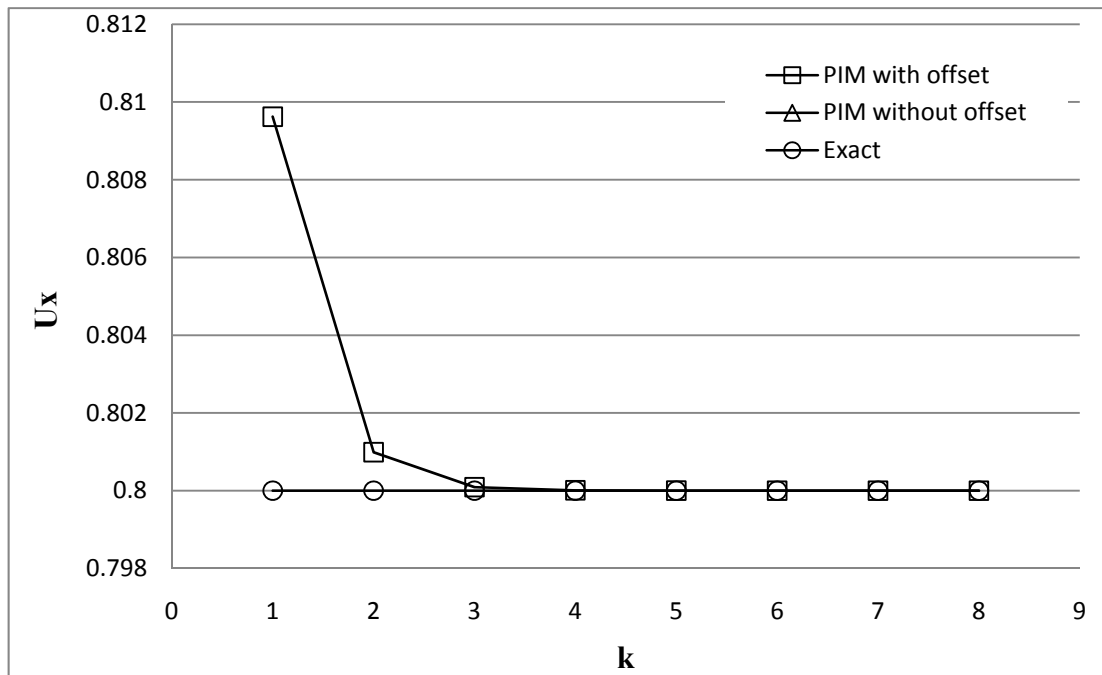


**Figure 6.5** The axial displacements ( $U_x$ ) at node 5 for different values of k (The patch of 4x3 regular distributed nodes)

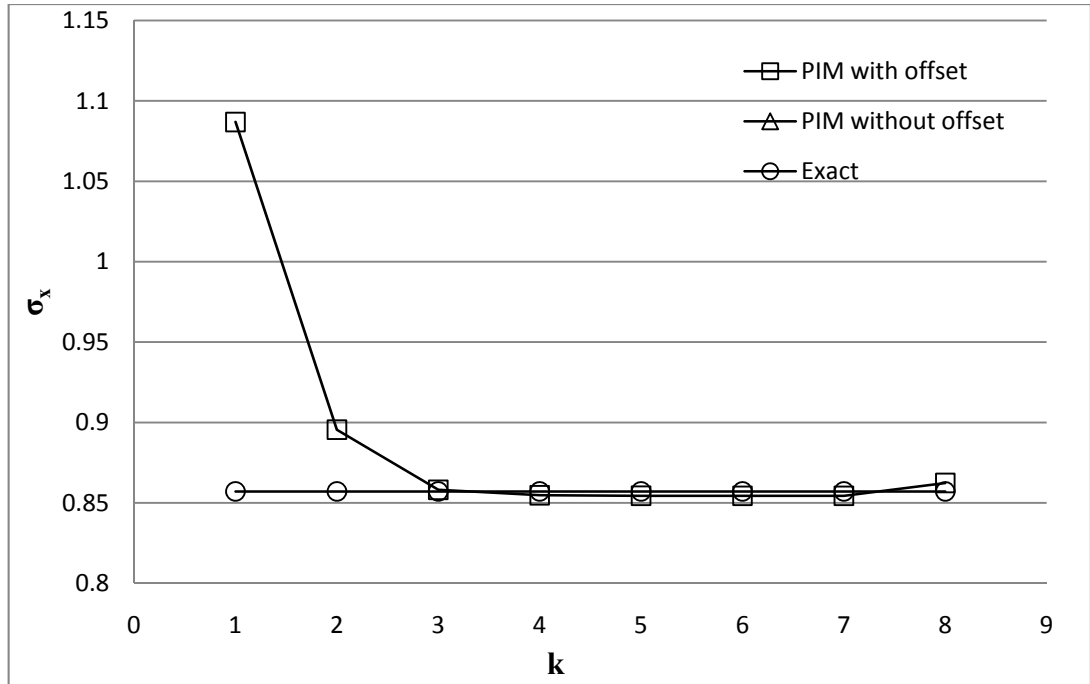


**Figure 6.6** The axial stress ( $\sigma_x$ ) at node 5 for different values of  $k$  (The patch of  $4 \times 3$  regular distributed nodes)

Table 6.3 and 6.4 show the shape functions of 9 and 12 irregular local domains for the nodes 5. The Kronecker Delta property is not affected and partition of unity property is affected from offsets in an average error of  $2E - 7$  for  $k = 6$ . However, this amount of error does not affect the displacements and stresses as shown in Figure 6.7, 6.8, 6.9 and 6.10 for  $k = 6$ .

**Table 6.3** PIM shape functions ( $\Phi$ ) for Node 5 for different values of  $k$  ( $3 \times 3$  regular nodes).

			PIM shape functions for Node 5 ( $\Phi$ )			
Node	x	y	Without Offset	k=4	k=5	k=6
1	0.0	2.0	0.00000000E+00	3.33814940E-20	2.08709398E-20	1.87116734E-21
2	0.0	1.0	0.00000000E+00	-4.44431974E-10	-4.4443197E-12	-4.4444311E-14
3	0.0	0.0	0.00000000E+00	-2.22207654E-14	-2.2220766E-17	-2.2222075E-20
4	1.0	2.0	0.00000000E+00	1.42221121E-04	1.42222112E-05	1.42222211E-06
<b>5</b>	<b>0.4</b>	<b>0.75</b>	<b>1.00000000E+00</b>	<b>1.00000000E+00</b>	<b>1.00000000E+00</b>	<b>1.00000000E+00</b>
6	1.0	0.0	0.00000000E+00	1.18843296E-14	-1.91699755E-15	-6.31615899E-16
7	2.0	2.0	0.00000000E+00	-7.11115605E-05	-7.1111560E-06	-7.1111159E-07
8	2.0	1.0	0.00000000E+00	-7.11084494E-05	-7.11108449E-06	-7.11110845E-07
9	2.0	0.0	0.00000000E+00	3.55545580E-05	3.5554558E-06	3.5555455E-07
$\Sigma \Phi$			<b>1.00000000E+00</b>	<b>1.00003556E+00</b>	<b>1.00000356E+00</b>	<b>1.00000036E+00</b>

**Table 6.4** PIM shape functions (  $\Phi$  ) for Node 5 for different values of  $k$  (4x3 regular nodes).

			PIM shape functions for Node 5 ( $\Phi$ )			
Node	x	y	Without Offset	k=4	k=5	k=6
1	0.0000	2.0000	-	-2.37587727E-14	-3.55271368E-15	-1.99840144E-15
2	0.0000	1.0000	-	9.86420520E-05	9.86669347E-06	9.86694226E-07
3	0.0000	0.0000	-	3.12422305E-05	3.12465735E-06	3.12470076E-07
4	0.6667	2.0000	-	-2.71367749E-04	-2.71345778E-05	-2.71343582E-06
5	<b>0.5000</b>	<b>1.2800</b>	-	<b>9.9999988E-01</b>	<b>1.00000000E+00</b>	<b>1.00000000E+00</b>
6	0.6667	0.0000	-	-3.05431214E-04	-3.05390101E-05	-3.05385990E-06
7	1.3333	2.0000	-	2.22072415E-04	2.22015379E-05	2.22009677E-06
8	1.6500	0.3300	-	3.06733783E-09	3.06741854E-11	3.17967874E-13
9	1.3333	0.0000	-	6.12525319E-09	6.12452311E-11	6.13731288E-13
10	2.0000	2.0000	-	4.03479082E-04	4.03404264E-05	4.03396784E-06
11	2.0000	1.0000	-	-5.55249728E-05	-5.55046566E-06	-5.55026252E-07
12	2.0000	0.0000	-	-1.29287103E-04	-1.29260437E-05	-1.29257772E-06
$\Sigma\Phi$			-	<b>9.99993822E-01</b>	<b>9.99999383E-01</b>	<b>9.99999938E-01</b>

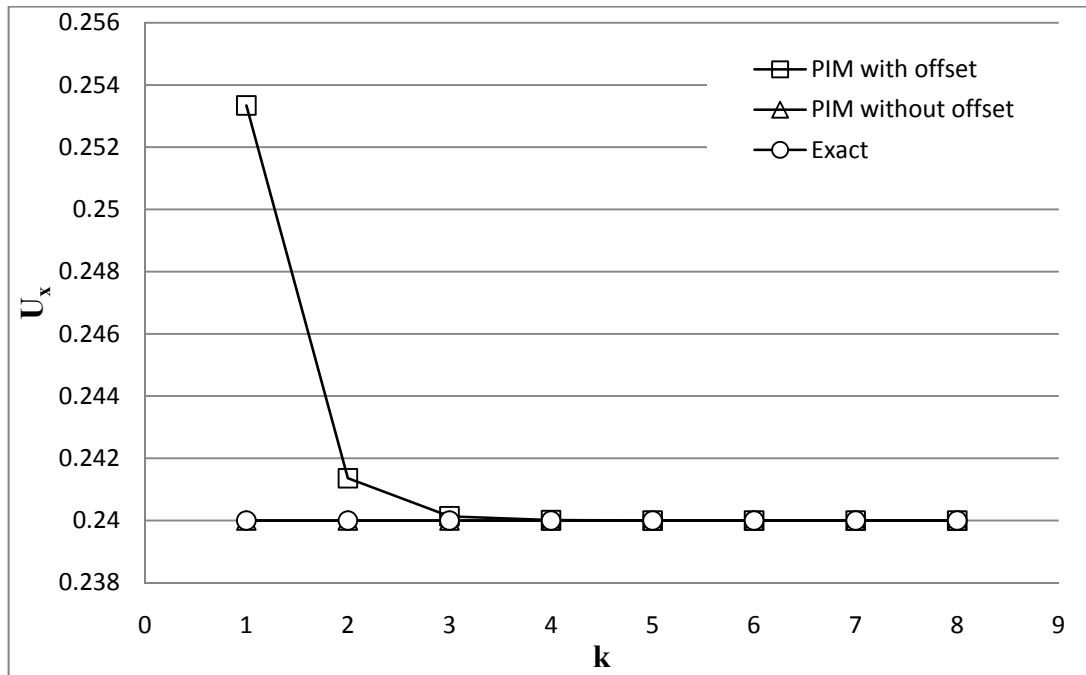


**Figure 6.7** The axial displacements ( $U_x$ ) at node 5 for different values of  $k$  (The patch of 9 irregular distributed nodes)

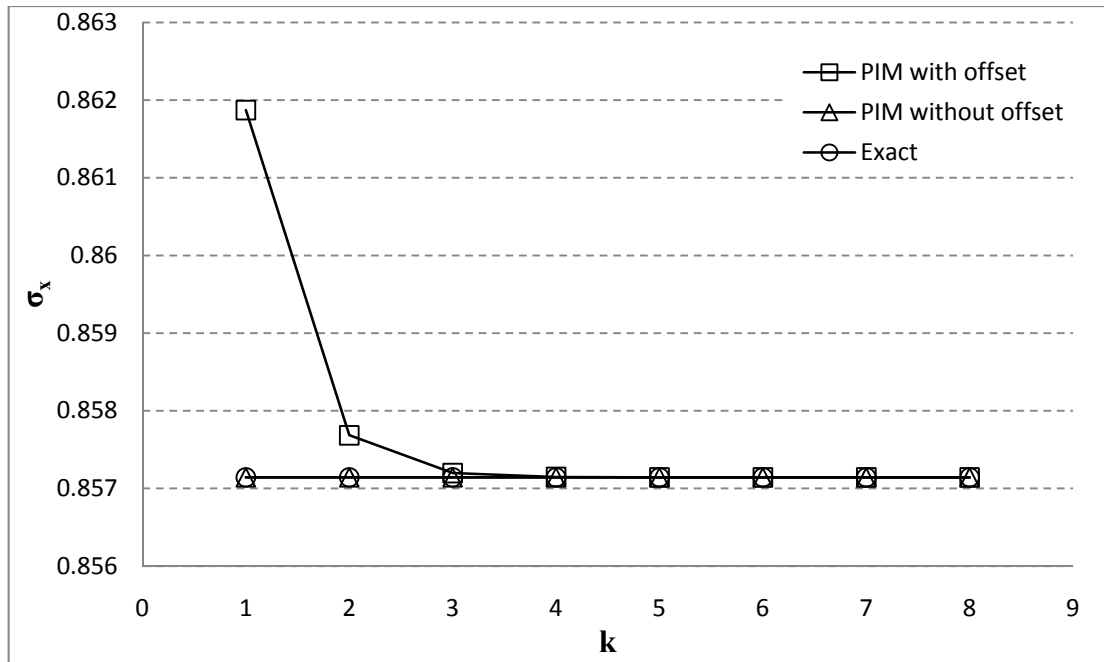


**Figure 6.8** The axial stress ( $\sigma_x$ ) at node 5 for different values of k (The patch of 9 irregular distributed nodes)

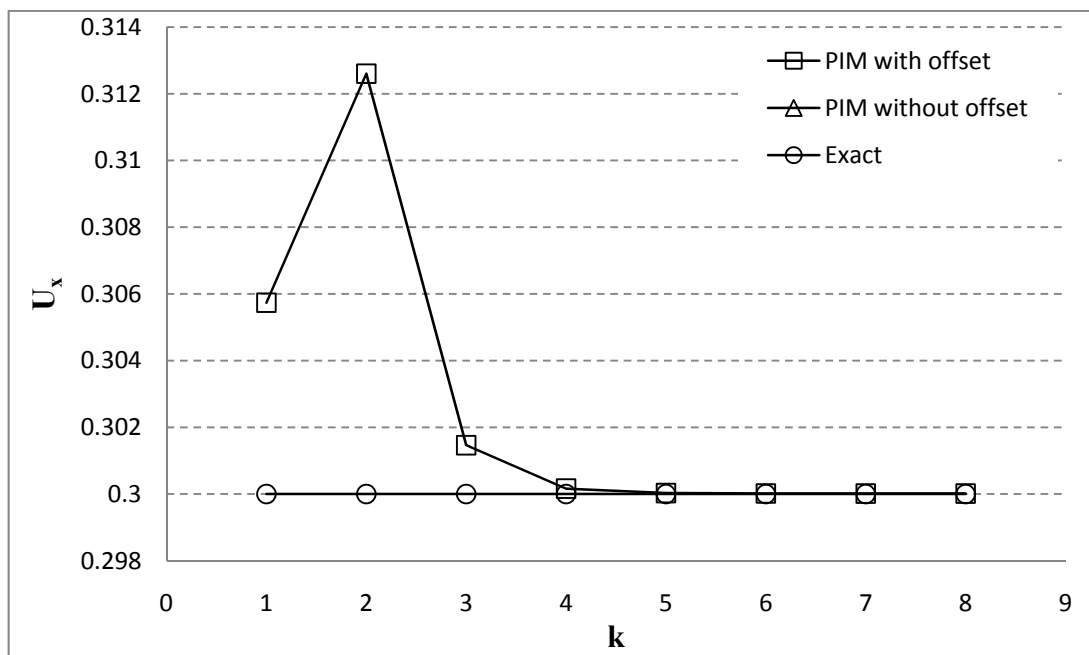


**Figure 6.9** The axial displacements ( $U_x$ ) at node 5 for different values of k (The patch of 12 irregular distributed nodes)

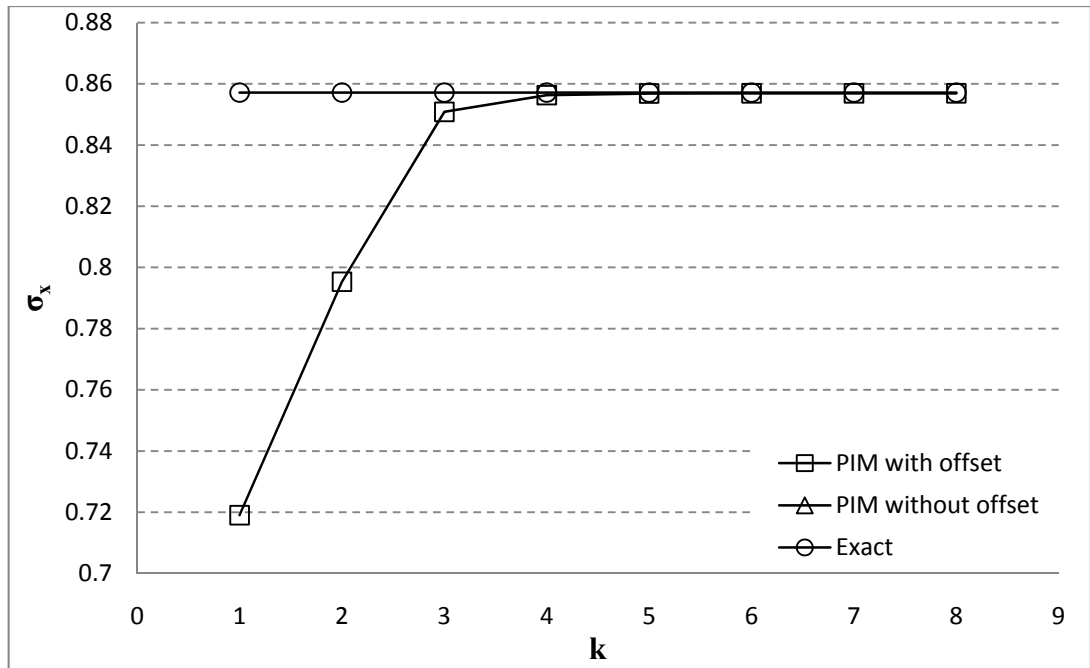


**Figure 6.10** The axial stress ( $\sigma_x$ ) at node 5 for different values of  $k$  (The patch of 12 irregular distributed nodes)

#### 6.4.2 Axially loaded plate

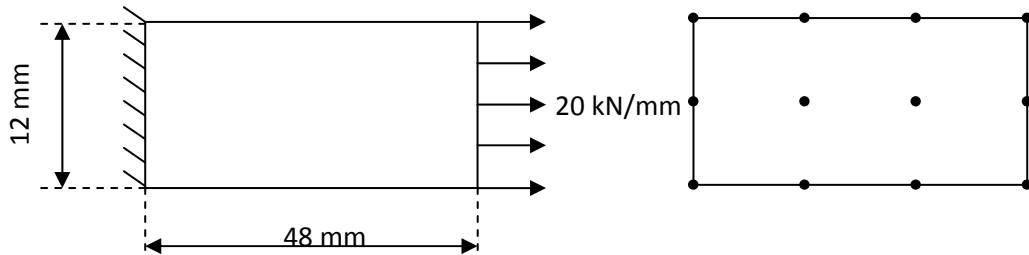


**Figure 6.11** Axially loaded plate and its PIM model

It is a plane stress problem. A rectangular plate with dimensions of 12 mm  $\times$  48 mm is loaded as shown in Figure 6.11. Rectangular influence domains are used with dimensions of 24 mm  $\times$  24 mm. The material parameters are taken as  $E = 200$  GPa and  $\nu = 0$ . 12 mm  $\times$  12 mm background cells are used with 3 $\times$ 3 gauss integration points.

The original PIM method does not give any solution because of singular moment matrices in the influence domain of nodes 1, 2, 3, 13, 14 and 15.  $k$  is taken as 6 for all influence domains without considering it has singular moment matrix or not. The displacements, which are obtained from PIM with diagonal offset algorithm, are same as the exact solutions as shown in Figure 6.12. Although, there are some

differences between the PIM stresses and exact stresses as shown in Figure 6.13, they can be reduced by increasing the number of nodes in the solution domain.

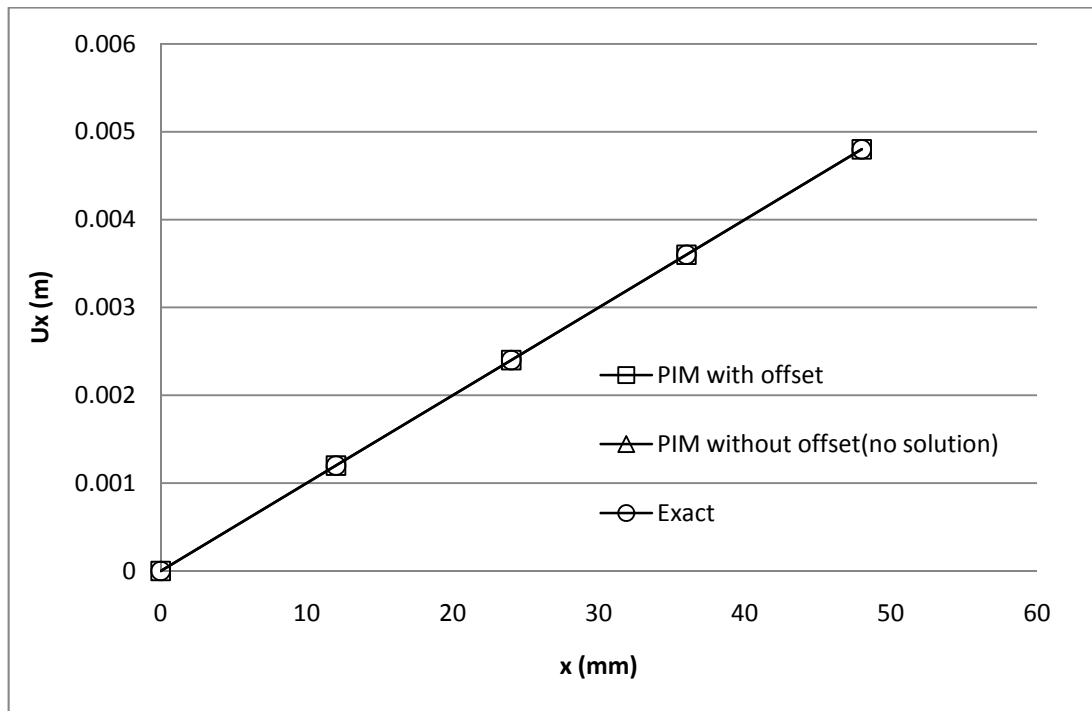


**Figure 6.12** Axial displacement distributions of rectangular plate with  $k=6$ .

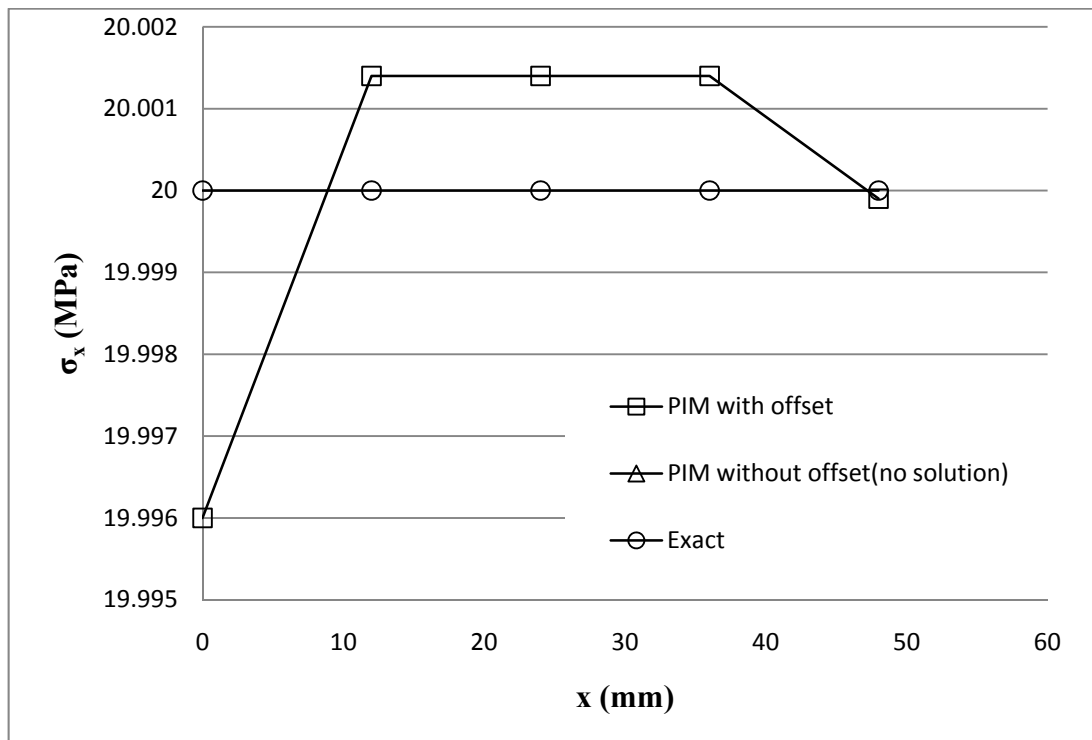


**Figure 6.13** Axial stress distributions of rectangular plate with  $k=6$ .

### 6.4.3 Cantilever beam

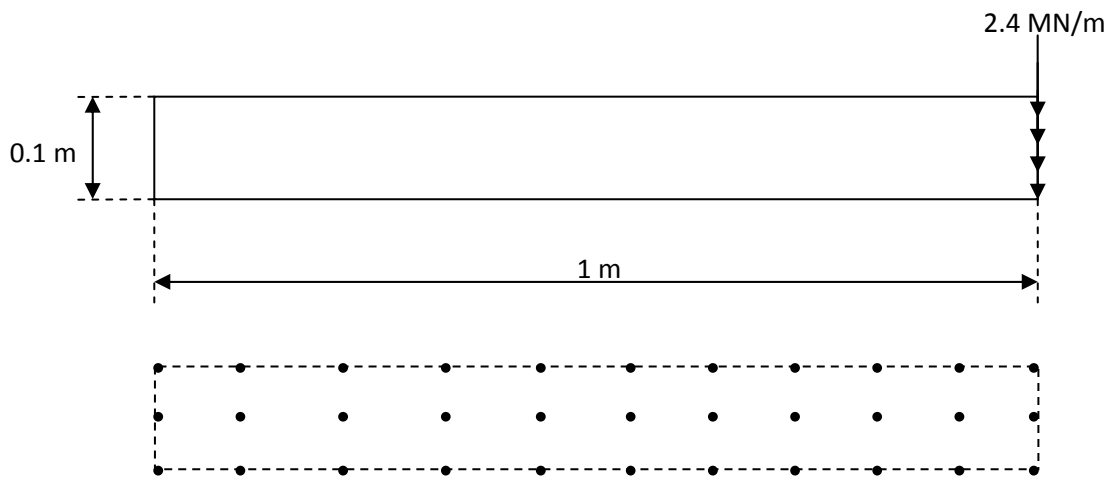


**Figure 6.14** Cantilever beam and its PIM model

A cantilever beam which is a classical benchmark test is solved as a plane stress problem. Its boundary conditions are shown in Figure 6.14. The material constants are as follows:  $E = 200$  GPa and  $\nu = 0$ . Its PIM model is obtained using 33 nodes, 10 background cells with  $3 \times 3$  gauss integration points and influence domains with dimensions of 0.1 m x 0.1 m.

The PIM without diagonal offset algorithm includes singular moment matrix at all nodes. Therefore, it does not give any solution. However, if the diagonal offset algorithm is used in the PIM with  $k = 6$ , the displacement and stress solutions shows a good agreement with exact solutions as shown in Figure 6.15 and 6.16.

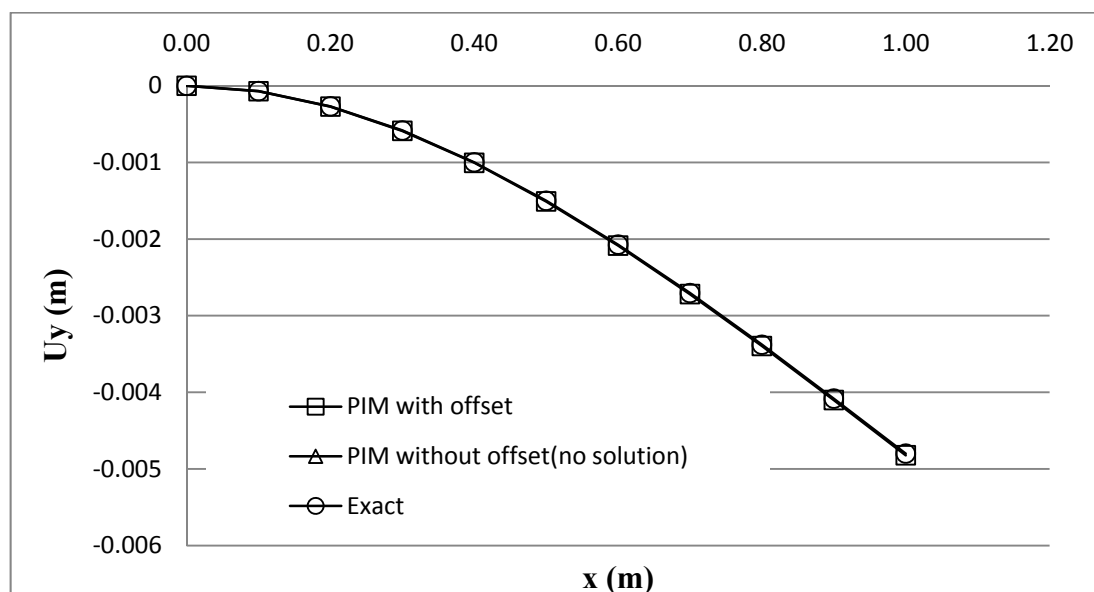


**Figure 6.15** Vertical displacement distributions along the neutral line of cantilever beam with  $k=6$ .



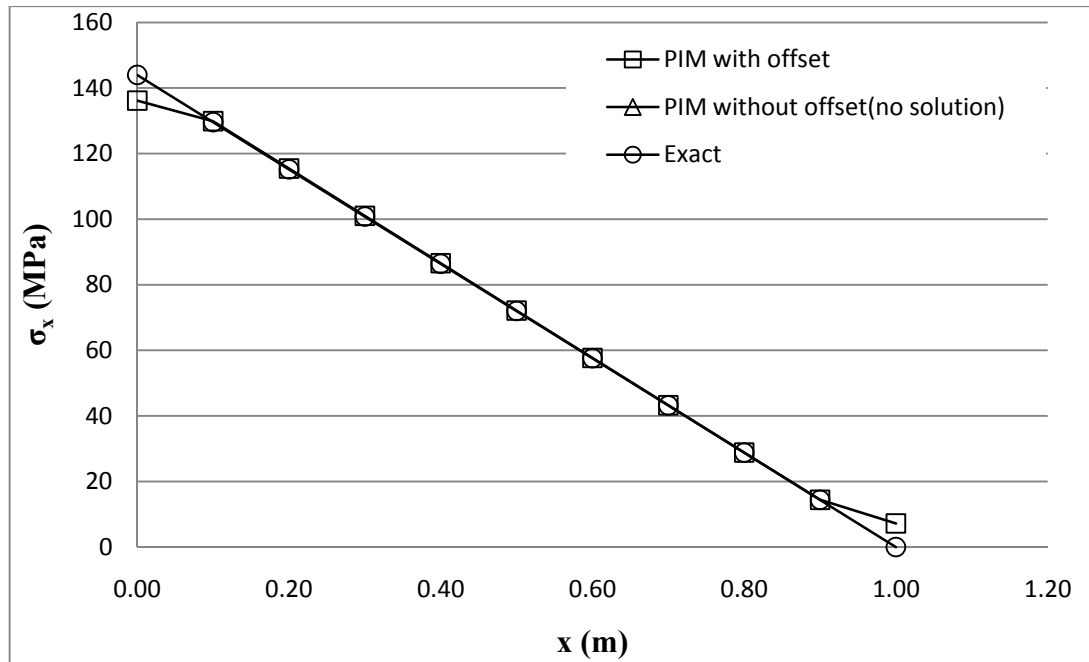


**Figure 6.16** Axial stress distributions along the upper line of cantilever beam with  $k=6$ .

## 6.5. Results and Discussions

It has been shown that the diagonal offset algorithm overcomes the singular moment matrix problem in the polynomial PIM and it eliminates the extra calculations caused from complex algorithms. Also, it doesn't decrease the efficiency of the PIM as other methods.

The results of the studies show that the Kronecker Delta function and partition of unity properties are affected from the diagonal offset algorithm. The amount of the error is directly related with the amount of offset. It is shown that PIM with the proposed algorithm gives nearly same results with the exact results for  $4 \leq k \leq 7$ . The solutions deviate from exact results for  $k < 4$  and  $k > 7$ .

## CHAPTER 7

### A REGULAR BASIS ALGORITHM FOR THE POLYNOMIAL POINT INTERPOLATION METHOD

#### 7.1 Introduction

As already specified before, Point Interpolation Method (PIM) has inherent properties that give advantages over the Mesh-free methods based on Moving Least Square (MLS) shape functions. These properties are the Kronecker delta function property of its shape functions and the simplicity of its computation algorithm. But in spite of its positives it has two negativities during its application. Detailed study of the first one, the singularity problem, was presented in the previous chapter. The second one is selection of the polynomial terms.

The selection of the polynomial terms and the relation between the selection process and the singularity are discussed in detail in the section 7.2. A general rule for the selection of polynomial terms are proposed in section 7.3 and the test of the proposed rule is done in section 7.4.

#### 7.2 A detailed view to the selection of the polynomial terms

The basis function is constructed by selecting the terms from the Pascal's triangle. However, there isn't any definite general rule or rules for the selection of the terms. Two properties are pointed in the literature for the construction of the basis function. One is the symmetrically selection of the terms from Pascal's triangle [1], and the other is the completeness of the basis function [2,87,94,95,115-117,119,125]. The  $p_i(x)$  was built utilizing the Pascal's triangle with complete basis, but the basis was provided with different terms [87,94,95,115-117]. Liew and Chen [125] were mentioned that the basis is chosen as a complete polynomial basis for computational accuracy. Liu et al. [119] were presented that basis should satisfy the completeness or quasi-completeness. The complete basis is a preference according to Liu and Gu [2]. Liu [1] and Liu et al. [119] were emphasized that the addition of higher order terms to the basis can be possible.

In addition to those, the reason of the singularity is based on the improper selection of polynomial terms and the singularity problem is eliminated with the appropriate selection of the polynomial terms [1,95]. It is shown that there is a gap in the selection of polynomial terms for the basis.

### **7.3 A regular basis algorithm for the polynomial point interpolation method**

In this part of the study, it is tried to eliminate the singularity problem by proposing an algorithm about the selection of the polynomial terms for basis functions. All the proposed singularity elimination algorithms are put into use when a singularity encountered. However, up to this step, most of the calculations including taking the inverse of moment matrix are generally completed. Therefore, an algorithm before all of these calculations can have important advantageous over existing algorithms. The purpose of regular basis algorithm is to eliminate singularity at the initial stage of shape function computation. Employment of it without losing any advantages of PIM is planned.

In this algorithm, terms of the basis functions are selected from the Pascal's triangle according to the position of the nodes. This is different from the original polynomial PIM. In the original polynomial PIM, there is not any relation shown between polynomial terms and their positions at the formulation. However, the source of singularity was explained with the positions of the nodes by Liu [1] and Liu and Gu [95]. Also, Wang and Liu [86] were emphasized that the node distribution in polynomial PIM is structured. But the structure is not defined. The idea behind the selection of polynomial terms according to the position of the nodes comes not only for elimination of singularity but also find a physical relation between the local domain and the terms.

The general form of the algorithm can be illustrated in the Figure 7.1. Selection of tip points in the local domains is starting point of the algorithm. Two tip points, one for x-direction and one for y-direction, are selected for a two-dimensional local domains. Tip points must be the last node of the support domain on the  $x$ - or  $y$ -directions for a two-dimensional domain. It is not important which side of the coordinate axes, left or right and up or down, is selected as long as it is consistent with the other local domains. The distances between the nodes of local domain are determined after the selection of tip points. The order of  $x$ -terms are increased for

every distance in  $x$ -direction between two adjacent nodes starting from the tip point and the order of  $y$ -terms are increased for each distance in  $y$ -direction. The order of the terms for the tip points is zero in the related direction.

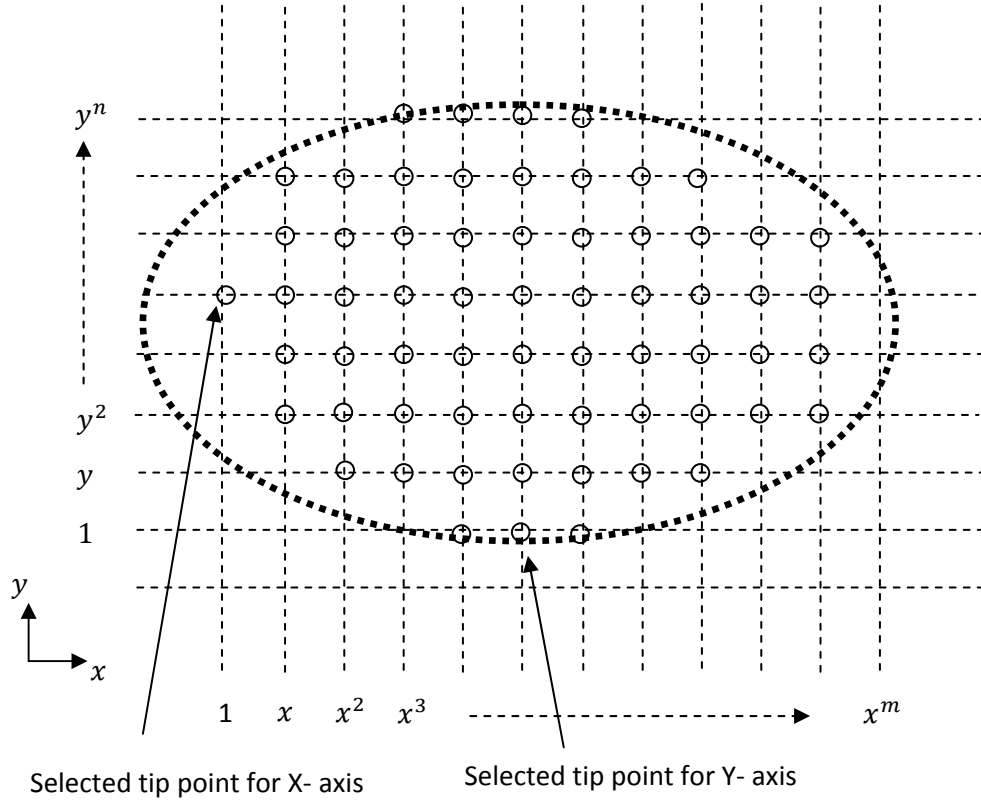


**Figure 7.1** A regular basis algorithm for selection of the basis function terms

The algorithm can also be used for the irregular distributed nodes. For example, consider a node configuration of a rectangular support domain as shown in Figure 7.2. The nodes, denoted by 1, 2, 9 and 10, are the last nodes on both  $x$ - and  $y$ -directions so any one can be selected for a tip point.

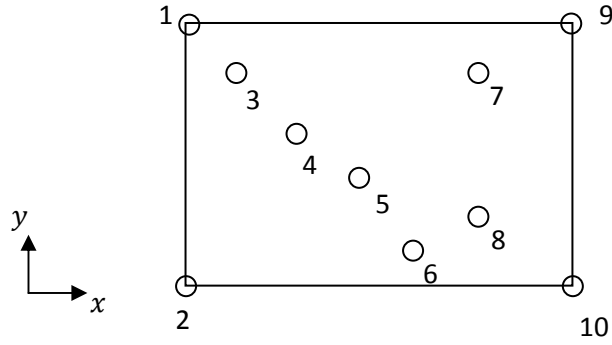


**Figure 7.2** A rectangular support domain with irregular distributed nodes

If node 1 is selected. The order of  $x$  and  $y$  terms of the nodes are obtained as shown in Figure 7.3. And the polynomial basis function is expressed as follows

$$\mathbf{p}^T = \{1, y^6, xy, x^2y^2, x^3y^3, x^4y^5, x^5y, x^5y^4, x^6, x^6y^6\}$$

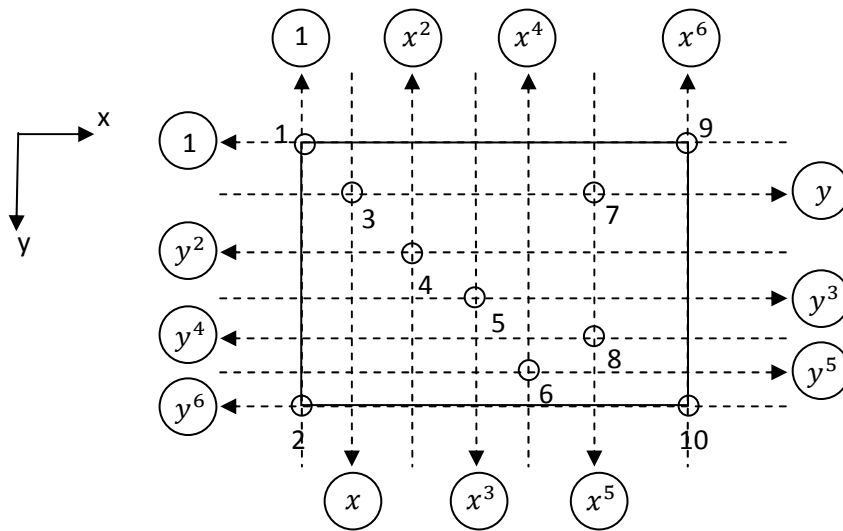


**Figure 7.3** Illustration of selection of the basis function terms for a rectangular support domain

For an arbitrary shape support domain, shown in Figure 7.4, the last nodes of support domain in  $x$ - and  $y$ -direction are different nodes. They aren't coincide. Two tip points, one for  $x$ -direction and one for  $y$ -direction, are selected. Any of the nodes numbered with 1 or 13 can be the tip point for  $x$ -direction and node 7 or node 10 can be the tip point for  $y$ -direction. The node 1 for  $x$ -direction and the node 10 for the  $y$ -direction are the selected tip points of each directions. The selected terms of each

nodes in  $x$ -, and  $y$ -directions are shown in Figure 7.5. The PBF with these terms has the following form:

$$\mathbf{p}^T = \{y^3, xy, xy^7, x^2y^6, x^3y^2, x^3y^4, x^4y^8, x^5y^4, x^6y^6, x^6y^2, x^7y^7, x^7y, x^8y^5\}$$

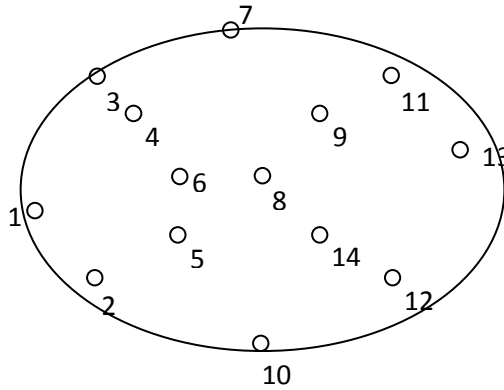


**Figure 7.4** An ellipse support domain with irregular distributed nodes

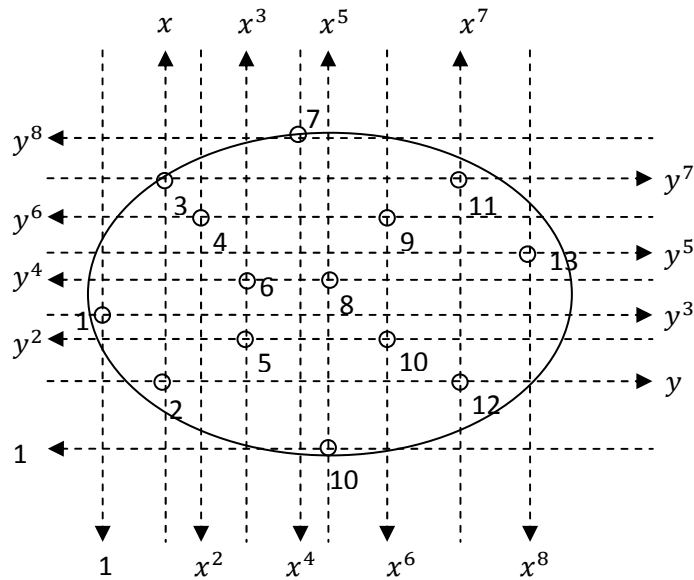


**Figure 7.5** Illustration of selection of the basis function terms for an ellipse support domain

## 7.4 Numerical Tests

### 7.4.1 Patch Tests

Four patch tests are prepared to verify the proposed algorithm. First patch is not a standard patch test. It is a problem found in the literature that polynomial PIM has singular moment matrix. The other three patches are the standard patch tests and also they are the situations that polynomial PIM have singularity problem potential.

The first patch is shown in Figure 7.6, and it includes six nodes in a support domain. These six nodes sit in two lines parallel to the  $x$  axis and in three lines parallel to the  $y$  axis.

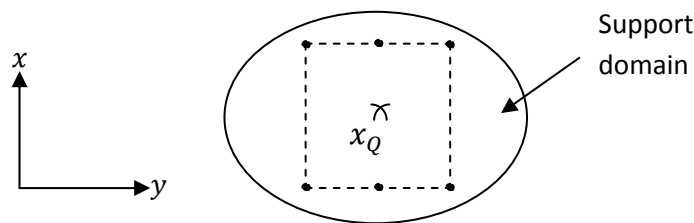


**Figure 7.6** A patch test causes singularity in original PIM

Figure 7.7.a, shows the second patch comprised form nine nodes in  $3 \times 3$  regular distribution. It has one interior node. Figure 7.7.b, shows the third patch with 25 nodes in  $5 \times 5$  format. This patch includes 9 interior nodes. Figure 7.7.c, shows the fourth patch that constructed using 49 regularly distributed nodes. 25 nodes of the fourth patch are interior nodes. The dimensions of second, third and fourth patches are  $2 \times 2$ . The material properties are taken as  $E = 1.0$  and  $\nu = 0.3$ . Prescribed displacements are applied to the boundary nodes. The prescribed displacements are linear and the value of them are  $u_x = 0.6x$  and  $u_y = 0.6y$ . A  $2 \times 2$  rectangular background cell and different gauss configuration are used for integration in these patch tests.

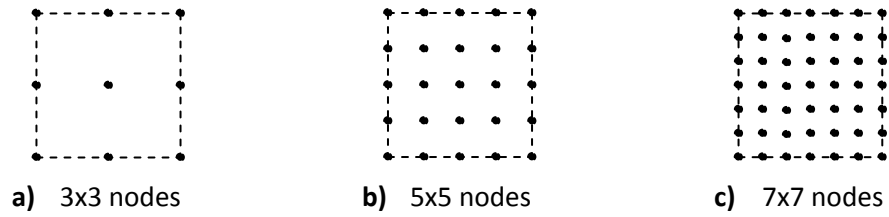


**Figure 7.7** Patch tests with regular node distributions

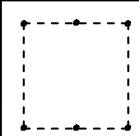
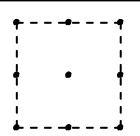
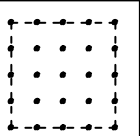
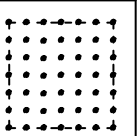
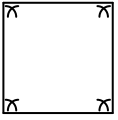
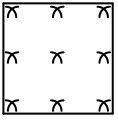
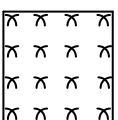
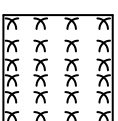
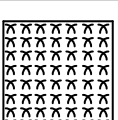
The results of the patch tests are shown in Table 1. The table shows that original polynomial PIM has singular moment matrix problem in all configuration of the first patch test and it fails in the first patch test. However, the proposed algorithm passes the patch test without having any singularity problem and giving good accuracy.

In the second patch test, the original polynomial PIM and the proposed algorithm are passed the patch test. In this patch, they are same because both of them use the same polynomial basis function.

The original polynomial PIM method fails in the third and fourth patch tests. In these tests it doesn't have any singularity problem but it doesn't give the accurate results. The proposed algorithm doesn't have any singularity problem in the third and fourth patch tests. However, the result obtained using  $2 \times 2$  or  $3 \times 3$  gauss point integrations aren't accurate in the third patch test. It passes the third patch with  $4 \times 4$ ,  $6 \times 6$  and  $8 \times 8$  gauss point configurations.



**Table 7.1.** Singularity and accuracy results of the patch tests.

		 3 x 2 nodes	 3 x 3 nodes	 5 x 5 nodes	 7 x 7 nodes	
Original PIM	Singularity:	FAILED	PASSED	PASSED	PASSED	 2 x 2 gauss points
	Accuracy:	-	PASSED	FAILED	FAILED	
Regular PIM	Singularity:	PASSED	PASSED	PASSED	PASSED	 3 x 3 gauss points
	Accuracy:	PASSED	PASSED	FAILED	FAILED	
Original PIM	Singularity:	FAILED	PASSED	PASSED	PASSED	 4 x 4 gauss points
	Accuracy:	-	PASSED	FAILED	FAILED	
Regular PIM	Singularity:	PASSED	PASSED	PASSED	PASSED	 6 x 6 gauss points
	Accuracy:	PASSED	PASSED	PASSED	FAILED	
Original PIM	Singularity:	FAILED	PASSED	PASSED	PASSED	 8 x 8 gauss points
	Accuracy:	-	PASSED	FAILED	FAILED	
Regular PIM	Singularity:	PASSED	PASSED	PASSED	PASSED	
	Accuracy:	PASSED	PASSED	PASSED	PASSED	

## 7.4.2 Case Studies

### 7.4.2.1 Axially Loaded Bar

In the first case study, an axially loaded bar is solved. One side of the bar is clamped and 83. kN/mm is applied to the other side as shown in Figure 7.8. The material properties are  $E = 200$  GPa and  $\nu = 0$ . The problem domain is represented by 15 nodes. The rectangular support domains are used for interpolation. The size of them are 0.12 m x 0.12 m. Therefore, 6-9 nodes are found in the support domains. Four background cells are used for integration.

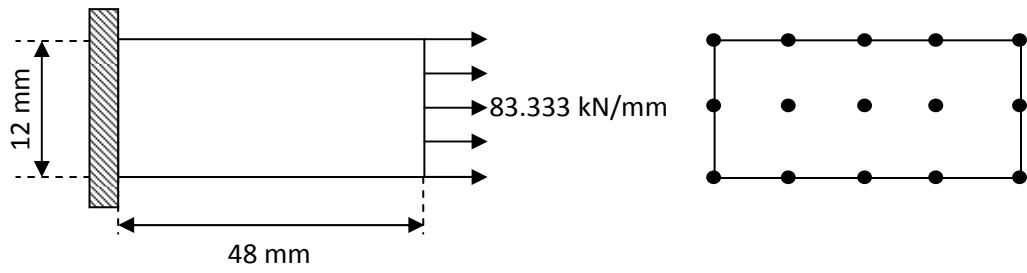


**Figure 7.8** Axially loaded bar and the PIM model.

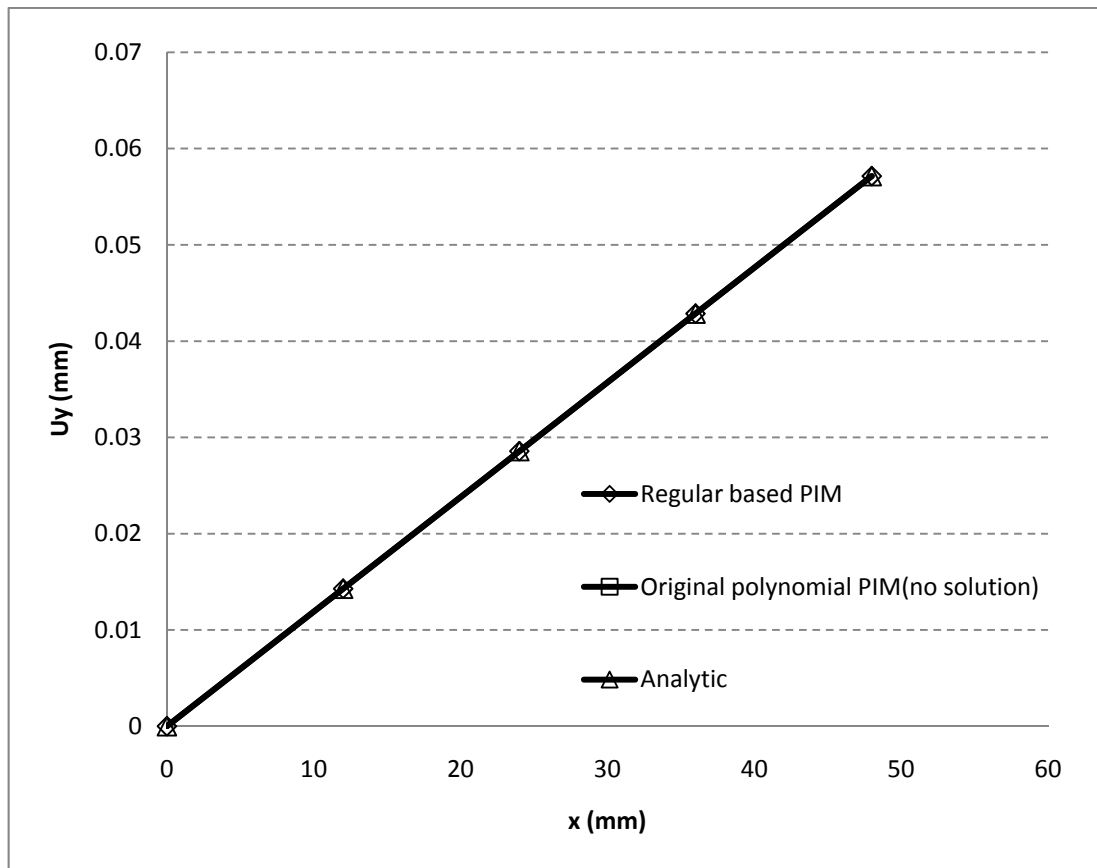


**Figure 7.9** The axial displacements of the bar.

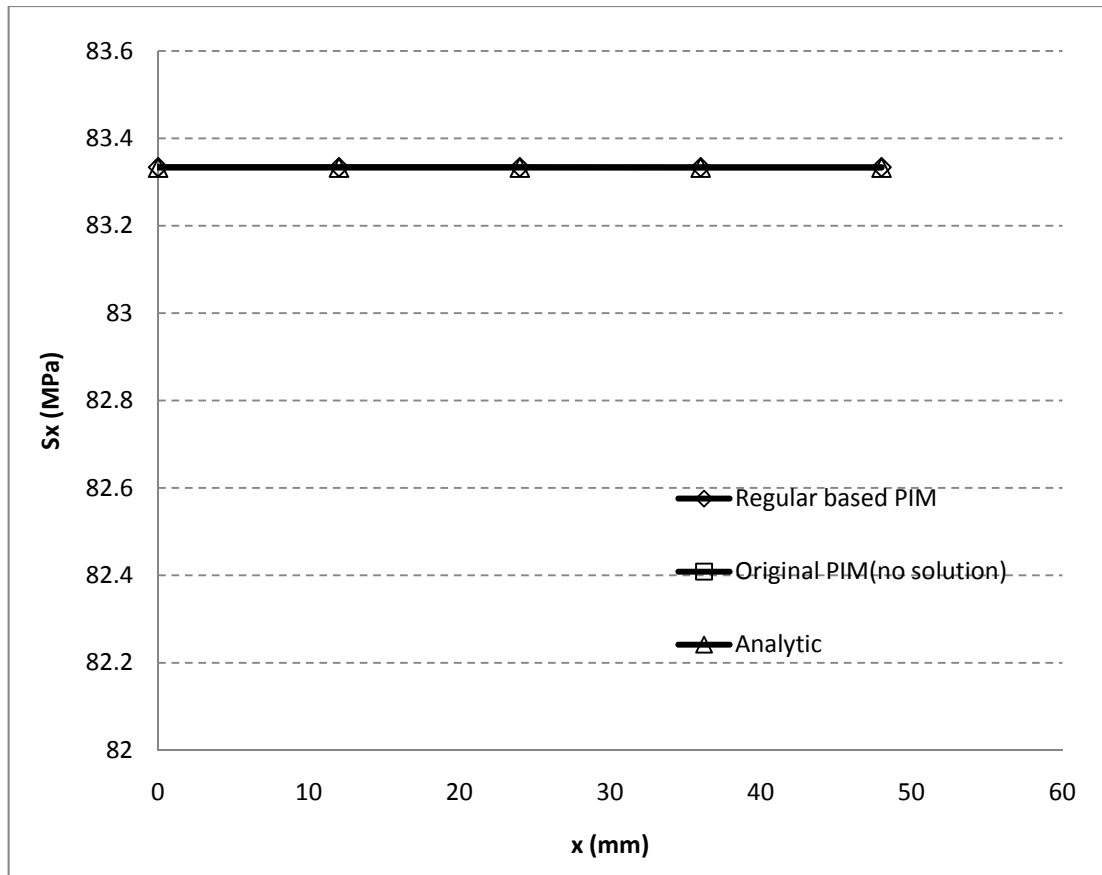


**Figure 7.10** The axial stress distributions of the bar.

The displacement and stress values in axial direction of the bar are computed using different support domain sizes. They are compared in Table 7.2. As seen in this Table, PIM with the regular basis gives an excellent accuracy even for small support domain sizes.

**Table 7.2** The displacement and stress values in axial direction of the bar for different sizes of the domains. (Original PIM has singularity problem. Only PIM with regular basis results listed.)

Node Coordinate		Domain Size 12x12 (6-9 nodes)		Domain Size 24x12 (9-12 nodes)		Domain Size 36x12 (12-15 nodes)		Domain Size 48x12 (15 nodes)	
		regular basis PIM		regular basis PIM		regular basis PIM		regular basis PIM	
X	Y	U <sub>x</sub>	S <sub>x</sub>	U <sub>x</sub>	S <sub>x</sub>	U <sub>x</sub>	S <sub>x</sub>	U <sub>x</sub>	S <sub>x</sub>
0	6	5.82E-16	8.33E+01	4.29E-16	8.33E+01	3.50E-16	8.33E+01	2.77E-16	8.33E+01
0	0	2.33E-15	8.33E+01	1.72E-15	8.33E+01	1.40E-15	8.33E+01	1.11E-15	8.33E+01
0	-6	5.82E-16	8.33E+01	4.29E-16	8.33E+01	3.50E-16	8.33E+01	2.77E-16	8.33E+01
12	6	1.43E-05	8.33E+01	1.43E-05	8.33E+01	1.43E-05	8.33E+01	1.43E-05	8.33E+01
12	0	1.43E-05	8.33E+01	1.43E-05	8.33E+01	1.43E-05	8.33E+01	1.43E-05	8.33E+01
12	-6	1.43E-05	8.33E+01	1.43E-05	8.33E+01	1.43E-05	8.33E+01	1.43E-05	8.33E+01
24	6	2.86E-05	8.33E+01	2.86E-05	8.33E+01	2.86E-05	8.33E+01	2.86E-05	8.33E+01
24	0	2.86E-05	8.33E+01	2.86E-05	8.33E+01	2.86E-05	8.33E+01	2.86E-05	8.33E+01
24	-6	2.86E-05	8.33E+01	2.86E-05	8.33E+01	2.86E-05	8.33E+01	2.86E-05	8.33E+01
36	6	4.29E-05	8.33E+01	4.29E-05	8.33E+01	4.29E-05	8.33E+01	4.29E-05	8.33E+01
36	0	4.29E-05	8.33E+01	4.29E-05	8.33E+01	4.29E-05	8.33E+01	4.29E-05	8.33E+01
36	-6	4.29E-05	8.33E+01	4.29E-05	8.33E+01	4.29E-05	8.33E+01	4.29E-05	8.33E+01
48	6	5.71E-05	8.33E+01	5.71E-05	8.33E+01	5.71E-05	8.33E+01	5.71E-05	8.33E+01
48	0	5.71E-05	8.33E+01	5.71E-05	8.33E+01	5.71E-05	8.33E+01	5.71E-05	8.33E+01
48	-6	5.71E-05	8.33E+01	5.71E-05	8.33E+01	5.71E-05	8.33E+01	5.71E-05	8.33E+01

#### 7.4.2.2 Cantilever Beam

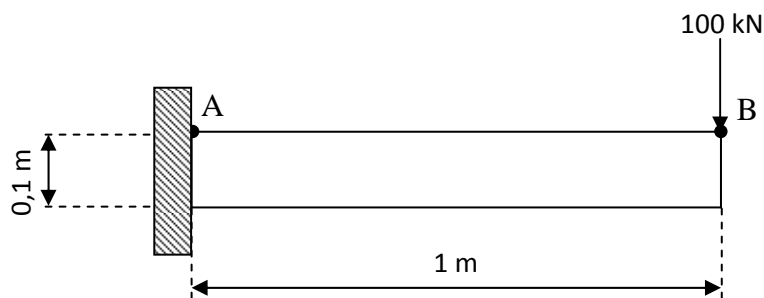


**Figure 7.11** The cantilever beam problem.

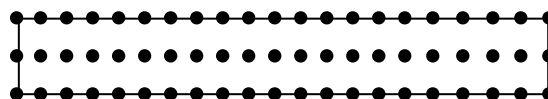


**Figure 7.12** The PIM model of cantilever beam problem.

In the second case study, an elasto-static cantilever beam problem is solved with the proposed algorithm. The cantilever beam is loaded as shown in Figure 7.11 and the model used for original PIM and regular basis PIM is shown in Figure 7.12. The material properties are as follows:  $E = 200$  GPa and  $\nu = 0$ . 63 nodes are used to represent the cantilever beam geometry. 10 background cells are used to evaluate the integrals. The size of the formed support domains are  $0.1 \text{ m} \times 0.1 \text{ m}$ . 9 – 15 nodes are used for interpolation in a local domain. The results are compared with analytical solution results in Figure 7.13 and Figure 7.14. The transverse displacement and stress values in  $x$  – direction of the bar along AB line are computed using different support domain sizes. They are shown in Table 7.3.

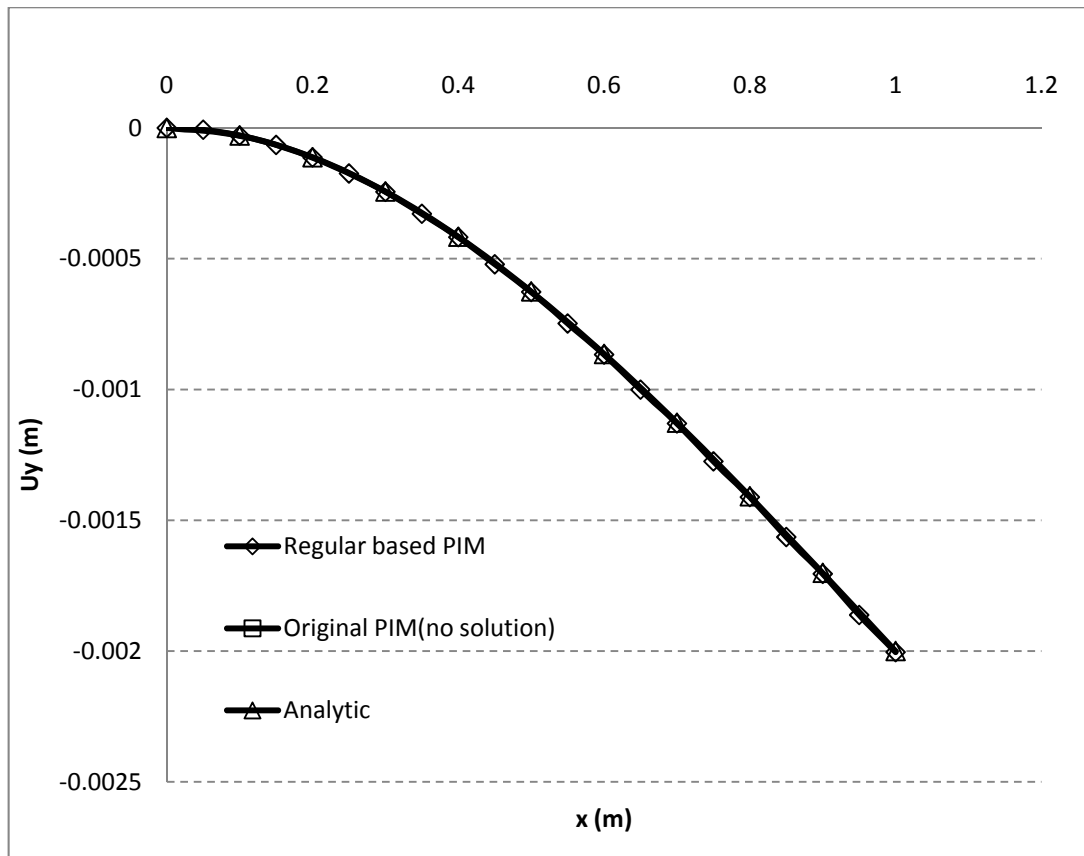


**Figure 7.13** The lateral displacements along the mid-point of the cantilever beam.

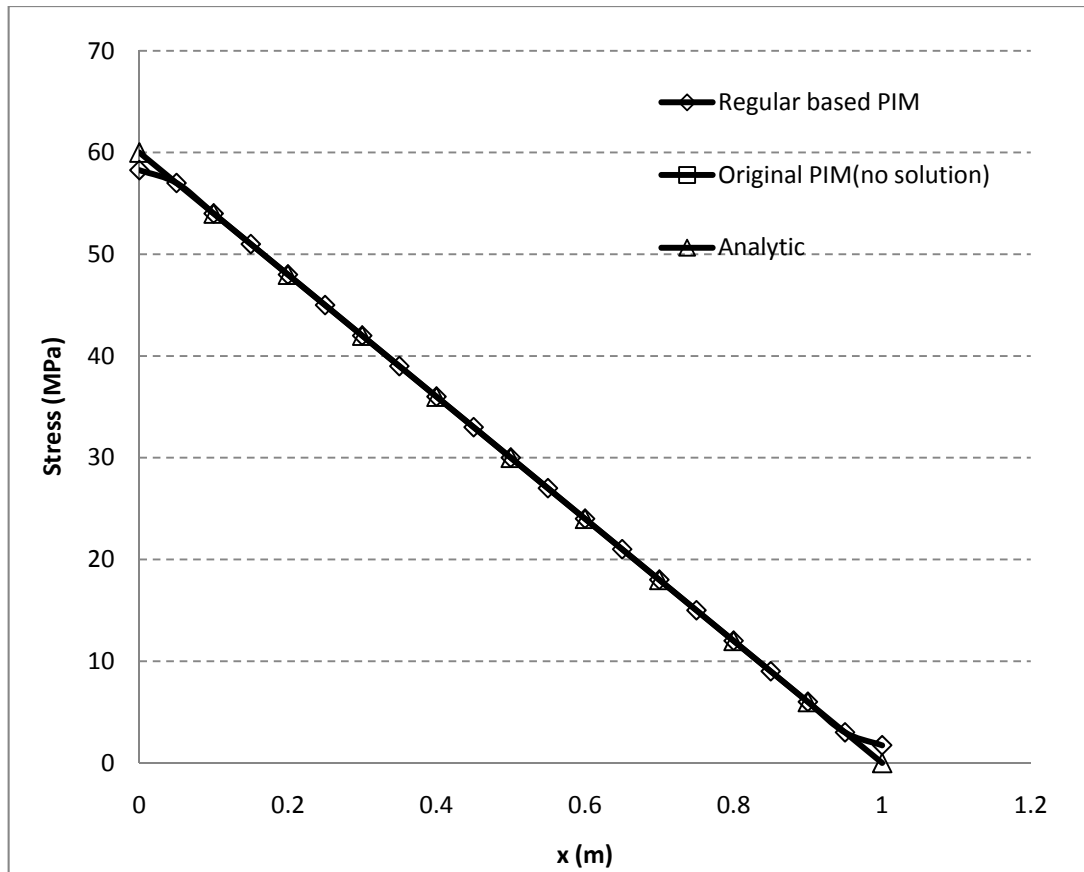


**Figure 7.14** The axial stress distributions along the top surface of the cantilever beam.

To investigate the effect of number of nodes in a local domain, the displacement and stress values along AB line of the cantilever beam are computed using different support domain sizes. They are compared in Table 7.3.

**Table 7.3** The transverse displacements and  $S_x$  along AB line using different domain sizes. (Original PIM has singularity problem. Only PIM with regular basis results listed.)

		Domain Size 0.05x0.05		Domain Size 0.05x0.1		Domain Size 0.1x0.1	
Node Coordinate		regular basis PIM		regular basis PIM		regular basis PIM	
X	Y	Uy	Sx	Uy	Sx	Uy	Sx
0	0.05	-3.74E-27	5.83E+07	6.08E-27	5.83E+07	3.55E-27	5.96E+07
0.05	0.05	-6.91E-06	5.70E+07	-6.83E-06	5.70E+07	-7.94E-06	5.75E+07
0.1	0.05	-2.94E-05	5.40E+07	-2.95E-05	5.40E+07	-2.99E-05	5.39E+07
0.15	0.05	-6.50E-05	5.10E+07	-6.48E-05	5.10E+07	-6.61E-05	5.10E+07
0.2	0.05	-1.13E-04	4.80E+07	-1.13E-04	4.80E+07	-1.14E-04	4.80E+07
0.25	0.05	-1.74E-04	4.50E+07	-1.74E-04	4.50E+07	-1.75E-04	4.50E+07
0.3	0.05	-2.44E-04	4.20E+07	-2.45E-04	4.20E+07	-2.46E-04	4.20E+07
0.35	0.05	-3.28E-04	3.90E+07	-3.28E-04	3.90E+07	-3.29E-04	3.90E+07
0.4	0.05	-4.18E-04	3.60E+07	-4.18E-04	3.60E+07	-4.19E-04	3.60E+07
0.45	0.05	-5.21E-04	3.30E+07	-5.21E-04	3.30E+07	-5.23E-04	3.30E+07
0.5	0.05	-6.27E-04	3.00E+07	-6.28E-04	3.00E+07	-6.29E-04	3.00E+07
0.55	0.05	-7.48E-04	2.70E+07	-7.47E-04	2.70E+07	-7.49E-04	2.70E+07
0.6	0.05	-8.66E-04	2.40E+07	-8.67E-04	2.40E+07	-8.69E-04	2.40E+07
0.65	0.05	-1.00E-03	2.10E+07	-1.00E-03	2.10E+07	-1.00E-03	2.10E+07
0.7	0.05	-1.13E-03	1.80E+07	-1.13E-03	1.80E+07	-1.13E-03	1.80E+07
0.75	0.05	-1.27E-03	1.50E+07	-1.27E-03	1.50E+07	-1.28E-03	1.50E+07
0.8	0.05	-1.41E-03	1.20E+07	-1.41E-03	1.20E+07	-1.41E-03	1.20E+07
0.85	0.05	-1.56E-03	9.00E+06	-1.56E-03	9.00E+06	-1.57E-03	8.99E+06
0.9	0.05	-1.70E-03	6.00E+06	-1.71E-03	6.00E+06	-1.71E-03	6.10E+06
0.95	0.05	-1.86E-03	3.00E+06	-1.86E-03	3.00E+06	-1.86E-03	2.53E+06
1	0.05	-2.00E-03	1.73E+06	-2.01E-03	1.73E+06	-2.01E-03	3.85E+05

### 7.4.2.3 Simply Supported Circular Plate

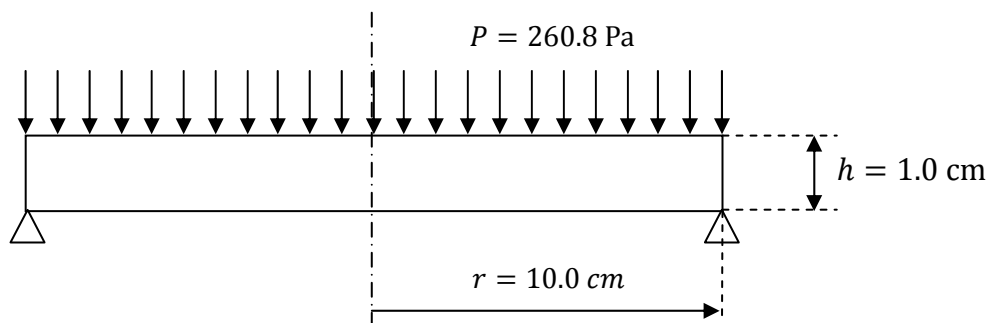


**Figure 7.15** Simply supported circular plate.

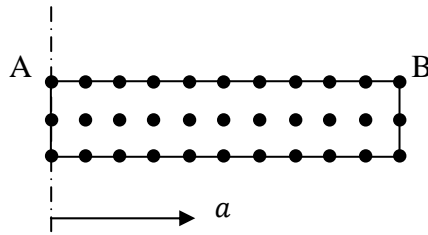


**Figure 7.16** The PIM model of simply supported circular plate.

In the third case study, the simply supported circular plate, shown in Figure 7.15, is analyzed. The plate is modeled by 33 nodes as illustrated in Figure 7.16. The material properties are as follows:  $E = 105$  GPa and  $\nu = 0.24$ . In the cantilever beam, 63 nodes are used to represent the cantilever beam geometry. The integration is done using 20 background cells. The size of the support domains are  $1.0 \text{ cm} \times 1.0 \text{ cm}$ . 6 – 9 nodes are used for interpolation in a local domain. The deflection profile of problem is shown in Figure 7.17. The displacement values are computed using different support domain sizes. They are shown in Table 7.4.

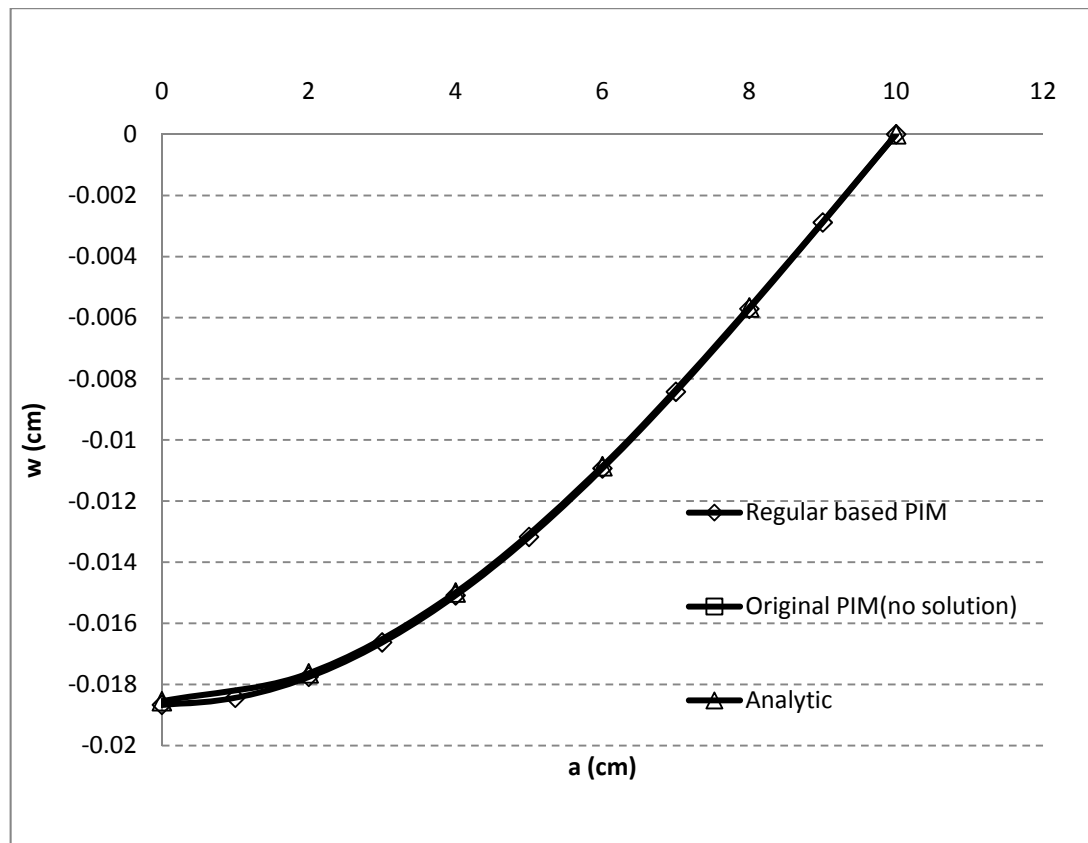


**Figure 7.17** The deflection profile of simply supported circular plate.



**Table 7.4** The deflection profile of simply supported circular plate for different domain sizes. (Original PIM has singularity problem. Only PIM with regular based results listed.)

		Domain Size 1.0x1.0 (6-9 nodes)		Domain Size 2.0x1.0 (9-15 nodes)		Domain Size 3.0x1.0 (12-21 nodes)	
Node Coordinate		Regular basis PIM		Regular basis PIM		Regular basis PIM	
R	Z	Ur	Uz	Ur	Uz	Ur	Uz
0.00	0	1.39E-07	-1.78E-04	-2.22E-09	-1.87E-04	-1.06E-09	-1.87E-04
0.01	0	2.75E-06	-1.74E-04	2.30E-06	-1.84E-04	2.30E-06	-1.84E-04
0.02	0	4.85E-06	-1.66E-04	4.53E-06	-1.77E-04	4.53E-06	-1.78E-04
0.03	0	6.72E-06	-1.55E-04	6.66E-06	-1.66E-04	6.66E-06	-1.66E-04
0.04	0	8.39E-06	-1.39E-04	8.63E-06	-1.51E-04	8.62E-06	-1.51E-04
0.05	0	9.83E-06	-1.21E-04	1.04E-05	-1.32E-04	1.04E-05	-1.32E-04
0.06	0	1.10E-05	-9.99E-05	1.19E-05	-1.09E-04	1.19E-05	-1.09E-04
0.07	0	1.20E-05	-7.67E-05	1.30E-05	-8.41E-05	1.30E-05	-8.42E-05
0.08	0	1.26E-05	-5.19E-05	1.39E-05	-5.70E-05	1.39E-05	-5.71E-05
0.09	0	1.29E-05	-2.62E-05	1.42E-05	-2.88E-05	1.42E-05	-2.89E-05
0.10	0	1.30E-05	-2.99E-17	1.42E-05	-2.17E-17	1.42E-05	-1.87E-17
0.00	0.5	1.57E-12	-1.78E-04	1.07E-09	-1.87E-04	8.45E-10	-1.87E-04
0.01	0.5	4.06E-09	-1.74E-04	4.90E-09	-1.85E-04	4.88E-09	-1.85E-04
0.02	0.5	8.11E-09	-1.67E-04	8.19E-09	-1.78E-04	8.25E-09	-1.78E-04
0.03	0.5	1.22E-08	-1.55E-04	1.25E-08	-1.67E-04	1.23E-08	-1.67E-04
0.04	0.5	1.62E-08	-1.40E-04	1.66E-08	-1.51E-04	1.70E-08	-1.51E-04
0.05	0.5	2.03E-08	-1.21E-04	2.04E-08	-1.32E-04	1.95E-08	-1.32E-04
0.06	0.5	2.44E-08	-1.00E-04	2.58E-08	-1.10E-04	2.71E-08	-1.10E-04
0.07	0.5	2.78E-08	-7.69E-05	2.61E-08	-8.44E-05	2.38E-08	-8.45E-05
0.08	0.5	3.52E-08	-5.21E-05	3.96E-08	-5.72E-05	4.18E-08	-5.73E-05
0.09	0.5	2.78E-08	-2.63E-05	2.38E-08	-2.89E-05	2.45E-08	-2.90E-05
0.10	0.5	4.82E-08	-2.39E-07	3.98E-08	-2.87E-07	3.13E-08	-3.26E-07
0.00	1	1.39E-07	-1.78E-04	2.82E-10	-1.87E-04	-9.41E-10	-1.87E-04
0.01	1	2.74E-06	-1.74E-04	-2.29E-06	-1.84E-04	-2.29E-06	-1.84E-04
0.02	1	4.84E-06	-1.66E-04	-4.51E-06	-1.77E-04	-4.51E-06	-1.78E-04
0.03	1	6.70E-06	-1.55E-04	-6.63E-06	-1.66E-04	-6.63E-06	-1.66E-04
0.04	1	8.35E-06	-1.39E-04	-8.59E-06	-1.51E-04	-8.59E-06	-1.51E-04
0.05	1	9.79E-06	-1.21E-04	-1.03E-05	-1.32E-04	-1.03E-05	-1.32E-04
0.06	1	1.10E-05	-9.99E-05	-1.18E-05	-1.09E-04	-1.18E-05	-1.09E-04
0.07	1	1.19E-05	-7.67E-05	-1.30E-05	-8.42E-05	-1.30E-05	-8.43E-05
0.08	1	1.26E-05	-5.20E-05	-1.38E-05	-5.71E-05	-1.38E-05	-5.72E-05
0.09	1	1.29E-05	-2.62E-05	-1.41E-05	-2.87E-05	-1.41E-05	-2.88E-05
0.10	1	1.28E-05	-2.03E-07	-1.40E-05	-2.75E-07	-1.40E-05	-3.38E-07

## 7.5 Results and Discussions

The regular basis PIM algorithm is proposed to define a rule for the selection of basis function terms. It is a simple and practical algorithm. It can be easily implemented in the PIM solutions, only the polynomial terms are changed in PIM solution procedure. It is stable and accurate even for small local domains. And also it eliminates the singularity problem without requiring extra any operations. However, it has a major drawback that it does not work for other than a regular node configuration in a local domain. The reason of this can be the requirement of completeness. The regular basis algorithm is far away to satisfy completeness for irregular node configurations. **But the results of case studies show that the PIM with regular basis algorithm gives excellent results for regular distributed nodes.** Therefore, the original PIM can be improved using proposed algorithm for the regular distributed nodes.

## CHAPTER 8

### CONCLUSIONS

The original PIM method is improved using two different algorithms. The diagonal offset method is a simple and practical method and makes the moment matrix invertible. Regular basis algorithm is used for appropriate selection of polynomial terms and it gives excellent results for regularly distributed nodes.

It has been shown that the diagonal offset algorithm overcomes the singular moment matrix problem in the polynomial PIM. It has significant advantages over the other singularity elimination algorithms

- eliminates the extra calculations,
- simple and practical algorithm,
- doesn't decrease the computation efficiency of the PIM,
- preserves accuracy of the PIM.

It is shown that PIM with the proposed algorithm gives nearly same results with the exact results for  $4 \leq k \leq 7$ . The solutions deviate from exact results for  $k < 4$  and  $k > 7$ .

The proposed regular basis algorithm is stable and accurate even for small local domains. And it also eliminates the singularity problem without requiring extra any operations. However, it has a major drawback that it does not work for other than a regular node configuration in a local domain. **But the results of case studies show that the PIM with regular basis algorithm gives excellent results for regularly distributed nodes.** Therefore, the original PIM can be improved using proposed algorithm for the regularly distributed nodes.

The RPIM method is also used for the solution of 2D elasticity problems. The effect of radial basis shape parameters are investigated in the solution of geometrically nonlinear and elasto-plastic problems.

It is observed that the node distribution characteristics is more effective than the shape parameters in the displacement and stress solutions. It is also shown that RPIM shape parameters usually affect the stresses more than displacements. The values of shape parameters are generally problem dependent. However, more stable results are obtained with shape parameters,  $q=1.03$  and  $\alpha_c=3$  and  $m=3$ .

It is also shown that when the same increase in the number of nodes is considered, improvements in the RPIM results are better than FEM with suggested values of shape parameters.

## **FUTURE WORKS**

The application of PIM to geometric nonlinear problems and elasto-plastic problems are planned. Also, the implementation of Moving-Least Square methods to these problems can be studied.

## APPENDIX

### A SAMPLE SOLUTION OF 2D GEOMETRICALLY NONLINEAR PROBLEMS USING RPIM

Taking large displacements into consideration, deflections and stresses in the axially loaded thin plate, shown in Figure A.1, are solved using RPIM. The material parameters are considered as  $E = 1000$ ,  $\nu = 0.25$  and thickness is  $h = 0.1$ . For simplicity, 4 nodes and single background cell are used. Load is applied in one step and the computations for the first two iterations are given.

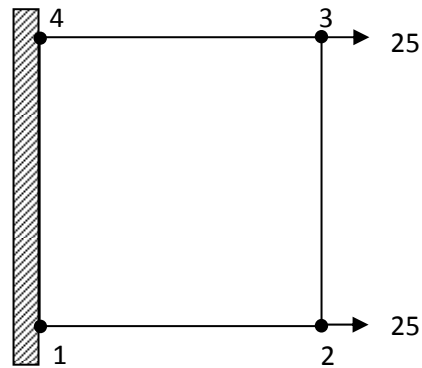


**Figure A.1** Thin plate

The coordinates of field nodes and background points are as follows:

Field Node	X-coordinate	Y-coordinate
1	0	0
2	1	0
3	1	1
4	0	1

Background Point	X-coordinate	Y-coordinate
1	0	0
2	1	0
3	1	1
4	0	1

Specified nodal loads:

Node	DOF	Value
2	1	25
3	1	25

Gauss quadrature points and weights of the background cell:

		Point	Weight	Jacobian
1	X	0.211324870586	1	0.25
	Y	0.211324870586		
2	X	0.788675129414	1	0.25
	Y	0.211324870586		
3	X	0.211324870586	1	0.25
	Y	0.788675129414		
4	X	0.788675129414	1	0.25
	Y	0.788675129414		

E=1000	$\nu=0.25$	Initial thickness=0.1	Plane stress analysis
--------	------------	-----------------------	-----------------------

Lame's constants:

$$\lambda = \frac{E\nu}{(1+\nu)(1-2\nu)} = 400$$

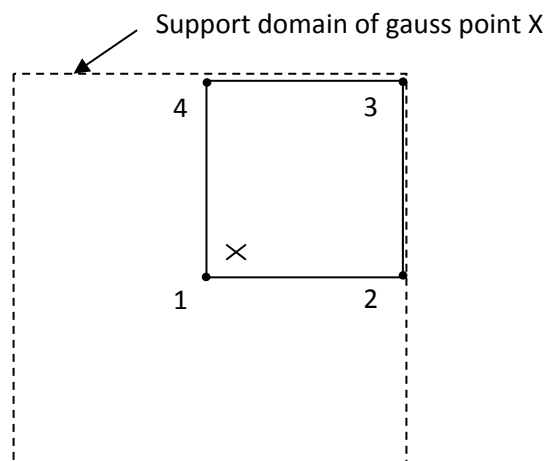
$$\mu = \frac{E}{2(1+\nu)} = 400$$

$$\gamma = \frac{2\mu}{(\lambda + 2\mu)} = 0.6667$$

Computation for stiffness matrix of support domain at  
 $\{ 0.211324870586, 0.211324870586 \}$  with *weight* = 1;

Dimensions of the support domain:

$$d_x = 1 \text{ and } d_y = 1;$$



Nodes of support domain are; *node 1, node 2, node 3* and *node 4*.

Interpolation functions and their derivatives:

$$\Phi(\mathbf{x}) = [\phi_1, \phi_2, \phi_3, \phi_4]$$

Node	1	2	3	4
$\phi$	0.622825041123	0.165850088290	4.547478229618E-02	0.165850088290
$\frac{\partial \phi}{\partial x}$	-0.790075558664	0.790075558664	0.209924441336	-0.209924441336
$\frac{\partial \phi}{\partial y}$	-0.790075558664	-0.209924441336	0.209924441336	0.790075558664

Deformation gradient is calculated using the Equation 4.1

$$F_{ij} = \sum_{I=1}^{NP} \left[ \frac{\partial \Phi_I}{\partial x_j} d_{iI} \right] + \delta_{ij}$$

where  $NP = 4$  and the displacement vector

$$\mathbf{d} = [0 \ 0 \ 0 \ 0 \ 0 \ 0 \ 0 \ 0]$$

Deformation gradient,  $F = \begin{bmatrix} 1 & 0 \\ 0 & 1 \end{bmatrix}$ ;

and arranged deformation gradient (Equation 4.16);

$$\bar{\mathbf{F}} = \begin{bmatrix} 1 & 0 & 0 & 0 \\ 0 & 0 & 0 & 1 \\ 0 & 1 & 1 & 0 \end{bmatrix}$$

Right Cauchy-Green tensor,  $c_1 = \begin{bmatrix} 1 & 0 \\ 0 & 1 \end{bmatrix}$

Left Cauchy-Green tensor,  $c_2 = \begin{bmatrix} 1 & 0 \\ 0 & 1 \end{bmatrix}$

Second PK stresses,  $\hat{\mathbf{S}} = \begin{bmatrix} 0 & 0 \\ 0 & 0 \end{bmatrix}$

Initial stress matrix,  $\bar{\mathbf{S}} = \begin{bmatrix} 0 & 0 & 0 & 0 \\ 0 & 0 & 0 & 0 \\ 0 & 0 & 0 & 0 \\ 0 & 0 & 0 & 0 \end{bmatrix}$

The matrix for derivatives of shape functions of support domain,

$$\mathbf{B}_1^T = \begin{bmatrix} -0.790075558664 & -0.790075558664 & 0 & 0 \\ 0 & 0 & -0.790075558664 & -0.790075558664 \end{bmatrix}$$

Internal force vector,  $\mathbf{r}_1 = [0 \ 0]$

The matrix for derivatives of shape functions of support domain,



$$\mathbf{B}_1^T = \begin{bmatrix} -0.790075558664 & -0.790075558664 & 0 & 0 \\ 0 & 0 & -0.790075558664 & -0.790075558664 \end{bmatrix}$$

$$\text{Material matrix, } \mathbf{D} = \begin{bmatrix} 1200 & 400 & 0 \\ 400 & 1200 & 0 \\ 0 & 0 & 400 \end{bmatrix}$$

$$\text{Current stiffness matrix, } \mathbf{k}_c = \begin{bmatrix} 24.96 & 12.48 \\ 12.48 & 24.96 \end{bmatrix}$$

$$\text{Geometric stiffness matrix, } \mathbf{k}_s = \begin{bmatrix} 0 & 0 \\ 0 & 0 \end{bmatrix}$$

Assembled current stiffness matrix,

$$\mathbf{K}_c = \begin{bmatrix} 24.96 & 12.48 & 0 & 0 & 0 & 0 & 0 & 0 \\ 12.48 & 24.96 & 0 & 0 & 0 & 0 & 0 & 0 \\ 0 & 0 & 0 & 0 & 0 & 0 & 0 & 0 \\ 0 & 0 & 0 & 0 & 0 & 0 & 0 & 0 \\ 0 & 0 & 0 & 0 & 0 & 0 & 0 & 0 \\ 0 & 0 & 0 & 0 & 0 & 0 & 0 & 0 \\ 0 & 0 & 0 & 0 & 0 & 0 & 0 & 0 \\ 0 & 0 & 0 & 0 & 0 & 0 & 0 & 0 \end{bmatrix}$$

Assembled geometric stiffness matrix,

$$\mathbf{K}_s = \begin{bmatrix} 0 & 0 & 0 & 0 & 0 & 0 & 0 & 0 \\ 0 & 0 & 0 & 0 & 0 & 0 & 0 & 0 \\ 0 & 0 & 0 & 0 & 0 & 0 & 0 & 0 \\ 0 & 0 & 0 & 0 & 0 & 0 & 0 & 0 \\ 0 & 0 & 0 & 0 & 0 & 0 & 0 & 0 \\ 0 & 0 & 0 & 0 & 0 & 0 & 0 & 0 \\ 0 & 0 & 0 & 0 & 0 & 0 & 0 & 0 \\ 0 & 0 & 0 & 0 & 0 & 0 & 0 & 0 \end{bmatrix}$$

The matrix for derivatives of shape functions of support domain,

$$\mathbf{B}_2^T = \begin{bmatrix} 0.790075558664 & -0.209924441336 & 0 & 0 \\ 0 & 0 & 0.790075558664 & -0.209924441336 \end{bmatrix}$$

$$\text{Current stiffness matrix, } \mathbf{k}_c = \begin{bmatrix} -17.06 & -4.58 \\ -4.58 & -1.26 \end{bmatrix}$$

$$\text{Geometric stiffness matrix, } \mathbf{k}_s = \begin{bmatrix} 0 & 0 \\ 0 & 0 \end{bmatrix}$$

Assembled current stiffness matrix,

$$\mathbf{K}_c = \begin{bmatrix} 24.96 & 12.48 & -17.06 & -4.58 & 0 & 0 & 0 & 0 \\ 12.48 & 24.96 & -4.58 & -1.26 & 0 & 0 & 0 & 0 \\ 0 & 0 & 0 & 0 & 0 & 0 & 0 & 0 \\ 0 & 0 & 0 & 0 & 0 & 0 & 0 & 0 \\ 0 & 0 & 0 & 0 & 0 & 0 & 0 & 0 \\ 0 & 0 & 0 & 0 & 0 & 0 & 0 & 0 \\ 0 & 0 & 0 & 0 & 0 & 0 & 0 & 0 \\ 0 & 0 & 0 & 0 & 0 & 0 & 0 & 0 \end{bmatrix}$$

Assembled geometric stiffness matrix,  $\mathbf{K}_s =$

$$\begin{bmatrix} 0 & 0 & 0 & 0 & 0 & 0 & 0 & 0 \\ 0 & 0 & 0 & 0 & 0 & 0 & 0 & 0 \\ 0 & 0 & 0 & 0 & 0 & 0 & 0 & 0 \\ 0 & 0 & 0 & 0 & 0 & 0 & 0 & 0 \\ 0 & 0 & 0 & 0 & 0 & 0 & 0 & 0 \\ 0 & 0 & 0 & 0 & 0 & 0 & 0 & 0 \\ 0 & 0 & 0 & 0 & 0 & 0 & 0 & 0 \\ 0 & 0 & 0 & 0 & 0 & 0 & 0 & 0 \end{bmatrix}$$

The matrix for derivatives of shape functions of support domain,

$$\mathbf{B}_3^T = \begin{bmatrix} 0.209924441336 & 0.209924441336 & 0 & 0 \\ 0 & 0 & 0.209924441336 & 0.209924441336 \end{bmatrix}$$

Current stiffness matrix,  $\mathbf{k}_c = \begin{bmatrix} -6.63 & -3.31 \\ -3.31 & -6.63 \end{bmatrix}$

Geometric stiffness matrix,  $\mathbf{k}_s = \begin{bmatrix} 0 & 0 \\ 0 & 0 \end{bmatrix}$

Assembled current stiffness matrix,

$$\mathbf{K}_c = \begin{bmatrix} 24.96 & 12.48 & -17.06 & -4.58 & -6.63 & -3.31 & 0 & 0 \\ 12.48 & 24.96 & -4.58 & -1.26 & -3.31 & -6.63 & 0 & 0 \\ 0 & 0 & 0 & 0 & 0 & 0 & 0 & 0 \\ 0 & 0 & 0 & 0 & 0 & 0 & 0 & 0 \\ 0 & 0 & 0 & 0 & 0 & 0 & 0 & 0 \\ 0 & 0 & 0 & 0 & 0 & 0 & 0 & 0 \\ 0 & 0 & 0 & 0 & 0 & 0 & 0 & 0 \\ 0 & 0 & 0 & 0 & 0 & 0 & 0 & 0 \end{bmatrix}$$

Assembled geometric stiffness matrix,  $\mathbf{K}_s =$

$$\begin{bmatrix} 0 & 0 & 0 & 0 & 0 & 0 & 0 & 0 \\ 0 & 0 & 0 & 0 & 0 & 0 & 0 & 0 \\ 0 & 0 & 0 & 0 & 0 & 0 & 0 & 0 \\ 0 & 0 & 0 & 0 & 0 & 0 & 0 & 0 \\ 0 & 0 & 0 & 0 & 0 & 0 & 0 & 0 \\ 0 & 0 & 0 & 0 & 0 & 0 & 0 & 0 \\ 0 & 0 & 0 & 0 & 0 & 0 & 0 & 0 \\ 0 & 0 & 0 & 0 & 0 & 0 & 0 & 0 \end{bmatrix}$$

The matrix for derivatives of shape functions of support domain,

$$\mathbf{B}_4^T = \begin{bmatrix} -0.209924441336 & 0.790075558664 & 0 & 0 \\ 0 & 0 & -0.209924441336 & 0.790075558664 \end{bmatrix}$$

Current stiffness matrix,  $\mathbf{k}_c = \begin{bmatrix} -1.26 & -4.58 \\ -4.58 & -17.06 \end{bmatrix}$

Geometric stiffness matrix,  $\mathbf{k}_s = \begin{bmatrix} 0 & 0 \\ 0 & 0 \end{bmatrix}$

Assembled current stiffness matrix,

$$\mathbf{K}_c = \begin{bmatrix} 24.96 & 12.48 & -17.06 & -4.58 & -6.63 & -3.31 & -1.26 & -4.58 \\ 12.48 & 24.96 & -4.58 & -1.26 & -3.31 & -6.63 & -4.58 & -17.06 \\ 0 & 0 & 0 & 0 & 0 & 0 & 0 & 0 \\ 0 & 0 & 0 & 0 & 0 & 0 & 0 & 0 \\ 0 & 0 & 0 & 0 & 0 & 0 & 0 & 0 \\ 0 & 0 & 0 & 0 & 0 & 0 & 0 & 0 \\ 0 & 0 & 0 & 0 & 0 & 0 & 0 & 0 \\ 0 & 0 & 0 & 0 & 0 & 0 & 0 & 0 \end{bmatrix}$$

$$\text{Assembled geometric stiffness matrix, } \mathbf{K}_s = \begin{bmatrix} 0 & 0 & 0 & 0 & 0 & 0 & 0 & 0 \\ 0 & 0 & 0 & 0 & 0 & 0 & 0 & 0 \\ 0 & 0 & 0 & 0 & 0 & 0 & 0 & 0 \\ 0 & 0 & 0 & 0 & 0 & 0 & 0 & 0 \\ 0 & 0 & 0 & 0 & 0 & 0 & 0 & 0 \\ 0 & 0 & 0 & 0 & 0 & 0 & 0 & 0 \\ 0 & 0 & 0 & 0 & 0 & 0 & 0 & 0 \\ 0 & 0 & 0 & 0 & 0 & 0 & 0 & 0 \end{bmatrix}$$

The matrix for derivatives of shape functions of support domain,

$$\mathbf{B}_2^T = \begin{bmatrix} 0.790075558664 & -0.209924441336 & 0 & 0 \\ 0 & 0 & 0.790075558664 & -0.209924441336 \end{bmatrix}$$

Internal force vector,  $\mathbf{r}_2 = [0 \ 0]$

The matrix for derivatives of shape functions of support domain,

$$\mathbf{B}_1^T = \begin{bmatrix} -0.790075558664 & -0.790075558664 & 0 & 0 \\ 0 & 0 & -0.790075558664 & -0.790075558664 \end{bmatrix}$$

$$\text{Material matrix, } \mathbf{D} = \begin{bmatrix} 1200 & 400 & 0 \\ 400 & 1200 & 0 \\ 0 & 0 & 400 \end{bmatrix}$$

$$\text{Current stiffness matrix, } \mathbf{k}_c = \begin{bmatrix} -17.06 & -4.58 \\ -4.58 & -1.26 \end{bmatrix}$$

$$\text{Geometric stiffness matrix, } \mathbf{k}_s = \begin{bmatrix} 0 & 0 \\ 0 & 0 \end{bmatrix}$$

Assembled current stiffness matrix,

$$\mathbf{K}_c = \begin{bmatrix} 24.96 & 12.48 & -17.06 & -4.58 & -6.63 & -3.31 & -1.26 & -4.58 \\ 12.48 & 24.96 & -4.58 & -1.26 & -3.31 & -6.63 & -4.58 & -17.06 \\ -17.06 & -4.58 & 0 & 0 & 0 & 0 & 0 & 0 \\ -4.58 & -1.26 & 0 & 0 & 0 & 0 & 0 & 0 \\ 0 & 0 & 0 & 0 & 0 & 0 & 0 & 0 \\ 0 & 0 & 0 & 0 & 0 & 0 & 0 & 0 \\ 0 & 0 & 0 & 0 & 0 & 0 & 0 & 0 \\ 0 & 0 & 0 & 0 & 0 & 0 & 0 & 0 \end{bmatrix}$$

Assembled geometric stiffness matrix,  $\mathbf{K}_s =$

$$\begin{bmatrix} 0 & 0 & 0 & 0 & 0 & 0 & 0 & 0 \\ 0 & 0 & 0 & 0 & 0 & 0 & 0 & 0 \\ 0 & 0 & 0 & 0 & 0 & 0 & 0 & 0 \\ 0 & 0 & 0 & 0 & 0 & 0 & 0 & 0 \\ 0 & 0 & 0 & 0 & 0 & 0 & 0 & 0 \\ 0 & 0 & 0 & 0 & 0 & 0 & 0 & 0 \\ 0 & 0 & 0 & 0 & 0 & 0 & 0 & 0 \\ 0 & 0 & 0 & 0 & 0 & 0 & 0 & 0 \end{bmatrix}$$

The matrix for derivatives of shape functions of support domain,

$$\mathbf{B}_2^T = \begin{bmatrix} 0.790075558664 & -0.209924441336 & 0 & 0 \\ 0 & 0 & 0.790075558664 & -0.209924441336 \end{bmatrix}$$

Current stiffness matrix,  $\mathbf{k}_c = \begin{bmatrix} 19.16 & -3.31 \\ -3.31 & 7.56 \end{bmatrix}$

Geometric stiffness matrix,  $\mathbf{k}_s = \begin{bmatrix} 0 & 0 \\ 0 & 0 \end{bmatrix}$

Assembled current stiffness matrix,

$$\mathbf{K}_c = \begin{bmatrix} 24.96 & 12.48 & -17.06 & -4.58 & -6.63 & -3.31 & -1.26 & -4.58 \\ 12.48 & 24.96 & -4.58 & -1.26 & -3.31 & -6.63 & -4.58 & -17.06 \\ -17.06 & -4.58 & 19.16 & -3.31 & 0 & 0 & 0 & 0 \\ -4.58 & -1.26 & -3.31 & 7.56 & 0 & 0 & 0 & 0 \\ 0 & 0 & 0 & 0 & 0 & 0 & 0 & 0 \\ 0 & 0 & 0 & 0 & 0 & 0 & 0 & 0 \\ 0 & 0 & 0 & 0 & 0 & 0 & 0 & 0 \\ 0 & 0 & 0 & 0 & 0 & 0 & 0 & 0 \end{bmatrix}$$

Assembled geometric stiffness matrix,  $\mathbf{K}_s =$

$$\begin{bmatrix} 0 & 0 & 0 & 0 & 0 & 0 & 0 & 0 \\ 0 & 0 & 0 & 0 & 0 & 0 & 0 & 0 \\ 0 & 0 & 0 & 0 & 0 & 0 & 0 & 0 \\ 0 & 0 & 0 & 0 & 0 & 0 & 0 & 0 \\ 0 & 0 & 0 & 0 & 0 & 0 & 0 & 0 \\ 0 & 0 & 0 & 0 & 0 & 0 & 0 & 0 \\ 0 & 0 & 0 & 0 & 0 & 0 & 0 & 0 \\ 0 & 0 & 0 & 0 & 0 & 0 & 0 & 0 \end{bmatrix}$$

The matrix for derivatives of shape functions of support domain,

$$\mathbf{B}_3^T = \begin{bmatrix} 0.209924441336 & 0.209924441336 & 0 & 0 \\ 0 & 0 & 0.209924441336 & 0.209924441336 \end{bmatrix}$$

Current stiffness matrix,  $\mathbf{k}_c = \begin{bmatrix} 4.53 & 1.21 \\ 1.21 & 0.33 \end{bmatrix}$

Geometric stiffness matrix,  $\mathbf{k}_s = \begin{bmatrix} 0 & 0 \\ 0 & 0 \end{bmatrix}$

Assembled current stiffness matrix,

$$\mathbf{K}_c = \begin{bmatrix} 24.96 & 12.48 & -17.06 & -4.58 & -6.63 & -3.31 & -1.26 & -4.58 \\ 12.48 & 24.96 & -4.58 & -1.26 & -3.31 & -6.63 & -4.58 & -17.06 \\ -17.06 & -4.58 & 19.16 & -3.31 & 4.53 & 1.21 & 0 & 0 \\ -4.58 & -1.26 & -3.31 & 7.56 & 1.21 & 0.33 & 0 & 0 \\ 0 & 0 & 0 & 0 & 0 & 0 & 0 & 0 \\ 0 & 0 & 0 & 0 & 0 & 0 & 0 & 0 \\ 0 & 0 & 0 & 0 & 0 & 0 & 0 & 0 \\ 0 & 0 & 0 & 0 & 0 & 0 & 0 & 0 \end{bmatrix}$$

$$\text{Assembled geometric stiffness matrix, } \mathbf{K}_s = \begin{bmatrix} 0 & 0 & 0 & 0 & 0 & 0 & 0 & 0 \\ 0 & 0 & 0 & 0 & 0 & 0 & 0 & 0 \\ 0 & 0 & 0 & 0 & 0 & 0 & 0 & 0 \\ 0 & 0 & 0 & 0 & 0 & 0 & 0 & 0 \\ 0 & 0 & 0 & 0 & 0 & 0 & 0 & 0 \\ 0 & 0 & 0 & 0 & 0 & 0 & 0 & 0 \\ 0 & 0 & 0 & 0 & 0 & 0 & 0 & 0 \\ 0 & 0 & 0 & 0 & 0 & 0 & 0 & 0 \end{bmatrix}$$

The matrix for derivatives of shape functions of support domain,

$$\mathbf{B}_4^T = \begin{bmatrix} -0.209924441336 & 0.790075558664 & 0 & 0 \\ 0 & 0 & -0.209924441336 & 0.790075558664 \end{bmatrix}$$

$$\text{Current stiffness matrix, } \mathbf{k}_c = \begin{bmatrix} -6.63 & 6.68 \\ 6.68 & -6.63 \end{bmatrix}$$

$$\text{Geometric stiffness matrix, } \mathbf{k}_s = \begin{bmatrix} 0 & 0 \\ 0 & 0 \end{bmatrix}$$

Assembled current stiffness matrix,

$$\mathbf{K}_c = \begin{bmatrix} 24.96 & 12.48 & -17.06 & -4.58 & -6.63 & -3.31 & -1.26 & -4.58 \\ 12.48 & 24.96 & -4.58 & -1.26 & -3.31 & -6.63 & -4.58 & -17.06 \\ -17.06 & -4.58 & 19.16 & -3.31 & 4.53 & 1.21 & -6.63 & 6.68 \\ -4.58 & -1.26 & -3.31 & 7.56 & 1.21 & 0.33 & 6.68 & -6.63 \\ 0 & 0 & 0 & 0 & 0 & 0 & 0 & 0 \\ 0 & 0 & 0 & 0 & 0 & 0 & 0 & 0 \\ 0 & 0 & 0 & 0 & 0 & 0 & 0 & 0 \\ 0 & 0 & 0 & 0 & 0 & 0 & 0 & 0 \end{bmatrix}$$

$$\text{Assembled geometric stiffness matrix, } \mathbf{K}_s = \begin{bmatrix} 0 & 0 & 0 & 0 & 0 & 0 & 0 & 0 \\ 0 & 0 & 0 & 0 & 0 & 0 & 0 & 0 \\ 0 & 0 & 0 & 0 & 0 & 0 & 0 & 0 \\ 0 & 0 & 0 & 0 & 0 & 0 & 0 & 0 \\ 0 & 0 & 0 & 0 & 0 & 0 & 0 & 0 \\ 0 & 0 & 0 & 0 & 0 & 0 & 0 & 0 \\ 0 & 0 & 0 & 0 & 0 & 0 & 0 & 0 \\ 0 & 0 & 0 & 0 & 0 & 0 & 0 & 0 \end{bmatrix}$$

The matrix for derivatives of shape functions of support domain,

$$\mathbf{B}_3^T = \begin{bmatrix} 0.209924441336 & 0.209924441336 & 0 & 0 \\ 0 & 0 & 0.209924441336 & 0.209924441336 \end{bmatrix}$$

Internal force vector,  $\mathbf{r}_3 = [0 \ 0]$

The matrix for derivatives of shape functions of support domain,

$$\mathbf{B}_1^T = \begin{bmatrix} -0.790075558664 & -0.790075558664 & 0 & 0 \\ 0 & 0 & -0.790075558664 & -0.790075558664 \end{bmatrix}$$

$$\text{Material matrix, } \mathbf{D} = \begin{bmatrix} 1200 & 400 & 0 \\ 400 & 1200 & 0 \\ 0 & 0 & 400 \end{bmatrix}$$

$$\text{Current stiffness matrix, } \mathbf{k}_c = \begin{bmatrix} -6.63 & -3.31 \\ -3.31 & -6.63 \end{bmatrix}$$

$$\text{Geometric stiffness matrix, } \mathbf{k}_s = \begin{bmatrix} 0 & 0 \\ 0 & 0 \end{bmatrix}$$

Assembled current stiffness matrix,

$$\mathbf{K}_c = \begin{bmatrix} 24.96 & 12.48 & -17.06 & -4.58 & -6.63 & -3.31 & -1.26 & -4.58 \\ 12.48 & 24.96 & -4.58 & -1.26 & -3.31 & -6.63 & -4.58 & -17.06 \\ -17.06 & -4.58 & 19.16 & -3.31 & 4.53 & 1.21 & -6.63 & 6.68 \\ -4.58 & -1.26 & -3.31 & 7.56 & 1.21 & 0.33 & 6.68 & -6.63 \\ -6.63 & -3.31 & 0 & 0 & 0 & 0 & 0 & 0 \\ -3.31 & -6.63 & 0 & 0 & 0 & 0 & 0 & 0 \\ 0 & 0 & 0 & 0 & 0 & 0 & 0 & 0 \\ 0 & 0 & 0 & 0 & 0 & 0 & 0 & 0 \end{bmatrix}$$

$$\text{Assembled geometric stiffness matrix, } \mathbf{K}_s = \begin{bmatrix} 0 & 0 & 0 & 0 & 0 & 0 & 0 & 0 \\ 0 & 0 & 0 & 0 & 0 & 0 & 0 & 0 \\ 0 & 0 & 0 & 0 & 0 & 0 & 0 & 0 \\ 0 & 0 & 0 & 0 & 0 & 0 & 0 & 0 \\ 0 & 0 & 0 & 0 & 0 & 0 & 0 & 0 \\ 0 & 0 & 0 & 0 & 0 & 0 & 0 & 0 \\ 0 & 0 & 0 & 0 & 0 & 0 & 0 & 0 \\ 0 & 0 & 0 & 0 & 0 & 0 & 0 & 0 \end{bmatrix}$$

The matrix for derivatives of shape functions of support domain,

$$\mathbf{B}_2^T = \begin{bmatrix} 0.790075558664 & -0.209924441336 & 0 & 0 \\ 0 & 0 & 0.790075558664 & -0.209924441336 \end{bmatrix}$$

$$\text{Current stiffness matrix, } \mathbf{k}_c = \begin{bmatrix} 4.53 & 1.21 \\ 1.21 & 0.33 \end{bmatrix}$$

$$\text{Geometric stiffness matrix, } \mathbf{k}_s = \begin{bmatrix} 0 & 0 \\ 0 & 0 \end{bmatrix}$$

Assembled current stiffness matrix,

$$\mathbf{K}_c = \begin{bmatrix} 24.96 & 12.48 & -17.06 & -4.58 & -6.63 & -3.31 & -1.26 & -4.58 \\ 12.48 & 24.96 & -4.58 & -1.26 & -3.31 & -6.63 & -4.58 & -17.06 \\ -17.06 & -4.58 & 19.16 & -3.31 & 4.53 & 1.21 & -6.63 & 6.68 \\ -4.58 & -1.26 & -3.31 & 7.56 & 1.21 & 0.33 & 6.68 & -6.63 \\ -6.63 & -3.31 & 4.53 & 1.21 & 0 & 0 & 0 & 0 \\ -3.31 & -6.63 & 1.21 & 0.33 & 0 & 0 & 0 & 0 \\ 0 & 0 & 0 & 0 & 0 & 0 & 0 & 0 \\ 0 & 0 & 0 & 0 & 0 & 0 & 0 & 0 \end{bmatrix}$$

$$\text{Assembled geometric stiffness matrix, } \mathbf{K}_s = \begin{bmatrix} 0 & 0 & 0 & 0 & 0 & 0 & 0 & 0 \\ 0 & 0 & 0 & 0 & 0 & 0 & 0 & 0 \\ 0 & 0 & 0 & 0 & 0 & 0 & 0 & 0 \\ 0 & 0 & 0 & 0 & 0 & 0 & 0 & 0 \\ 0 & 0 & 0 & 0 & 0 & 0 & 0 & 0 \\ 0 & 0 & 0 & 0 & 0 & 0 & 0 & 0 \\ 0 & 0 & 0 & 0 & 0 & 0 & 0 & 0 \\ 0 & 0 & 0 & 0 & 0 & 0 & 0 & 0 \end{bmatrix}$$

The matrix for derivatives of shape functions of support domain,

$$\mathbf{B}_3^T = \begin{bmatrix} 0.209924441336 & 0.209924441336 & 0 & 0 \\ 0 & 0 & 0.209924441336 & 0.209924441336 \end{bmatrix}$$

$$\text{Current stiffness matrix, } \mathbf{k}_c = \begin{bmatrix} 1.76 & 0.88 \\ 0.88 & 1.76 \end{bmatrix}$$

$$\text{Geometric stiffness matrix, } \mathbf{k}_s = \begin{bmatrix} 0 & 0 \\ 0 & 0 \end{bmatrix}$$

Assembled current stiffness matrix,

$$\mathbf{K}_c = \begin{bmatrix} 24.96 & 12.48 & -17.06 & -4.58 & -6.63 & -3.31 & -1.26 & -4.58 \\ 12.48 & 24.96 & -4.58 & -1.26 & -3.31 & -6.63 & -4.58 & -17.06 \\ -17.06 & -4.58 & 19.16 & -3.31 & 4.53 & 1.21 & -6.63 & 6.68 \\ -4.58 & -1.26 & -3.31 & 7.56 & 1.21 & 0.33 & 6.68 & -6.63 \\ -6.63 & -3.31 & 4.53 & 1.21 & 1.76 & 0.88 & 0 & 0 \\ -3.31 & -6.63 & 1.21 & 0.33 & 0.88 & 1.76 & 0 & 0 \\ 0 & 0 & 0 & 0 & 0 & 0 & 0 & 0 \\ 0 & 0 & 0 & 0 & 0 & 0 & 0 & 0 \end{bmatrix}$$

$$\text{Assembled geometric stiffness matrix, } \mathbf{K}_s = \begin{bmatrix} 0 & 0 & 0 & 0 & 0 & 0 & 0 & 0 \\ 0 & 0 & 0 & 0 & 0 & 0 & 0 & 0 \\ 0 & 0 & 0 & 0 & 0 & 0 & 0 & 0 \\ 0 & 0 & 0 & 0 & 0 & 0 & 0 & 0 \\ 0 & 0 & 0 & 0 & 0 & 0 & 0 & 0 \\ 0 & 0 & 0 & 0 & 0 & 0 & 0 & 0 \\ 0 & 0 & 0 & 0 & 0 & 0 & 0 & 0 \\ 0 & 0 & 0 & 0 & 0 & 0 & 0 & 0 \end{bmatrix}$$

The matrix for derivatives of shape functions of support domain,

$$\mathbf{B}_4^T = \begin{bmatrix} -0.209924441336 & 0.790075558664 & 0 & 0 \\ 0 & 0 & -0.209924441336 & 0.790075558664 \end{bmatrix}$$

Current stiffness matrix,  $\mathbf{k}_c = \begin{bmatrix} 0.33 & 1.21 \\ 1.21 & 4.53 \end{bmatrix}$

Geometric stiffness matrix,  $\mathbf{k}_s = \begin{bmatrix} 0 & 0 \\ 0 & 0 \end{bmatrix}$

Assembled current stiffness matrix,

$$\mathbf{K}_c = \begin{bmatrix} 24.96 & 12.48 & -17.06 & -4.58 & -6.63 & -3.31 & -1.26 & -4.58 \\ 12.48 & 24.96 & -4.58 & -1.26 & -3.31 & -6.63 & -4.58 & -17.06 \\ -17.06 & -4.58 & 19.16 & -3.31 & 4.53 & 1.21 & -6.63 & 6.68 \\ -4.58 & -1.26 & -3.31 & 7.56 & 1.21 & 0.33 & 6.68 & -6.63 \\ -6.63 & -3.31 & 4.53 & 1.21 & 1.76 & 0.88 & 0.33 & 1.21 \\ -3.31 & -6.63 & 1.21 & 0.33 & 0.88 & 1.76 & 1.21 & 4.53 \\ 0 & 0 & 0 & 0 & 0 & 0 & 0 & 0 \\ 0 & 0 & 0 & 0 & 0 & 0 & 0 & 0 \end{bmatrix}$$

Assembled geometric stiffness matrix,  $\mathbf{K}_s = \begin{bmatrix} 0 & 0 & 0 & 0 & 0 & 0 & 0 & 0 \\ 0 & 0 & 0 & 0 & 0 & 0 & 0 & 0 \\ 0 & 0 & 0 & 0 & 0 & 0 & 0 & 0 \\ 0 & 0 & 0 & 0 & 0 & 0 & 0 & 0 \\ 0 & 0 & 0 & 0 & 0 & 0 & 0 & 0 \\ 0 & 0 & 0 & 0 & 0 & 0 & 0 & 0 \\ 0 & 0 & 0 & 0 & 0 & 0 & 0 & 0 \\ 0 & 0 & 0 & 0 & 0 & 0 & 0 & 0 \end{bmatrix}$

The matrix for derivatives of shape functions of support domain,

$$\mathbf{B}_4^T = \begin{bmatrix} -0.209924441336 & 0.790075558664 & 0 & 0 \\ 0 & 0 & -0.209924441336 & 0.790075558664 \end{bmatrix}$$

Internal force vector,  $\mathbf{r}_4 = [0 \quad 0]$

The matrix for derivatives of shape functions of support domain,

$$\mathbf{B}_1^T = \begin{bmatrix} -0.790075558664 & -0.790075558664 & 0 & 0 \\ 0 & 0 & -0.790075558664 & -0.790075558664 \end{bmatrix}$$

Material matrix,  $\mathbf{D} = \begin{bmatrix} 1200 & 400 & 0 \\ 400 & 1200 & 0 \\ 0 & 0 & 400 \end{bmatrix}$

Current stiffness matrix,  $\mathbf{k}_c = \begin{bmatrix} -1.26 & -4.58 \\ -4.58 & -17.06 \end{bmatrix}$

Geometric stiffness matrix,  $\mathbf{k}_s = \begin{bmatrix} 0 & 0 \\ 0 & 0 \end{bmatrix}$

Assembled current stiffness matrix,



$$\mathbf{K}_c = \begin{bmatrix} 24.96 & 12.48 & -17.06 & -4.58 & -6.63 & -3.31 & -1.26 & -4.58 \\ 12.48 & 24.96 & -4.58 & -1.26 & -3.31 & -6.63 & -4.58 & -17.06 \\ -17.06 & -4.58 & 19.16 & -3.31 & 4.53 & 1.21 & -6.63 & 6.68 \\ -4.58 & -1.26 & -3.31 & 7.56 & 1.21 & 0.33 & 6.68 & -6.63 \\ -6.63 & -3.31 & 4.53 & 1.21 & 1.76 & 0.88 & 0.33 & 1.21 \\ -3.31 & -6.63 & 1.21 & 0.33 & 0.88 & 1.76 & 1.21 & 4.53 \\ -1.26 & -4.58 & 0 & 0 & 0 & 0 & 0 & 0 \\ -4.58 & -17.06 & 0 & 0 & 0 & 0 & 0 & 0 \end{bmatrix}$$

$$\text{Assembled geometric stiffness matrix, } \mathbf{K}_s = \begin{bmatrix} 0 & 0 & 0 & 0 & 0 & 0 & 0 & 0 \\ 0 & 0 & 0 & 0 & 0 & 0 & 0 & 0 \\ 0 & 0 & 0 & 0 & 0 & 0 & 0 & 0 \\ 0 & 0 & 0 & 0 & 0 & 0 & 0 & 0 \\ 0 & 0 & 0 & 0 & 0 & 0 & 0 & 0 \\ 0 & 0 & 0 & 0 & 0 & 0 & 0 & 0 \\ 0 & 0 & 0 & 0 & 0 & 0 & 0 & 0 \\ 0 & 0 & 0 & 0 & 0 & 0 & 0 & 0 \end{bmatrix}$$

The matrix for derivatives of shape functions of support domain,

$$\mathbf{B}_2^T = \begin{bmatrix} 0.790075558664 & -0.209924441336 & 0 & 0 \\ 0 & 0 & 0.790075558664 & -0.209924441336 \end{bmatrix}$$

$$\text{Current stiffness matrix, } \mathbf{k}_c = \begin{bmatrix} -6.63 & 6.68 \\ 6.68 & -6.63 \end{bmatrix}$$

$$\text{Geometric stiffness matrix, } \mathbf{k}_s = \begin{bmatrix} 0 & 0 \\ 0 & 0 \end{bmatrix}$$

Assembled current stiffness matrix,

$$\mathbf{K}_c = \begin{bmatrix} 24.96 & 12.48 & -17.06 & -4.58 & -6.63 & -3.31 & -1.26 & -4.58 \\ 12.48 & 24.96 & -4.58 & -1.26 & -3.31 & -6.63 & -4.58 & -17.06 \\ -17.06 & -4.58 & 19.16 & -3.31 & 4.53 & 1.21 & -6.63 & 6.68 \\ -4.58 & -1.26 & -3.31 & 7.56 & 1.21 & 0.33 & 6.68 & -6.63 \\ -6.63 & -3.31 & 4.53 & 1.21 & 1.76 & 0.88 & 0.33 & 1.21 \\ -3.31 & -6.63 & 1.21 & 0.33 & 0.88 & 1.76 & 1.21 & 4.53 \\ -1.26 & -4.58 & -6.63 & 6.68 & 0 & 0 & 0 & 0 \\ -4.58 & -17.06 & 6.68 & -6.63 & 0 & 0 & 0 & 0 \end{bmatrix}$$

$$\text{Assembled geometric stiffness matrix, } \mathbf{K}_s = \begin{bmatrix} 0 & 0 & 0 & 0 & 0 & 0 & 0 & 0 \\ 0 & 0 & 0 & 0 & 0 & 0 & 0 & 0 \\ 0 & 0 & 0 & 0 & 0 & 0 & 0 & 0 \\ 0 & 0 & 0 & 0 & 0 & 0 & 0 & 0 \\ 0 & 0 & 0 & 0 & 0 & 0 & 0 & 0 \\ 0 & 0 & 0 & 0 & 0 & 0 & 0 & 0 \\ 0 & 0 & 0 & 0 & 0 & 0 & 0 & 0 \\ 0 & 0 & 0 & 0 & 0 & 0 & 0 & 0 \end{bmatrix}$$

The matrix for derivatives of shape functions of support domain,

$$\mathbf{B}_3^T = \begin{bmatrix} 0.209924441336 & 0.209924441336 & 0 & 0 \\ 0 & 0 & 0.209924441336 & 0.209924441336 \end{bmatrix}$$

Current stiffness matrix,  $\mathbf{k}_c = \begin{bmatrix} 0.33 & 1.21 \\ 1.21 & 4.53 \end{bmatrix}$

Geometric stiffness matrix,  $\mathbf{k}_s = \begin{bmatrix} 0 & 0 \\ 0 & 0 \end{bmatrix}$

Assembled current stiffness matrix,

$$\mathbf{K}_c = \begin{bmatrix} 24.96 & 12.48 & -17.06 & -4.58 & -6.63 & -3.31 & -1.26 & -4.58 \\ 12.48 & 24.96 & -4.58 & -1.26 & -3.31 & -6.63 & -4.58 & -17.06 \\ -17.06 & -4.58 & 19.16 & -3.31 & 4.53 & 1.21 & -6.63 & 6.68 \\ -4.58 & -1.26 & -3.31 & 7.56 & 1.21 & 0.33 & 6.68 & -6.63 \\ -6.63 & -3.31 & 4.53 & 1.21 & 1.76 & 0.88 & 0.33 & 1.21 \\ -3.31 & -6.63 & 1.21 & 0.33 & 0.88 & 1.76 & 1.21 & 4.53 \\ -1.26 & -4.58 & -6.63 & 6.68 & 0.33 & 1.21 & 0 & 0 \\ -4.58 & -17.06 & 6.68 & -6.63 & 1.21 & 4.53 & 0 & 0 \end{bmatrix}$$

Assembled geometric stiffness matrix,  $\mathbf{K}_s = \begin{bmatrix} 0 & 0 & 0 & 0 & 0 & 0 & 0 & 0 \\ 0 & 0 & 0 & 0 & 0 & 0 & 0 & 0 \\ 0 & 0 & 0 & 0 & 0 & 0 & 0 & 0 \\ 0 & 0 & 0 & 0 & 0 & 0 & 0 & 0 \\ 0 & 0 & 0 & 0 & 0 & 0 & 0 & 0 \\ 0 & 0 & 0 & 0 & 0 & 0 & 0 & 0 \\ 0 & 0 & 0 & 0 & 0 & 0 & 0 & 0 \\ 0 & 0 & 0 & 0 & 0 & 0 & 0 & 0 \end{bmatrix}$

The matrix for derivatives of shape functions of support domain,

$$\mathbf{B}_4^T = \begin{bmatrix} -0.209924441336 & 0.790075558664 & 0 & 0 \\ 0 & 0 & -0.209924441336 & 0.790075558664 \end{bmatrix}$$

Current stiffness matrix,  $\mathbf{k}_c = \begin{bmatrix} 7.56 & -3.31 \\ -3.31 & 19.16 \end{bmatrix}$

Geometric stiffness matrix,  $\mathbf{k}_s = \begin{bmatrix} 0 & 0 \\ 0 & 0 \end{bmatrix}$

Assembled current stiffness matrix,

$$\mathbf{K}_c = \begin{bmatrix} 24.96 & 12.48 & -17.06 & -4.58 & -6.63 & -3.31 & -1.26 & -4.58 \\ 12.48 & 24.96 & -4.58 & -1.26 & -3.31 & -6.63 & -4.58 & -17.06 \\ -17.06 & -4.58 & 19.16 & -3.31 & 4.53 & 1.21 & -6.63 & 6.68 \\ -4.58 & -1.26 & -3.31 & 7.56 & 1.21 & 0.33 & 6.68 & -6.63 \\ -6.63 & -3.31 & 4.53 & 1.21 & 1.76 & 0.88 & 0.33 & 1.21 \\ -3.31 & -6.63 & 1.21 & 0.33 & 0.88 & 1.76 & 1.21 & 4.53 \\ -1.26 & -4.58 & -6.63 & 6.68 & 0.33 & 1.21 & 7.56 & -3.31 \\ -4.58 & -17.06 & 6.68 & -6.63 & 1.21 & 4.53 & -3.31 & 19.16 \end{bmatrix}$$

Assembled geometric stiffness matrix,  $\mathbf{K}_s =$

$$\begin{bmatrix} 0 & 0 & 0 & 0 & 0 & 0 & 0 & 0 \\ 0 & 0 & 0 & 0 & 0 & 0 & 0 & 0 \\ 0 & 0 & 0 & 0 & 0 & 0 & 0 & 0 \\ 0 & 0 & 0 & 0 & 0 & 0 & 0 & 0 \\ 0 & 0 & 0 & 0 & 0 & 0 & 0 & 0 \\ 0 & 0 & 0 & 0 & 0 & 0 & 0 & 0 \\ 0 & 0 & 0 & 0 & 0 & 0 & 0 & 0 \\ 0 & 0 & 0 & 0 & 0 & 0 & 0 & 0 \end{bmatrix}$$

Tangential stiffness matrix,

$$\mathbf{K}_T = \begin{bmatrix} 53.46 & 19.99 & -33.46 & 0 & -26.53 & -20.00 & 6.53 & 0 \\ 19.99 & 53.46 & 0 & 6.53 & -20.00 & -26.53 & 0 & -33.46 \\ -33.46 & 0 & 53.46 & -20.00 & 6.53 & 0 & -26.53 & 20.00 \\ 0 & 6.53 & -20.00 & 53.46 & 0 & -33.46 & 20.00 & -26.53 \\ -26.53 & -20.00 & 6.53 & 0 & 53.46 & 20.00 & -33.46 & 0 \\ -20.00 & -26.53 & 0 & -33.46 & 20.00 & 53.46 & 0 & 6.53 \\ 6.53 & 0 & -26.53 & 20.00 & -33.46 & 0 & 53.46 & -20.00 \\ 0 & -33.46 & 20.00 & -26.53 & 0 & 6.53 & -20.00 & 53.46 \end{bmatrix}$$

External force vector,

$$\mathbf{R}_E = \begin{bmatrix} 0 \\ 0 \\ 50 \\ 0 \\ 25 \\ 0 \\ 0 \\ 0 \end{bmatrix}$$

Internal force vector,

$$\mathbf{R}_I = \begin{bmatrix} 0 \\ 0 \\ 0 \\ 0 \\ 0 \\ 0 \\ 0 \\ 0 \end{bmatrix}$$

Residual force vector,

$$\mathbf{R} = \mathbf{R}_E - \mathbf{R}_I = \begin{bmatrix} 0 \\ 0 \\ 50 \\ 0 \\ 25 \\ 0 \\ 0 \\ 0 \end{bmatrix}$$

System of equations

$$\mathbf{K}_T \begin{bmatrix} \Delta u_1 \\ \Delta v_1 \\ \Delta u_2 \\ \Delta v_2 \\ \Delta u_3 \\ \Delta v_3 \\ \Delta u_4 \\ \Delta v_4 \end{bmatrix} = \begin{bmatrix} 0 \\ 0 \\ 50 \\ 0 \\ 25 \\ 0 \\ 0 \\ 0 \end{bmatrix}$$

Essential boundary conditions:

Node	DOF	Value
1	$\Delta u_1$	0
	$\Delta v_1$	0
4	$\Delta u_4$	0
	$\Delta v_4$	0

Solution of system equations, we get

Node	$u$	$v$
1	0	0
2	0.451276683714	0.103830051137
3	0.451276683710	-0.103830051133
4	0	0

Current configuration II:

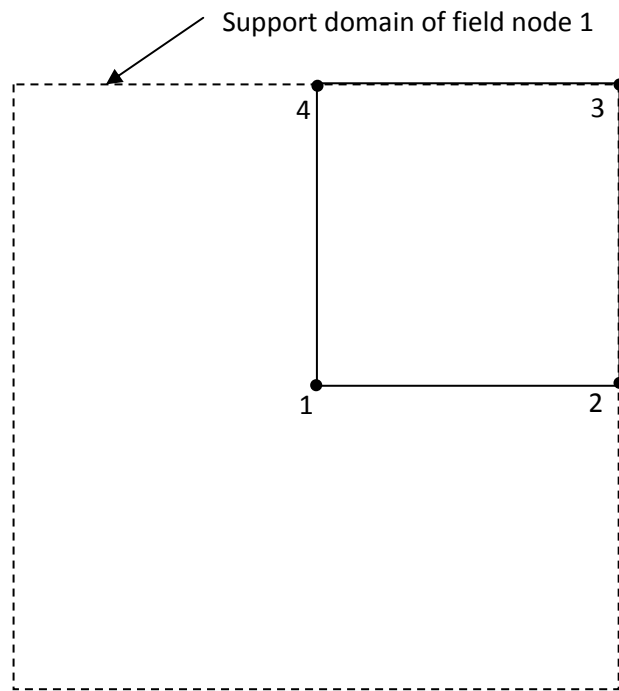
Field Node	X-coordinate	Y-coordinate
1	0	0
2	1	0
3	1	1
4	0	1

Updated coordinates		
Field Node	X-coordinate	Y-coordinate
1	0	0
2	1.451276683714	0.103830051137
3	1.451276683710	0.896169949
4	0	1

Computation for Cauchy stresses at  $\{0,0\}$  ;

Dimensions of the support domain:

$$d_x = 1 + 0.451276683714 \text{ and } d_y = 1 + 0.103830051137;$$



Nodes of support domain are; 1,2,3 and 4.

Interpolation functions and their derivatives:

$$\Phi(\mathbf{x}) = [\phi_1, \phi_2, \phi_3, \phi_4]$$

Node	1	2	3	4
$\phi$	1.000000000000	0.000000000000	0.000000000000	0.000000000000
$\frac{\partial \phi}{\partial x}$	-0.978933935835	0.978933935835	0.02106606416451	-0.0210660641645
$\frac{\partial \phi}{\partial y}$	-0.978933935835	-0.0210660641645	0.02106606416451	0.978933935835

Deformation gradient is calculated using the Equation 4.1

$$F_{ij} = \sum_{l=1}^{NP} \left[ \frac{\partial \Phi_l}{\partial x_j} d_{il} \right] + \delta_{ij}$$

where  $NP = 4$  and the displacement vector

$$\mathbf{d} = \begin{bmatrix} 0.00 \\ 0.00 \\ 0.451276683714 \\ 0.103830051137 \\ 0.451276683714 \\ -0.103830051133 \\ 0.00 \\ 0.00 \end{bmatrix}$$

Deformation gradient,

$$F = \begin{bmatrix} 1.45127668371 & -7.097621101959E - 14 \\ 9.945547009832E - 02 & 0.995625418961 \end{bmatrix};$$

Right Cauchy-Green tensor,

$$c_1 = \begin{bmatrix} 2.11609540322 & 9.902039408452E - 02 \\ 9.902039408452E - 02 & 0.991269974882 \end{bmatrix}$$

Left Cauchy-Green tensor,  $c_2 = \begin{bmatrix} 2.10620401269 & 0.144337404821 \\ 0.144337404821 & 1.00116136541 \end{bmatrix}$

Cauchy stresses,  $\hat{\sigma} = \begin{bmatrix} 422.996380278 & 45.1725653200 \\ 45.1725653200 & 77.1566360536 \end{bmatrix}$

Computation for Cauchy stresses at  $\{ 1, 0 \}$  ;

Nodes of support domain are; 1,2,3 and 4.

Interpolation functions and their derivatives:

Node	1	2	3	4
$\phi$	0.000000000000	1.000000000000	0.000000000000	0.000000000000
$\frac{\partial \phi}{\partial x}$	-0.978933935836	0.978933935836	0.02106606416446	-0.0210660641644
$\frac{\partial \phi}{\partial y}$	-0.0210660641645	-0.97893393583	0.978933935836	0.02106606416450

Deformation gradient,

$$F = \begin{bmatrix} 1.45127668371 & -3.299749362640E - 12 \\ 9.945547009833E - 02 & 0.796714478768 \end{bmatrix};$$

Right Cauchy-Green tensor,

$$c_1 = \begin{bmatrix} 2.11609540322 & 7.923761301526E - 02 \\ 7.923761301526E - 02 & 0.634753960679 \end{bmatrix}$$

Left Cauchy-Green tensor,  $c_2 = \begin{bmatrix} 2.10620401269 & 0.144337404819 \\ 0.144337404819 & 0.644645351211 \end{bmatrix}$

Cauchy stresses,  $\hat{\sigma} = \begin{bmatrix} 436.805509354 & 52.4087255264 \\ 52.4087255264 & -93.8845555425 \end{bmatrix}$

Computation for Cauchy stresses at  $\{ 1, 1 \}$  ;

Nodes of support domain are; 1,2,3 and 4.

Interpolation functions and their derivatives:

Node	1	2	3	4
$\phi$	0.000000000000	0.000000000000	1.000000000000	0.000000000000
$\frac{\partial \phi}{\partial x}$	-0.02106606416450	0.02106606416450	0.978933935835	-0.978933935835
$\frac{\partial \phi}{\partial y}$	-0.02106606416451	-0.978933935835	0.978933935835	0.02106606416451

Deformation gradient,

$$F = \begin{bmatrix} 1.45127668371 & -3.299804873791E - 12 \\ -9.945547009458E - 02 & 0.796714478768 \end{bmatrix};$$

Right Cauchy-Green tensor,

$$c_1 = \begin{bmatrix} 2.11609540321 & -7.923761302184E - 02 \\ -7.923761302184E - 02 & 0.634753960679 \end{bmatrix}$$

$$\text{Left Cauchy-Green tensor, } c_2 = \begin{bmatrix} 2.10620401268 & -0.144337404818 \\ -0.144337404818 & 0.644645351211 \end{bmatrix}$$

$$\text{Cauchy stresses, } \hat{\sigma} = \begin{bmatrix} 436.805509350 & -52.4087255264 \\ -52.4087255264 & -93.8845555436 \end{bmatrix}$$

Computation for Cauchy stresses at  $\{0,1\}$ ;

Nodes of support domain are; 1,2,3 and 4.

Interpolation functions and their derivatives:

Node	1	2	3	4
$\phi$	0.000000000000	0.000000000000	0.000000000000	1.000000000000
$\frac{\partial \phi}{\partial x}$	-0.0210660641645	0.0210660641645	0.978933935836	-0.978933935836
$\frac{\partial \phi}{\partial y}$	-0.978933935836	-0.02106606416446	0.02106606416446	0.978933935836

Deformation gradient,

$$F = \begin{bmatrix} 1.45127668371 & -7.103692634125E - 14 \\ -9.945547009458E - 02 & 0.995625418961 \end{bmatrix};$$

Right Cauchy-Green tensor,

$$c_1 = \begin{bmatrix} 2.11609540321 & -9.902039408100E - 02 \\ -9.902039408100E - 02 & 0.991269974882 \end{bmatrix}$$

$$\text{Left Cauchy-Green tensor, } c_2 = \begin{bmatrix} 2.10620401268 & -0.144337404816 \\ -0.144337404816 & 1.00116136541 \end{bmatrix}$$

$$\text{Cauchy stresses, } \hat{\sigma} = \begin{bmatrix} 422.996380276 & -45.1725653183 \\ -45.1725653183 & 77.1566360530 \end{bmatrix}$$

For the difference between successive solutions we check

$$\frac{\|\mathbf{u}_{r+1} - \mathbf{u}_r\|_2}{\|\mathbf{u}_{r+1}\|_2} \leq \text{tolerance or}$$

$$\frac{\sqrt{(\mathbf{u}_{r+1} - \mathbf{u}_r) \cdot (\mathbf{u}_{r+1} - \mathbf{u}_r)}}{\sqrt{\mathbf{u}_{r+1} \cdot \mathbf{u}_{r+1}}} \leq \text{tolerance or}$$

$$\frac{\sqrt{\sum_{i=1}^n (u_i^{r+1} - u_i^r)^2}}{\sqrt{\sum_{i=1}^n (u_i^{r+1})^2}} \leq \text{tolerance}$$

$$\|\mathbf{u}_{r+1} - \mathbf{u}_r\|_2 = 0.428862649561$$

$$\|\mathbf{u}_{r+1}\|_2 = 0.428862649561$$

$$\text{convergence parameter} = \frac{\|\mathbf{u}_{r+1} - \mathbf{u}_r\|_2}{\|\mathbf{u}_{r+1}\|_2} = 1.000000000000$$

### Iteration 2:

Computation for stiffness matrix of support domain at  
 $\{0.211324870586, 0.211324870586\}$  with  $\text{weight} = 1$ ;

Nodes of support domain are; *node 1, node 2, node 3* and *node 4*.

Interpolation functions and their derivatives:

Node	1	2	3	4
$\phi$	0.622825041123	0.165850088290	4.547478229618E-02	0.165850088290
$\frac{\partial \phi}{\partial x}$	-0.790075558664	0.790075558664	0.209924441336	-0.209924441336
$\frac{\partial \phi}{\partial y}$	-0.790075558664	-0.209924441336	0.209924441336	0.790075558664

Deformation gradient is calculated using the Equation 4.1

$$F_{ij} = \sum_{I=1}^{NP} \left[ \frac{\partial \phi_I}{\partial x_j} d_{iI} \right] + \delta_{ij}$$

where  $NP = 4$  and the displacement vector

$$\mathbf{d} = \begin{bmatrix} 0.00 \\ 0.00 \\ 0.451276683714 \\ 0.103830051137 \\ 0.451276683714 \\ -0.103830051133 \\ 0.00 \\ 0.00 \end{bmatrix}$$



Deformation gradient,

$$F = \begin{bmatrix} 1.45127668371 & -7.076839114717E - 13 \\ 6.023712018033E - 02 & 0.956407069043 \end{bmatrix};$$

and arranged deformation gradient (Equation 4.16);

$$\bar{F} = \begin{bmatrix} 1.45127668371 & 0 & 0.06023712018 & 0 \\ 0 & 0.00 & 0 & 0.956407069 \\ 0 & 1.45127668371 & 0.956407069 & 0.06023712018 \end{bmatrix}$$

Right Cauchy-Green tensor,

$$c_1 = \begin{bmatrix} 2.10983252334 & 5.761120755824E - 02 \\ 5.761120755824E - 02 & 0.914714481716 \end{bmatrix}$$

Left Cauchy-Green tensor,

$$c_2 = \begin{bmatrix} 2.10620401269 & 8.742072801104E - 02 \\ 8.742072801104E - 02 & 0.918342992363 \end{bmatrix}$$

$$\text{Second PK stresses, } \hat{\mathbf{S}} = \begin{bmatrix} 251.596774166 & 9.34683905931 \\ 9.34683905931 & 57.7008906161 \end{bmatrix}$$

Initial stress matrix,

$$\bar{\mathbf{S}} = \begin{bmatrix} 251.596774166 & 9.34683905931 & 0 & 0 \\ 9.34683905931 & 57.7008906161 & 0 & 0 \\ 0 & 0 & 251.596774166 & 9.34683905931 \\ 0 & 0 & 9.34683905931 & 57.7008906161 \end{bmatrix}$$

The matrix for derivatives of shape functions of support domain,

$$\mathbf{B}_1^T = \begin{bmatrix} -0.790075558664 & -0.790075558664 & 0 & 0 \\ 0 & 0 & -0.790075558664 & -0.790075558664 \end{bmatrix}$$

$$\text{Internal force vector, } \mathbf{r}_1 = [-7.48006764162 \quad -1.57705825624]$$

The matrix for derivatives of shape functions of support domain,

$$\mathbf{B}_1^T = \begin{bmatrix} -0.790075558664 & -0.790075558664 & 0 & 0 \\ 0 & 0 & -0.790075558664 & -0.790075558664 \end{bmatrix}$$

Material matrix,

$$\mathbf{D} = \begin{bmatrix} 231.089474011 & 208.538992457 & -14.5546440096 \\ 208.538992457 & 1229.43343515 & -33.5709797001 \\ -14.5546440096 & -33.5709797001 & 163.156634593 \end{bmatrix}$$

$$\text{Current stiffness matrix, } \mathbf{k}_c = \begin{bmatrix} 12.00 & 7.50 \\ 7.50 & 19.52 \end{bmatrix}$$

$$\text{Geometric stiffness matrix, } \mathbf{k}_s = \begin{bmatrix} 5.11 & 0 \\ 0 & 5.11 \end{bmatrix}$$

Assembled current stiffness matrix,

$$\mathbf{K}_c = \begin{bmatrix} 12.00 & 7.50 & 0 & 0 & 0 & 0 & 0 & 0 \\ 7.50 & 19.52 & 0 & 0 & 0 & 0 & 0 & 0 \\ 0 & 0 & 0 & 0 & 0 & 0 & 0 & 0 \\ 0 & 0 & 0 & 0 & 0 & 0 & 0 & 0 \\ 0 & 0 & 0 & 0 & 0 & 0 & 0 & 0 \\ 0 & 0 & 0 & 0 & 0 & 0 & 0 & 0 \\ 0 & 0 & 0 & 0 & 0 & 0 & 0 & 0 \\ 0 & 0 & 0 & 0 & 0 & 0 & 0 & 0 \end{bmatrix}$$

Assembled geometric stiffness matrix,

$$\mathbf{K}_s = \begin{bmatrix} 5.11 & 0 & 0 & 0 & 0 & 0 & 0 & 0 \\ 0 & 5.11 & 0 & 0 & 0 & 0 & 0 & 0 \\ 0 & 0 & 0 & 0 & 0 & 0 & 0 & 0 \\ 0 & 0 & 0 & 0 & 0 & 0 & 0 & 0 \\ 0 & 0 & 0 & 0 & 0 & 0 & 0 & 0 \\ 0 & 0 & 0 & 0 & 0 & 0 & 0 & 0 \\ 0 & 0 & 0 & 0 & 0 & 0 & 0 & 0 \\ 0 & 0 & 0 & 0 & 0 & 0 & 0 & 0 \end{bmatrix}$$

The matrix for derivatives of shape functions of support domain,

$$\mathbf{B}_2^T = \begin{bmatrix} 0.790075558664 & -0.209924441336 & 0 & 0 \\ 0 & 0 & 0.790075558664 & -0.209924441336 \end{bmatrix}$$

Current stiffness matrix,  $\mathbf{k}_c = \begin{bmatrix} -5.81 & -2.45 \\ -3.69 & 2.44 \end{bmatrix}$

Geometric stiffness matrix,  $\mathbf{k}_s = \begin{bmatrix} -3.79 & 0 \\ 0 & -3.79 \end{bmatrix}$

Assembled current stiffness matrix,

$$\mathbf{K}_c = \begin{bmatrix} 12.00 & 7.50 & -5.81 & -2.45 & 0 & 0 & 0 & 0 \\ 7.50 & 19.52 & -3.69 & 2.44 & 0 & 0 & 0 & 0 \\ 0 & 0 & 0 & 0 & 0 & 0 & 0 & 0 \\ 0 & 0 & 0 & 0 & 0 & 0 & 0 & 0 \\ 0 & 0 & 0 & 0 & 0 & 0 & 0 & 0 \\ 0 & 0 & 0 & 0 & 0 & 0 & 0 & 0 \\ 0 & 0 & 0 & 0 & 0 & 0 & 0 & 0 \\ 0 & 0 & 0 & 0 & 0 & 0 & 0 & 0 \end{bmatrix}$$

Assembled geometric stiffness matrix,

$$\mathbf{K}_s = \begin{bmatrix} 5.11 & 0 & -3.79 & 0 & 0 & 0 & 0 & 0 \\ 0 & 5.11 & 0 & -3.79 & 0 & 0 & 0 & 0 \\ 0 & 0 & 0 & 0 & 0 & 0 & 0 & 0 \\ 0 & 0 & 0 & 0 & 0 & 0 & 0 & 0 \\ 0 & 0 & 0 & 0 & 0 & 0 & 0 & 0 \\ 0 & 0 & 0 & 0 & 0 & 0 & 0 & 0 \\ 0 & 0 & 0 & 0 & 0 & 0 & 0 & 0 \\ 0 & 0 & 0 & 0 & 0 & 0 & 0 & 0 \end{bmatrix}$$

The matrix for derivatives of shape functions of support domain,

$$\mathbf{B}_3^T = \begin{bmatrix} 0.209924441336 & 0.209924441336 & 0 & 0 \\ 0 & 0 & 0.209924441336 & 0.209924441336 \end{bmatrix}$$

Current stiffness matrix,  $\mathbf{k}_c = \begin{bmatrix} -3.18 & -1.99 \\ -1.99 & -5.18 \end{bmatrix}$

Geometric stiffness matrix,  $\mathbf{k}_s = \begin{bmatrix} -1.35 & 0 \\ 0 & -1.35 \end{bmatrix}$

Assembled current stiffness matrix,

$$\mathbf{K}_c = \begin{bmatrix} 12.00 & 7.50 & -5.81 & -2.45 & -3.18 & -1.99 & 0 & 0 \\ 7.50 & 19.52 & -3.69 & 2.44 & -1.99 & -5.18 & 0 & 0 \\ 0 & 0 & 0 & 0 & 0 & 0 & 0 & 0 \\ 0 & 0 & 0 & 0 & 0 & 0 & 0 & 0 \\ 0 & 0 & 0 & 0 & 0 & 0 & 0 & 0 \\ 0 & 0 & 0 & 0 & 0 & 0 & 0 & 0 \\ 0 & 0 & 0 & 0 & 0 & 0 & 0 & 0 \\ 0 & 0 & 0 & 0 & 0 & 0 & 0 & 0 \end{bmatrix}$$

Assembled geometric stiffness matrix,

$$\mathbf{K}_s = \begin{bmatrix} 5.11 & 0 & -3.79 & 0 & -1.35 & 0 & 0 & 0 \\ 0 & 5.11 & 0 & -3.79 & 0 & -1.35 & 0 & 0 \\ 0 & 0 & 0 & 0 & 0 & 0 & 0 & 0 \\ 0 & 0 & 0 & 0 & 0 & 0 & 0 & 0 \\ 0 & 0 & 0 & 0 & 0 & 0 & 0 & 0 \\ 0 & 0 & 0 & 0 & 0 & 0 & 0 & 0 \\ 0 & 0 & 0 & 0 & 0 & 0 & 0 & 0 \\ 0 & 0 & 0 & 0 & 0 & 0 & 0 & 0 \end{bmatrix}$$

The matrix for derivatives of shape functions of support domain,

$$\mathbf{B}_4^T = \begin{bmatrix} -0.209924441336 & 0.790075558664 & 0 & 0 \\ 0 & 0 & -0.209924441336 & 0.790075558664 \end{bmatrix}$$

Current stiffness matrix,  $\mathbf{k}_c = \begin{bmatrix} -2.99 & -3.05 \\ -1.81 & -16.77 \end{bmatrix}$

Geometric stiffness matrix,  $\mathbf{k}_s = \begin{bmatrix} 0.03 & 0 \\ 0 & 0.03 \end{bmatrix}$

Assembled current stiffness matrix,

$$\mathbf{K}_c = \begin{bmatrix} 12.00 & 7.50 & -5.81 & -2.45 & -3.18 & -1.99 & -2.99 & -3.05 \\ 7.50 & 19.52 & -3.69 & 2.44 & -1.99 & -5.18 & -1.81 & -16.77 \\ 0 & 0 & 0 & 0 & 0 & 0 & 0 & 0 \\ 0 & 0 & 0 & 0 & 0 & 0 & 0 & 0 \\ 0 & 0 & 0 & 0 & 0 & 0 & 0 & 0 \\ 0 & 0 & 0 & 0 & 0 & 0 & 0 & 0 \\ 0 & 0 & 0 & 0 & 0 & 0 & 0 & 0 \\ 0 & 0 & 0 & 0 & 0 & 0 & 0 & 0 \end{bmatrix}$$

Assembled geometric stiffness matrix,

$$\mathbf{K}_s = \begin{bmatrix} 5.11 & 0 & -3.79 & 0 & -1.35 & 0 & 0.03 & 0 \\ 0 & 5.11 & 0 & -3.79 & 0 & -1.35 & 0 & 0.03 \\ 0 & 0 & 0 & 0 & 0 & 0 & 0 & 0 \\ 0 & 0 & 0 & 0 & 0 & 0 & 0 & 0 \\ 0 & 0 & 0 & 0 & 0 & 0 & 0 & 0 \\ 0 & 0 & 0 & 0 & 0 & 0 & 0 & 0 \\ 0 & 0 & 0 & 0 & 0 & 0 & 0 & 0 \\ 0 & 0 & 0 & 0 & 0 & 0 & 0 & 0 \end{bmatrix}$$

The matrix for derivatives of shape functions of support domain,

$$\mathbf{B}_2^T = \begin{bmatrix} 0.790075558664 & -0.209924441336 & 0 & 0 \\ 0 & 0 & 0.790075558664 & -0.209924441336 \end{bmatrix}$$

Internal force vector,  $\mathbf{r}_2 = [7.14094640179 \quad 0.183344097664]$

The matrix for derivatives of shape functions of support domain,

$$\mathbf{B}_1^T = \begin{bmatrix} -0.790075558664 & -0.790075558664 & 0 & 0 \\ 0 & 0 & -0.790075558664 & -0.790075558664 \end{bmatrix}$$

Material matrix,

$$\mathbf{D} = \begin{bmatrix} 231.089474011 & 208.538992457 & -14.5546440096 \\ 208.538992457 & 1229.43343515 & -33.5709797001 \\ -14.5546440096 & -33.5709797001 & 163.156634593 \end{bmatrix}$$

Current stiffness matrix,  $\mathbf{k}_c = \begin{bmatrix} -5.81 & -3.69 \\ -2.45 & 2.44 \end{bmatrix}$

Geometric stiffness matrix,  $\mathbf{k}_s = \begin{bmatrix} -3.79 & 0 \\ 0 & -3.79 \end{bmatrix}$

Assembled current stiffness matrix,

$$\mathbf{K}_c = \begin{bmatrix} 12.00 & 7.50 & -5.81 & -2.45 & -3.18 & -1.99 & -2.99 & -3.05 \\ 7.50 & 19.52 & -3.69 & 2.44 & -1.99 & -5.18 & -1.81 & -16.77 \\ -5.81 & -3.69 & 0 & 0 & 0 & 0 & 0 & 0 \\ -2.45 & 2.44 & 0 & 0 & 0 & 0 & 0 & 0 \\ 0 & 0 & 0 & 0 & 0 & 0 & 0 & 0 \\ 0 & 0 & 0 & 0 & 0 & 0 & 0 & 0 \\ 0 & 0 & 0 & 0 & 0 & 0 & 0 & 0 \\ 0 & 0 & 0 & 0 & 0 & 0 & 0 & 0 \end{bmatrix}$$

Assembled geometric stiffness matrix,

$$\mathbf{K}_s = \begin{bmatrix} 5.11 & 0 & -3.79 & 0 & -1.35 & 0 & 0.03 & 0 \\ 0 & 5.11 & 0 & -3.79 & 0 & -1.35 & 0 & 0.03 \\ -3.79 & 0 & 0 & 0 & 0 & 0 & 0 & 0 \\ 0 & -3.79 & 0 & 0 & 0 & 0 & 0 & 0 \\ 0 & 0 & 0 & 0 & 0 & 0 & 0 & 0 \\ 0 & 0 & 0 & 0 & 0 & 0 & 0 & 0 \\ 0 & 0 & 0 & 0 & 0 & 0 & 0 & 0 \\ 0 & 0 & 0 & 0 & 0 & 0 & 0 & 0 \end{bmatrix}$$

The matrix for derivatives of shape functions of support domain,

$$\mathbf{B}_2^T = \begin{bmatrix} 0.790075558664 & -0.209924441336 & 0 & 0 \\ 0 & 0 & 0.790075558664 & -0.209924441336 \end{bmatrix}$$

Current stiffness matrix,  $\mathbf{k}_c = \begin{bmatrix} 8.22 & -2.16 \\ -2.16 & 3.62 \end{bmatrix}$

Geometric stiffness matrix,  $\mathbf{k}_s = \begin{bmatrix} 3.91 & 0 \\ 0 & 3.91 \end{bmatrix}$

Assembled current stiffness matrix,

$$\mathbf{K}_c = \begin{bmatrix} 12.00 & 7.50 & -5.81 & -2.45 & -3.18 & -1.99 & -2.99 & -3.05 \\ 7.50 & 19.52 & -3.69 & 2.44 & -1.99 & -5.18 & -1.81 & -16.77 \\ -5.81 & -3.69 & 8.22 & -2.16 & 0 & 0 & 0 & 0 \\ -2.45 & 2.44 & -2.16 & 3.62 & 0 & 0 & 0 & 0 \\ 0 & 0 & 0 & 0 & 0 & 0 & 0 & 0 \\ 0 & 0 & 0 & 0 & 0 & 0 & 0 & 0 \\ 0 & 0 & 0 & 0 & 0 & 0 & 0 & 0 \\ 0 & 0 & 0 & 0 & 0 & 0 & 0 & 0 \end{bmatrix}$$

Assembled geometric stiffness matrix,

$$\mathbf{K}_s = \begin{bmatrix} 5.11 & 0 & -3.79 & 0 & -1.35 & 0 & 0.03 & 0 \\ 0 & 5.11 & 0 & -3.79 & 0 & -1.35 & 0 & 0.03 \\ -3.79 & 0 & 3.91 & 0 & 0 & 0 & 0 & 0 \\ 0 & -3.79 & 0 & 3.91 & 0 & 0 & 0 & 0 \\ 0 & 0 & 0 & 0 & 0 & 0 & 0 & 0 \\ 0 & 0 & 0 & 0 & 0 & 0 & 0 & 0 \\ 0 & 0 & 0 & 0 & 0 & 0 & 0 & 0 \\ 0 & 0 & 0 & 0 & 0 & 0 & 0 & 0 \end{bmatrix}$$

The matrix for derivatives of shape functions of support domain,

$$\mathbf{B}_3^T = \begin{bmatrix} 0.209924441336 & 0.209924441336 & 0 & 0 \\ 0 & 0 & 0.209924441336 & 0.209924441336 \end{bmatrix}$$

Current stiffness matrix,  $\mathbf{k}_c = \begin{bmatrix} 1.54 & 0.98 \\ 0.65 & -0.64 \end{bmatrix}$

Geometric stiffness matrix,  $\mathbf{k}_s = \begin{bmatrix} 1.00 & 0 \\ 0 & 1.00 \end{bmatrix}$

Assembled current stiffness matrix,

$$\mathbf{K}_c = \begin{bmatrix} 12.00 & 7.50 & -5.81 & -2.45 & -3.18 & -1.99 & -2.99 & -3.05 \\ 7.50 & 19.52 & -3.69 & 2.44 & -1.99 & -5.18 & -1.81 & -16.77 \\ -5.81 & -3.69 & 8.22 & -2.16 & 1.54 & 0.98 & 0 & 0 \\ -2.45 & 2.44 & -2.16 & 3.62 & 0.65 & -0.64 & 0 & 0 \\ 0 & 0 & 0 & 0 & 0 & 0 & 0 & 0 \\ 0 & 0 & 0 & 0 & 0 & 0 & 0 & 0 \\ 0 & 0 & 0 & 0 & 0 & 0 & 0 & 0 \\ 0 & 0 & 0 & 0 & 0 & 0 & 0 & 0 \end{bmatrix}$$

Assembled geometric stiffness matrix,

$$\mathbf{K}_s = \begin{bmatrix} 5.11 & 0 & -3.79 & 0 & -1.35 & 0 & 0.03 & 0 \\ 0 & 5.11 & 0 & -3.79 & 0 & -1.35 & 0 & 0.03 \\ -3.79 & 0 & 3.91 & 0 & 1.00 & 0 & 0 & 0 \\ 0 & -3.79 & 0 & 3.91 & 0 & 1.00 & 0 & 0 \\ 0 & 0 & 0 & 0 & 0 & 0 & 0 & 0 \\ 0 & 0 & 0 & 0 & 0 & 0 & 0 & 0 \\ 0 & 0 & 0 & 0 & 0 & 0 & 0 & 0 \\ 0 & 0 & 0 & 0 & 0 & 0 & 0 & 0 \end{bmatrix}$$

The matrix for derivatives of shape functions of support domain,

$$\mathbf{B}_4^T = \begin{bmatrix} -0.209924441336 & 0.790075558664 & 0 & 0 \\ 0 & 0 & -0.209924441336 & 0.790075558664 \end{bmatrix}$$

$$\text{Current stiffness matrix, } \mathbf{k}_c = \begin{bmatrix} -3.95 & 4.87 \\ 3.96 & -5.42 \end{bmatrix}$$

$$\text{Geometric stiffness matrix, } \mathbf{k}_s = \begin{bmatrix} -1.12 & 0 \\ 0 & -1.12 \end{bmatrix}$$

Assembled current stiffness matrix,

$$\mathbf{K}_c = \begin{bmatrix} 12.00 & 7.50 & -5.81 & -2.45 & -3.18 & -1.99 & -2.99 & -3.05 \\ 7.50 & 19.52 & -3.69 & 2.44 & -1.99 & -5.18 & -1.81 & -16.77 \\ -5.81 & -3.69 & 8.22 & -2.16 & 1.54 & 0.98 & -3.95 & 4.87 \\ -2.45 & 2.44 & -2.16 & 3.62 & 0.65 & -0.64 & 3.96 & -5.42 \\ 0 & 0 & 0 & 0 & 0 & 0 & 0 & 0 \\ 0 & 0 & 0 & 0 & 0 & 0 & 0 & 0 \\ 0 & 0 & 0 & 0 & 0 & 0 & 0 & 0 \\ 0 & 0 & 0 & 0 & 0 & 0 & 0 & 0 \end{bmatrix}$$

Assembled geometric stiffness matrix,

$$\mathbf{K}_s = \begin{bmatrix} 5.11 & 0 & -3.79 & 0 & -1.35 & 0 & 0.03 & 0 \\ 0 & 5.11 & 0 & -3.79 & 0 & -1.35 & 0 & 0.03 \\ -3.79 & 0 & 3.91 & 0 & 1.00 & 0 & -1.12 & 0 \\ 0 & -3.79 & 0 & 3.91 & 0 & 1.00 & 0 & 1.12 \\ 0 & 0 & 0 & 0 & 0 & 0 & 0 & 0 \\ 0 & 0 & 0 & 0 & 0 & 0 & 0 & 0 \\ 0 & 0 & 0 & 0 & 0 & 0 & 0 & 0 \\ 0 & 0 & 0 & 0 & 0 & 0 & 0 & 0 \end{bmatrix}$$

The matrix for derivatives of shape functions of support domain,

$$\mathbf{B}_3^T = \begin{bmatrix} 0.209924441336 & 0.209924441336 & 0 & 0 \\ 0 & 0 & 0.209924441336 & 0.209924441336 \end{bmatrix}$$

$$\text{Internal force vector, } \mathbf{r}_3 = [1.98746689933 \quad 0.419027104135]$$

The gradient matrix,

$$\mathbf{B}_1^T = \begin{bmatrix} -0.790075558664 & -0.790075558664 & 0 & 0 \\ 0 & 0 & -0.790075558664 & -0.790075558664 \end{bmatrix}$$

Material matrix,

$$\mathbf{D} = \begin{bmatrix} 231.089474011 & 208.538992457 & -14.5546440096 \\ 208.538992457 & 1229.43343515 & -33.5709797001 \\ -14.5546440096 & -33.5709797001 & 163.156634593 \end{bmatrix}$$

Current stiffness matrix,  $\mathbf{k}_c = \begin{bmatrix} -3.18 & -1.99 \\ -1.99 & -5.18 \end{bmatrix}$

Geometric stiffness matrix,  $\mathbf{k}_s = \begin{bmatrix} -1.35 & 0 \\ 0 & -1.35 \end{bmatrix}$

Assembled current stiffness matrix,

$$\mathbf{K}_c = \begin{bmatrix} 12.00 & 7.50 & -5.81 & -2.45 & -3.18 & -1.99 & -2.99 & -3.05 \\ 7.50 & 19.52 & -3.69 & 2.44 & -1.99 & -5.18 & -1.81 & -16.77 \\ -5.81 & -3.69 & 8.22 & -2.16 & 1.54 & 0.98 & -3.95 & 4.87 \\ -2.45 & 2.44 & -2.16 & 3.62 & 0.65 & -0.64 & 3.96 & -5.42 \\ -3.18 & -1.99 & 0 & 0 & 0 & 0 & 0 & 0 \\ -1.99 & -5.18 & 0 & 0 & 0 & 0 & 0 & 0 \\ 0 & 0 & 0 & 0 & 0 & 0 & 0 & 0 \\ 0 & 0 & 0 & 0 & 0 & 0 & 0 & 0 \end{bmatrix}$$

Assembled geometric stiffness matrix,

$$\mathbf{K}_s = \begin{bmatrix} 5.11 & 0 & -3.79 & 0 & -1.35 & 0 & 0.03 & 0 \\ 0 & 5.11 & 0 & -3.79 & 0 & -1.35 & 0 & 0.03 \\ -3.79 & 0 & 3.91 & 0 & 1.00 & 0 & -1.12 & 0 \\ 0 & -3.79 & 0 & 3.91 & 0 & 1.00 & 0 & 1.12 \\ -1.35 & 0 & -1.35 & 0 & 0 & 0 & 0 & 0 \\ 0 & -1.35 & 0 & -1.35 & 0 & 0 & 0 & 0 \\ 0 & 0 & 0 & 0 & 0 & 0 & 0 & 0 \\ 0 & 0 & 0 & 0 & 0 & 0 & 0 & 0 \end{bmatrix}$$

The matrix for derivatives of shape functions of support domain,

$$\mathbf{B}_2^T = \begin{bmatrix} 0.790075558664 & -0.209924441336 & 0 & 0 \\ 0 & 0 & 0.790075558664 & -0.209924441336 \end{bmatrix}$$

Current stiffness matrix,  $\mathbf{k}_c = \begin{bmatrix} 1.54 & 0.65 \\ 0.98 & -0.64 \end{bmatrix}$

Geometric stiffness matrix,  $\mathbf{k}_s = \begin{bmatrix} 1.00 & 0 \\ 0 & 1.00 \end{bmatrix}$

Assembled current stiffness matrix,

$$\mathbf{K}_c = \begin{bmatrix} 12.00 & 7.50 & -5.81 & -2.45 & -3.18 & -1.99 & -2.99 & -3.05 \\ 7.50 & 19.52 & -3.69 & 2.44 & -1.99 & -5.18 & -1.81 & -16.77 \\ -5.81 & -3.69 & 8.22 & -2.16 & 1.54 & 0.98 & -3.95 & 4.87 \\ -2.45 & 2.44 & -2.16 & 3.62 & 0.65 & -0.64 & 3.96 & -5.42 \\ -3.18 & -1.99 & 1.54 & 0.65 & 0 & 0 & 0 & 0 \\ -1.99 & -5.18 & 0.98 & -0.64 & 0 & 0 & 0 & 0 \\ 0 & 0 & 0 & 0 & 0 & 0 & 0 & 0 \\ 0 & 0 & 0 & 0 & 0 & 0 & 0 & 0 \end{bmatrix}$$

Assembled geometric stiffness matrix,

$$\mathbf{K}_s = \begin{bmatrix} 5.11 & 0 & -3.79 & 0 & -1.35 & 0 & 0.03 & 0 \\ 0 & 5.11 & 0 & -3.79 & 0 & -1.35 & 0 & 0.03 \\ -3.79 & 0 & 3.91 & 0 & 1.00 & 0 & -1.12 & 0 \\ 0 & -3.79 & 0 & 3.91 & 0 & 1.00 & 0 & 1.12 \\ -1.35 & 0 & 1.00 & 0 & 0 & 0 & 0 & 0 \\ 0 & -1.35 & 0 & 1.00 & 0 & 0 & 0 & 0 \\ 0 & 0 & 0 & 0 & 0 & 0 & 0 & 0 \\ 0 & 0 & 0 & 0 & 0 & 0 & 0 & 0 \end{bmatrix}$$

The matrix for derivatives of shape functions of support domain,

$$\mathbf{B}_3^T = \begin{bmatrix} 0.209924441336 & 0.209924441336 & 0 & 0 \\ 0 & 0 & 0.209924441336 & 0.209924441336 \end{bmatrix}$$

$$\text{Current stiffness matrix, } \mathbf{k}_c = \begin{bmatrix} 0.84 & 0.52 \\ 0.52 & 1.37 \end{bmatrix}$$

$$\text{Geometric stiffness matrix, } \mathbf{k}_s = \begin{bmatrix} 0.36 & 0 \\ 0 & 0.36 \end{bmatrix}$$

Assembled current stiffness matrix,

$$\mathbf{K}_c = \begin{bmatrix} 12.00 & 7.50 & -5.81 & -2.45 & -3.18 & -1.99 & -2.99 & -3.05 \\ 7.50 & 19.52 & -3.69 & 2.44 & -1.99 & -5.18 & -1.81 & -16.77 \\ -5.81 & -3.69 & 8.22 & -2.16 & 1.54 & 0.98 & -3.95 & 4.87 \\ -2.45 & 2.44 & -2.16 & 3.62 & 0.65 & -0.64 & 3.96 & -5.42 \\ -3.18 & -1.99 & 1.54 & 0.65 & 0.84 & 0.52 & 0 & 0 \\ -1.99 & -5.18 & 0.98 & -0.64 & 0.52 & 1.37 & 0 & 0 \\ 0 & 0 & 0 & 0 & 0 & 0 & 0 & 0 \\ 0 & 0 & 0 & 0 & 0 & 0 & 0 & 0 \end{bmatrix}$$

Assembled geometric stiffness matrix,

$$\mathbf{K}_s = \begin{bmatrix} 5.11 & 0 & -3.79 & 0 & -1.35 & 0 & 0.03 & 0 \\ 0 & 5.11 & 0 & -3.79 & 0 & -1.35 & 0 & 0.03 \\ -3.79 & 0 & 3.91 & 0 & 1.00 & 0 & -1.12 & 0 \\ 0 & -3.79 & 0 & 3.91 & 0 & 1.00 & 0 & 1.12 \\ -1.35 & 0 & 1.00 & 0 & 0.36 & 0 & 0 & 0 \\ 0 & -1.35 & 0 & 1.00 & 0 & 0.36 & 0 & 0 \\ 0 & 0 & 0 & 0 & 0 & 0 & 0 & 0 \\ 0 & 0 & 0 & 0 & 0 & 0 & 0 & 0 \end{bmatrix}$$

The matrix for derivatives of shape functions of support domain,

$$\mathbf{B}_4^T = \begin{bmatrix} -0.209924441336 & 0.790075558664 & 0 & 0 \\ 0 & 0 & -0.209924441336 & 0.790075558664 \end{bmatrix}$$

$$\text{Current stiffness matrix, } \mathbf{k}_c = \begin{bmatrix} 0.79 & 0.81 \\ 0.48 & 4.45 \end{bmatrix}$$

$$\text{Geometric stiffness matrix, } \mathbf{k}_s = \begin{bmatrix} -0.009 & 0 \\ 0 & -0.009 \end{bmatrix}$$

Assembled current stiffness matrix,



$$\mathbf{K}_c = \begin{bmatrix} 12.00 & 7.50 & -5.81 & -2.45 & -3.18 & -1.99 & -2.99 & -3.05 \\ 7.50 & 19.52 & -3.69 & 2.44 & -1.99 & -5.18 & -1.81 & -16.77 \\ -5.81 & -3.69 & 8.22 & -2.16 & 1.54 & 0.98 & -3.95 & 4.87 \\ -2.45 & 2.44 & -2.16 & 3.62 & 0.65 & -0.64 & 3.96 & -5.42 \\ -3.18 & -1.99 & 1.54 & 0.65 & 0.84 & 0.52 & 0.79 & 0.81 \\ -1.99 & -5.18 & 0.98 & -0.64 & 0.52 & 1.37 & 0.48 & 4.45 \\ 0 & 0 & 0 & 0 & 0 & 0 & 0 & 0 \\ 0 & 0 & 0 & 0 & 0 & 0 & 0 & 0 \end{bmatrix}$$

Assembled geometric stiffness matrix,

$$\mathbf{K}_s = \begin{bmatrix} 5.11 & 0 & -3.79 & 0 & -1.35 & 0 & 0.03 & 0 \\ 0 & 5.11 & 0 & -3.79 & 0 & -1.35 & 0 & 0.03 \\ -3.79 & 0 & 3.91 & 0 & 1.00 & 0 & -1.12 & 0 \\ 0 & -3.79 & 0 & 3.91 & 0 & 1.00 & 0 & 1.12 \\ -1.35 & 0 & 1.00 & 0 & 0.36 & 0 & -0.009 & 0 \\ 0 & -1.35 & 0 & 1.00 & 0 & 0.36 & 0 & -0.009 \\ 0 & 0 & 0 & 0 & 0 & 0 & 0 & 0 \\ 0 & 0 & 0 & 0 & 0 & 0 & 0 & 0 \end{bmatrix}$$

The matrix for derivatives of shape functions of support domain,

$$\mathbf{B}_4^T = \begin{bmatrix} -0.209924441336 & 0.790075558664 & 0 & 0 \\ 0 & 0 & -0.209924441336 & 0.790075558664 \end{bmatrix}$$

Internal force vector,  $\mathbf{r}_4 = [-1.64834565951 \quad 0.974687054442]$

The matrix for derivatives of shape functions of support domain,

$$\mathbf{B}_i^T = \begin{bmatrix} -0.790075558664 & -0.790075558664 & 0 & 0 \\ 0 & 0 & -0.790075558664 & -0.790075558664 \end{bmatrix}$$

Material matrix,

$$\mathbf{D} = \begin{bmatrix} 231.089474011 & 208.538992457 & -14.5546440096 \\ 208.538992457 & 1229.43343515 & -33.5709797001 \\ -14.5546440096 & -33.5709797001 & 163.156634593 \end{bmatrix}$$

Current stiffness matrix,  $\mathbf{k}_c = \begin{bmatrix} -2.99 & -1.81 \\ -3.05 & -16.77 \end{bmatrix}$

Geometric stiffness matrix,  $\mathbf{k}_s = \begin{bmatrix} 0.03 & 0 \\ 0 & 0.03 \end{bmatrix}$

Assembled current stiffness matrix,

$$\mathbf{K}_c = \begin{bmatrix} 12.00 & 7.50 & -5.81 & -2.45 & -3.18 & -1.99 & -2.99 & -3.05 \\ 7.50 & 19.52 & -3.69 & 2.44 & -1.99 & -5.18 & -1.81 & -16.77 \\ -5.81 & -3.69 & 8.22 & -2.16 & 1.54 & 0.98 & -3.95 & 4.87 \\ -2.45 & 2.44 & -2.16 & 3.62 & 0.65 & -0.64 & 3.96 & -5.42 \\ -3.18 & -1.99 & 1.54 & 0.65 & 0.84 & 0.52 & 0.79 & 0.81 \\ -1.99 & -5.18 & 0.98 & -0.64 & 0.52 & 1.37 & 0.48 & 4.45 \\ -2.99 & -1.81 & 0 & 0 & 0 & 0 & 0 & 0 \\ -3.05 & -16.77 & 0 & 0 & 0 & 0 & 0 & 0 \end{bmatrix}$$

Assembled geometric stiffness matrix,

$$\mathbf{K}_s = \begin{bmatrix} 5.11 & 0 & -3.79 & 0 & -1.35 & 0 & 0.03 & 0 \\ 0 & 5.11 & 0 & -3.79 & 0 & -1.35 & 0 & 0.03 \\ -3.79 & 0 & 3.91 & 0 & 1.00 & 0 & -1.12 & 0 \\ 0 & -3.79 & 0 & 3.91 & 0 & 1.00 & 0 & 1.12 \\ -1.35 & 0 & 1.00 & 0 & 0.36 & 0 & -0.009 & 0 \\ 0 & -1.35 & 0 & 1.00 & 0 & 0.36 & 0 & -0.009 \\ 0.03 & 0 & 0 & 0 & 0 & 0 & 0 & 0 \\ 0 & 0.03 & 0 & 0 & 0 & 0 & 0 & 0 \end{bmatrix}$$

The matrix for derivatives of shape functions of support domain,

$$\mathbf{B}_2^T = \begin{bmatrix} 0.790075558664 & -0.209924441336 & 0 & 0 \\ 0 & 0 & 0.790075558664 & -0.209924441336 \end{bmatrix}$$

$$\text{Current stiffness matrix, } \mathbf{k}_c = \begin{bmatrix} -3.95 & 3.96 \\ 4.87 & -5.42 \end{bmatrix}$$

$$\text{Geometric stiffness matrix, } \mathbf{k}_s = \begin{bmatrix} -1.12 & 0 \\ 0 & -1.12 \end{bmatrix}$$

Assembled current stiffness matrix,

$$\mathbf{K}_c = \begin{bmatrix} 12.00 & 7.50 & -5.81 & -2.45 & -3.18 & -1.99 & -2.99 & -3.05 \\ 7.50 & 19.52 & -3.69 & 2.44 & -1.99 & -5.18 & -1.81 & -16.77 \\ -5.81 & -3.69 & 8.22 & -2.16 & 1.54 & 0.98 & -3.95 & 4.87 \\ -2.45 & 2.44 & -2.16 & 3.62 & 0.65 & -0.64 & 3.96 & -5.42 \\ -3.18 & -1.99 & 1.54 & 0.65 & 0.84 & 0.52 & 0.79 & 0.81 \\ -1.99 & -5.18 & 0.98 & -0.64 & 0.52 & 1.37 & 0.48 & 4.45 \\ -2.99 & -1.81 & -3.95 & 3.96 & 0 & 0 & 0 & 0 \\ -3.05 & -16.77 & 4.87 & -5.42 & 0 & 0 & 0 & 0 \end{bmatrix}$$

Assembled geometric stiffness matrix,

$$\mathbf{K}_s = \begin{bmatrix} 5.11 & 0 & -3.79 & 0 & -1.35 & 0 & 0.03 & 0 \\ 0 & 5.11 & 0 & -3.79 & 0 & -1.35 & 0 & 0.03 \\ -3.79 & 0 & 3.91 & 0 & 1.00 & 0 & -1.12 & 0 \\ 0 & -3.79 & 0 & 3.91 & 0 & 1.00 & 0 & 1.12 \\ -1.35 & 0 & 1.00 & 0 & 0.36 & 0 & -0.009 & 0 \\ 0 & -1.35 & 0 & 1.00 & 0 & 0.36 & 0 & -0.009 \\ 0.03 & 0 & -1.12 & 0 & 0 & 0 & 0 & 0 \\ 0 & 0.03 & 0 & -1.12 & 0 & 0 & 0 & 0 \end{bmatrix}$$

The matrix for derivatives of shape functions of support domain,

$$\mathbf{B}_3^T = \begin{bmatrix} 0.209924441336 & 0.209924441336 & 0 & 0 \\ 0 & 0 & 0.209924441336 & 0.209924441336 \end{bmatrix}$$

$$\text{Current stiffness matrix, } \mathbf{k}_c = \begin{bmatrix} 0.79 & 0.48 \\ 0.81 & 4.45 \end{bmatrix}$$

$$\text{Geometric stiffness matrix, } \mathbf{k}_s = \begin{bmatrix} -0.009 & 0 \\ 0 & -0.009 \end{bmatrix}$$

Assembled current stiffness matrix,

$$\mathbf{K}_c = \begin{bmatrix} 12.00 & 7.50 & -5.81 & -2.45 & -3.18 & -1.99 & -2.99 & -3.05 \\ 7.50 & 19.52 & -3.69 & 2.44 & -1.99 & -5.18 & -1.81 & -16.77 \\ -5.81 & -3.69 & 8.22 & -2.16 & 1.54 & 0.98 & -3.95 & 4.87 \\ -2.45 & 2.44 & -2.16 & 3.62 & 0.65 & -0.64 & 3.96 & -5.42 \\ -3.18 & -1.99 & 1.54 & 0.65 & 0.84 & 0.52 & 0.79 & 0.81 \\ -1.99 & -5.18 & 0.98 & -0.64 & 0.52 & 1.37 & 0.48 & 4.45 \\ -2.99 & -1.81 & -3.95 & 3.96 & 0.79 & 0.48 & 0 & 0 \\ -3.05 & -16.77 & 4.87 & -5.42 & 0.81 & 4.45 & 0 & 0 \end{bmatrix}$$

Assembled geometric stiffness matrix,

$$\mathbf{K}_s = \begin{bmatrix} 5.11 & 0 & -3.79 & 0 & -1.35 & 0 & 0.03 & 0 \\ 0 & 5.11 & 0 & -3.79 & 0 & -1.35 & 0 & 0.03 \\ -3.79 & 0 & 3.91 & 0 & 1.00 & 0 & -1.12 & 0 \\ 0 & -3.79 & 0 & 3.91 & 0 & 1.00 & 0 & 1.12 \\ -1.35 & 0 & 1.00 & 0 & 0.36 & 0 & -0.009 & 0 \\ 0 & -1.35 & 0 & 1.00 & 0 & 0.36 & 0 & -0.009 \\ 0.03 & 0 & -1.12 & 0 & -0.009 & 0 & 0 & 0 \\ 0 & 0.03 & 0 & -1.12 & 0 & -0.009 & 0 & 0 \end{bmatrix}$$

The matrix for derivatives of shape functions of support domain,

$$\mathbf{B}_4^T = \begin{bmatrix} -0.209924441336 & 0.790075558664 & 0 & 0 \\ 0 & 0 & -0.209924441336 & 0.790075558664 \end{bmatrix}$$

$$\text{Current stiffness matrix, } \mathbf{k}_c = \begin{bmatrix} 6.15 & -2.63 \\ -2.63 & 17.73 \end{bmatrix}$$

$$\text{Geometric stiffness matrix, } \mathbf{k}_s = \begin{bmatrix} 0 & 0 \\ 0 & 0 \end{bmatrix}$$

Assembled current stiffness matrix,

$$\mathbf{K}_c = \begin{bmatrix} 12.00 & 7.50 & -5.81 & -2.45 & -3.18 & -1.99 & -2.99 & -3.05 \\ 7.50 & 19.52 & -3.69 & 2.44 & -1.99 & -5.18 & -1.81 & -16.77 \\ -5.81 & -3.69 & 8.22 & -2.16 & 1.54 & 0.98 & -3.95 & 4.87 \\ -2.45 & 2.44 & -2.16 & 3.62 & 0.65 & -0.64 & 3.96 & -5.42 \\ -3.18 & -1.99 & 1.54 & 0.65 & 0.84 & 0.52 & 0.79 & 0.81 \\ -1.99 & -5.18 & 0.98 & -0.64 & 0.52 & 1.37 & 0.48 & 4.45 \\ -2.99 & -1.81 & -3.95 & 3.96 & 0.79 & 0.48 & 6.15 & -2.63 \\ -3.05 & -16.77 & 4.87 & -5.42 & 0.81 & 4.45 & -2.63 & 17.73 \end{bmatrix}$$

Assembled geometric stiffness matrix,

$$\mathbf{K}_s = \begin{bmatrix} 5.11 & 0 & -3.79 & 0 & -1.35 & 0 & 0.03 & 0 \\ 0 & 5.11 & 0 & -3.79 & 0 & -1.35 & 0 & 0.03 \\ -3.79 & 0 & 3.91 & 0 & 1.00 & 0 & -1.12 & 0 \\ 0 & -3.79 & 0 & 3.91 & 0 & 1.00 & 0 & 1.12 \\ -1.35 & 0 & 1.00 & 0 & 0.36 & 0 & -0.009 & 0 \\ 0 & -1.35 & 0 & 1.00 & 0 & 0.36 & 0 & -0.009 \\ 0.03 & 0 & -1.12 & 0 & -0.009 & 0 & 3.64 & 0 \\ 0 & 0.03 & 0 & -1.12 & 0 & -0.009 & 0 & 3.64 \end{bmatrix}$$

Tangential stiffness matrix,

$$\mathbf{K}_T = \begin{bmatrix} 37.72 & 13.37 & -18.33 & 2.06 & -19.01 & -13.98 & -0.38 & -1.46 \\ 13.37 & 53.40 & -0.56 & 8.61 & -14.27 & -28.61 & 1.46 & -33.40 \\ -18.33 & -0.56 & 39.09 & -14.88 & -1.75 & 1.16 & -19.01 & 14.27 \\ 2.06 & 8.61 & -14.88 & 61.87 & -1.16 & -41.87 & 13.98 & -28.61 \\ -19.01 & -14.27 & -1.75 & -1.16 & 39.09 & 14.88 & -18.33 & 0.56 \\ -13.98 & -28.61 & 1.16 & -41.87 & 14.88 & 61.87 & -2.06 & 8.61 \\ -0.38 & 1.46 & -19.01 & 13.98 & -18.33 & -2.06 & 37.72 & -13.37 \\ -1.46 & -33.40 & 14.27 & -28.61 & 0.56 & 8.61 & -13.37 & 53.40 \end{bmatrix}$$

External force vector,

$$\mathbf{R}_E = \begin{bmatrix} 0 \\ 0 \\ 50 \\ 0 \\ 25 \\ 0 \\ 0 \\ 0 \end{bmatrix}$$

Internal force vector,

$$\mathbf{R}_I = \begin{bmatrix} -17.6383579717 \\ -2.03537002612 \\ 17.6383579717 \\ 3.37248101854 \\ 17.6383579717 \\ -3.37248101852 \\ -17.6383579717 \\ 2.03537002610 \end{bmatrix}$$

Residual force vector,

$$\mathbf{R} = \mathbf{R}_E - \mathbf{R}_I = \begin{bmatrix} 17.6383579717 \\ 2.03537002612 \\ 7.36164202831 \\ -3.37248101854 \\ 7.36164202833 \\ 3.37248101852 \\ 17.6383579717 \\ -2.03537002610 \end{bmatrix}$$

System of equations

$$\mathbf{K}_T \begin{bmatrix} \Delta u_1 \\ \Delta v_1 \\ \Delta u_2 \\ \Delta v_2 \\ \Delta u_3 \\ \Delta v_3 \\ \Delta u_4 \\ \Delta v_4 \end{bmatrix} = \begin{bmatrix} 17.6383579717 \\ 2.03537002612 \\ 7.36164202831 \\ -3.37248101854 \\ 7.36164202833 \\ 3.37248101852 \\ 17.6383579717 \\ -2.03537002610 \end{bmatrix}$$

Essential boundary conditions:

Node	DOF	Value
1	$\Delta u_1$	0
	$\Delta v_1$	0
4	$\Delta u_4$	0
	$\Delta v_4$	0

Solution of system equations, we get

Node	$u$	$v$
1	0	0
2	0.196215871018	$-2.151724744991E - 03$
3	0.196215871019	$2.151724742667E - 03$
4	0	0

Total nodal values:

Node	$u$	$v$
1	0	0
2	0.647492554732	0.101678326392
3	0.647492554729	$-0.101678326391$
4	0	0

Current configuration II:

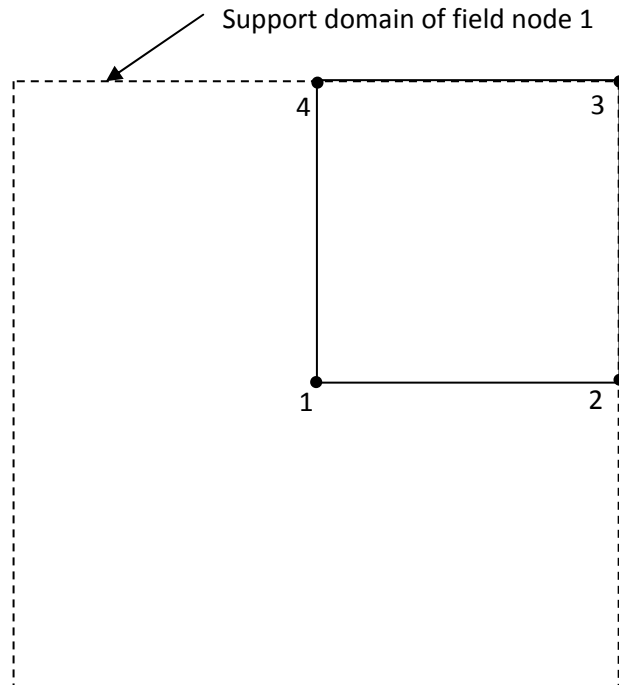
Field Node	X-coordinate	Y-coordinate
1	0	0
2	1	0
3	1	1
4	0	1

Updated coordinates		
Field Node	X-coordinate	Y-coordinate
1	0	0
2	1.647492554732	0.101678326392
3	1.647492554732	0.898321674
4	0	1

Computation for Cauchy stresses at  $\{0,0\}$  ;

Dimensions of the support domain:

$$d_x = 1 + 0.647492554732 \text{ and } d_y = 1 + 0.101678326392;$$



Nodes of support domain are; 1,2,3 and 4.

Interpolation functions and their derivatives:

Node	1	2	3	4
$\phi$	1.00000000000	0.00000000000	0.00000000000	0.00000000000
$\frac{\partial \phi}{\partial x}$	-0.98261272217	0.982612722173	0.01738727782706	-0.017387277827
$\frac{\partial \phi}{\partial y}$	-0.98261272217	-0.017387277827	0.01738727782707	0.982612722173

$$\mathbf{d} = \begin{bmatrix} 0.00 \\ 0.00 \\ 0.647492554732 \\ 0.101678326392 \\ 0.647492554732 \\ -0.101678326391 \\ 0.00 \\ 0.00 \end{bmatrix}$$

Deformation gradient,

$$F = \begin{bmatrix} 1.64749255473 & -4.445402379538E - 14 \\ 9.814250777226E - 02 & 0.996464181380 \end{bmatrix};$$

Right Cauchy-Green tensor,

$$c_1 = \begin{bmatrix} 2.72386366973 & 9.779549366580E - 02 \\ 9.779549366580E - 02 & 0.992940864773 \end{bmatrix}$$

$$\text{Left Cauchy-Green tensor, } c_2 = \begin{bmatrix} 2.71423171790 & 0.161689050857 \\ 0.161689050857 & 1.00257281661 \end{bmatrix}$$

$$\text{Cauchy stresses, } \hat{\sigma} = \begin{bmatrix} 587.716066780 & 46.4747612840 \\ 46.4747612840 & 95.7288950128 \end{bmatrix}$$

Computation for Cauchy stresses at  $\{1, 0\}$ ;

Nodes of support domain are; 1,2,3 and 4.

Interpolation functions and their derivatives:

Node	1	2	3	4
$\phi$	0.000000000000	1.000000000000	0.000000000000	0.000000000000
$\frac{\partial \phi}{\partial x}$	-0.98261272217	0.98261272217	0.0173872778269	-0.0173872778269
$\frac{\partial \phi}{\partial y}$	-0.0173872778269	-0.98261272217	0.98261272217	0.01738727782693

Deformation gradient,

$$F = \begin{bmatrix} 1.64749255473 & -2.508215857233E - 12 \\ 9.814250777228E - 02 & 0.800179165837 \end{bmatrix};$$

Right Cauchy-Green tensor,

$$c_1 = \begin{bmatrix} 2.72386366973 & 7.853158999824E - 02 \\ 7.853158999824E - 02 & 0.640286697440 \end{bmatrix}$$

$$\text{Left Cauchy-Green tensor, } c_2 = \begin{bmatrix} 2.71423171790 & 0.161689050856 \\ 0.161689050856 & 0.649918649271 \end{bmatrix}$$

$$\text{Cauchy stresses, } \hat{\sigma} = \begin{bmatrix} 631.616045025 & 53.7939542833 \\ 53.7939542833 & -55.1810030893 \end{bmatrix}$$

Computation for Cauchy stresses at  $\{1, 1\}$ ;

Nodes of support domain are; 1,2,3 and 4.

Interpolation functions and their derivatives:

Node	1	2	3	4
$\phi$	0.000000000000	0.000000000000	1.000000000000	0.000000000000
$\frac{\partial \phi}{\partial x}$	-1.738727782693E-02	0.0173872778269	0.982612722173	-0.982612722173
$\frac{\partial \phi}{\partial y}$	-0.0173872778269	-0.982612722173	0.982612722173	0.0173872778269

Deformation gradient,

$$F = \begin{bmatrix} 1.64749255473 & -2.508215857233E - 12 \\ -9.814250777086E - 02 & 0.800179165837 \end{bmatrix};$$

Right Cauchy-Green tensor,

$$c_1 = \begin{bmatrix} 2.72386366972 & -7.853159000536E - 02 \\ -7.853159000536E - 02 & 0.640286697440 \end{bmatrix}$$

Left Cauchy-Green tensor,  $c_2 = \begin{bmatrix} 2.71423171789 & -0.161689050857 \\ -0.161689050857 & 0.649918649271 \end{bmatrix}$

$$\text{Cauchy stresses, } \hat{\sigma} = \begin{bmatrix} 631.616045023 & -53.7939542838 \\ -53.7939542838 & -55.1810030899 \end{bmatrix}$$

Computation for Cauchy stresses at  $\{0, 1\}$ ;

Nodes of support domain are; 1,2,3 and 4.

Interpolation functions and their derivatives:

Node	1	2	3	4
$\phi$	0.000000000000	0.000000000000	0.000000000000	1.000000000000
$\frac{\partial \phi}{\partial x}$	-0.017387277826	0.01738727782693	0.982612722173	-0.98261272217
$\frac{\partial \phi}{\partial y}$	-0.982612722173	-0.01738727782696	0.01738727782696	0.982612722173

Deformation gradient,

$$F = \begin{bmatrix} 1.64749255473 & -4.436208345115E - 14 \\ -9.814250777086E - 02 & 0.996464181380 \end{bmatrix};$$

Right Cauchy-Green tensor,

$$c_1 = \begin{bmatrix} 2.72386366972 & -9.779549366455E - 02 \\ -9.779549366455E - 02 & 0.992940864774 \end{bmatrix}$$

Left Cauchy-Green tensor,  $c_2 = \begin{bmatrix} 2.71423171789 & -0.161689050855 \\ -0.161689050855 & 1.00257281661 \end{bmatrix}$

$$\text{Cauchy stresses, } \hat{\sigma} = \begin{bmatrix} 587.716066778 & -46.4747612833 \\ -46.4747612833 & 95.7288950126 \end{bmatrix}$$

$$\|\mathbf{u}_{r+1} - \mathbf{u}_r\|_2 = 7.701059591799E - 02$$

$$\|\mathbf{u}_{r+1}\|_2 = 0.859170180978$$

$$\text{convergence parameter} = \frac{\|\mathbf{u}_{r+1} - \mathbf{u}_r\|_2}{\|\mathbf{u}_{r+1}\|_2} = 0.299388865239$$



## LIST OF REFERENCES

- [1] Liu G.R. (2003). *Meshfree methods: moving beyond the finite element method*. CRC Press, Boca Raton.
- [2] Liu G.R., Gu Y.T. (2005), *An introduction to Meshfree methods and their programming*. Springer: Berlin.
- [3] Lucy L.B. (1977). A numerical approach to the testing of the fission hypothesis. *The Astronomical Journal*, **82 (12)**, 1013-1024.
- [4] Gingold R.A., Monaghan J.J. (1977). Smoothed particle hydrodynamics - Theory and application to non-spherical stars. *Mon. Not. R. Astr. Soc.*, **181**,375-389.
- [5] Liu G.R. (2003). *Smoothed Particle Hydrodynamics - A Meshfree Particle Method*. World Scientific, New Jersey.
- [6] Liu W.K., Li S. (2002). Meshfree and particle methods and their applications. *Appl. Mech. Rev.*, **55 (1)**, 34 pages (doi:10.1115/1.1431547).
- [7] Nayroles B., Touzot G. and Villon P. (1992). Generalizing the finite element method: diffuse approximation and diffuse elements. *Comp. Mech.*, **10**, 307-318.
- [8] Breitkopf P., Rassinieux A., Savignat J.M., Villon P. (2004). Integration constraint in diffuse element method. *Comput. Methods Appl. Mech. Engrg.*, **193**, 1203-1220.
- [9] Belytschko, T., Lu. Y.Y. and Gu, L. (1994). Element-free Galerkin methods. *Int. J. Numer. Meth. Engng.*, 37, 229-256.
- [10] Belytschko T., Y. Krongauz, D. Organ, et al. (1996). Meshless method: an overview and recent developments. *Comput. Methods Appl. Mech. Eng.*, **139**, 3-47.
- [11] Lu Y.Y., TBelytschko T., Gu L.( 1994). A new implementation of the element free Galerkin method, *Comput. Methods Appl. Mech. Eng.*, **113**, 397-414.

- [12] Belytschko T., Krongauz Y., Fleming M., et al. (1996). Smoothing and accelerated computations in the element free Galerkin method, *Comput. Appl. Math.*, **74**, 111-126.
- [13] Mukherjee Y.X., Mukherjee S. (1997). On boundary conditions in the element-free Galerkin method, *Computational Mechanics* **19**, 264-270.
- [14] Kaljevic I., Saigal S. (1997). An improved element free Galerkin formulation, *Int. J. Numer. Meth. Engng.*, **40**, 2953-2974.
- [15] Zhu T., Atluri S.N. (1998). A modified collocation method and a penalty formulation for enforcing the essential boundary conditions in the element free Galerkin method, *Computational Mechanics* **21**, 211-222.
- [16] Lei Gu, (2003). Moving kriging interpolation and element-free Galerkin method, *Int. J. Numer. Meth. Engng.*, **56**:1-11
- [17] Pang Zuohui (2000). Treatment of point loads in element free Galerkin method (EFGM), *Commun. Numer. Meth. Engng.*, **16**:335-341.
- [18] Huerta A., Mendez S.F. (2001). Locking in the incompressible limit for the element-free Galerkin method, *Int. J. Numer. Meth. Engng.*, **51**:1361-1383.
- [19] Recio D.P., Jorge R.M.N., Dinis L.M.S. (2007). On the use of element-free Galerkin Method for problems involving incompressibility, *Engineering Analysis with Boundary Elements*, **31**, 103-115.
- [20] Dolbow J., Belytschko T. (1999). Volumetric locking in the element free Galerkin method, *Int. J. Numer. Meth. Engng.*, **46(6)**; 925-942
- [21] Belytschko T., L. Gu, and Lu Y.Y. (1994). Fracture and crack growth by element free Galerkin methods, *Modeling Simulations Mater. Sci. Eng.*, **2**, 519-534.
- [22] Belytschko T., Y. Y. Lu, L. Gu and M. Tabbara (1995). Element-free Galerkin methods for static and dynamic fracture, *Int. J. Solids Structures*, **32**, 2547-2570.
- [23] Sukumar N., Moran B., Black T., Belytschko T. (1997). An element-free Galerkin method for three-dimensional fracture mechanics, *Computational Mechanics* **20**, 170-175.
- [24] Xu Y., Saigal S. (1998). Element free galerkin study of steady quasi-static crack growth in plane strain tension in elastic-plastic materials, *Computational Mechanics* **22**, 255-265.

- [25] Krysl P., Belytschko T. (1999). The Element Free Galerkin method for dynamic propagation of arbitrary 3-D cracks, *Int. J. Numer. Meth. Engng*, **44** (6): 767-800.
- [26] Xu Y., Saigal S. (1999). An Element Free Galerkin analysis of steady dynamic growth of a mode I crack in elastic-plastic materials, *International Journal of Solids and Structures*, **36** (7): 1045-1079.
- [27] Lee S.H., Yoon Y.C. (2003). An improved crack analysis technique by element-free Galerkin method with auxiliary supports, *Int. J. Numer. Meth. Engng.*, **56**:1291-1314.
- [28] Lee G.H., Chung H.J, Choi C.K. (2003). Adaptive crack propagation analysis with the element-free Galerkin method, *Int. J. Numer. Meth. Engng.*, **56**:331-350.
- [29] Brighenti R. (2005). Application of the element-free Galerkin meshless method to 3-D fracture mechanics problems, *Engineering Fracture Mechanics* **72**, 2808-2820.
- [30] Krysl P., Belytschko T. (1995). Analysis of thin plates by the element-free Galerkin method, *Journal Computational Mechanics*, **17**, 26-35.
- [31] Nukulchai W.K., Barry W., Yasoontorn K.S., Bouillard P.H. (2001). On elimination of shear locking in the element-free Galerkin method, *Int. J. Numer. Meth. Engng.*, **52**:705-725.
- [32] Nair R.G., Rao G.V., Singh G. (2003). Demonstration of a simple method to satisfy homogenous boundary conditions in element-free Galerkin method through the vibration problem of Timoshenko beam, *Commun. Numer. Meth. Engng.*, **19**:155-168
- [33] Liew K.M., Ren J., Kitipornchai S. (2004). Analysis of the pseudoelastic behavior of a SMA beam by the element-free Galerkin method, *Engineering Analysis with Boundary Elements* **28**, 497-507.
- [34] Dai K.Y., Liu G.R., Han X., Lim K.M. (2005). Thermomechanical analysis of functionally graded material (FGM) plates using element-free Galerkin method, *Computers and Structures* **83**, 1487-1502.
- [35] Liu L., Chua L.P., Ghista D.N. (2006). Element-free Galerkin method for static and dynamic analysis of spatial shell structures, *Journal of Sound and Vibration* **295**, 388-406.

- [36] Belinha J., Dinis L.M.J.S. (2006). Elasto-plastic analysis of plates by the element free Galerkin method *Engineering Computations*, **23 (5-6)**: 525-551.
- [37] Belinha J., Dinis L.M.J.S. (2006). Analysis of plates and laminates using the element-free Galerkin method, *Computers and Structures* **84**, 1547-1559.
- [38] Belinha J., Dinis L.M.J.S. (2007). Nonlinear analysis of plates and laminates using the element free Galerkin method, *Composite Structures* **78**, 337-350.
- [39] Liew K.M., Lim H.K., Tan M.J., He X.Q. (2002). Analysis of laminated composite beams and plates with piezoelectric patches using the element-free Galerkin method, *Computational Mechanics* **29**, 486-497.
- [40] Chen X.L., Liu G.R., Lim S.P. (2003). An element free Galerkin method for the free vibration analysis of composite laminates of complicated shape, *Composite Structures* **59**, 279-289.
- [41] Singh I.V., Masa Tanaka, Endo M. (2007). Thermal analysis of CNT-based nano-composites by element free Galerkin method, *Comput Mech*, **39**: 719-728.
- [42] Belytschko T., D. Organ, Y. Krongauz (1995). A coupled finite element-element-free Galerkin method, *Journal Computational Mechanics*, **17(3)**, 186-195.
- [43] Liu G.R., Gu Y.T. (2000). Coupling of element free Galerkin and hybrid boundary element methods using modified variational formulation, *Computational Mechanics* **26 (2)**: 166-173.
- [44] Gu Y.T., Liu G.R. (2001). A coupled element free Galerkin/boundary element method for stress analyses of two dimensional solids, *Comput. Methods Appl. Mech. Eng.*, **190**, 4405-4419.
- [45] Gu Y.T., Liu G.R. (2003). Hybrid boundary point interpolation methods and their coupling with the element free Galerkin method, *Engineering Analysis with Boundary Elements*, **27**, 905-917
- [46] Zhao G.M., Song S.C. (2005). New algorithm of coupling element-free Galerkin with finite element method, *Applied mathematics and mechanics-English edition* **26 (8)**: 982-988.

- [47] Denoual C. (2007). Modeling dislocation by coupling Peierls-Nabarro and element-free Galerkin methods, *Comput. Methods Appl. Mech. Engrg.* **196**, 1915-1923.
- [48] Barry W., Saigal S. (1999). A three-dimensional element-free Galerkin elastic and elastoplastic formulation, *Int. J. Numer. Meth. Engng.* **46**, 671-693.
- [49] Pamin J., Askes H., de Borst R. (2003). Two gradient plasticity theories discretized with the element-free Galerkin method, *Comput. Methods Appl. Mech. Engrg.* **192**, 2377-2403.
- [50] Kargarnovin M. H., Toussi H. E., Fariborz S. J. (2004). Elasto-plastic element-free Galerkin method, *Computational Mechanics* **33**, 206-214.
- [51] Bobaru F., Mukherjee S. (2001). Shape sensitivity analysis and shape optimization in planar elasticity using the element-free Galerkin method, *Comput. Methods Appl. Mech. Engrg.*, **190 (32-33)**: 4319-4337.
- [52] Gurgel A.G., W.F. Sales, C.S. de Barcellos, J. Bonney, E.O. Ezugwu (2006). An element-free Galerkin method approach for estimating sensitivity of machined surface parameters, *International Journal of Machine Tools & Manufacture* **46**, 1637-1642.
- [53] Modaressi H., Aubert P. (1998). Element-free Galerkin method for deforming multiphase porous media, *Int. J. Numer. Meth. Engng.* **42**, 313-340.
- [54] Karim M.R., Nogami T., Wang J.G. (2002). Analysis of transient response of saturated porous elastic soil under cyclic loading using element-free Galerkin method, *International Journal of Solids and Structures* **39**, 6011-6033.
- [55] Rossi R., Alves M.K. (2004). Recovery based error estimation and adaptivity applied to a modified element-free Galerkin method, *Computational Mechanics*, **33 (3)**: 194-205.
- [56] Lee C.K., Zhou C.E. (2004). On error estimation and adaptive refinement for element free Galerkin method Part I: stress recovery and a posteriori error estimation, *Computers and Structures* **82**, 413-428.
- [57] Lee C.K., Zhou C.E. (2004). On error estimation and adaptive refinement for element free Galerkin method Part II: adaptive refinement, *Computers and Structures* **82**, 429-443.

- [58] Bobaru F., Rachakonda S. (2006). E(FG)2: a new fixed-grid shape optimization method based on the element-free galerkin mesh-free analysis, *Struct Multidisc Optim*, **32**: 215-228.
- [59] Luo Y., Combe U.H. (2003). A gradient-based adaptation procedure and its implementation in the element-free Galerkin method, *Int. J. Numer. Meth. Engng*; **56**:1335-1354.
- [60] Singh I.V., Tanaka M. (2006). Heat transfer analysis of composite slabs using meshless element free Galerkin method, *Comput. Mech.* **38**: 521-532.
- [61] Ling Liu, Haitian Yang (2007). A paralleled element-free Galerkin analysis for structures with cyclic symmetry, *Engineering with Computers*, **23**:137-144.
- [62] Saigal S., Barry W. (2000). A slices based Element Free Galerkin formulation, *Computational Mechanics* **25**, 220-229.
- [63] Atluri S.N. and Zhu T. (1998). A new meshless local Petrov-Galerkin (MLPG) approach in computational mechanics, *Computational Mechanics*, **22**, 117-127.
- [64] Krongauz Y., Belytschko T., A Petrov-Galerkin Diffuse Element Method (PG DEM) and its comparison to EFG, *Computational Mechanics* **19** (1997) 327-333.
- [65] Huang M. (2006). A construction of multiscale bases for Petrov-Galerkin methods for integral equations, *Advances in Computational Mathematics* **25**: 7-22.
- [66] Deeks A.J., Augarde C.E. (2005). A meshless local Petrov-Galerkin scaled boundary method, *Comput Mech* **36**: 159-170
- [67] Zhang Y. (2006). Convergence of meshless Petrov-Galerkin method using radial basis functions, *Applied Mathematics and Computation* **183**, 307-321.
- [68] Wang K., Zhou S., Shan G. (2005). The natural neighbour Petrov-Galerkin method for elasto-statics, *Int. J. Numer. Meth. Engng.*, **63**:1126-1145
- [69] Atluri S.N., Shen S. (2005). The basis of meshless domain discretization: the meshless local Petrov-Galerkin (MLPG) method, *Advances in Computational Mathematics*, **23**: 73-93.

- [70] Deeks A.J., Augarde C.E. (2007). A hybrid meshless local Petrov-Galerkin method for unbounded domains, *Comput. Methods Appl. Mech. Engrg.* **196**, 843-852.
- [71] Chen T., Raju I.S. (2003). A coupled finite element and meshless local Petrov-Galerkin method for two-dimensional potential problems, *Comput. Methods Appl. Mech. Engrg.* **192**, 4533-4550.
- [72] Atluri S.N., Zhu T.L. (2000). The meshless local Petrov-Galerkin (MLPG) approach for solving problems in elasto-statics, *Computational Mechanics* **25**, 169-179.
- [73] Atluri S. N., Cho J.Y., Kim H.G. (1999). Analysis of thin beams, using the meshless local Petrov-Galerkin method, with generalized moving least squares interpolations, *Computational Mechanics* **24**, 334-347.
- [74] Qian L.F., Batra R.C. Chen L.M. (2004). Analysis of cylindrical bending thermoelastic deformations of functionally graded plates by a meshless local Petrov-Galerkin method, *Computational Mechanics* **33**, 263-273.
- [75] Li Q., Soric J., Jarak T., Atluri S.N. (2005). A locking-free meshless local Petrov-Galerkin formulation for thick and thin plates, *Journal of Computational Physics* **208**, 116-133.
- [76] Sladek J., Sladek V., Zhang Ch., Krivacek J., Wen P. H. (2006). Analysis of orthotropic thick plates by meshless local Petrov-Galerkin (MLPG) method, *Int. J. Numer. Meth. Engng.*, **67**:1830-1850.
- [77] Sladek J., Sladek V., Krivacek J., Wen P. H., Zhang Ch., Sladek J. (2007). Meshless local Petrov-Galerkin (MLPG) method for Reissner-Mindlin plates under dynamic load, *Comput. Methods Appl. Mech. Engrg.* **196**, 2681-2691.
- [78] Liu G.R., Gu Y.T. (2000). Meshless local Petrov-Galerkin (MLPG) method in combination with finite element and boundary element approaches *Computational Mechanics*, **26**,536-546.
- [79] Batra R.C., Porfiri M., Spinello D. (2004). Treatment of material discontinuity in two meshless local Petrov-Galerkin (MLPG) formulations of axisymmetric transient heat conduction, *Int. J. Numer. Meth. Engng.*, **61**:2461-2479.

- [80] Wu Y.L., Liu G.R., Gu Y.T. (2005). Application of meshless local Petrov-Galerkin (MLPG) approach to simulation of incompressible flow, *Numerical Heat Transfer, Part B*, **48**: 459-475.
- [81] Sladek J., Sladek V., Hellmich Ch., Eberhardsteiner J. (2007). Heat conduction analysis of 3-D axisymmetric and anisotropic FGM bodies by meshless local Petrov-Galerkin method, *Comput. Mech.* **39**: 323-333.
- [82] YT Gu, GR Liu (2001). A meshless local Petrov-Galerkin (MLPG) method for free and forced vibration analyses for solids, *Computational Mechanics* **27 (3)**: 188-198.
- [83] Cho J.R., Lee H.W. (2007). 2-D frictionless dynamic contact analysis of large deformable bodies by Petrov-Galerkin natural element method, *Computers and Structures*.
- [84] Bialecki B., Ganesh M., Mustapha K. (2006). A Petrov-Galerkin Method with Quadrature for Semi-linear Second-order Hyperbolic Problems, *Numerical Methods for Partial Differential Equations*, **22**, 1052-1069.
- [85] Tang Z., Shen S., Atluri S.N. (2003). Analysis of Materials with Strain-Gradient Effects: A Meshless Local Petrov-Galerkin(MLPG) Approach, with Nodal Displacements only, *CMES*, 4, 1, 177-196.
- [86] Wang J.G. and Liu G.R. (2002), A point interpolation meshless method based on radial basis functions, *Int. J. Numer. Meth. Engng* ; **54**:1623–1648.
- [87] Liu G.R., Gu Y.T., Dai K.Y. (2004), Assessment and applications of point interpolation methods for computational mechanics, *Int. J. Numer. Meth. Engng* **59** (10): 1373-1397.
- [88] Liu GR. (1999). A point assembly method for stress analysis for solid. In *Impact Response of Materials and Structures*, Shim VPW et al. (eds), Oxford University Press, 475–480.
- [89] Gosz J., Liu W.K. (1996), Admissible approximations for essential boundary conditions in the reproducing kernel particle method., *Computat. Mech.* 19, 120-135.
- [90] Günther F.C., Liu W.K. (1998), Implementation of boundary conditions for meshless methods. *Comput. Meth. Appl. Mech. Engng.*, 163(1-4), 205-230.



- [91] Liu G.R., Yang K.Y. (1998), In: A penalty method for enforcing essential boundary conditions in element free Galerkin method., *Proceedings of the Second HPC Asia'98*, Singapore, 715-721.
- [92] Liu W.K., Chen Y., Jun S., Chen J.S., Belytschko T., Pan C., Uras R.A., Chang C.T. (1996), Overview and applications of the reproducing kernel particle methods. *Arch. Comput. Meth. Engrg.*, State Art Rev. 3,3-80.
- [93] Liu, G.R., Gu Y.T. (1999), A point interpolation method, *in Proc. 4th Asia-Pacific Conference on Computational Mechanics*, Singapore, 1009-1014.
- [94] Liu G.R., Gu Y.T. (2001), A point interpolation method for two-dimensional solids, *Int. J. Numer. Methods Engrg.* **50**, 937–951.
- [95] Liu G.R., Gu Y.T. (2003), A matrix triangularization algorithm for the polynomial point interpolation method, *Comput. Methods Appl. Mech. Engrg.*; **192**: 2269–2295.
- [96] K. Y. Dai, G. R. Liu, K. M. Lim, Y. T. Gu (2003). Comparison between the radial point interpolation and the Kriging interpolation used in meshfree methods, *Comput. Mech.* **32**, 60–70.
- [97] Schaback R, Wendland H.(2000). Characterization and construction of radial basis functions. In *Multivariate Approximation and Applications*, Dyn N, Leviatan D, Levin D, Pinkus A (eds). Cambridge University Press: Cambridge, MA.
- [98] Powell MJD. (1992). The theory of radial basis function approximation in 1990. In *Advances in Numerical Analysis* Light FW (ed.). OUP: Oxford, UK., 303–322.
- [99] Fang H and Wang Q, On the effectiveness of assessing model accuracy at design points for radial basis functions, *Commun. Numer. Meth. Engng* (in press).
- [100] Liu G.R. (2006). Zhang J, Li H, Lam KY, Kee BBT, Radial point interpolation based finite difference method for mechanics problems, *Int. J. Numer. Meth. Engng.*, **68**:728–754.
- [101] Liu X, Liu GR, Tai K, Lam KY, (2005). Radial point interpolation collocation method (RPICM) for the solution of nonlinear poisson problems, *Comput. Mech.*, **36**: 298–306.

- [102] Kanber B., Bozkurt Ö.Y. (2008). A diagonal offset algorithm for the polynomial point interpolation method, *Commun. Numer. Meth. Engng.*, **24**, 1909-1922.
- [103] Gu, Y.T. and Liu, G.R. (2001). A Local Point Interpolation Method (LPIM) For Static And Dynamic Analysis Of Thin Beams, *Computer Methods in Applied Mechanics and Engineering*. **190**, 5515-5528.
- [104] G.R. Liu, G.Y. Zhang, Y.Y. Wang, Z.H. Zhong, G.Y. Li, X. Han (2007). A nodal integration technique for meshfree radial point interpolation method (NI-RPIM), *International Journal of Solids and Structures* **44**, 3840-3860.
- [105] C. Zuppa, A. Cardona (2003). A collocation meshless method based on local optimal point interpolation, *Int. J. Numer. Meth. Engng*, **57 (4)**: 509-536.
- [106] Y. L. Wu, G. R. Liu (2003). A meshfree formulation of local radial point interpolation method (LRPIM) for incompressible flow simulation, *Computational Mechanics*, **30 (5-6)**: 355-365.
- [107] G. R. Liu and Y. T. Gu (2001). A local radial point interpolation method (LRPIM) for free vibration analyses of 2-d solids, *Journal of Sound and Vibration*, **246(1)**, 29-46.
- [108] Liu GR, Gu YT. (2001). A local point interpolation method for stress analysis of two-dimensional solids. *Structural Engineering and Mechanics*, **11(2)**:221–236.
- [109] Gu Y.T., Liu G.R. (2002), A boundary point interpolation method for stress analysis of solids, *Computational Mechanics*, **28**, 47-54.
- [110] Liu G.R., Zhang G.Y. (2008), Upper bound solution to elasticity problems: A unique property of the linearly conforming point interpolation method (LCPIM), *Int. J. Numer. Meth. Engng.*, **74**, 1128–1161.
- [111] Liu G.R., Zhang G.Y., Dai K.Y. (2005), A linearly conforming point interpolation method (LC-PIM) for 2D solid mechanics problems., *International Journal of Computational Methods*, **2 (4)**, 645-665.
- [112] Zhang G.Y., Liu G.R., Wang Y.Y., Huang H.T., Zhong Z.H., Li G.Y., Han X. (2007), A linearly conforming point interpolation method (LC-

- PIM) for three-dimensional elasticity problems., *Int. J. Numer. Meth. Engng.*, **72**, 1524–1543.
- [113] Xu X., Liu G.R., Zhang G.Y. (2009), A point interpolation method with least square strain field (PIM-LSS) for solution bounds and ultra-accurate solutions using triangular mesh., *Comput. Methods Appl. Mech. Engrg.*, **198**, 1486–1499.
- [114] Liu G.R., Xu X., Zhang G.Y., Gu Y.T. (2009), An extended Galerkin weak form and a point interpolation method with continuous strain field and superconvergence., *Comput. Mech.*, **43**, 651–673.
- [115] Liu G.R., Gu Y.T. (2004), Boundary meshfree methods based on the boundary point interpolation methods., *Engineering Analysis with Boundary Elements*, **28**, 475–487.
- [116] Liu G.R., Gu Y.T. (2002), Comparisons of two meshfree local point interpolation methods for structural analyses. *Computational Mechanics*, **29**, 107–121.
- [117] L. Liu, L.P. Chua, D.N. Ghista (2007). Applications of point interpolation method for spatial general shells structures, *Comput. Methods Appl. Mech. Engrg.* **196**, 1633–1647.
- [118] S.C. Wu, G.R. Liu, H.O. Zhang, G.Y. Zhang (2009). A node-based smoothed point interpolation method (NS-PIM) for thermoelastic problems with solution bounds. *International Journal of Heat and Mass Transfer*, 52: 1464-1471.
- [119] G. R. Liu, K. Y. Dai, K. M. Lim, Y. T. Gu (2002). A point interpolation mesh free method for static and frequency analysis of two-dimensional piezoelectric structures, *Comp. Mech.*, **29**, 510–519.
- [120] Li H., Wang Q.X., Lam K.Y. (2004). A variation of local point interpolation method (vLPIM) for analysis of microelectromechanical systems (MEMS) device. *Engineering Analysis with Boundary Elements*, **28**, 1261–1270.
- [121] Gu Y.T., Liu G.R. (2003), Hybrid boundary point interpolation methods and their coupling with the element free Galerkin method., *Engineering Analysis with Boundary Elements*, **27**, 905–917.

- [122] G. R. Liu, G. Y. Zhang, Y. T. Gu, Y. Y. Wang (2005). A meshfree radial point interpolation method (RPIM) for three-dimensional solids, *Comput Mech.*, **36**: 421–430.
- [123] L. M. J. S. Dinis, R. M. N. Jorge, J. Belinha (2007). Analysis of 3D solids using the natural neighbour radial point interpolation method, *Comput. Methods Appl. Mech. Engrg.* **196 (13-16)**: 2009-2028.
- [124] Liu G.R., Dai K.Y., Lim K.M. and Gu Y.T. (2003), A Radial Point Interpolation Method For Simulation Of Two-Dimensional Piezoelectric Structures, *Smart Materials and Structures*, 12, 171-180.
- [125] Liew K.M., Chen X.L. (2004), Buckling of rectangular Mindlin plates subjected to partial in-plane edge loads using the radial point interpolation method, *International Journal of Solids and Structures*, **41 (5-6)**: 1677-1695
- [126] K. M. Liew, X. L. Chen (2004). Mesh-free radial point interpolation method for the buckling analysis of Mindlin plates subjected to in-plane point loads, *Int. J. Numer. Meth. Engng*, **60 (11)**: 1861-1877.
- [127] Y. Liu, Y. C. Hon, K. M. Liew (2006). A meshfree Hermite-type radial point interpolation method for Kirchhoff plate problems, *Int. J. Numer. Meth. Engng*, **66 (7)**: 1153-1178.
- [128] K. Y. Dai, G. R. Liu, K. M. Lim, X. Han, S. Y. Du (2004). A meshfree radial point interpolation method for analysis of functionally graded material (FGM) plates, *Computational Mechanics* **34**, 213–223.
- [129] K. M. Liew, X. L. Chen and J. N. Reddy (2004), Mesh-free radial basis function method for buckling analysis of non-uniformly loaded arbitrarily shaped shear deformable plates, *Comput. Methods in Applied Mechanics and Engineering*, 193 (3-5), 205-224.
- [130] L. Liu, L. P. Chua, D. N. Ghista (2006). Conforming radial point interpolation method for spatial shell structures on the stress-resultant shell theory, *Archive of applied mechanics*, **75 (4-5)**: 248-267.
- [131] Y. Li, G.R. Liu, M. T. Luan, K.Y. Dai, Z.H. Zhong, G.Y. Li, X. Han (2007). Contact analysis for solids based on linearly conforming radial point interpolation method, *Comput. Mech.*, **39**: 537–554.

- [132] W. Hu, L. G. Yao, Z. Z. Hua (2007). Parallel point interpolation method for three-dimensional metal forming simulations, *Engineering analysis with Boundary Elements*, **31** (4): 326-342.
- [133] X. Zhao, G.R. Liu, K.Y. Dai, Z.H. Zhong, G.Y. Li, X. Han (2009). Free-vibration analysis of shells via a linearly conforming radial point interpolation method (LC-RPIM), *Finite Elements in Analysis and Design*, **45**, 917–924.
- [134] X. Zhao, G. R. Liu, K. Y. Dai, Z. H. Zhong, G. Y. Li, X. Han (2009). A linearly conforming radial point interpolation method (LC-RPIM) for shells, *Comput. Mech*, **43**, 403–413.
- [135] X. Zhao, G. R. Liu, K. Y. Dai, Z. H. Zhong, G. Y. Li, X. Han (2008). Geometric nonlinear analysis of plates and cylindrical shells via a linearly conforming radial point interpolation method, *Comput Mech*, **42**, 133–144.
- [136] J. G. Wang, G. R. Liu (2002). On the optimal shape parameters of radial basis functions used for 2-D meshless methods, *Comput. Methods Appl. Mech. Engrg.* **191**, 2611–2630.
- [137] L.M.J.S. Dinis, R.M. Natal Jorgea, J. Belinha (2008). Analysis of plates and laminates using the natural neighbour radial point interpolation method, *Engineering Analysis with Boundary Elements*, **32**, 267–279.
- [138] Kargamovin M.H., Toussi H.E., Fariborz S.J. (2004). Elasto-plastic element-free Galerkin method. *Computational Mechanics*, **33**, 206-214.
- [139] Rao B.N., Rahman S. (2004). An enriched meshless method for non-linear fracture mechanics. *Int. J. Numer. Meth. Engng.*, **59**, 197-223.
- [140] Xu Y., Saigal S. (1999). An Element Free Galerkin analysis of steady dynamic growth of a mode I crack in elastic-plastic materials. *International Journal of Solids and Structures*, **36**, 1045-1079.
- [141] Xu Y., Saigal S. (1998). Element free galerkin study of steady quasi-static crack growth in plane strain tension in elastic-plastic materials. *Computational Mechanics*, **22**, 255-265.

- [142] Belinha J., Dinis L.M.J.S., (2006). Elasto-plastic analysis of plates by the element free Galerkin method. *Engineering Computations*, **23(5)**, 525 – 551.
- [143] Liu T., Liu G., Wang Q.(2006). An elemen-free Galerkin-finite element coupling method for elastoplastic contact problem, *J. Tribol.*, **128**, 1–9.
- [144] Liu L., Dong X., Li C. (2009). Adaptive finite element-element-free Galerkin coupling method for bulk metal forming process. *Journal Zhejiang University Science A.*, **10(3)**, 353-360.
- [145] Barry W., Saigal S. (1999). A three-dimensional element-free Galerkin method elastic and elastoplastic formulation. *Int. J. Numer. Meth. Engng.*, **46**, 671-693.
- [146] Guo Y.M., Naknishi K., Yokouchi Y. (2005). A nonlinear rigid-plastic analysis for metal forming problem using the rigid-plastic point collocation method. *Advances in Engineering Software*, **36**, 234-242.
- [147] Liu W.K., Jun S., Li S. Andee J., Belytschko T. (1995). Reproducing kernel particle methods for structural dynamics. *Int. J. Numer. Methods Eng.*, **38**, 1655-1679.
- [148] Chen J.S., Pan C., Wu C.T., Roque C. (1998). A Lagrangian reproducing kernel particle method for metal forming analysis. *Comput Mech.*, **22**, 289–307.
- [149] Shangwu X., Liu W.K., Cao J., Rodriques J.M.C., Martins P.A.F. (2003). On the utilization of reproducing kernel particle method for the numerical simulation of plane strain rolling. *International Journal of Machine Tools and Manufacture*, **43(1)**, 89-102.
- [150] Shangwu X., Liu W.K., Cao J., Li C.S., Rodriques J.M.C., Martins P.A.F. (2005). Simulation of bulk metal forming processes using reproducing kernel particle method. *Computers and Structures*, **83(8-9)**, 574-587.

- [151] Chen J.S., Pan C., Wu C.T. (1997). Large deformation analysis of rubber based on a reproducing kernel particle method. *Computational Mechanics*, **19**, 211-227.
- [152] Foroutan M., Dalayeli H., Sadeghian M. (2007). Simulation of Large Deformations of Rubbers by the RKPM Method. *Proceedings of World Academy of Science, Engineering and Technology*, **20**, 178-182.
- [153] Dai K.Y., Liu G.R., Han X., Li Y. (2006). Inelastic analysis of 2D solids using a weak-form RPIM based on deformation theory. *Comput. Methods Appl. Mech. Engrg.*, **195**, 4179-4193.
- [154] Wang H., Li G.Y., Zhong Z.H. (2007). Parallel point interpolation method for three-dimensional metal forming simulations. *Engineering Analysis with Boundary Elements*, **31**, 326-342.
- [155] Dinis L.M.J.S., Natal J.R.M., Belinha J. (2009). The nonlinear analysis of 3D beams using a Radial Point Interpolation Meshless Method. *EUROMECH Solid Mechanics Conference*, Lisbon, Portugal.
- [156] Bhatti M. A.(2006). *Advanced topics in finite element analysis of structures*. John Wiley & Sons Inc: New York.
- [157] Y. T. Gu, Q.X. Wang, K. Y. Lam (2007). A meshless local Kriging method for large deformation analyses, *Comput. Methods Appl. Mech. Engrg.*, **196**, 1673–1684.
- [158] J. S. Chen, C. Pan, C. T. Wu (1997). Large deformation analysis of rubber based on a reproducing kernel particle method, *Computational Mechanics*, **19**, 211 – 227.
- [159] Y. T. Gu, C. Yan and P. K. D. V. Yarlagadda (2008). An Advanced Meshless Technique for Large Deformation Analysis of Metal Forming, *9th Global Congress on Manufacturing and Management*, Queensland, Australia.
- [160] J. R. Cho, H. W. Lee (2006). 2-D large deformation analysis of nearly incompressible body by natural element method, *Computers and Structures*, **84**, 293–304.

- [161] Cook Robert D., Malkus David S., Plesha Michael E., and Witt Robert J. (2002). *Concepts and Applications of Finite Element Analysis* Madison, University of Wisconsin.
- [162] Owen D.R., and Hinton E. (1980). *Finite Elements in Plasticity* Swansea, Pineridge Pres Limited.
- [163] Lubliner, J. (1990), *Plasticity theory*. Macmillan, Publishing, New York.
- [164] EA de Souza Neto, D Peri'c, DRJ Owen (2008). *Computational Methods for Plasticity: Theory and Applications*, Singapore, John Wiley & Sons Ltd.



## CURRICULUM VITAE

### PERSONAL INFORMATION

Surname, Name: BOZKURT Ömer Yavuz  
Nationality: Turkish (TC)  
Date and Place of Birth: 10 December 1978 , Gaziantep  
Marital Status: Married  
Phone: +90 535 367 1590  
Fax: +90 342 360 1104  
email: oybozkurt@gantep.edu.tr

### EDUCATION

Degree	Institution	Year of Graduation
MS	Gaziantep University, Graduate School of Natural and Applied Sciences	2006
BS	Gaziantep University, Department of Mechanical Engineering	2003
High School	Nizip Hasan Çapan Anatolian High School	1997

### WORK EXPERIENCE

Year	Place	Enrollment
2004- Present	Gaziantep University	Research Assistant

### FOREIGN LANGUAGES

English

### PUBLICATIONS

1. Kanber B., Bozkurt Ö.Y. (2008). A diagonal offset algorithm for the polynomial point interpolation method, *Commun. Numer. Meth. Engng.*, **24**, 1909-1922.
2. Kanber B., Bozkurt Ö.Y. (2007). Elastik, Büyük Deformasyon Problemlerinin Ağsız Noktasal İnterpolasyon Yöntemiyle Çözümü, *XV. Ulusal Mekanik Kongresi*, 521-531.
3. Kanber B., Bozkurt Ö.Y. (2009). Geometrically Nonlinear Analysis of 2D solids using Radial Point Interpolation Method, *2<sup>nd</sup> South-East European Conferences on Computational Mechanics*, 47.
4. Kanber B., Bozkurt Ö.Y. (2009). Radyal Noktasal İnterpolasyon Yönteminde Şekil Parametrelerinin Etkilerinin Araştırılması, *XVI. Ulusal Mekanik Kongresi*, 761-771.

### HOBBIES

RC model aircrafts and helicopters